To the Graduate Council:

I am submitting herewith a dissertation written by Terri Lynn Tramel entitled "An Improved Gas Nozzle for Laser Surface Alloying." I have examined the final copy of this dissertation for form and content and recommend that it be accepted in partial fulfillment of the requirement for the degree of Doctor of Philosophy, with a Major in Engineering Science.

Mary Helen McCay, Major Professor

We have read this dissertation
and recommend its acceptance:

Accepted for the Council:

Interim Vice Provost and
Dean of the Graduate School

An Improved Gas Nozzle for Laser Surface Alloying

A Dissertation
Presented for the
Doctor of Philosophy
Degree
The University of Tennessee, Knoxville

Terri Lynn Brock Tramel
May 2001

DEDICATION

This dissertation is dedicated to my husband

Robert Wallace Tramel

and my mother

Shirley C. Brock

who have given me love and encouragement,

and

my new son

Mark Robert Tramel.

ACKNOWLEDGMENTS

Research is not done in a vacuum by one person, and this research was no exception. I would like to thank the people at the University of Tennessee's Space Institute for all their help and support in my education over the past ten years. The CLA's staff: Newt Wright, Scott Scarbourgh, and Doug Warenberg were invaluable for getting the experiments done. Thanks goes out to the aeropropulsion group (Jim Goodman and Ricky Meek) for letting me use their water tunnel and Gary Payne for the all the machine shop work. A special thanks goes out to Oak Ridge National Laboratory's Dave Braski for letting me return for more Auger work. Lastly, thanks goes out to Mary Helen McCay for helping me finish this degree.

ABSTRACT

An experimental research project was undertaken to characterize the flow field surrounding the molten metal during laser alloying. In addition, an objective of this project was to design a protective gas nozzle system for laser alloying that would control the entrainment of the outside gas, provide a gentle pressure to the molten metal and not adversely effect the alloying process.

Existing nozzle geometries were selected for evaluation in a water tunnel simulation. The water tunnel simulation visualized a complex, three-dimensional oblique flow field, which was created by the Nd:YAG's optics/gas delivery package being configured 15 degrees from normal to the work surface to prevent reflection back into the optics. From the water tunnel simulation two geometries were characterized in gas trials with argon, nitrogen and helium gases. A convergent (conic) geometry and divergent geometry were evaluated by measuring the pressure field and oxygen content impinging on an instrumented flat plate. A divergent nozzle geometry was used in creating laser alloyed surfaces, and those surfaces were examined for oxygen content.

The water tunnel simulation provided general knowledge about the oblique jet impingement flowfield (with its recirculation zones and entrainment patterns), nozzle geometry selection (the 7 degree simple divergent), and the revelation about the unsteady swirling motion feeding into the nozzle entrance and proceeding through the entire flowfield. The water tunnel results suggest that possible improved protection of the molten metal can be achieved by changing the processing direction of the laser beam, providing a shroud gas around the jet, and improving the flow quality before the nozzle

entrance. The gas trials verified the flow patterns seen in the water tunnel simulation, and provided more specific flowfield details (impingement pressure profiles and percent oxygen profiles) with three gases helium, argon, and nitrogen. The laser alloy surfaces created were analyzed by Scanning Auger Microprobe, which could not provide definitive percent oxygen measurement.

TABLE OF CONTENTS

CHAPTER		PAGE
I.	INTRODUCTION	1
	The Need for a New Nozzle Design	1
	General Overview of Jets Used For Material Processing	3
	Current Protective Gas Nozzle Configuration	5
	General Comments on Laser Processing	7
	Technical Requirements for the New Nozzle Design	8
II.	BACKGROUND	11
	Summary of Previous Jet Impingement Research	11
	Theoretical Jet Flow	16
	Theoretical Jet Impingement Flow	18
	Surrounding Fluid Entrainment	21
	Subsonic Nozzle Geometries	26
	Laser Induced Surface Improvement, LISI^{SM}	37
	Jet Impingement for Laser Surface Alloying	40
	Work Zone Definition and Determination	41
III.	PLAN TO DEVELOP THE NOZZLE	46
	Calculation of Maximum Nozzle Pressure	47
	Nozzle Flow Simulation-Water Tunnel	50
	Nozzle Gas Flow Trials	51
	Laser Trials	52
IV.	WATER TUNNEL SIMULATION	53
	UTSI's Water Tunnel	53
	Data Acquisition	57
	Water Tunnel Experimental Procedure	59
	Water Tunnel Models Description	60
	Nozzle Geometry Water Simulation Evaluation	72
	Each Nozzle Geometry's Water Simulation Evaluation	77
	Water Tunnel Conclusions	87
V.	GAS TRIALS	88
	Hardware and Re Differences	88
	Gas Trials Test Plan	91
	Experimental Setup	93
	Experimental Procedure	98
	General Gas Trials Results	104
	Specific Gas Trials Results	116

VI. LASER TRIALS 138
Laser Trial's Hardware 138
LISI[SM] Surface Procedure 140
LISI[SM] Sample Analysis 143
Results of the Laser Trials 145

VII. CONCLUSIONS AND RECOMMENDATIONS 154
General Conclusions 154
Specific Conclusions 155
Recommendations 158

LIST OF REFERENCES. 161

APPENDICES 167
Appendix A- Calculations 168
Appendix B- Supplemental Background 180
Appendix C- Supplemental Gas Trial Information. 193

VITA. 199

LIST OF FIGURES

FIGURE **PAGE**

1. Current Gas Delivery Package Configuration 6

2. Turbulent Round Jet Flow Development Showing Different Regions and Velocity Profiles 17

3. Schematic of a Jet Impinging On a Flat Plate, Showing the Three Distinct Flow Regimes 20

4. Schematics of Ideal Jet Entrainment 22
   a) Round Turbulent Jet Issuing into an Open Medium
   b) Near-field Flow Vortex Structure in a Natural Free Round Jet

5. Conic Nozzle Geometry 27
   a) Generic Conic Nozzle Geometry
   b) Conic Laser Cutting Nozzle 1
   c) Conic Laser Cutting Nozzle 1

6. Examples of Bellmouth Nozzle Geometries 29
   a) Schematic of a Generic Bellmouth Nozzle Geometry
   b) A Closed Circuit Subsonic Wind Tunnel

7. Divergent Nozzle Geometry Examples 31
   a) Generic Divergent Nozzle Geometry
   b) A Plasma Spray Gun Contoured Divergent Nozzle
   c) Convex Divergent With A Straight Pipe Nozzle
   d) Concave Divergent with a Straight Pipe Nozzle
   e) Straight Angle Water Nozzle
   f) Convex Divergent With a Straight Pipe Water Nozzle

8. Examples of Convergent/divergent Nozzle Geometry 35
   a) Generic Geometry
   b) Laval Laser Cutting Nozzle

9. Examples of Shrouded Nozzles 36
   a) Contoured Dievergent Nozzle of a Plasma Spray Gun
   b) Assist Gas in Laser Cutting

10. Cross Sectional Stages of Laser Surface Alloying 38

11. A Schematic of UTSI's Closed Circuit Water Tunnel 54

12. The 3X Plenum and Nozzle Model Installed into the UTSI's Water Tunnel 55

13. Water Tunnel Evaluation Criteria 58

14. Div1 Nozzle Geometry. 62
a) Sketch
b) Side View
c) Bottom View

15. Div1 Nozzle with Holed Shroud Geometry. 63
a) Sketch
b) Bottom View
c.) Side View

16. Conic Nozzle Geometry. 64
a) Sketch
b) Bottom View
c) Side View

17. 60° Contraction Nozzle Geometry. 66
a) Sketch
b) Bottom View
c) Side View

18. Concave Nozzle Geometry. 67
a) Sketch
b) Side View
c) Bottom View

19. Convex Geometry. 68
a) Sketch
b) Side View
c) Bottom View

20. Rough Concave Nozzle Geometry 69
a) Sketch
b) Side View
c) Bottom View

21. 7° Simple Divergent Nozzle with Holed Shroud Geometry. 70
a) Side View
b) Bottom View

22. 7° Simple Divergent Nozzle With Slotted Shroud. 71
a) Sketch
b) Side View
c) Bottom View

23. General Features of Oblique Jet Impingement 73

24. Swirling Motion in Plenum 75

25. The General Flow Fields of the Three Working Distances. 76

26. Nozzle Edge Entrainment. 80
a. Front Nozzle Edge Entrainment.
b. Side Nozzle Edge Entrainment.
c. Rear Nozzle Edge Entrainment

27. 7° Simple Divergent Nozzle Nozzle Entrainment. 81
a) Rear Nozzle Edge Entrainment Without Shroud Flow
b) Rear Nozzle Edge Entrainment With 2 GPM of Shroud Flow

28. Rear Jet Entrainment. 82
a) Into Jet
b) Being Pulled Into a Nozzle

29. Front Jet Entrainment 84

30. Recirculation Zones. 85
a) Rear Recirculation Zone
b) Front Recirculation Zone

31. Differences between. 90
a) Gas Delivery Package I
b) Gas Delivery Package II

32. Picture of the Gas Trials Experimental Setup. 95

33. Instrumented Copper Plate Used in the Gas Trials. 95

34. Gas Trial's Conic Nozzle. 99
a) Sketch
b) Side View
c) Bottom View

35. Gas Trial's 7° Simple Divergent Nozzle. 100
a) Sketch
b) Side View

36. Gas Trials 7° Simple Nozzle With Shroud. 101
a) Sketch
b) Top View
c) Bottom View

37. The Copper Plate's Static Tap Arrangement 103

38. Jet Entrainment in the Gas Trials with the Conic Nozzle. 105

39. Nozzle Edge Entrainment During the Gas Trials with the 7° Simple Nozzle with Shroud. 105

40. Raw Pressure Data from the Conic Nozzle, Impingement Angle of 15°, Working Distance of 6.30mm, with Ar Gas. 107

41. Typical He Pressure Profile, Taken with the 7° Simple Nozzle Without Shroud. 109

42. Increasing Flowrate Results in Increasing Imingement Pressure. 111

43. Increasing the Working Distance Results in Decreasing Pressure. 112

44. Pressure Profile Indicating Impingement Region. 113

45. Conic Nozzle, Ar, Showing the Percent O_2 at 117
a) 15° Impingement
b) 0° Impingement

46. Conic Nozzle, N_2, Showing the Percent O_2 at. 118
a) 15° Impingement
b) 0° Impingement

47. Conic Nozzle, He, Showing the Percent O_2 at. 119
a) 15° Impingement
b) 0° Impingement

48. Conic Nozzle, Ar, Showing the Pressure Distribution at 122
a) 15° Impingement
b) 0° Impingement

49. 7° Simple Nozzle, Ar, Showing the Percent O_2 at. 123
a) 15° Impingement
b) 0° Impingement

50. 7° Simple Nozzle, N_2, Showing the Percent O_2 at. 124
a) 15° Impingement
b) 0° Impingement

51. 7° Simple Nozzle, He, Showing the Percent O_2 at. 125
a) 15° Impingement
b) 0° Impingement

52. 7° Simple Nozzle, with Ar Gas, Comparison of 127
a) Without the Shroud
b) With the Shroud Flow at Normal Impingement Angle

53. 7° Simple Nozzle, with Ar Gas, Comparison of 128
a) Without the Shroud
b) With the Shroud Flow at Oblique Impingement Angle

54. 7° Simple Nozzle, with N_2 Gas, Comparison of 129
a) Without the Shroud
b) With the Shroud Flow at Normal Impingement Angle

55. 7° Simple Nozzle, with N_2 Gas, Comparison of 130
a) Without the Shroud
b) With the Shroud Flow at Oblique Impingement Angle

56. 7° Simple Nozzle, with He Gas, Comparison of 131
a) Without the Shroud
b) With the Shroud Flow at Normal Impingement Angle

57. 7° Simple Nozzle, with He Gas, Comparison of 132
a) Without the Shroud
b) With the Shroud Flow at Oblique Impingement Angle

58. Argon Gas Nozzle Comparison. 134

59. Nozzle Comparison with He Gas. 135

60. N_2 Gas Comparison of the Nozzles 136

61. The Nd:YAG Laser Setup for Processing LISI^{SM} Surfaces 139

62. Full Scale Protective Gas Nozzle 141
a) Side View
b) Bottom View

63. Percent Oxygen Measured with the Processing Nozzle Using. 147
He Gas, with Oblique Jet Impingement

64. Percent Oxygen Measured with the Processing Nozzle Using. 148
N_2 Gas, with Oblique Jet Impingement

65. Percent Oxygen Measured with the Processing Nozzle Using. 149
Ar Gas, with Oblique Jet Impingement

66. SEM Photograph of a Typical Cross-section of Chromium on 153
1010 Steel Alloy Layer

A-1. Workzone Calculation of Steel at R=0.58, 4mm Line Beam. 170

A-2. Workzone Calculation of Steel at R=0.0, 4mm Line Beam. 171

A-3. Workzone Calculation of Aluminum at R=0.8. 172

A-4. Workzone Calculation of Aluminum at R=0.0. 173

B-1. The Area-Mach Number Relationship Plotted, Showing
The Two Values of Mach Number for Each Area
Ratio. 183

B-2. The Geometry for Converging Nozzle Flow into a Receiver 184

B-3. Mass Flow in a Converging Nozzle. 187
a) Ideal Mass Flow
b) Actual Mass Flow

B-4. The Effect of the Boundary Layer on Subsonic Flow. 189
a) Subsonic Diffuser
b) Subsonic Nozzle

B-5. The Converging/Diverging Nozzle Flow. 191
a) Generic Converging/Diverging Geometry
b) Flow Regimes of a Converging/Diverging Nozzle

NOMENCLATURE

A^*	Nozzle Area at Throat
A	Nozzle Exit Area (or the Area M is Being Calculated)
A_2	Cross Sectional Area at Position 2
Ar	Argon
B	Pressure Balance Equation Constant
C_p	Specific Heat of a Gas at a Constant Pressure
°C	Degrees Centigrade
CFD	Computational Fluid Dynamics
cfhr	Cubic feet per hour
Cm	Centimeter
CNC	Computer Numerical Controlled
D	Critical Dimension, Diameter at the Nozzle Exit
F	Entrainment Factor
GPM	Gallons per minute
h	Local Heat Transfer Coefficient
He	Helium
hp	horse power
I_0	Normal Incident Light (Laser) Intensity
I	Light (Laser) Intensity
K	Thermal Conductivity of the Metal
LISI^{SM}	Laser Induced Surface Improvement
M	Mach Number

$\dot{m}_o$	Mass Flowrate of the Gas
m	Nondimensional X Position
mm	millimeter
mm/min	millimeter per minute
n	Nondimensional r (radial) Position
N/m^2	Newtons per meters squared
NASA	National Aeronautics and Space Administration
Nd	Neodymium
N_2	Diatomic nitrogen
O_2	Diatomic oxygen
P	Power
P_0	Total Pressure
P_e	Static Pressure at the Nozzle Exit
p_c	Critical Pressure
p_{jet}	Jet Pressure
p_r	Recoil Pressure
p_{surten}	Molten metal surface tension pressure
p_1	Static Pressure at Station 1
p_2	Static Pressure at Station 2
q	Rate of Heat Transfer
r	Radial Location
R	Reflectivity

Rad	Radius of the melt pool
Re	Reynolds Number
SEM	Scanning Electron Microscope
SM	Special Mark
T	Static Temperature
T_s	Temperature of Metal Surface
T_c	Temperature of Cooling Gas
T_i	Initial Jet Temperature
Ti	Titanium
$T\infty$	Temperature at Infinity, Usually the Surrounding Temperature
T_w	Temperature of the Wall
T'	Isotherm temperature
T_0	Initial Temperature of the Metal
UTSI	University of Tennessee Space Institute
V	Velocity of the Gas
VSTOL	Vertical/Short Take Off and Landing
X	Horizontal Location

γ	Gamma, Ratio of Specific Heats of the Gas
ρ_m	Density of the Metal
ρ	Rho, Density of the Gas

δ	Delta, Difference of a Parameter at Two Locations
v_1	Velocity at Station 1
μ	Viscosity of the Gas
α	Thermal diffusivity
σ	Surface Tension
°C	Degrees Celsius

CHAPTER I

INTRODUCTION

This research was initiated to develop a protective gas nozzle designed specifically to meet the needs of the laser surface modification process used to produce Laser Induced Surface Improvement, or LISI^{SM} surfaces. Gas systems are often used with laser systems to provide an inert atmosphere for the laser beam to interact with the material, provide propulsive force to propel the molten and vaporized metal out of the way, or to be a source of energy for an exothermic reaction to take place with the material [1][1]. LISI^{SM} is a laser created alloy surface developed by University of Tennessee Space Institute, UTSI, researchers that has been proven successful in alloying the surface of several commercial metals.

The application of LISI^{SM} includes the melting of both the precursor (a pre-applied slurry mixture of desired elements) and the substrate with the laser, convective mixing of the molten materials, and the rapid cooling and solidification of the molten metal mixture. LISI^{SM} has been used to create wear and corrosion-resistant alloy layers on the surface of steels and aluminums [2 and 3]. LISI^{SM} has been performed on small objects in the pristine laboratory environment. It is now time to apply LISI^{SM} to more objects in a non-laboratory environment. In order to enable that, a protective gas nozzle system must be developed for LISI^{SM}.

THE NEED FOR A NEW NOZZLE DESIGN

The purpose of the process to create the LISI^{SM} surface is to put the desired elements or elemental compounds into the surface of a metal. The primary elemental/compound delivery system is the slurry pre-cursor. For instance, if silicon or silicon carbide is desired it is contained in the pre-cursor. The laser beam melts both the

[1] Numbers in brackets refer to similarly numbered references located in the List of References.

precursor and the surface of the substrate, forming a mixture of liquid metal. However, many liquid metals can absorb oxygen, nitrogen or both. Depending on the other elements present, oxides or nitrides can form. When the liquid metal resolidifies, the presence of some oxides or nitrides can be detrimental to the mechanical properties of the resolidified metal. For instance, when titanium is between 400°C and 650°C it will absorb nitrogen and oxygen. Since titanium's liquidus temperature is 1670°C, this means it is absorbing nitrogen and oxygen while in the heated solid state. The presence of these elements in solid titanium makes the metal brittle and prone to cracking [4 and 5]. This is a common defect in titanium welding and, therefore, gas shielding practices exist to eliminate the problem like the American Welding Society's Recommended Practices for Gas Tungsten Arc Welding of Titanium Pipe and Tubing [4].

In order to utilize laser surface alloying to its fullest potential, control of the presence of each element in the alloy layer must be achieved. That is, what goes into the precursor must be controlled and what elements are absorbed in the molten metal must also be controlled. This research project was undertaken to first understand the nozzle flow characteristics that effect the control of the gas around the molten metal, and second, to develop a protective gas nozzle design that utilizes the knowledge obtained in a practical manner.

In general, the practical challenge is to take gas from a high-pressure cylinder and deliver it to the workpiece in a manner that reduces or eliminates the air to which the molten metal is exposed during the laser operation. The basic delivery system to be evaluated is a contoured subsonic nozzle and the basic workpiece to be evaluated is a flat piece of metal. Nozzle flows impinging on a flat surface occur in many diverse engineering applications ranging

from the high tech aerospace applications to the relatively low-tech industrial cooling/drying applications. Many different applications were reviewed for this research, but the seven general areas reviewed for nozzle impingement on a flat surface were the jet engine exhaust nozzles, laser cutting nozzles, laser welding shield systems, plasma spray guns, combustor fuel nozzles, industrial drying/cooling nozzles, and water jet cutting nozzles.

GENERAL OVERVIEW OF JETS USED FOR MATERIAL PROCESSING

Jets produced by nozzles have been of interest in the field of aerodynamics for a long time. A nozzle is defined as a short tube with a constriction in it designed to speed up or direct a flow. This flow is referred to as a jet. Nozzles are used to produce jets in applications from aircraft engines to garden hoses and are usually described by the speed range of the flow. Subsonic nozzles produce a jet speed less than the speed of sound; sonic nozzles produce a jet at the speed of sound; and supersonic nozzles produce a jet at a speed greater than the speed of sound. The area of interest for this research is that of jets (produced by a nozzle) hitting a near-flat surface. A jet hitting a surface is normally referred to as jet-impingement.

Many of the laser material processes, laser cutting, laser drilling, laser alloying, and laser welding, sometimes require shield gas assistance to enhance the process. Gas delivery systems are used regularly during laser cutting, to enhance the process, normally in three different ways. First by physically removing the vaporized and molten metal, secondly by providing the fuel for the exothermic chemical reaction that actually does the cutting, and lastly by suppressing or controlling the plasma cloud. When cutting, the gas delivery system provides the pressure for the ejection to take place. In some cases to speed up the laser cutting process, the shield gas provides the oxidizer that burns the metal and aids in its removal. When laser cutting (or laser drilling), the ionization of the metal can lead to the formation of a plasma cloud that can block the

laser beam's access to the metal. The shield gas removes the plasma cloud from between the laser beam and the workpiece, allowing for uninterrupted cutting. The goal of the supersonic shield gas nozzle for laser cutting is to provide the jet velocity and jet pressure, so that the molten material is expulsed while also controlling or suppressing the ionization of the shield gas. The supersonic nozzle is used for supplying a higher pressure to the molten metal for removing it out of the kerf region (or the cut region).

Welding of certain metals, like titanium, require a shield gas of Argon or Helium to protect the molten metal from contamination. The goal is to protect the molten metal with a gentle flow of gas that displaces the surrounding air, while the molten metal of the weld solidifies. These nozzle delivery systems must provide a low pressure gas jet that aids in the solidification process, but does not expulse the molten metal [5]. Usually the gas delivery system for welding consists of holes drilled in a manifold type device plumbed at a gas bottle to shield the top of the weld bead (the gas is usually Argon or Helium). Thought is usually not given to the design of the gas orifice; the idea is just to flood the area with the gas and displace the surrounding air. With some welding applications a welding box or a bagged system is used to protect the bottom of the weld bead. The goal here is to take a volume of space and displace the air with Argon or Helium. The welding is then performed in the volume now void of air.

Shield gas nozzle systems used for laser alloying and laser cladding also requires gentle gas flow around the laser/material interaction zone, like welding. In the laser surface alloying application, the low-pressure requirement dictates that the nozzle will be a subsonic nozzle (one that produces the lowest possible impingement pressure). Supersonic nozzles require a large total pressure that would remove the molten metal. Later calculations will show that the pressure required for laser alloying is so low that the nozzle is in the low subsonic regime. Recent research has evaluated the flow dynamics of a laser cladding metal feed system, but the research did not evaluate the shield gas

aerodynamics [6]. This research dealt with delivering the powder metal to the interaction point of the laser and the substrate.

CURRENT PROTECTIVE GAS NOZZLE CONFIGURATION

All protective type gas nozzles produce jets to supply gas (normally inert gas) to the workpiece. The nozzle configuration used in the laser surface processing to create the LISI[SM] surface is shown in Figure 1. The gas delivery package consists of a cylindrical structure 50.8 mm in diameter by approximately 165 mm long. At the top of the package are the input ports for the cooling water, the fiber optic cable, and the gas. The fiber optic cable from the Nd:YAG laser is mounted in the center of the package, while the cooling water and the gas are fed through the outside walls of the gas delivery package. As the laser beam exits the fiber optic cable, the beam diverges until it reaches the first lens in a series of collimating and focusing lenses that encompass the remainder of the gas delivery package. The protective gas nozzle is mounted on the end of the gas delivery package with the gas itself being injected perpendicular to the entrance of the nozzle.

The orientation of the gas delivery package to the surface of the workpiece is vital to the process. The optics produces a line beam that measures approximately 4 mm by 700 microns at focus. Maximum energy delivered by the beam occurs at focus, and therefore optimal processing is reached when the gas delivery package is placed where the workpiece surface is near or at focus. This occurs for this particular gas delivery package at 50 mm from the exit of the protective gas nozzle. The package is oriented 15 degrees from normal to the workpiece to prevent the back reflection of the laser beam off the work surface from damaging the optics. The processing speed for this gas delivery package ranges from 1000 mm/min to approximately 5000 mm/min for most steel and aluminum applications.

The conic nozzle used is mounted by screwing into the gas delivery package. The entrance of the conic nozzle is 15.875 mm diameter, with a convergence angle of 7

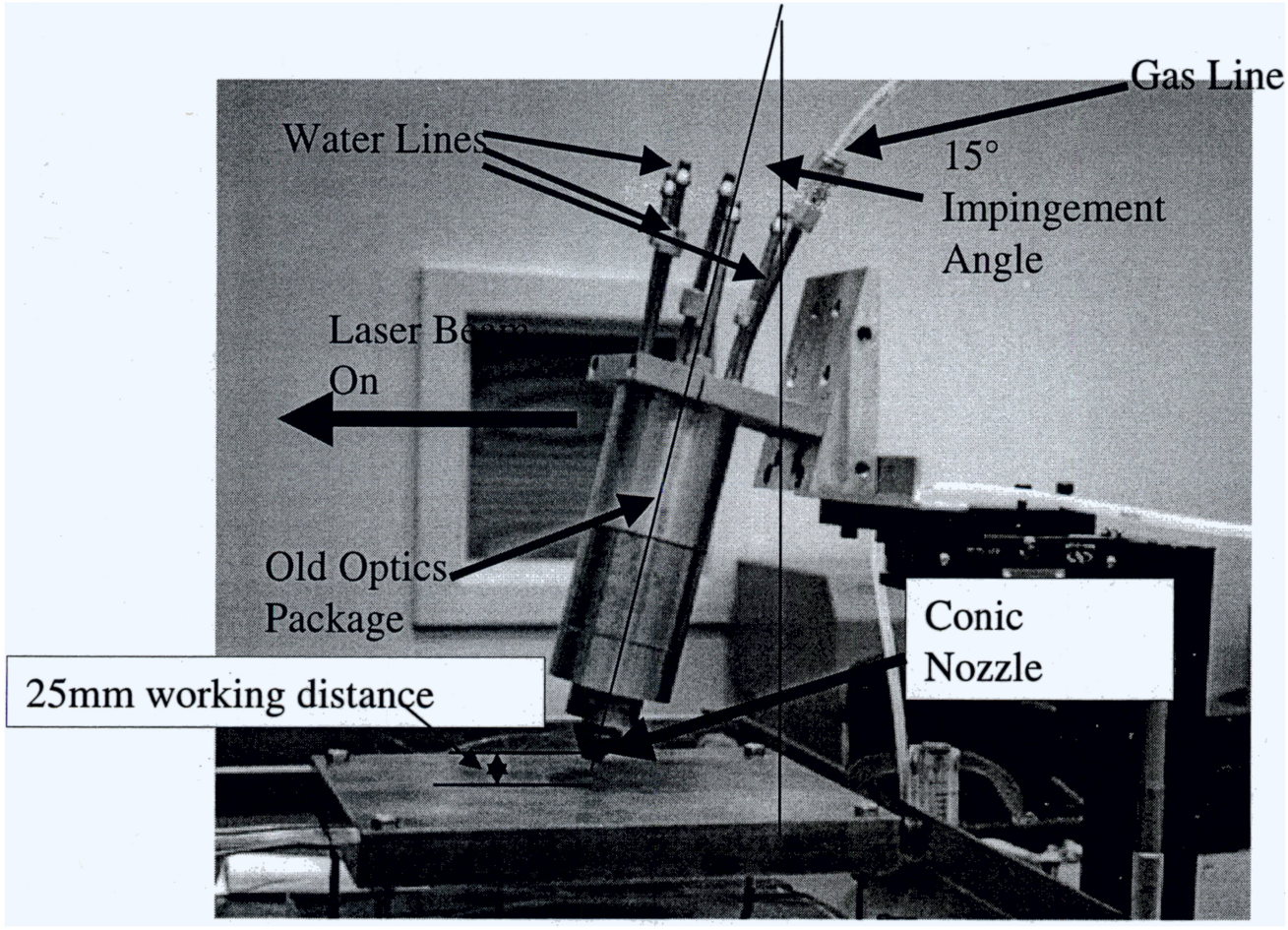

Figure 1: Current Gas Delivery Package Configuration

degrees, and a length of 29.62mm. This results in an exit diameter of 9.5mm and 16.92 mm of the nozzle extending beyond the optics package. The jet from the protective gas nozzle is injected into ambient air; therefore the nozzle exit static pressure is ambient pressure $1.01325X10^5$ N/m^2 (or 14.7 psi). The total pressure of the gas is set at a level that "feels right" to the operator.

GENERAL COMMENTS ON LASER PROCESSING

This research was initiated to research the aerodynamic flow field of the protective gas nozzles used for laser surface alloying and to develop a nozzle geometry that produces an exceptable alloy surface. This research also highlights some fundamental processing differences between using a CO_2 laser for processing and using a Nd:YAG laser for processing. The CO_2 laser's beam delivery system consists of mirrors and lens, while the Nd:YAG's delivery system is normally a fiber optic cable. The CO_2's beam is usually oriented normal to the work piece surface. Any reflective energy bouncing off the workpiece surface and absorbed delivery system, is not large enough to cause short term damage. The hardware for the CO_2's delivery system is usually too far way from the work surface to absorb any of the reflective energy. The Nd:YAG's delivery system is a fiber optic cable expanded and focused by optics in a gas delivery package that is only millimeters away from the workpiece. The gas delivery package does absorb some of the reflective energy bouncing off the workpiece. If the gas delivery package is oriented normal to the surface of the workpiece, a large amount of energy is absorbed. Past experience has shown that the absorbed reflected energy is enough to break the lens and melt the end of the fiber optic cable. The gas delivery package is thus tilted 15 degree away from normal to the workpiece surface to reduce some of the reflective energy from being absorbed by the optics. With internal water cooling and the 15 degree tilt, the heat absorbed by the optics is manageable. This 15 degree tilt, while it seems minor, has a tremendous effect on the flow field, since it adds significant additional

asymmetries. The flow field becomes skewed and certain flow complexities occur in parts of the flow pattern. The jet impingement is now more complex.

Other differences between processing with a CO_2 mirror/lens system and processing with a Nd:YAG's fiber optics cable/lens system should be noted. Previous use of laser processing has been with drilling and cutting, processes that in the past were performed with a CO_2 for relatively short periods of time (measured in seconds). Now laser surface alloying is being performed on Nd:YAG laser systems for longer periods of time (measured in tens of minutes), adding much more heat to the optics. With laser surface alloying, heat management becomes vital. Each piece of hardware from the beginning of the fiber optics cable to the gas nozzle at the end of the gas delivery package must have some sort of cooling. This cooling is often not a part of the standard hardware delivered by the laser manufacturer and must be added for laser surface alloying large areas.

As laser processing technology advances, new complexities emerge with hardware or procedures that have been used for years. This research addresses just one of those new complexities: the protective gas nozzle for laser surface alloying with a fiber optics delivery system at a 15 degree angle (as measured normal to the surface of the workpiece).

TECHNICAL REQUIREMENTS FOR THE NEW NOZZLE DESIGN

In general, the overall objectives for this research project is to design a protective gas nozzle system for LISI^{SM} that (in order of priority):

1) Controls entrainment of the outside environment. By controlling entrainment, the new gas nozzle system will provide a protective environment for the molten metal to form the desired homogenous alloy layer.

2) Provides gentle pressure to the workpiece so that the molten metal is not adversely effected (does not remove the molten pool).

Consider the case of a jet being injected into a surrounding environment. Entrainment is the physical phenomenon of the surrounding fluid being pulled into the jet by the lower pressure at the edge of the jet. In this case of the jet injecting into an ambient environment, the surrounding fluid is air and the entrainment of that air into the jet pulls air over the molten metal and contaminates the resolidified metal. Controlling the gaseous contamination can only be achieved when the entrainment is controlled. The volume of space around the molten metal where the entrainment must be controlled will be named the work zone. The goal of this research is to control the entrainment of the surrounding air so that the air is not drawn into the work zone.

The review of the current state of jet impingement (to be summarized in Chapter 2) shows that the requirements for a laser surface alloying protective gas nozzle do not fit exactly into any known research areas. The low pressure requirement drives the nozzle to be in the subsonic range, while all of the laser cutting nozzles are high pressure supersonic nozzles, and most of the aerodynamic applications are also supersonic nozzles. Acoustic research experimented with subsonic nozzles, but while that research performed extensive pressure field measurements, it did not analyze the entrainment of the surrounding air. The goals of the plasma spray nozzle most closely match the goals of the laser surface alloying nozzle. Both nozzles are subsonic nozzles and both nozzle designs address entrainment. The major difference lies in the fact that the entrainment for the plasma spray nozzle must be controlled inside the nozzle itself, while with laser surface alloying the entrainment must be controlled in the free jet/impingement region in addition to the nozzle itself. The entrainment must be controlled to prevent dust or unwanted gaseous elements from contaminating the final alloy layer. The research

documented here expands the current state of impingement flow and it helps address the new complexities of Nd:YAG material processing.

CHAPTER II

BACKGROUND

SUMMARY OF PREVIOUS JET IMPINGEMENT RESEARCH

The 1970's and 1980's have produced a large volume of work dealing with jet impingement, mainly due to the Marines Harrier Jump Jet (a VSTOL fighter aircraft) and the US Air Force's Y-17 short take-off and landing transport aircraft program. The Vertical and Short Take-Off, VSTOL, vehicles produced jets hitting the ground, and jets (both supersonic and subsonic) hitting the surfaces of various airfoils [7,8,9,10, 11, and 12]. Even though most of this work deals with supersonic flow, many of the previous research efforts started with subsonic nozzle jet impingement, which is directly related to the current research. The Harrier program produced a large body of research with two engine jets impinging on the ground. The Harrier researchers were concerned with effects of the jet engine impingement on the lift characteristics in ground effect of the aircraft and obviously engine ingestion. They began their research with the most basic jet impingement problem, a single subsonic jet impinging normally on a flat plate, then progressed to single supersonic jet impingement, and finally ended with dual supersonic jet impingement. The Y-17 researchers evaluated blowing part of the engine exhaust over the wing and the flaps of the aircraft to increase the lift during take-off and landing to decrease the amount of runway needed. Again, the researchers began with a subsonic jet impinging normally to a flat plate then moved to oblique impingement on curved surfaces.

Recent research efforts in laser cutting have concentrated on determining the flowfield characteristics that improve cut quality and in designing conic/supersonic shield gas nozzle designs for laser cutting that provide the desirable flow characteristics [13, 14, 15, 16, 17, 18, 19, 20, 21, 22, 23, 24, and 25]. The goal of the supersonic shield gas nozzle for laser cutting is to provide the jet velocity and jet pressure so that the molten material is expulsed while also controlling or suppressing the ionization of the shield gas. The supersonic nozzle is used for supplying a higher pressure to the molten metal for removing it out of the kerf region. The recent work concentrated on improving the quality of the cut and increasing the speed of the cutting process [14]. The effects of conic and supersonic Laval nozzles have been evaluated [18], along with the effects of using different combinations of Nitrogen, Argon, Air and Oxygen gases [19]. Numerical simulation showed that the kerf cut quality was better when the flow remained attached in the kerf region [15].

Jet-impingement in industrial applications is used mainly for drying or cooling sheets during the manufacture process. The goal here is to understand the convective heat transfer that is occurring in order to optimize the process for economic considerations. The equation governing the convective heat transfer is Newton's law of cooling:

$$q=h(Ts-Tc)$$

Where q is the rate of heat transfer, h is the local heat transfer coefficient, Ts is the temperature of the surface, and Tc is the temperature of the cooling gas. While the equation is simple, the difficulty in heat transfer is determining h. h is completely dependent on the aerodynamics that are occurring for each application and a majority of

the research found deals with understanding the relationship between the aerodynamics and h for specific applications. The entrainment of the surrounding environment into the cooling jet can have a serious detrimental effect on h if the surrounding environment's temperature is significantly different from that of the cooling jet. This effect is significant enough that some research concentrates solely on entrainment.

The metal fabrication process is concerned with blow drying sheets of molten metal to form sheet metal. H. Martin [26] performed an exhaustive study of nozzle configuration for blow drying sheets of material in industry. His work was mainly concerned with the heat transfer and mass (usually water) removal on the surface of the flat plate. Unlike most early researchers, Martin did mention entrainment; however, he thought the effects were minimal. Later researchers have concentrated their efforts on studying the heat transfer occurring on the surface of the flat plate from the impinging gas jet. Striegl and Diller looked at how the effect of entrainment of the surrounding fluid on the local heat transfer rates of a single jet and then of multiple jets [27 and 28]. Their conclusion was that whenever there is a temperature difference between the jet and the surrounding fluid, then there would be an entrainment effect on the local heat transfer rates. They found that the effects were most pronounced in the wall jet region, that region of flow away from the impingement point of the jet.

NASA Lewis has been studying the acoustics associated with jets from turbine engines. One phenomenon that they encountered was that there was an increase in sound power emanating from impinging jets relative to free jets. To evaluate this problem Lewis performed sensitive velocity and pressure measurements in a subsonic turbulent jet

impinging normal to a large flat plate. They were able to determine that the increase in sound power was due to the increase in the volume of the highly turbulent flow [29]. However, the effects of entrainment on sound power were not addressed.

Another relevant class of jet flows is that of water jet flow. The water jet flow reviewed were the flows associated with water jet cutting nozzles and water jet fire fighting nozzles. Research for the water jet cutting nozzles concentrated on the delivery of the maximum amount of total pressure to the object for cutting. The research for fire fighting nozzles concentrated on a combination of range and volume designed to deliver optimum fire-fighting use. In his work on studying the effect of nozzle geometry design on the stability and performance of turbulent water jets [30], Theobald tested straight edged divergent nozzles, concaved divergent nozzles, and convex divergent nozzles. He found that the concaved divergent nozzle with a smooth contraction between the supply to the outlet produced the best water jet in terms of stability, range and distribution, this particular geometric configuration may be applicable to the LISI^{SM} design.

Other nozzle applications that are relevant to this research are the plasma spray gun nozzle and the combustor fuel nozzle. The purpose of the plasma spray gun is to deposit thermal spray powders onto a substrate. Plasma guns use a subsonic nozzle with injection of a secondary gas to minimize the mixing of the surrounding air with the nozzle jet. Any addition of oxygen to the nozzle gas flow results in oxidation of the injected powders prior to their impact on the substrate, resulting in reduced adherence to the substrate. In designing the shrouding attachment nozzles, certain constraints exist. As the powder particles tend to disperse radially along the nozzle length, divergent

nozzles are required, and most of the commercially made nozzles are simple diverging conical nozzles. The research conducted by Janovic and Mostaghimi [31] studied the influence of nozzle exit angle, gas flow rate, energy losses and the shape of the nozzle exit. A combination of numerical and experimental simulations was performed to evaluate different geometries and develop the shrouded contoured divergent nozzle. The final design consists of a subsonic nozzle with the contour of a streamline, surrounded by sixteen shroud jets. The contour of the nozzle was based on the analysis of the streamlines calculated by a mathematical model, which solves the fully elliptic Navier-Stokes system of differential equations. The addition of the gas shroud improved the entrainment in the free jet region by delaying the mixing of the surrounding air with the nozzle flow. This resulted in lower concentrations of entrained air in the free jet region.

Small gas-turbine engines are very dependent on the performance of fuel nozzles for combustion efficiency. In this particular application, multiple nozzles are mounted onto the combustor chamber and inject fuel into the chamber. The fuel nozzles must provide the flow pattern necessary to entrain the air and mix it with the injected fuel. Fuel nozzles must adequately atomize and disperse liquid fuel into the combustor. The design of these small nozzles is complex, with jet swirls being introduced axially along the nozzle length. These nozzles involved four and five gas inputs and would add too much complexity for a laser surface alloying application. The research by Smith, Fuller and Crocker [32] evaluated different injection angles/combinations with numerical analysis (mathematical simulation) to narrow the alternatives down to four configurations

for combustion rig testing. The thirty numerical evaluations were performed using the commercial computational fluid dynamics, CFD, package called CFD-ACE.

THEORECTICAL JET FLOW

The flow produced by the nozzle is called a jet. Supersonic jets are characterized by the formation of shock waves and/or expansion waves beginning at the nozzle exit plane and forming downstream. Since the jets of interest for this research project are subsonic jets, the development of supersonic jets will not be covered here. What will be covered here is the subsonic turbulent jet discharging into an environment of slower velocity flow. Abramovick [33] says that laminar jets are very rare and almost all jets are turbulent, while Popiel and Trass [34] believe that the flow starts off with a laminar boundary layer out of the nozzle that transitions to turbulent soon after. The laminar boundary layer (or shear layer) is smooth and orderly, but given enough length naturally wants to become a turbulent boundary layer which is characterized by boundary that is erratic and disorderly.

For our purposes, only round jets will be considered. Figure 2, shows a round jet development. The flow is divided into three distinct regions. The first region consists of the potential core surrounded by a shear layer or jet boundary layer, which in turn is surrounded by a fluid having its own velocity. The potential core has the uniform velocity created by the conditions at the nozzle exit, and its length varies from 4 exit diameters to 6 nozzle exit diameter [33]. One of the basic characteristics of jet flow is that the static pressure remains constant throughout the flow, because the velocity in the potential core remains constant. The second region starts at around 5 nozzle exit

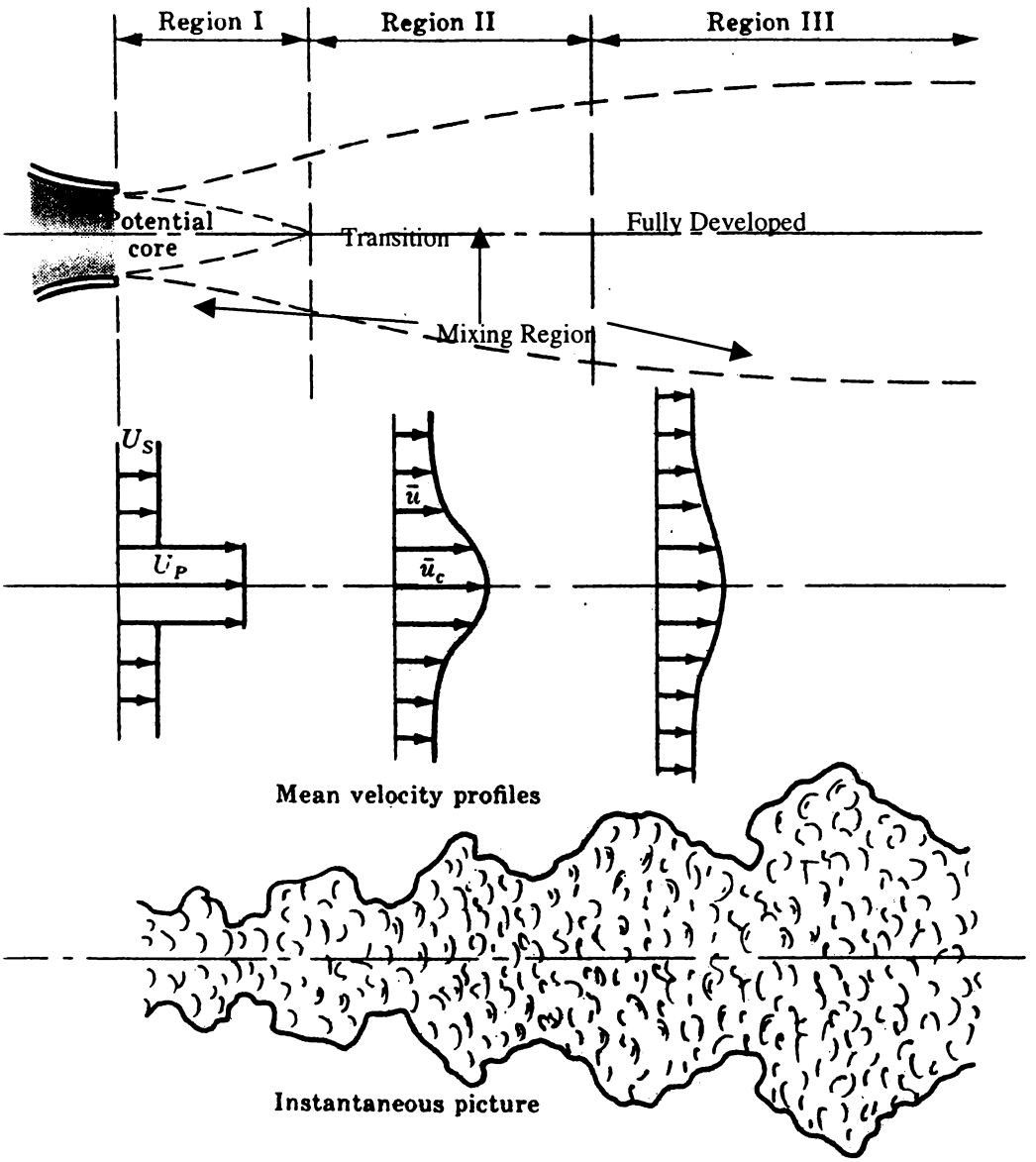

Figure 2. Turbulent Round Jet Flow Development Showing Different Regions and Velocity Profiles [8 and 61].

diameters and extends to approximately 8 nozzle exit diameters and is a transition region. The potential core is absent, but no established velocity profile exists yet. Region three is where the effect of the potential core is negligible and the flow is characterized by the familiar Gausian velocity distribution, similar to developed pipe flow.

The thickness of the jet boundary layer, or shear layer starts off zero at the nozzle exit and grows as the jet moves downstream. In the first region, the jet boundary layer is laminar, and is intrinsically unstable. The jet boundary layer grows because the particles of the surrounding fluid start to be pulled along with the jet and commingle with the particles of the jet that have slowed down, and it grows because it is unstable. This commingling of the two groups of particles increases downstream and causes the jet boundary layer to grow and gradual consume the non-viscous, potential core flow. The second region, the transitional region, is also where the jet boundary layer begins to lose its ordered structure and the transitional to turbulent flow is just showing. The beginning of the third region, where the velocity field becomes fully developed, is also marked by the complete transition to turbulent flow with its disorganized large turbulent eddies. Several analysis methods have been developed for determining the velocity distribution in the jet. Hughes and Brighton present a short table of velocity profiles for different types of nozzle, while Abramovich has a whole book to developing velocity profiles for different types of turbulent jets.

THEORETICAL JET IMPINGEMENT FLOW

The flow pattern of a subsonic jet changes when a flat surface is placed in front of the jet and the complexity increases. The following is a description of the

flowfield if the flat surface is placed in the flowfield downstream of the potential core flow, and in the area where the flow is fully developed. The impinging flow is divided into three distinct regions as shown in Figure 3. The free jet region which is basically the jet flow described previously issuing into an unbounded medium, the stagnation region (or impingement region), in which the flow changes direction with a large pressure gradient, and the wall-jet region, in which the flow spreads out with zero pressure gradient [35]. Although these regions can be considered separately, they are all influenced by each other.

While many researchers quoted a potential core length of 4 or 5 nozzle exit diameters [8, 33 and 61], others believe that the potential core length is a function of Reynolds number and nozzle geometry and can vary from 2 nozzle diameters for square orifices to 21 for Reynolds number, Re, of 500. Re is a nondimensional number that is the ratio of viscous forces to dynamic forces, and gives an indication of the importance of viscosity on the flow phenomena. For a nozzle geometry, $Re=\rho VD/\mu$, where ρ is the density of the fluid, V the velocity of the fluid at the nozzle exit plane, D is the diameter of the nozzle exit plane, and μ is the viscosity of the fluid. The distance that the uniform nozzle exit velocity is maintained must be established for each specific nozzle geometry, and Hrycak, Lee, Gauntner and Livingood's research [36] does provide for empirical data to use as a guideline, but should be verified experimentally. The stagnation flow region begins approximately 1.2 to 1.5 nozzle diameters from the surface. This region can be divided again into two additional regions. The first region of the stagnation region is where the uniformed vertical jet velocity is decelerated and reaccelerated horizontally.

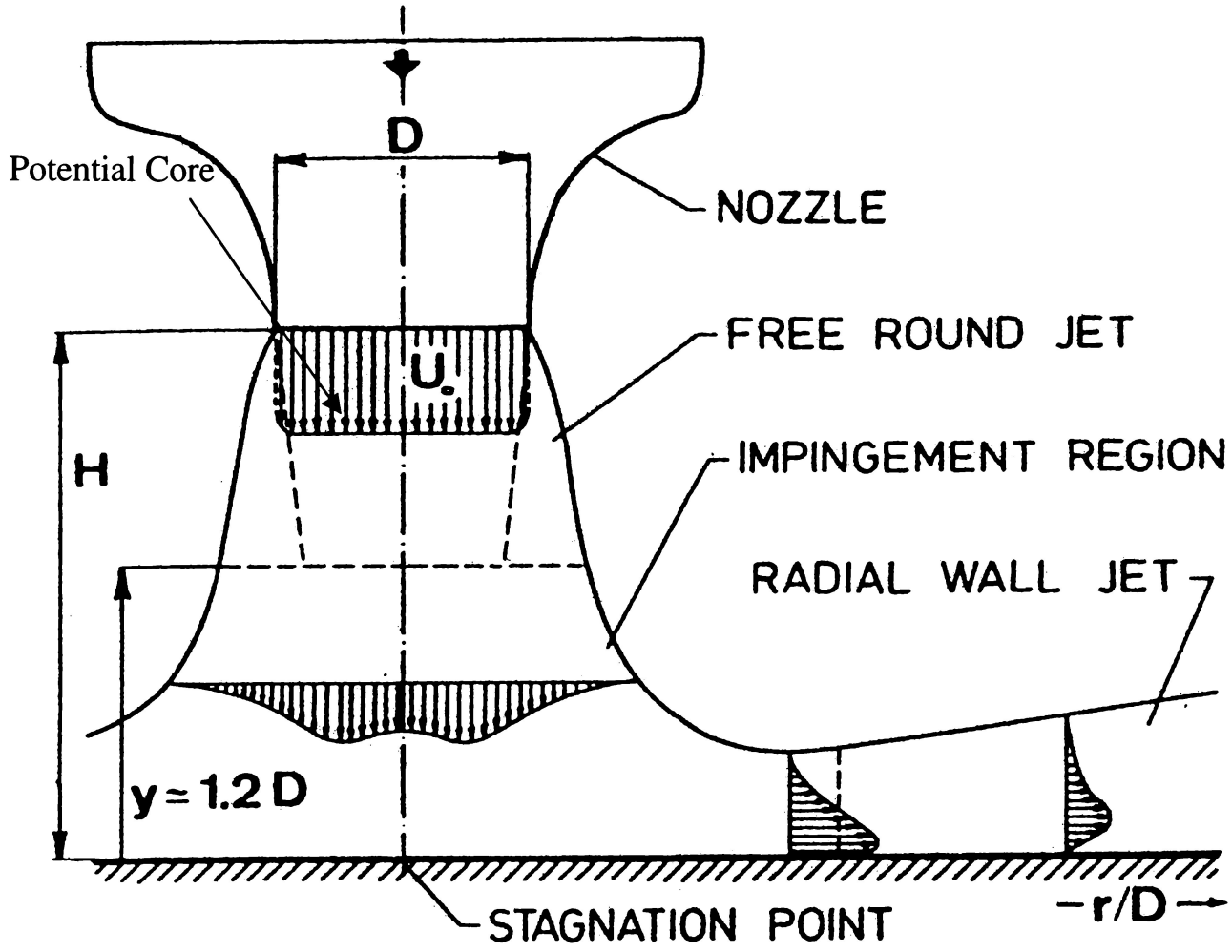

Figure 3: Schematic of a Jet Impinging on a Flat Plate, Showing the Three Distinct Flow Regimes [34].

Beneath this redirected flow is a traditional boundary layer flow that restricts the effects of viscosity to a thin layer adjacent to the surface of the plate. Martin experimentally determined that the boundary layer thickness is roughly one-hundredth of the nozzle diameter. The accelerating flow in the stagnation region produces a laminar boundary layer. The wall flow begins at the point where the accelerating flow reaches a maximum. Like the stagnation region the wall jet region has two distinctive regions within itself, and like the stagnation region there is a thin boundary layer region next to the surface. Unlike the stagnation region the outer region of the wall jet region is a thick layer of turbulent mixing. This turbulent mixing causes the flow to slow down from its maximum at the interface of the stagnation region, to zero at the edge of the wall jet region.

SURROUNDING FLUID ENTRAINMENT

All jets issuing into an open medium have a shear layer that grabs the surrounding fluid and pulls it into the jet itself, as shown in Figure 4. When the jet impinges onto a flat surface all the boundaries of the flow field: the jet flow region, the stagnation flow region and the wall-jet region, entrain the surrounding fluid because each region has an outer shear layer. The extent of the entrainment is dependent on the condition of that surrounding shear layer. The laminar shear layer that starts to appear at the nozzle exit does not entrain as much of the surrounding fluid as the highly turbulent flow of the wall-jet region. The wall-jet region starts at the point where the redirected flow reaches a maximum velocity, and ends when that redirected flow reaches a minimum (normally zero). What causes the velocity of the wall-jet to decrease is that the

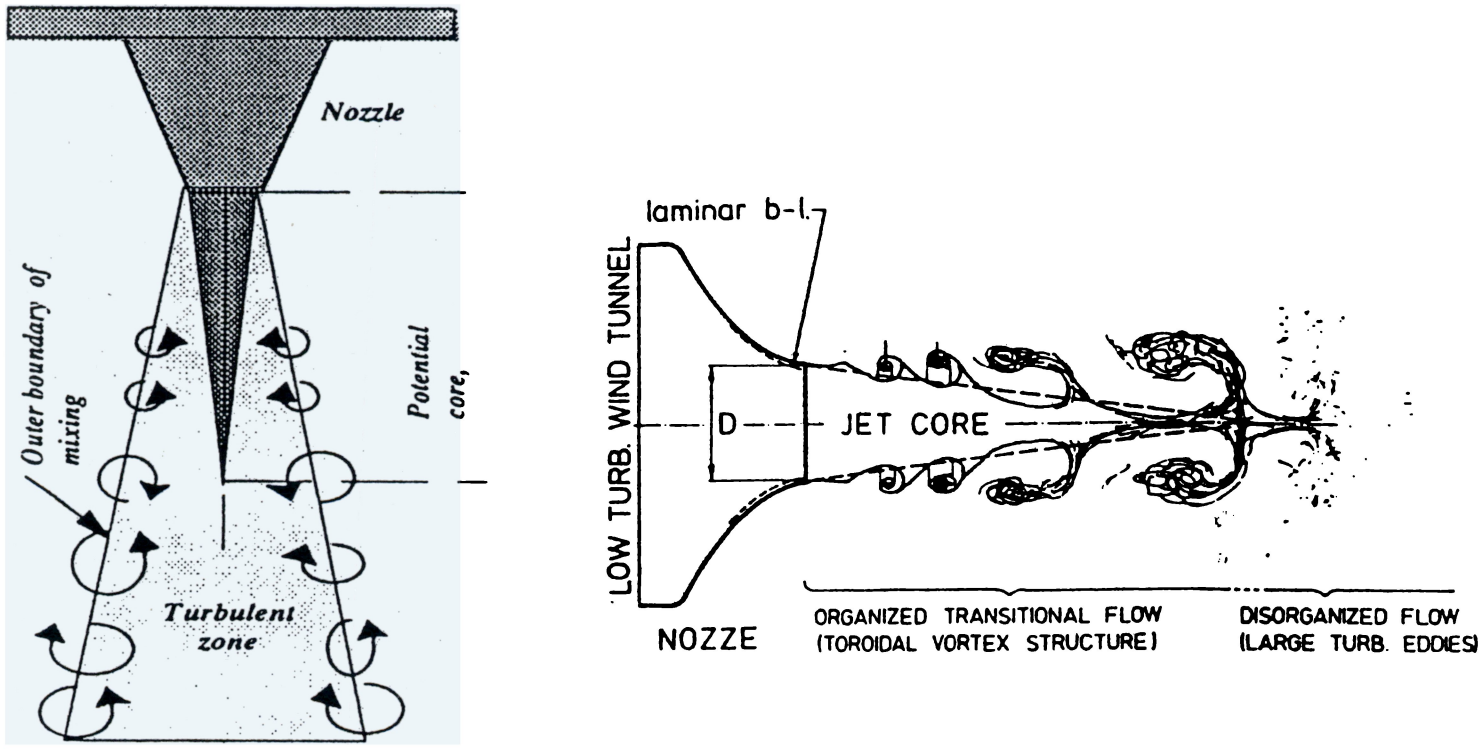

(a) (b)

Figure 4: Schematics of ideal jet entrainment (a) round turbulent jet issuing into an open medium [55] and (b) near-field flow vortex structure in a natural free round jet [34].

highly turbulent flow is pulling in surrounding fluid particles into the wall-jet region and increasing the mass flow. Due to the conservation of momentum, when the mass flow increases the velocity of that mass flow must decrease, and ultimately when enough mass flow is entrained the velocity will reach zero

Much of the jet impingement research that deals with entrainment, is looking at the effects of the surrounding fluid temperature on the ability of a jet to cool/heat the plate that is being impinged upon [27 and 28]. The driving factor for entrainment in these flows is the temperature difference between the jet and the temperature of the driving fluid. If the goal of the jet impingement is to heat the plate, then the entrainment of a surrounding fluid with a temperature less than the jet temperature will cause a decrease in the heat transfer efficiency of the jet. For the heat transfer jet impingement, the Entrainment factor, F, is used to quantify the effects of entrainment on the heat transfer at the surface of the flat plate. F is defined as:

$$F = \frac{T_i - T_\infty}{T_i - T_w}$$

When the initial jet temperature, Ti, equals the temperature of the surrounding fluid, $T\infty$, F equals zero, thermal entrainment does not have an effect on heat transfer. The other extreme is when F equals one and thermal entrainment has the maximum effect on heat transfer. This occurs when the temperature of the wall, T_w, equals $T\infty$. Striegl and Diller's numerical and experimental work shows that entrainment of the room

temperature air must be controlled or it will lead to significant alteration of the jet temperature and consequently the measured heat transfer. Their work also determined that the entrainment effects were most pronounced in the wall jet region of the jet impingement flow, and that the entrainment effects on heat transfer occurs whether it was a single jet or an array of jets.

In order to get a better understanding of the effect of the outer shear layer on entrainment, the vortex structure of the shear layer must be examined. Popiel and Trass [34] performed experiments with a smoke-wire visualization technique to gain a deeper physical insight into the vortex structure of free and impinging round subsonic jets; while Fondse, Leijdens and Ooms [37] developed an empirical relationship through velocity measurements in a free, round, turbulent jet. Both set of researchers concluded that entrainment is most severe when the shear layer develops into toroidal vortex structures. Figure 4b shows a schematic of a near-field flow vortex structure in the natural free round jet. At the nozzle exit the shear layer thickness is zero and a laminar circular shear layer begins. This laminar shear layer is a low-turbulent flow that is intrinsically unstable. In this unstability lies the seed from which the later turbulent development is born. As the jet progresses downstream, this instability wave amplifies and is subsequently rolled up into a train of discrete toroidal vortices. As theses toroidal vortices gather strength, the trailing edge of each vortex causes a transfer of surrounding fluid toward the jet axis and the potential core is "eaten up" by the entrainment of the surrounding fluid and all that remains is a disorganized flow with large turbulent eddies. The amount of surrounding fluid entrained is a function of the strength of the vortices

formed by the jet. Fondse, Leijdens and Ooms found that the laminar shear layer formed at the nozzle exit allows for the development of organized structure and the ability of that organized structure to gather together and grow (coalescence). The condition of the jet structure at the nozzle exit, whether it is laminar or turbulent, influences the entire downstream shear layer development. Popiel and Trass experimentally verified that conclusion by tripping the shear layer at the nozzle exit and causing it to become turbulent at the nozzle exit. What happens is that the shear layer can't develop the tordial vortices as quickly as it did before, that the mixing and entrainment processes that destroyed the potential core can be delayed.

What does the effect of placing a flat plate in the developing tordial vortex flow have on the flow and the subsequent entrainment? Popiel and Trass's research shows that as the plate is approached by the jet, the vortices stretch, increasing in diameter. The component of jet velocity normal to the wall tends to zero, while the radial component becomes increasingly stronger. Their smoke wire technique showed ring-shaped wall eddies induced by large –scaled toroidal vortices, which have stretched and diverged in the radial direction. The eddies begin at the point where the jet toroidal vortices reach the plate. Around 1-2 nozzle diameters of where the toroidal vortices reaches the plate, the toroidal vortices and the wall eddies forming between the vortices combine and become the fully turbulent wall jet. This fully turbulent flow in the wall jet region enhances the entrainment rate and the mixing process. Both references [36 and 37] found that the initial laminar shear layer can be tripped with wire at the nozzle exit to transition to turbulent shear flow. This turbulent shear layer is low in strength and when

it hits the plate, the position where the wall jet because fully turbulent is delayed. This reduces the entrainment of the surrounding fluid in the area around the stagnation point.

SUBSONIC NOZZLE GEOMETRIES

The literature survey found five general geometric classes of nozzles. The conic (or convergent), the bellmouth, the divergent, the Laval, and the shrouded nozzles. Each geometry had its positive and negative attributes for each application.

A general schematic of the conic geometric class is shown in Figure 5a. The geometry usually consists of a conduit of one diameter transitioning to a smaller diameter (the larger area converges to the smaller area). Normally the cross-section is circular, but when Fieret and Ward were performing research on conic nozzles for laser cutting they tested both circular and rectangular cross-sections. Circular conic nozzles are the most inexpensive ones to manufacture for delivering a fluid. Circular conic nozzles can provide either subsonic or subsonic jet depending on the pressure ratio across the nozzle. Almost all of the early laser cutting systems came with a conic nozzle and were used at high pressure. Figure 5b and c shows two conic geometry's tested by La Rocca, Borsati, and Cantello when they were conducting their research into how to control the fluid-dynamic effects in laser cutting. The purpose of the gas in laser cutting is to remove the molten metal out of the kerf and leave a nice smooth cut. What La Rocca and company found was that the fluid dynamics of the conic nozzle geometry can cause large pressure losses and flow field instabilities, when used supersonically, that can degrade the quality of the laser cut.

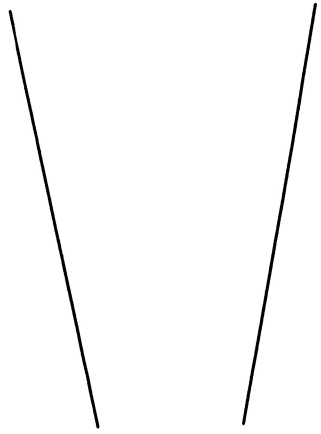

(a)

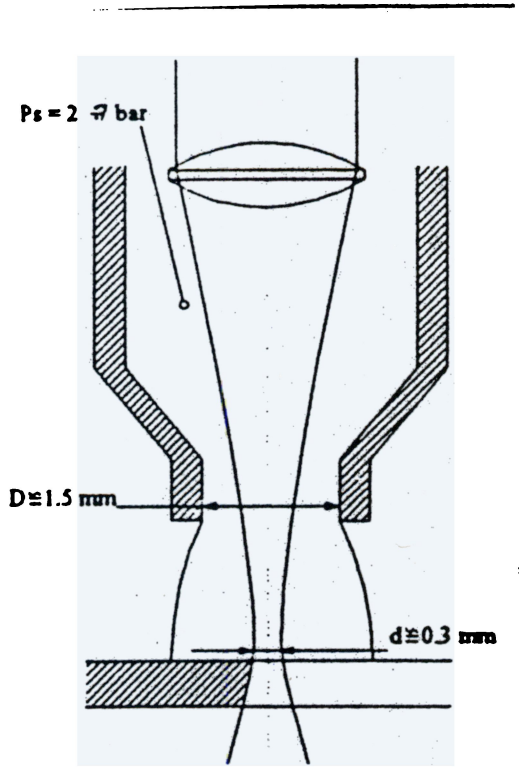

(b)

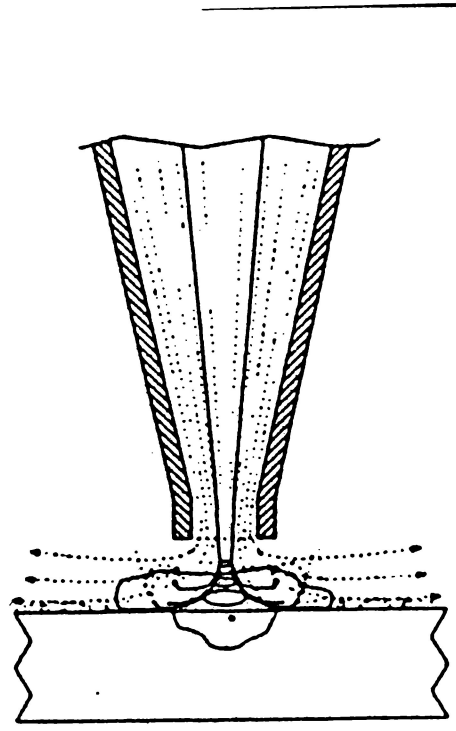

(c)

Figure 5: Conic nozzle geometry (a) generic conic geometry (b) conic laser cutting nozzle 1 [13] (c) conic laser cutting nozzle 1 [13].

Bellmouth nozzle geometries are used in windtunnels and in industrial application to deliver high quality flow. Figure 6a shows the general geometry of the bellmouth nozzle. Both the conic nozzle and the bellmouth nozzle geometry goes from a large cross-sectional area down to a smaller cross-sectional area. The difference is that with the bellmouth geometry the larger cross-sectional area is much, much, larger than the smaller cross-sectional area, and the transition to the smaller cross-sectional area occurs rather quickly in a smooth contour that looks like a bell shape. Again, the bellmouth can be used subsonically or supersonically, but it is generally used for delivering high quality subsonic flow. The reason the flow is of higher quality is that the larger duct, if long enough, allows the flow to lose most velocity components other than the velocity component in the axially direction. Figure 6b [38] shows the bellmouth nozzle in a subsonic wind tunnel.

The divergent nozzle is the opposite of the converging or conic nozzle. With this geometry the cross-sectional area starts at a minimum then increases to a maximum, as shown in Figure 7a. Many different variations of the divergent nozzle have been evaluated for various applications. Figure 7b shows the contoured divergent nozzle geometry developed by Jankovic and Mostaghimi for a plasma gun. Here the goal was to minimize the entrainment of surrounding air into the nozzle itself, and a computational fluid dynamics code was used to calculate the streamlines necessary to prevent entrainment. Theobald evaluated various divergent geometries for use in fire-fighting nozzles. Here the goal is to develop a geometry that produces a combination of

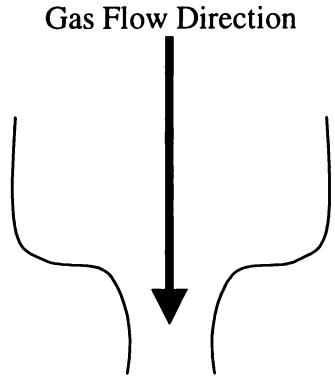

(a)

Figure 6: Examples of bellmouth nozzle geometries a) Schematic of a generic bellmouth nozzle geometry.

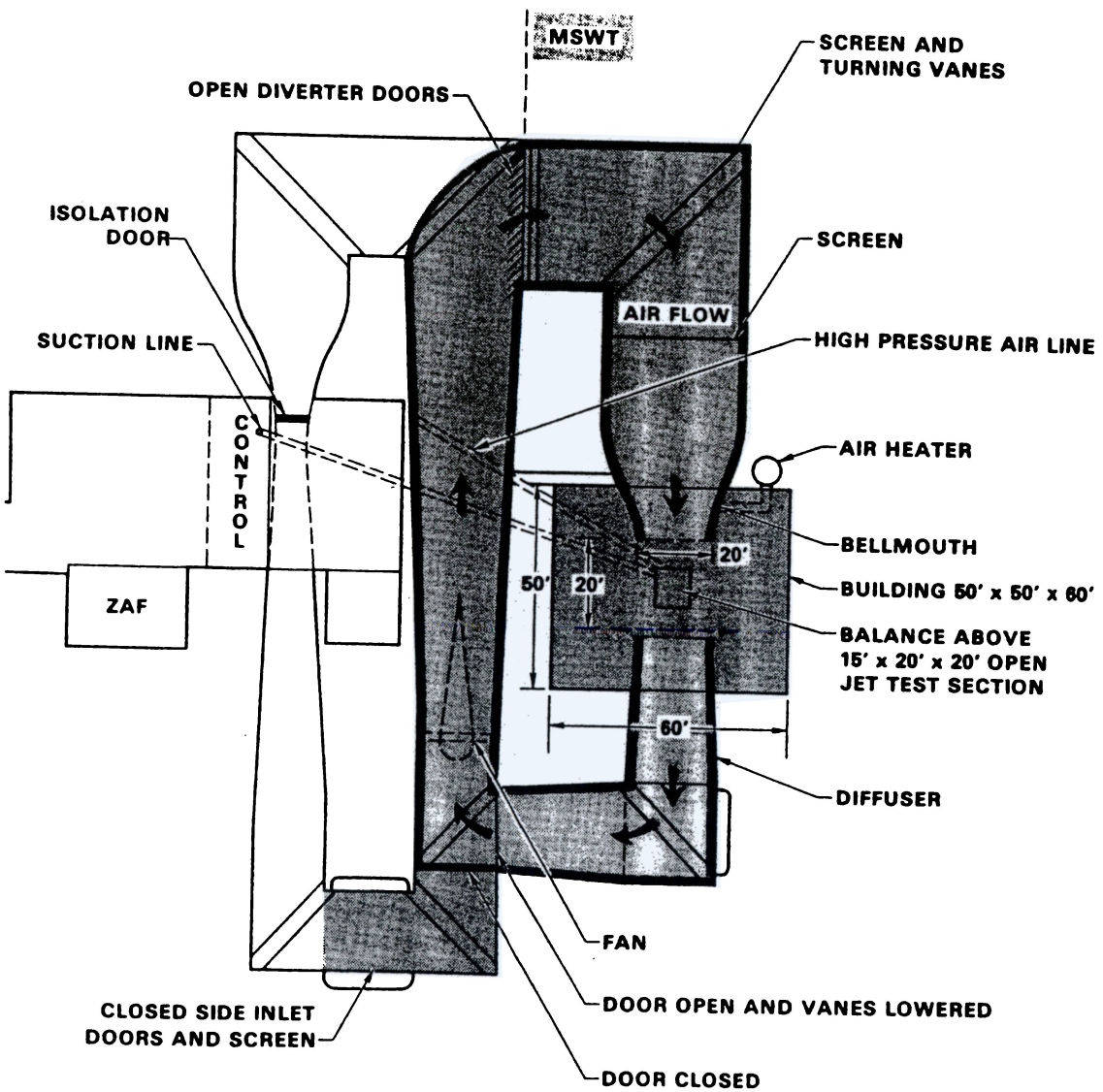

(b)

Figure 6: (continued)

Examples of bellmouth nozzle geometries, (b) a closed circuit subsonic wind tunnel [38].

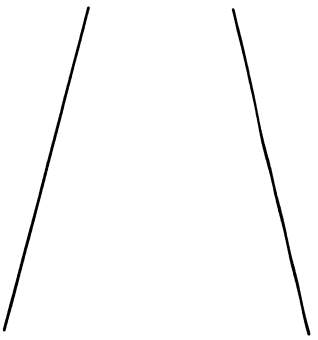

(a)

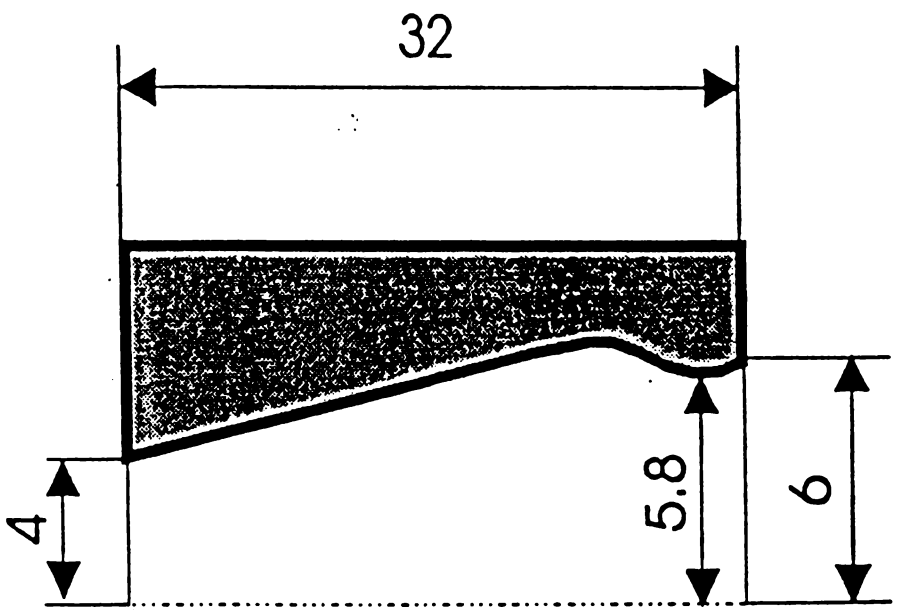

(b)

Figure 7: Divergent nozzle geometry examples (a) generic divergent nozzle geometry and (b) a plasma spray gun contoured divergent nozzle [31].

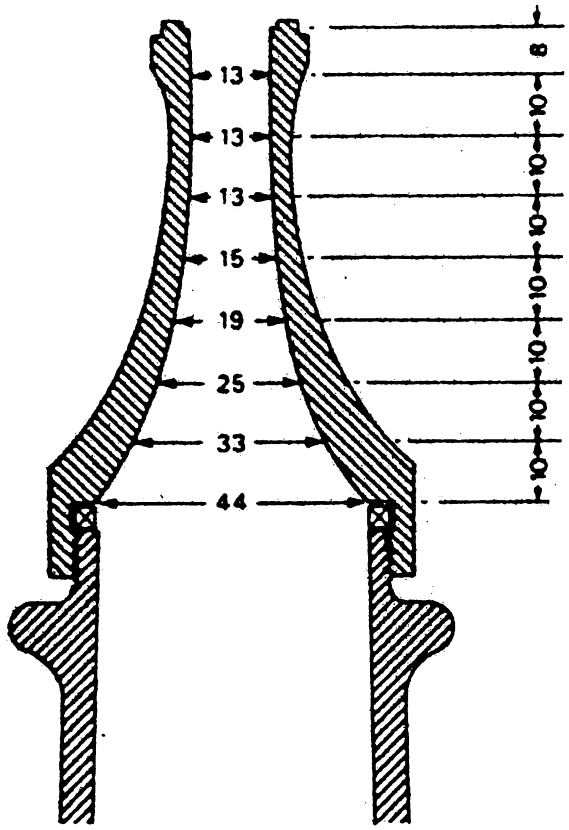

Convex nozzle fitted to standard taper branch

(c)

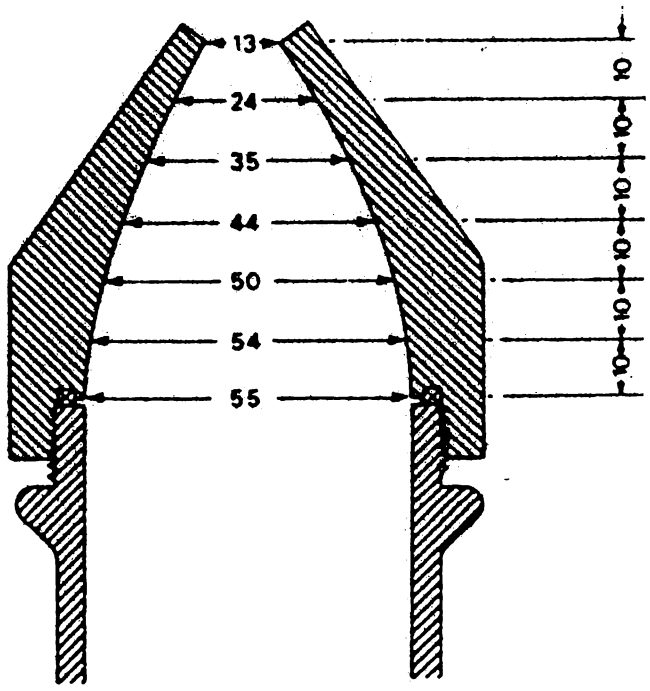

Concave nozzle (Rouse type) fitted to parallel branch

(d)

Figure 7: (continued)

Divergent nozzle geometry examples (c) convex divergent with a straight pipe nozzle [30] (d) concave divergent with a straight pipe nozzle [30].

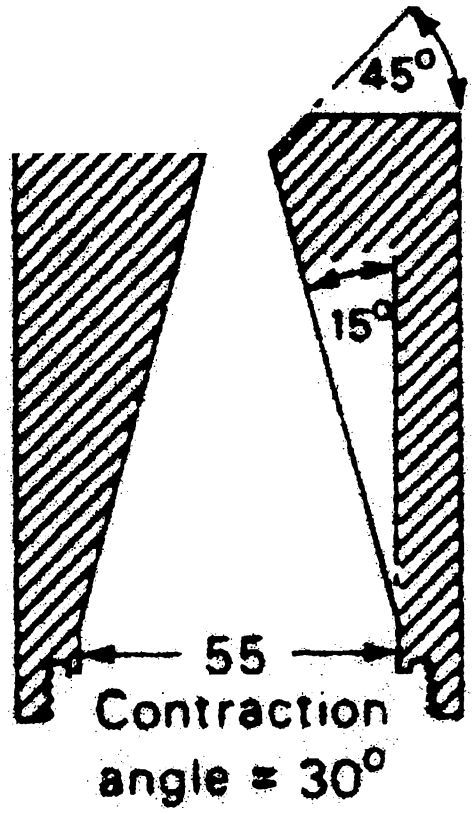

(e)

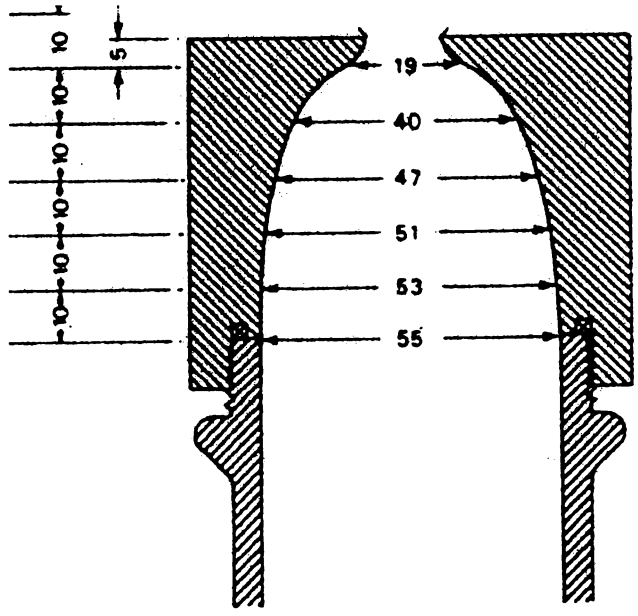

Experimental concave nozzle fitted to parallel branch

(f)

Figure 7: (continued)

Divergent nozzle geometry examples (e) straight angle water nozzle [30] (f) convex divergent with a straight pipe water nozzle [30].

maximum range and volume of water. Figures 7c, d, and e presents three of the geometries he evaluated: the convex divergent (17c), the concave divergent (7d) and the straight angle divergent (7e). For the fire-fighting application the concave divergent with a straight section (7f) produced the best range and distribution of the water; while the straight angle divergent (at 30 degree angle, 7c) produced the best stable jet.

A common nozzle geometry is the Laval nozzle shown in Figure 8a. As mentioned before, in order to produce a good quality supersonic flow the flow must converge to a throat then expand to the design condition. For supersonic applications this is the best general geometry. This geometry of nozzles has been heavily researched for the application of laser cutting nozzles. Only one example will be presented here. Man and company researched the shock structure of a laser cutting supersonic nozzle. Their design of a Laval nozzle to produce a uniform flow at the nozzle exit is presented in Figure 8b. They took great care to shape divergent section to avoid reflected waves impinging on the wall boundary in order to get uniform supersonic flow out of the nozzle.

The last general nozzle geometric classification is that of the shrouded nozzle. The shrouded nozzle supplies a secondary flowrate around the primary jet flow produced by any nozzle geometry. This flow is normally added at the nozzle exit plane. The purpose of this secondary flow is to provide to the shear layer a known and desired gas to be entrained into the primary jet. Figure 9 shows two different approaches to supplying this secondary flow to subsonic nozzle flow. Figure 9a shows sixteen holes drilled into a manifold around the primary jet produced by a contoured divergent nozzle. For this application the primary gas and the shroud gas are both argon and the purpose of

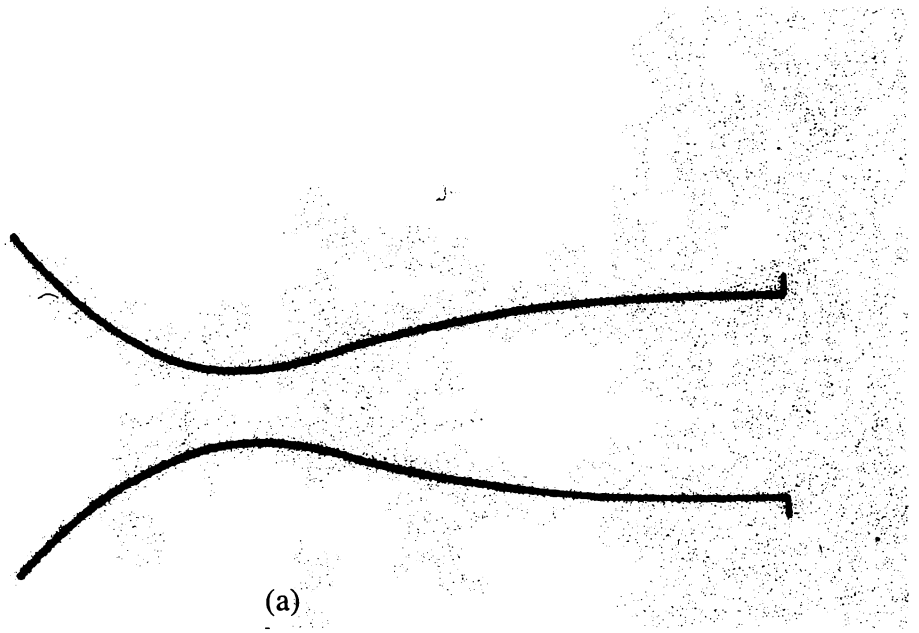

(a)

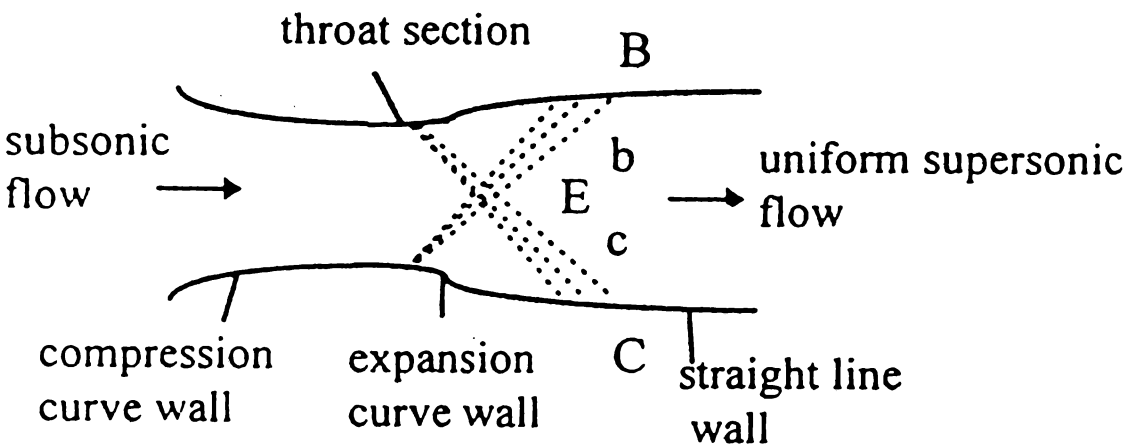

(b)

Figure 8: Examples of convergent/divergent nozzle geometry (a) generic geometry (b) Laval laser cutting nozzle [39].

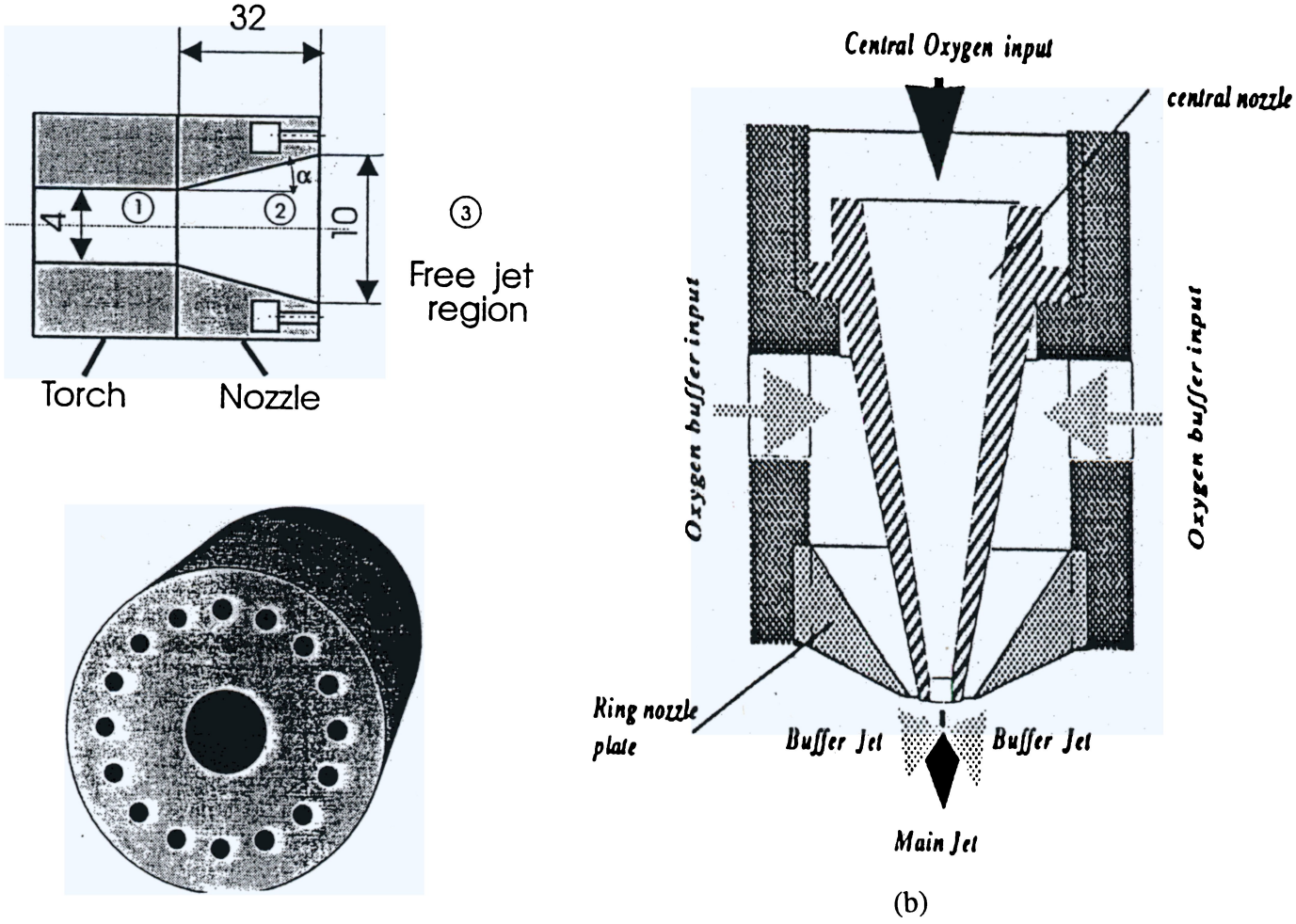

(a)

(b)

Figure 9: Examples of shrouded nozzles (a) contoured divergent nozzle of a plasma spray gun [31] and (b) assist gas nozzle in laser cutting [40].

the shroud is to prevent/minimize surrounding air from being entrained into nozzle and degrading the performance of the plasma nozzle. Figure 9b shows another application of a shrouded nozzle around a conic nozzle. This shrouded nozzle's application is for supplying oxygen to the surface of a piece of metal being cut by a exothermic reaction with a laser beam. Here the goal is to minimize the air (with 72% nitrogen) being entrained to the kerf area of the cut. The second shrouded nozzle configuration, shown in Figure 8d, was tested by O'Neill, Gabzdyl, and Steen [40] with various secondary flowrate. For their particular nozzle geometry it took 30 liters per minute to minimize the entrainment of the surrounding nitrogen to less than .01 percent. Increasing the shroud flowrate further increases the entrainment slightly, around .05 percent at 80 liters per minute.

LASER INDUCED SURFACE IMPROVEMENT, LISI^{SM}

Laser surface treatment can be classified into four main groups: the non-melting processes, the melting processes, the vaporization processes and the photolytic processes [41]. This study concentrates on one of the melting processes: a laser alloy surface called LISI^{SM}. Surface alloying is a process where a thin layer at the surface of a metal is melted by a laser beam with the simultaneous addition or infiltration of preplaced powder of desired alloying element. With LISI^{SM}, the desired alloying element, in a liquid binder, is sprayed and dried prior to applying the laser beam. This rapid melting and resolidification changes the surface chemical composition of the metallic substrate. Figure 10 shows the cross sectional sequence of laser surface modification in its various stages. Figure 10(a) shows that the substrate B coated with a powder layer of A is

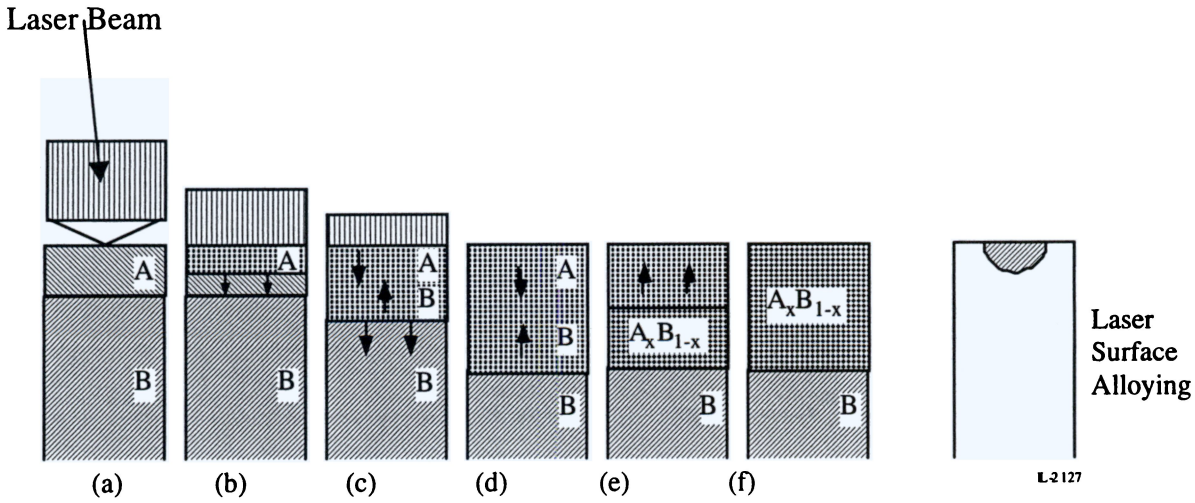

Figure 10: Cross Sectional Stages of Laser Surface Alloying [41]. A is the powder layer and B is the substrate metal. The process begins with a) the laser beam being applied to the top of the powder layer, b) is where the powder layer is begins to melt, c) is where the powder layer is completely melted and the substrate begins to melt, d) is where the substrate stops melting (maximum depth), e) is where the convective forces start to mix the molten powder with the molten substrate and resolidification begins, and finally f) is where the resolidification ends. The final product is the alloy layer consisting of a mixture of the elements in A and B.

irradiated with the laser beam. A large fraction of the laser energy is lost by specular and diffuse reflection in most metals and for most laser wavelengths used for laser materials processing. However, a part of the laser energy is absorbed by the surface, and it raises the surface temperature above the melting point instantaneously. The liquid-solid interface moves through the alloy element layer towards the substrate, as shown by the solid arrow in Figure 10(b). Within a short time, the liquid-solid interface reaches the substrate and mixing begins between the element A and the substrate B (Figure 10c). By the time the maximum melt depth is achieved (Figure 10(d)), the laser beam has swept across the spot and solidification starts as shown in Figure 10(e). Solidification completes very quickly and forms a surface alloy of A_XB_{1-X} (Figure 10(f)). Solidification is very rapid in laser surface alloying, due to high cooling rates. Thus, solid state diffusion can be neglected. Rapid solidification often leads to novel metastable phase(s) and sometimes even metallic glasses. The modified surface thus processed can have superior chemical, physical and mechanical properties. The depth of the laser modified zone can be controlled by the laser power and the speed. The major independent process variables for laser surface modification are as follows: (1) laser power, (2) traverse speed, (3) thickness of the precoated powder layer, (4) beam shape and size, (5) thermophysical properties (e.g. thermal conductivity, reflectivity, viscosity etc.) of the substrate and the mixing element, (6) degree of overlapping of each laser track, and (7) shield gas pressure and composition. By controlling these process parameters, depth, width, solute content, microstructure of the laser alloyed zone and surface texture can be altered according to the requirements. This study will concentrate

on the effects of the shielding gas; a description of the other effects can be found in the article by Mazumder[41].

The shield gas can assist in the rapid solidification by increasing the cooling rate and "freezing" the molten metal. The shield gas pressure and composition can effect the alloy layer itself. A gentle shield gas pressure allows the melt pool to remain stationary and allow the convection forces (driven by the surface tension and the convective heat transfer [42]) in the melt pool to more homogeneously mix the added metal elements, while a high pressure gas flow may spread out the metal pool reducing the amount of convective mixing that occurs. The shield gas system can also aid in the solidification process, thus allowing the surface to be textured. The shield gas composition can aid in the creation of a nitride or an oxide at the surface just by using nitrogen or oxygen.

Laser surface modification offers several advantages over other surface modification techniques. The laser beam has an excellent spatial resolution, which makes it ideal for depositing coatings on miniature size components, such as electronic sensors, to be used at high temperature. Another advantage of laser surface modification comes from the fact that some laser beams can be transported to any remote corner through fiber optics. This allows deposition of coatings on components or parts that are remotely located. In a surprising study, it has been also shown that laser surface modification is cheaper than other surfacing techniques [43].

JET IMPINGMENT FOR LASER SURFACE ALLOYING

The purpose of the shield gas nozzle system is to protect the molten metal during the melting and resolidification process and to control all the elements being added to the

molten metal. The protection comes from the desire not to have adverse environmental contaminates in the final alloy layer. For example, in a dusty industrial shop entrainment of dust into the molten metal could have an adverse effect on mechanical properties of the alloy layer. In addition, when molten metal comes into contact with air, nitrides and oxides can form. In some alloy layers, the nitrides and oxides can cause embrittlement and/or cracking, which may not be desired. For some laser surface alloying applications nitrides or oxides are wanted for visual effects. For instance, a desirable gold color is obtained when nitrogen is absorbed into the alloy layer during the melting process to form a nitride. The whole point of the laser surface alloying process is to put the desired elements into the alloy layer, and that cannot be done unless the composition of the gas above the molten metal is controlled.

The composition of the gas can be controlled if the entrainment is controlled. From the jet literature review minimizing/preventing the surrounding fluid from being entrained into the jet can occur by four ways: placing the impinging surface within the potential core of the jet, tripping the initial shear layer into becoming turbulent, shaping the nozzle geometry, and providing a shroud flow to be entrained by the shear layer. The goal of this research project will be to apply some of the above techniques until a combination is found to deliver an acceptable entrainment around the impingement surface that produces the desired elements in the alloy layer.

WORK ZONE DEFINITION AND DETERMINATION

The surface area that needs to be protected by the assist gas will be called the work zone for this research. The work zone for steel and aluminum is the area around the

laser beam interaction point that is melted. Steel and aluminum in the molten state will interact with the oxygen and nitrogen in the air and form oxides and nitrides, which is what the assist gas is trying to prevent. Many factors effect the size of the work zone. The size, shape and power of the laser beam at the interaction point are important for determining the temperature distribution throughout the metal. Also, three main categories of material properties effect the ability of the laser beam to melt the material: laser light absorption (material surface finish, absorption coefficient, and reflectivity at the laser wavelength), thermal transport of the material (thermal conductivity and thermal diffusivity), and the thermodynamic properties of the material (density, heat capacity, melting temperature, and the latent heat of fusion) [44]. The beam resulting from the optics that is used in producing LISI^{SM} surfaces, is a line beam approximately 4 mm wide by 700 microns thick at focus. The power output (after losses through the optics) of the Rofin-Sinar 2000W Nd:YAG laser is approximately 1500W. The line optics was designed to deliver a wide beam to the material that results in a wider, smoother melt track.

The reflectivity, R, of each material is given for a normal incident beam on a clean surface of the metal. For carbon steel the R is approximately 0.58, while for aluminum it is 0.80 (all numbers are for a wavelength of 1.06 microns). This means that 58% and 80% of the laser light normally incident on the surface of clean carbon steel and aluminum is reflected off the surface and does not contribute toward melting. (Note: due to this reflection, the 1500W output of the Nd:YAG laser is offset 15 degrees from the normal to the surface to prevent any back reflection from the surface of the material from

bouncing back toward the optics package and causing heat damage to the optics package). Based on the above information, the laser energy absorbed into carbon steel and aluminum is:

$P=(1-R)* I_{\square}$

P=(1-0.58)*1500W=630W (carbon steel)

P=(1-0.80)*1500W=300W (aluminum)

To determine the shape is of the melt zone around the line beam, the approach used here will be to determine the shape of the melt zone around a single point, then to impose that shape along a series of points to make up a 4mm long line. This approach should overestimate the size of the melt zone, as the heat input for the line beam is only slightly bigger than the heat input for a single point source. If the nozzle protects the area of the series of single point sources, than it will definitely protect the small area of the line beam. Rosenthal [45] first developed the theory for a temperature distribution on the surface, near a moving point source. He made the assumptions that the physical coefficients of the material are constants, the heat losses throughout the surface to the atmosphere are neglected, and that the interaction of the point source with the material is performed over a sufficient length that a quasi-stationary state is formed [46]. Once the quasi-stationary state is reached in the piece of material, there will be no change in the temperature distribution around the point heat source. Adams [47] presented engineering relationships according the direct calculation of peak temperatures or cooling rates from

welding variables and thermal properties by taking Rosenthal's approach and applying a cylindrical coordinate system.

The temperature distribution is given by:

$$T' - T_0 = \frac{qV}{4\pi K\alpha} \frac{\exp\left[m - \sqrt{m^2 + n^2}\right]}{\sqrt{m^2 + n^2}}$$

where

$$m = \frac{XV}{2\alpha} \qquad n = \frac{rV}{2\alpha}$$

Here T' is the steady state temperature in the solid at point (X,r), where the source is at the origin and the X direction is parallel to the direction of motion of the source (positive X is opposite to the direction of the source). r is the distance perpendicular to motion of the source. T_0 is the initial temperature of the plate of material. V is the velocity of the point source, q is the rate of heat flow from the source (calculated earlier), m and n are nondimensional coordinates. Thermal diffusivity, α, of the metal is the ability of the metal to achieve thermal equilibrium in response to the suddent application of heat, and α is defined by:

$$\alpha = \frac{K}{c_p \rho_m}$$

where K is the thermal conductivity of the metal, ρ_m is the density of the metal, and c_p is the specific heat of the metal.

Two calculations for each metal were performed with the Adams equation, one for a q that assumes 100% of the incident laser energy is absorbed into the metal and contributes to the temperature distribution, and the second calculation assumes that the metal has a clean surface and that the previously calculated amount of incident laser energy is reflected. What is occurring during the laser surface alloying process lies somewhere between the two extremes, since R for the metal with the precursor is unknown, therefore, calculations for both extremes were performed. The results are presented in Appendix A-1. For the calculations, T' will be assumed to be the melting temperature for steel and aluminum, T_0 is assumed to be ambient temperature (300 °K), and the temperature profile will be found by assuming a X and calculating a r.

Steel with R=0 (no reflection), being lased with a 4mm line beam, has a melt area that is oblong shaped and is roughly 6.23mm high by 4.61 mm long. Steel with R=0.58 (58% of the laser energy is being reflected), being lased with a 4mm line beam, has a melt area that is again oblong shaped, but it is roughly 5.43mm high by 2.14mm long. In the worst case scenario, the protective gas nozzle will have to protect a steel molten pool of 6.23mm high by 4.61mm long. The calculations for the melt zone size for aluminum is also presented in Appendix A-1. The protective gas nozzle will have to protect an area roughly 6.76mm high by 2.85mm long for aluminum.

CHAPTER III

PLAN TO DEVELOP THE NOZZLE

Chapter 2 reviewed many nozzle applications. The laser surface alloying nozzle requires a low pressure nozzle, which implies a subsonic nozzle. The subsonic nozzles geometries reviewed in Chapter 2 include the laval nozzle, the conic nozzle and the divergent nozzle. The applications most similar to laser surface alloying were Jankovic and Mostaghimi's shrouded contoured nozzle and the various divergent geometries that Theobald tested. Some of these geometries were evaluated for laser surface alloying.

In general, a subsonic nozzle produces a jet whose speed at the nozzle exit is less than Mach one. Assuming that the nozzle exit issues into a room (like during laser surface alloying), the nozzle exit static pressure is atmospheric pressure (at sea level, atmospheric pressure is $1.01379X10^5$ N/m^2). The isentropic pressure relation is:

$$\frac{P_0}{P_e} = \left(1 + \frac{\gamma - 1}{2} M^2\right)^{\frac{\gamma}{\gamma - 1}} \quad [48]$$

Where P_0 is the total pressure at the entrance of the nozzle geometry, P_e is the static pressure at the nozzle geometry exit, M is the Mach number at the nozzle exit and γ is the ratio of specific heats (specific heat at constant pressure to the specific heat at constant volume). At M equal to 1, in air, the nozzle pressure ratio is 0.5283. If P_e is $1.01379X10^5$ N/m^2, then P_0 would be $1.91897X10^5$ N/m^2. That means that in order to

keep the nozzle in the subsonic regimes the P_0 applied to the nozzle entrance must be less than $1.91897X10^5$ N/m^2. Subsonic nozzle flow can be again divided into two additional classes: compressible (ρ varying) and incompressible (ρ constant). M is defined as a measure of compressibility. For low subsonic M, (M=0.30 and below), the derivative of ρ is zero. There is no change in the ρ of the gas from the entrance of the nozzle to the exit of the nozzle. For flow above M 0.30, the ρ varies significantly and must be accounted for. If the maximum pressure to be delivered by the protective gas nozzle results in a M less than 0.30 then the water tunnel simulation (which is incompressible) would be valid.

CALCULATION OF MAXIMUM NOZZLE PRESSURE

One of the requirements of the laser surface alloying nozzle is that the pressure supplied be gentle enough to the work zone so that the molten metal is not adversely effected (the pressure should not be high enough to remove the molten metal). In order to determine the maximum pressure, the forces on the molten metal must be balanced. The force balance equation is:

$$p_p + p_r + p_{jet} = p_{surten}$$

where p_p is the proton pressure, p_r is the recoil pressure of the molten metal, p_{jet} is the jet pressure, and p_{surten} is the molten metal surface tension pressure. For this purpose, the proton pressure is so small that it is ignored, and the desire here is to not move the molten metal so the sum of the recoil pressure and the jet pressure must be less than the surface

tension pressure. B is the safety factor, or by how much that recoil pressure and the jet pressure must remain below the surface tension pressure.

$$p_r + p_{jet} < Bp_{surten} [49]$$

$$p_r = 0.55\left[p_{\substack{saturation \\ vapor}}(T_s) \right] [49]$$

$$p_{r_{steel}} = 0.55(75Pa) = 41.25Pa$$

$$p_{r_{Al}} = 0.55(1X10^{-6}Pa) = 5.5X10^{-7}$$

Recoil pressure of the molten steel is 41.25 N/m^2 and recoil pressure of aluminum is $5.5X10^{-7}$ N/m^2. Since both pressures are small compared to ambient pressure, recoil pressure is assumed to be insignificant. The jet pressure is what we are looking for, as it will determine the desired nozzle operating condition. The equation coefficient B, is a buffer factor used to make the results conservative. We will use 0.5 for B. The surface tension of the molten metal is given by the following equation:

$$p_{surten} = \frac{\sigma}{R_{ad}} [50]$$

where σ is the surface tension of the liquid metal, and R_{ad} is the radius of the melt pool, taken to be the thickness of the alloy layer for this calculation. For aluminum and iron the surface tensions are:

$$P_{surtenAl} = \frac{914X10^{-3}N}{500X10^{-6}mm} = 1828Pa$$

$$p_{surtenFe} = \frac{1872X10^{-3}N}{500X10^{-6}mm} = 3744Pa$$

Therefore, the jet pressure must be less than:

$$p_{jetAl} = (0.5)(1828) = 914N/m^2 = 0.1325psi$$

$$p_{jetFe} = (0.5)(3744Pa) = 1872N/m^2 = 0.2714psi$$

To determine the Mach number of the nozzle providing this jet force, the isentropic pressure relationship previously presented is used. For a γ of 1.4 (air), the pressure ratios are:

$$Fe = \frac{14.7 + .2715(psia)}{14.7(psia)} \rightarrow M = 0.17$$

$$Al = \frac{14.7 + .1325(psia)}{14.7(psia)} \rightarrow M = 0.12$$

For both iron and aluminum, the maximum nozzle exit M is in the incompressible (M<0.3) range. The M number for iron and aluminum are so close together that for convenience, a design M=0.15 will be used throughout the rest of the research.

NOZZLE FLOW SIMULATION-WATER TUNNEL

Experimental simulation occurs when the flow conditions for a model test are completely similar if all relevant dimensionless parameters have the same corresponding values for model and prototype" [5]. The water tunnel can be a good simulation for some types of flow. In general, water is an incompressible fluid, a fluid in which the density variations are negligible. If the proper dimensionless parameters are copied, the water tunnel can successfully simulate other incompressible flow fields. In this case, the desire is to have a nozzle to produce M=0.15 flow, an incompressible flow, that impinges on a flat plate in an open air environment. For incompressible flows without a free-surface the geometric and dynamic similarity must exist between the water tunnel model and the laser prototype nozzle. Geometric similarity is met by having the model match the length ratio of the prototype nozzle. Physically the model must look exactly like the prototype except for scale. If the prototype nozzle has an exit diameter of 1 mm and a length of 3 mm, the model must maintain that diameter to length ratio of 1:3. The scale between the model and the prototype is determined by the dimensionless parameter that assures that dynamic similarity, Re (Reynolds Number). Re is the measure of the ratio of the inertia effects to the viscosity effects, and it must be simulated in the water tunnel. As this particular simulation does not have a free-surface to model (no surface waves or open channels) then the Froude number does not have to be modeled. The Froude number is the ratio of inertia forces to the gravity forces, and does not need to be simulated in the water tunnel for this application. From the literature search, five or six nozzle geometries

were tested in the water tunnel. The water tunnel results was then used to select a geometry to be tested in prototype gas trials.

The first step in determining the water tunnel simulation is to calculate the Re of the prototype nozzle. In order to calculate the Re, the gases to be used in the prototype must be chosen. To prevent oxygen contamination of the alloy layer during the laser alloying process, nitrogen can be used in the prototype nozzle. To prevent oxygen (O_2) and nitrogen (N_2) contamination during the alloying process, argon (Ar) or helium (He) can be used in the prototype nozzle. In order to calculate the Re for each gas in the prototype nozzle, a prototype nozzle exit diameter must be assumed. The nozzle prototype diameter was arbitrarily chosen to be 20.7mm because it was a nice fit into the 50.8mm diameter gas delivery package. The Re calculation for each prototype gas is given in Appendix A-2. The Re for the He is 23,000 and can be provided by a water flowrate of 17 GPM (gallons per minute) passing through a nozzle three times larger than the prototype nozzle. The Re for the Ar is 74,000 and can be provided by a flowrate of 18GPM of water through a nozzle the same size of the prototype. The Re for the N_2 is 66,000 and can be provided by a water flowrate of 16.3 GPM through a nozzle the same size of the prototype.

NOZZLE GAS FLOW TRIALS

From the water tunnel results one geometry was selected to be built in a prototype nozzle fitted for the Nd:YAG laser's optics package. This prototype nozzle was being tested to characterize the nozzle flow from the selected geometry, at different working distances. A copper plate with static pressure taps was first used as the impingement

surface. From these static taps, the pressure profile in the impingement region was measured, to verify that the pressure was acceptable. The amount of oxygen entrained by the jet was measured by sampling gases from the static ports and analyzing the captured volume for percent oxygen content. Smoke was injected into the flow to visualize flow patterns (similar to the dye injection that was used with the water tunnel).

LASER TRIALS

After the jet impingement flow has been fully characterized by the gas flow trials, then the laser surface alloying technique was used to create LISI^{SM} surfaces on steel with the new protective gas nozzle and the knowledge gained from the water tunnel simulation and the gas trials. These surfaces were metallurgically analyzed and compared to surfaces create without any type of protective gas. The surfaces were analyzed for oxygen content with a Scanning Auger Microprobe analysis of the alloy layer (both surface and cross-section) and X-ray analysis. The SEM was used to take high resolution photos of the alloy layer and to perform elemental analysis for comparison with the Auger data. Profilometer data will be taken to measure the surface roughness created by the different gas and nozzle combinations.

CHAPTER IV

WATER TUNNEL SIMULATION

The general aspects of a water tunnel simulation of any flow field were presented in Chapter 3. In this chapter the specifics of how the water tunnel simulation was carried out will be presented, in addition to the results and conclusions of the water tunnel simulation. All water tunnel experimentation was carried out in the UTSI water tunnel I, located in the propulsion lab facility.

UTSI'S WATER TUNNEL

The UTSI water tunnel is a closed circuit facility. Normally an aerodynamic model is placed in the test section, water flow is moved around the model by the facility propeller, and dye is injected to visualize the flow pattern. This basic closed circuit facility is shown in Figure 11. A basic description will be given here, but for a more detailed description please refer to reference 52. The goal was to simulate subsonic incompressible jet impingement with the water tunnel. For this research effort, the circuit was not closed, but two additional water supplies and one outlet was added. One of the additional water supplies was for the main jet flow and the other was for secondary jet flow (or shroud flow). The existing water tunnel test section was used as a stationary medium for the jet to inject into. The actual setup is shown in Figure 12. The floor of the test section is used as the impingement surface. The water supply for the nozzle is not part of the closed circuit water tunnel system; therefore, in order to balance the mass of water that was entering the test section, a bleed valve on the water tunnel's filter system

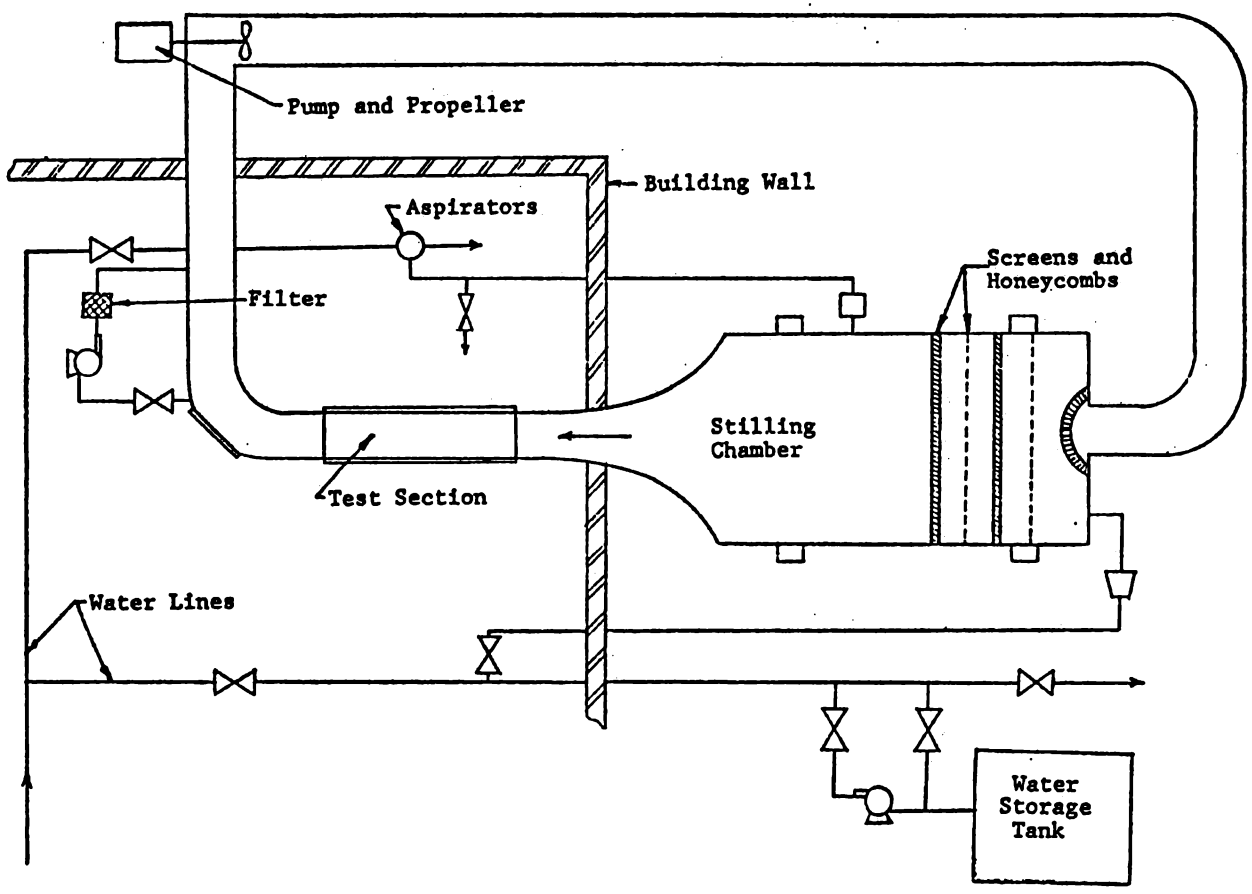

Figure 11: A schematic of UTSI's closed circuit water tunnel[52].

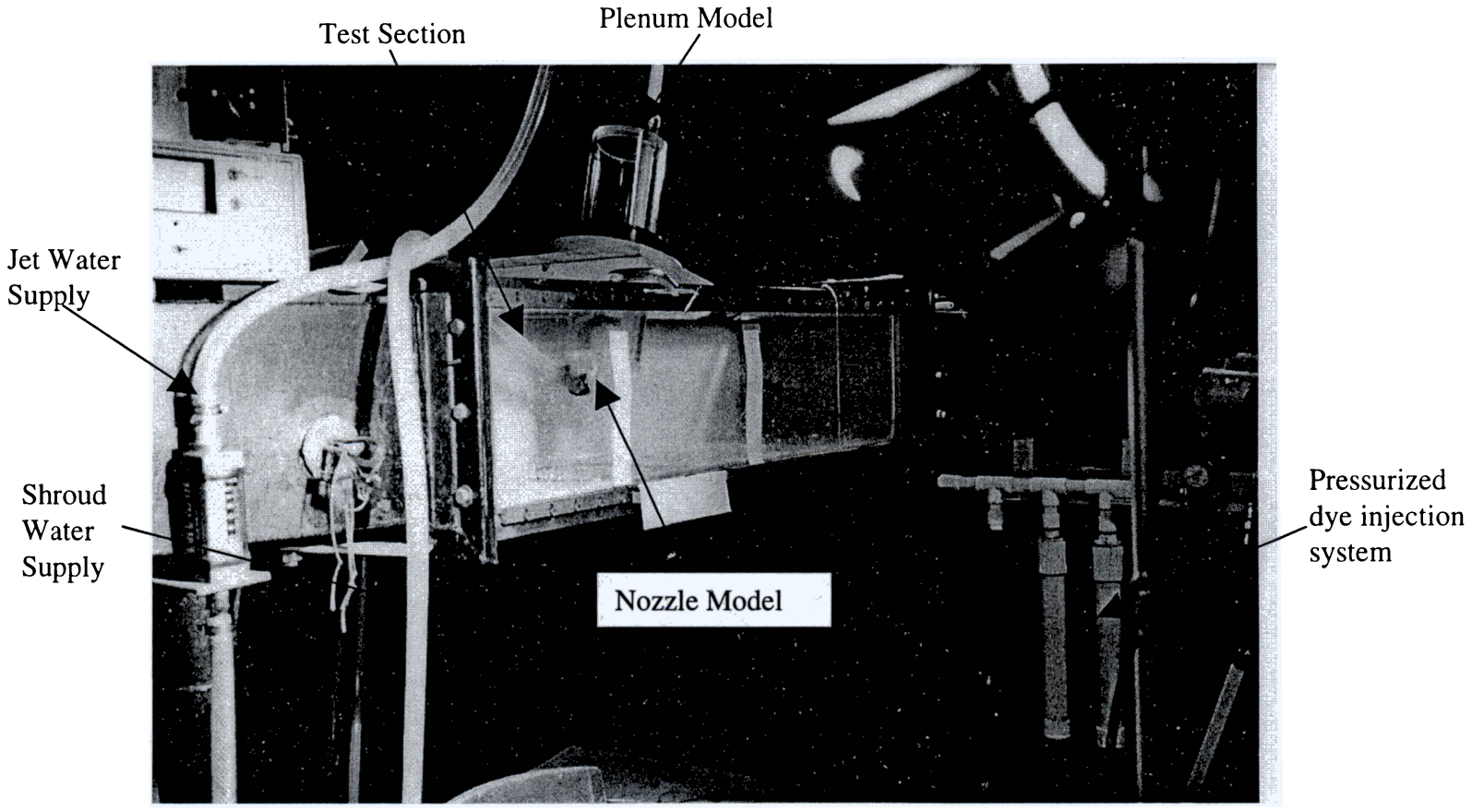

Figure 12: The 3X plenum and nozzle model installed into the UTSI water tunnel.

was opened during testing.

The existing closed circuit water tunnel system main components are the stilling chamber, the test section, the propeller and the ducting that connects the sections. A majority of the system is located outside the building. The stilling chamber is located directly behind the building and is 154.94 cm (61 inches) in diameter and 284.48 cm (112 inches) long. It contains four stainless steel screens and two aluminum honeycombs. The test section is made out of 1.27 cm (0.5 inch) thick Plexiglas on three sides (the top is open). The size of the test section is 45.72 cm (18 inches) across, 30.48 cm (12 inches) deep, and 134.62 cm (59 inches) long. The tunnel is powered by a 25.4 cm (10 inch) diameter 2-bladed propeller connected to a 746-watt (1-hp) motor. The continuously variable motor allows the flow in the test section to be varied from 2.54 cm/sec (1 inch/sec) to 30 cm/sec (1 foot/sec). The test section is slightly diverged to account for boundary layer growth.

The water tunnel was designed and built for a high level of flow quality in the test section. The screens and honeycomb in the stilling chamber are for minimizing flow turbulence in the test section. The water can also be filtered to remove impurities and pumped by aspirator pumps to degas the water. This particular test project's goal was to evaluate different nozzle geometries and did not need the filtration or degassing, but the filter's bypass valve was used for bleeding some of the water off to balance the water being injected by the nozzle. This kept the open test section from flooding the room.

The water tunnel simulation relies on the ability to record the flow patterns outlined by the injected dye. The particular dye used for this application consisted of

whole milk, alcohol and industrial red food coloring. The milk holds the dye together longer (needed for turbulent flow), the alcohol adds buoyancy (making the dye neutrally buoyant), and of course food coloring adds the color. The back wall and the bottom wall of the test section are painted white, to aid in seeing the red dye. Normally the water in the test section was used as the surrounding environment for the jet, it was not moving for data gathering. After a few tests the test section becomes cloudy with the red dye, and the tunnel was turned on and the water in the test section was allowed to run through the filtering system to remove the dye.

DATA ACQUISITION

The data for the water tunnel experimentation consists of visual observations noted in a lab book, recorded by still pictures, and recorded by video. In the viewable area, the water tunnel's walls were covered with scales to aid in measuring the size of the flow field phenomena observed. A few still pictures were taken with a Pentax IQZoom 90 WR camera, but problems with the auto-focus on the camera limited its use. The main data acquisition medium was the 16 bit-digital video camera, the Canon Optura. As visual data obtained in this manner can be rather subjective, a common procedure was used throughout the water tunnel evaluations for consistency. Visual observations were made in the same areas of the flow field and compared. Figure 13 shows the evaluation criteria used for the side view. The flow field was divided into five regions: 1) the impingement region where the size was estimated, 2) the rear recirculation zone where strength was rated low, medium or high, 3) the rear nozzle entrainment where the entrainment was rated none, low, high, 4) front nozzle entrainment where the

DATA SHEET

Nozzle:

L/D:

GPM:

Size:

Shroud:

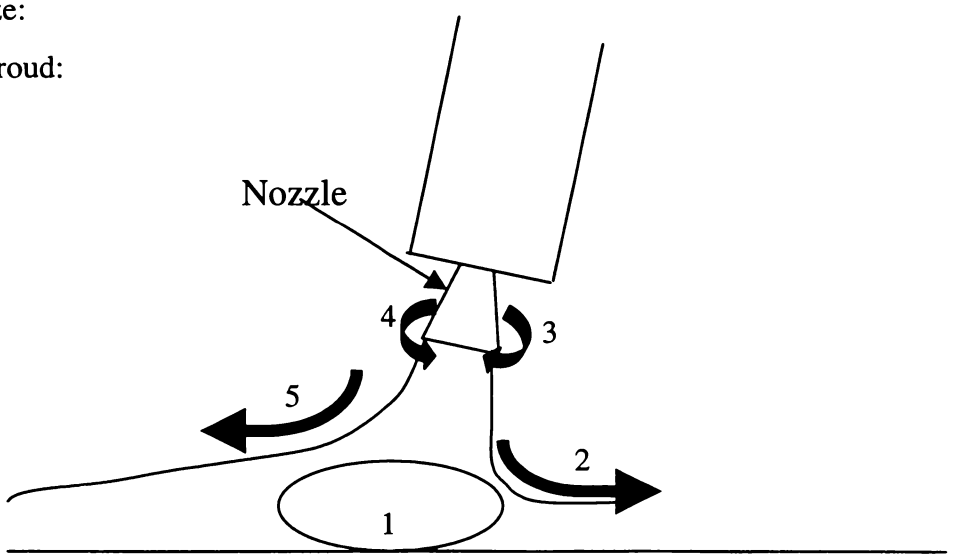

1. Size of impingement zone
2. Strength of rear recirculation:
3. Amount of rear nozzle entrainment
4. Amount of front nozzle entrainment
5. Strength of front recirculation

Figure 13. Water tunnel evaluation criteria.

entrainment was rated none, low, high, and 5) where the front recirculation was rated low, medium or high. In addition to the observations made at the five regions, the general front and rear jet entrainment is noted. The rating system for the entrainment strength was subjective. The ratings of none, low and high were an effort to consistently describe the velocity of the entrained fluid. The rating system for recirculation reflect the fact that recirculation was always present, so a strength of rotation was visually estimated and assigned a rating of low, medium or high.

WATER TUNNEL EXPERIMENTAL PROCEDURE

The general test procedure was as follows: the nozzle model was installed into the plenum model and the working distance was set and measured. The scales were installed or repaired and then the water tunnel was filled up. While the tunnel was filling, the dye was mixed and put into the injection system reservoir and pressurized by an electric pump. The camera was angled and the zoom was set for each region of interest. Once the water tunnel was filled, the jet flow was started and set to the desired flowrate (measured by a Hedline flowmeter, 0-30 GPM), the shroud flow was set (measured by a Hedline flowmeter, 0-2 GPM), and the bleed on the filter was opened. The dye was injected into the region of interest and the video camera recorded the observation. Each of the five regions was evaluated. The stagnation point was found and the impingement area was estimated by moving the dye wand on the water tunnel bottom wall, and noted in the lab book. The nozzle edge entrainment and jet entrainment were both evaluated and noted in the lab book. The water tunnel was drained after the end of each test session.

WATER TUNNEL MODELS DESCRIPTION

The Helium simulation required a geometry that was three times the prototype estimate. The water tunnel nozzle selection evaluation was done with the 3X geometries because the larger the geometries' flow phenomena were easier to see. Nine different nozzle geometries were tested, three with shroud capabilities. The geometries came from experience, literature reviews, and general diffuser design criteria. Table 1 presents all the geometries tested in the water tunnel and gives a short description with reference.

Div1 (as shown in Figure 14) was the first subsonic nozzle contour developed before the literature survey was complete and it is based on conversation with Dr. Merkle on subsonic nozzles [53]. To evaluate the effects of secondary shroud flow on the jet (like reference 31), a version of Div1 with shroud flow was built (as shown in Figure 15). This shroud configuration consisted of eight ¼ inch holes drilled into a manifold surrounding the main jet; later more holes were drilled for a total of sixteen. In order to improve the aerodynamic performance for laser surface alloying, the aerodynamic performance of the current conic nozzle must be reviewed. A copy of the current nozzle was made and is referred to as the conic nozzle (as shown in Figure 16).

The successful turbulent nozzle geometries evaluated by Theobald were thought to be a good starting place for laser surface alloying assist gas nozzle geometries, because they provided the best coverage of the fluid on to a surface. While nozzles for cutting purposes have high impact energy, Theobald's fire-fighting nozzles are evaluated for a combination of maximum range and volume of the water (a combination needed for fire-

TABLE 1. The Nozzle Geometries Evaluated By the Water Tunnel Simulation.

Name	Description	Reference:	Figures
Div1	7° divergent first 2/3 14° divergent last 1/3	[53]	14a, b and c
Div1 w/shroud	Same as above with 8-16 ¼ " holes shroud	[53]&[31]	15a, b and c
Conic	7° convergent (existing)	Existing	16a, b, and c
60° Contraction	45° entrance, 30° divergence angle, then straight	[30]	17a, b, and c
Simple 7° W/holed shroud	7° divergent, rough attempt at a concave	[54] & [30]	18a, b, and c
Rough Convex	Rough attempt at a convex nozzle	[30]	19a, b, and c
Convex	Gentle convex taper	[30]	20a, b, and c
Concave	Abrupt large concave	[30]	21a, b, and c
Simple 7° W/slotted shroud	The 7° geometry with a slotted shroud added	[54], [30] &[55]	22a, b, and c

(a)

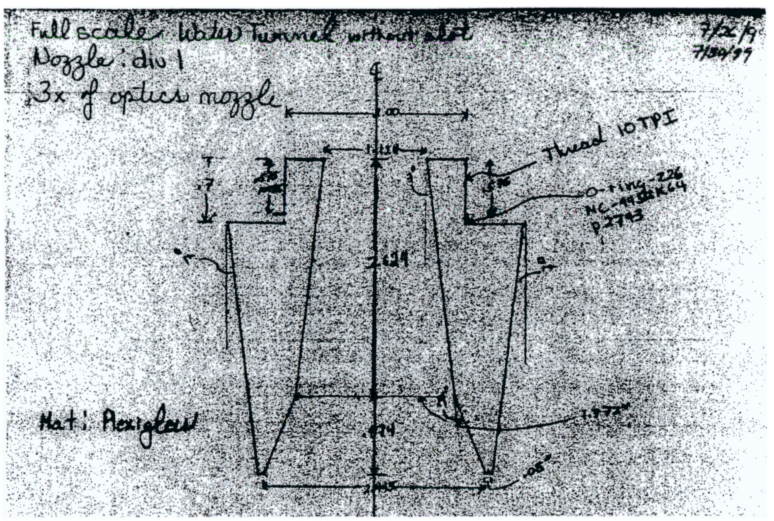

(b)

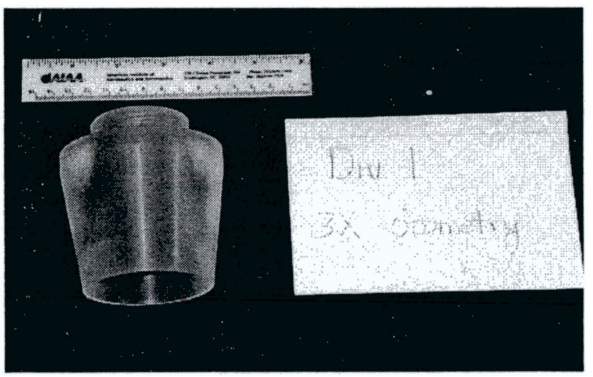

(c)

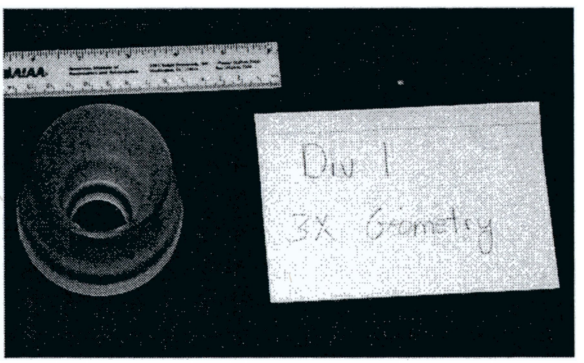

Figure 14: Div1 nozzle geometry a) sketch b)side View c) bottom View

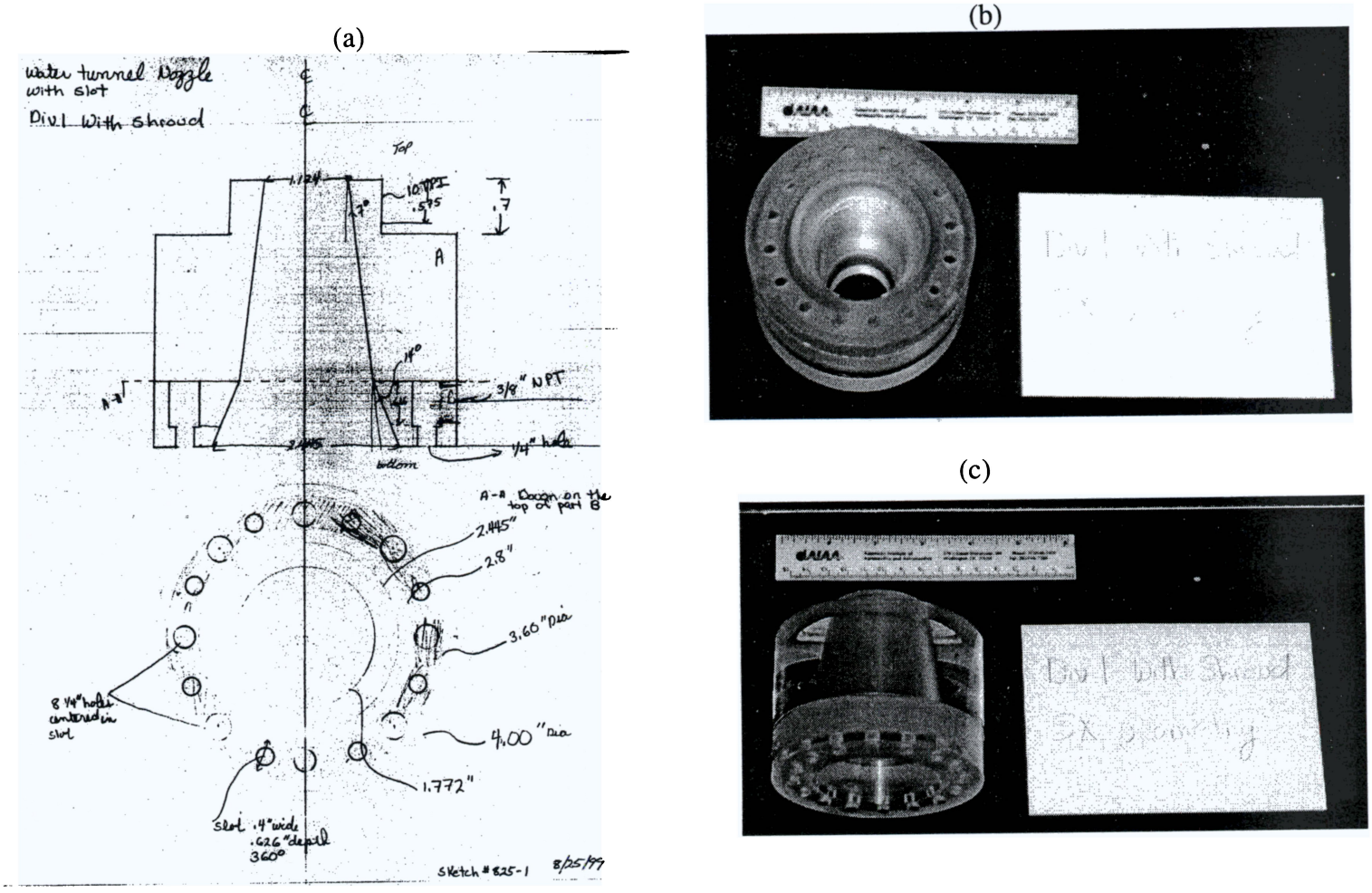

Figure 15: Div1 nozzle with holed shroud geometry a) sketch, b) bottom view and c) side view.

(a)

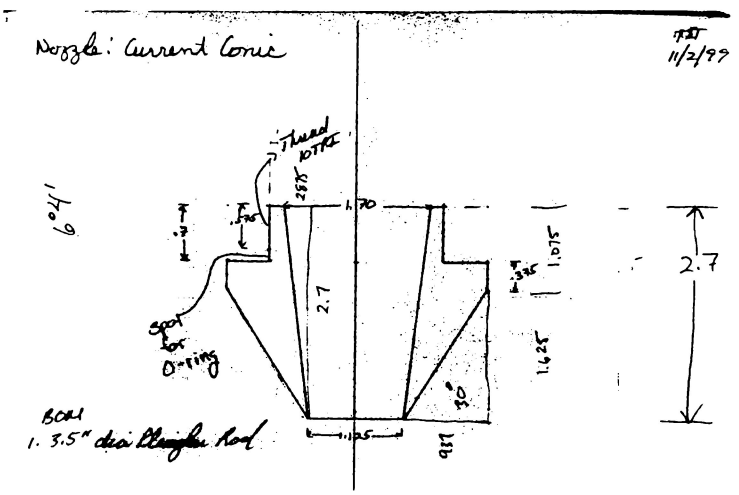

(b)

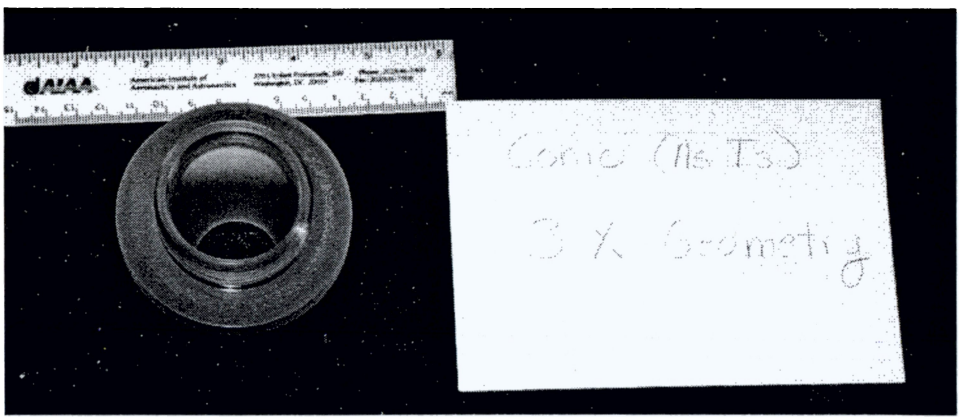

(c)

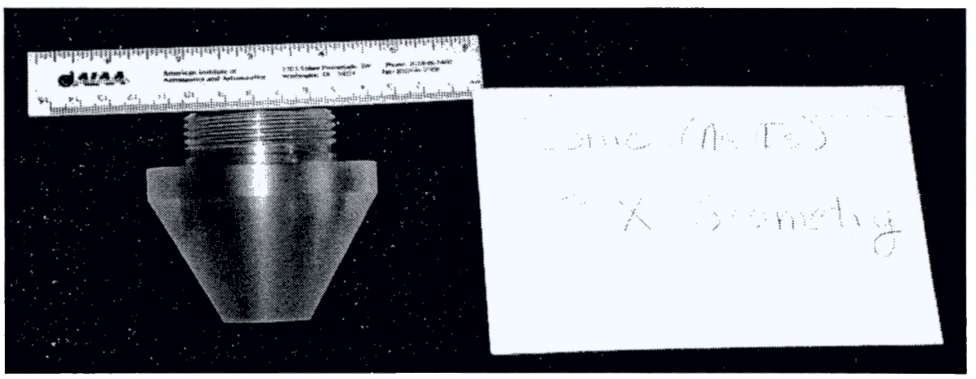

Figure 16: Conic nozzle geometry a) sketch, b) bottom View, c) side View

fighting). One of each of the major type of divergent geometries that Theobald tested was chosen for evaluation for laser surface alloying. The best straight angle divergent (60° contraction angle, Figure 17), the best concave (the non Rouse type, Figure 18), and the smaller convex (Figure 19) were modified for use in water tunnel simulation. The concave and the convex are contoured geometries that require a computer numerical controlled, CNC, lathe to machine, which was not readily available. While the CNC machining was being arranged, a straight edged approximation to the convex and concave contours were machined, these were respectively called the 7° Simple Divergent, and the Rough Concave (Figure 20).

Two different shroud designs were tested with two different geometries. The first shroud design tested was the "holed" shroud, as shown in Figures 15 and 21. This particular design came from the plasma gun geometry that Jankovic and Mostaghimi tested. Eight ¼ inch holes were first tested with the Div1 geometry, and later 8 more holes were added because the nozzle edge entrainment was going between the holes. The 7° Simple Divergent geometry was evaluated with both the "holed" shroud (Figure 21) and the "slotted" shroud (as shown in Figure 22). The holed shroud geometry showed that the shroud flow did help control the nozzle edge entrainment, but some entrainment (a small amount) still came between the holes. For more complete control of nozzle edge entrainment, the continuous slotted shroud used by O'Neill, Gabzdyl, and Steen in their laser cutting application was better than the holed shroud [55].

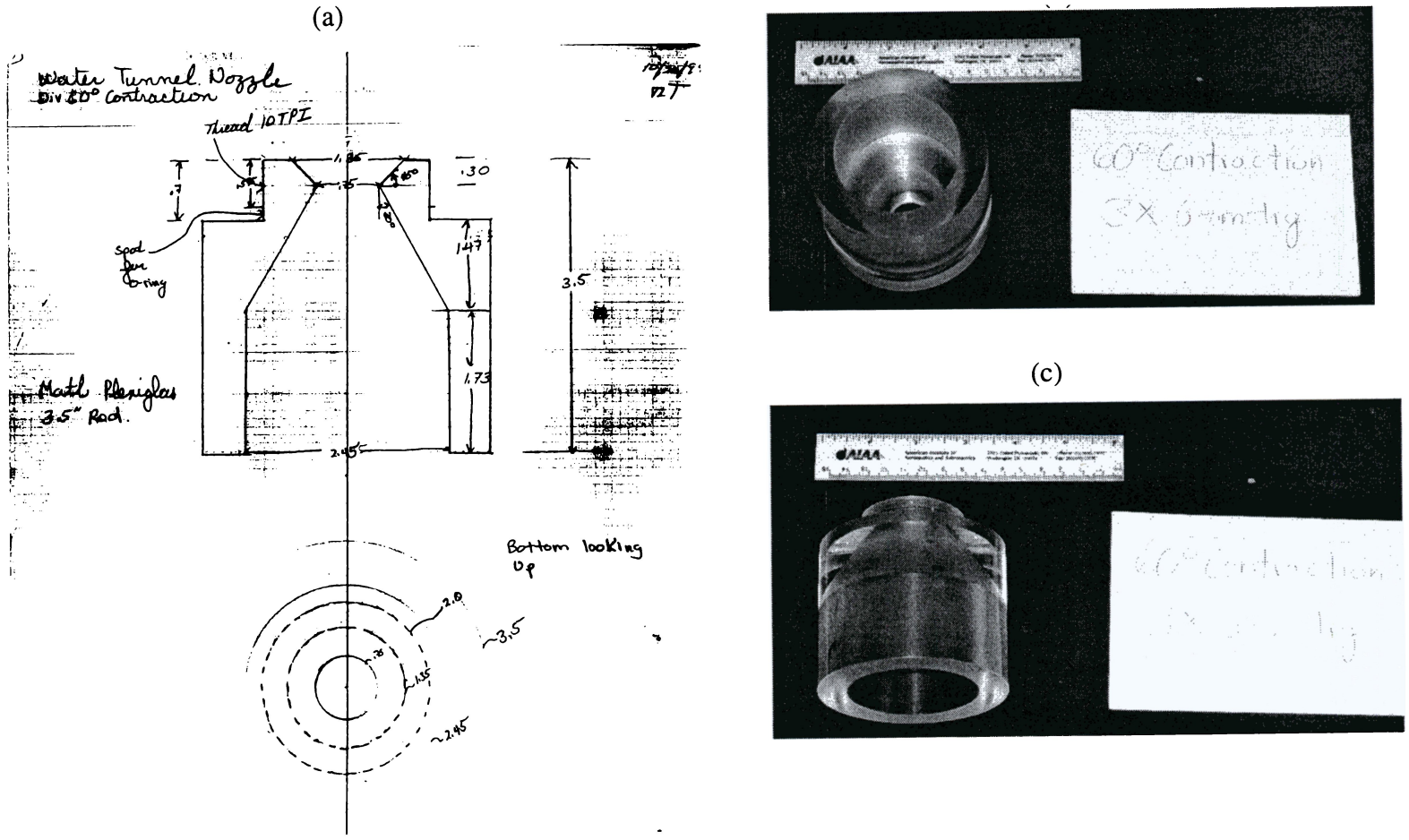

Figure 17: 60°contraction nozzle geometry a) sketch, b) bottom view and c) side view.

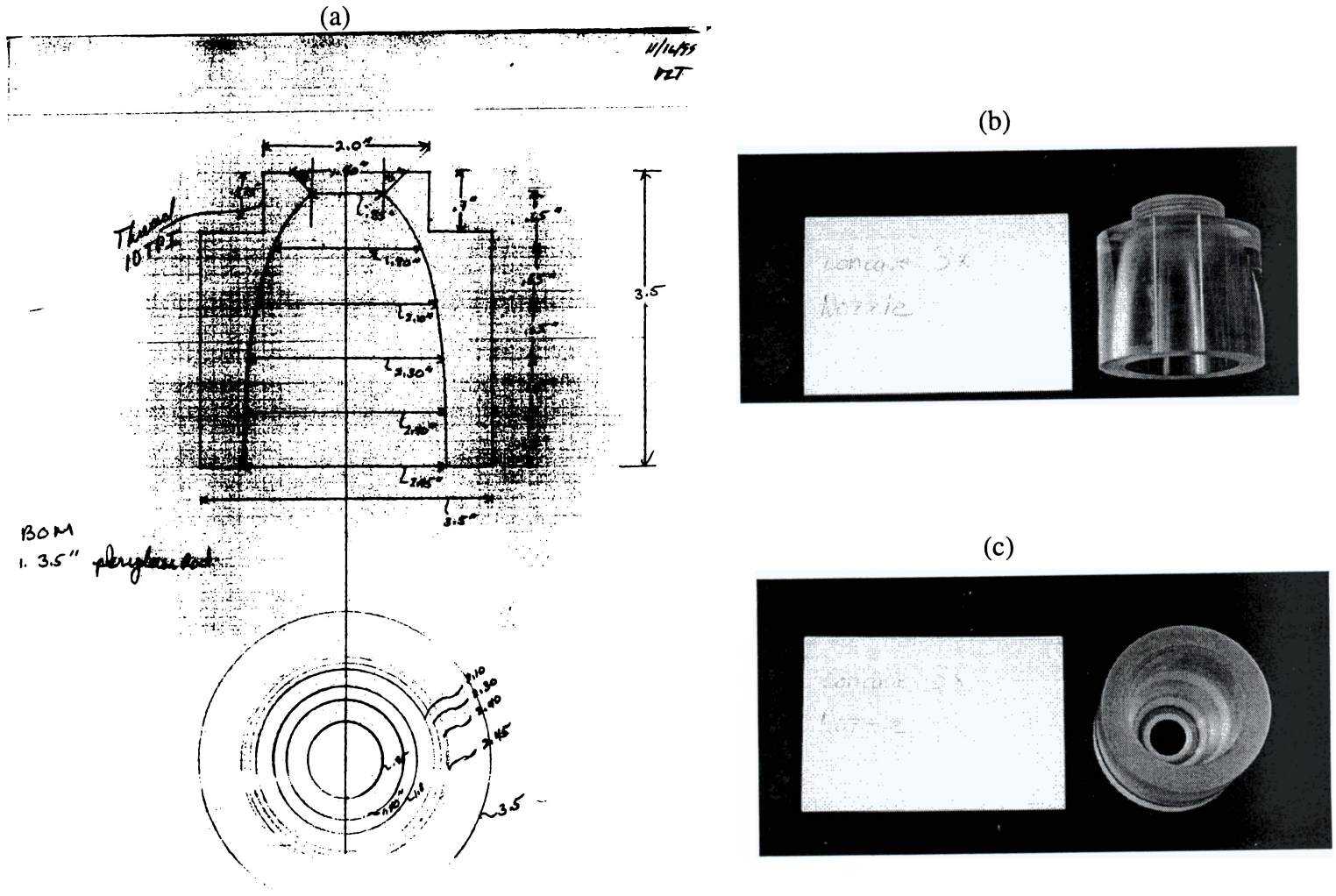

Figure 18: Concave nozzle geometry a) sketch, b) side view and c) bottom view.

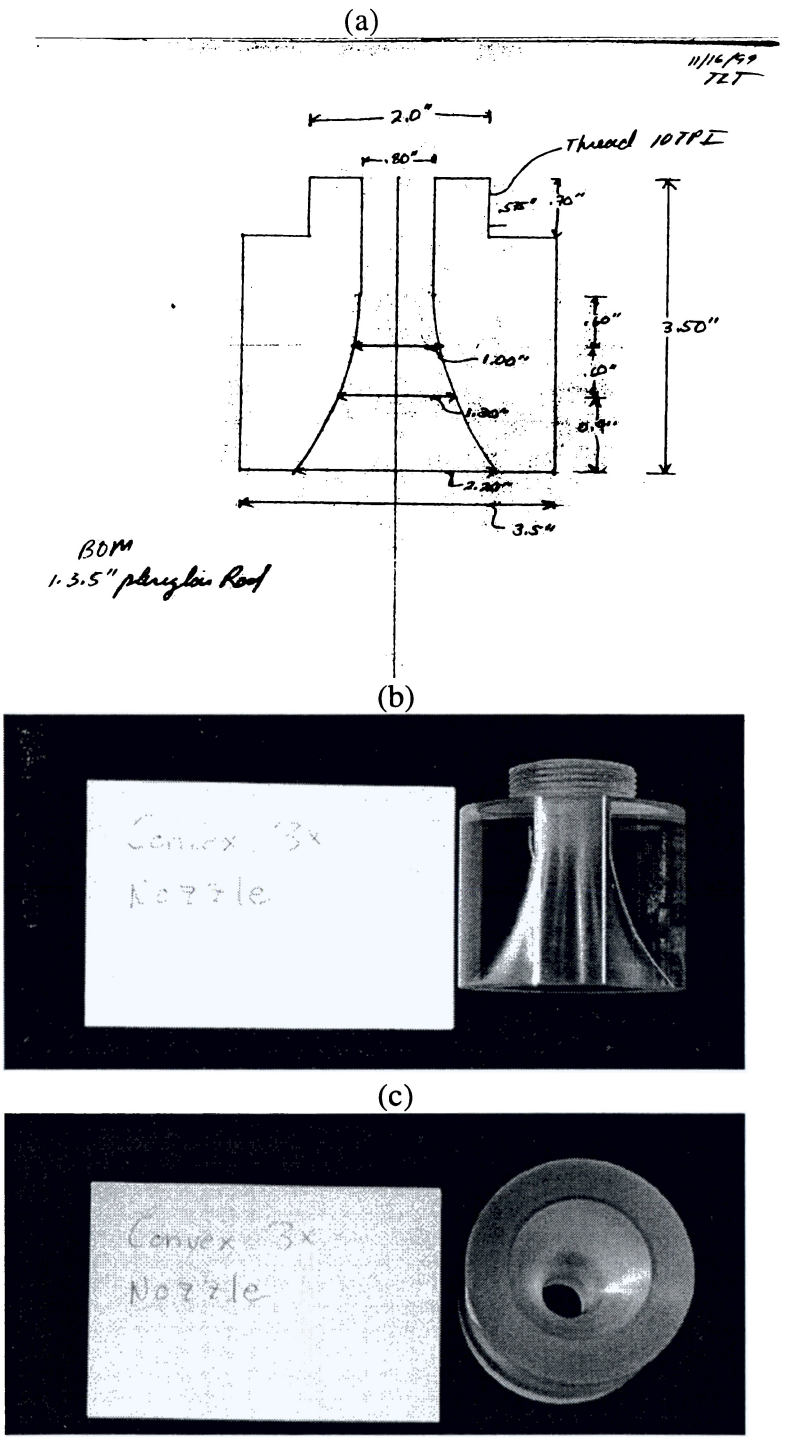

Figure 19: Convex geometry a) sketch, b) side View, c) Bottom View

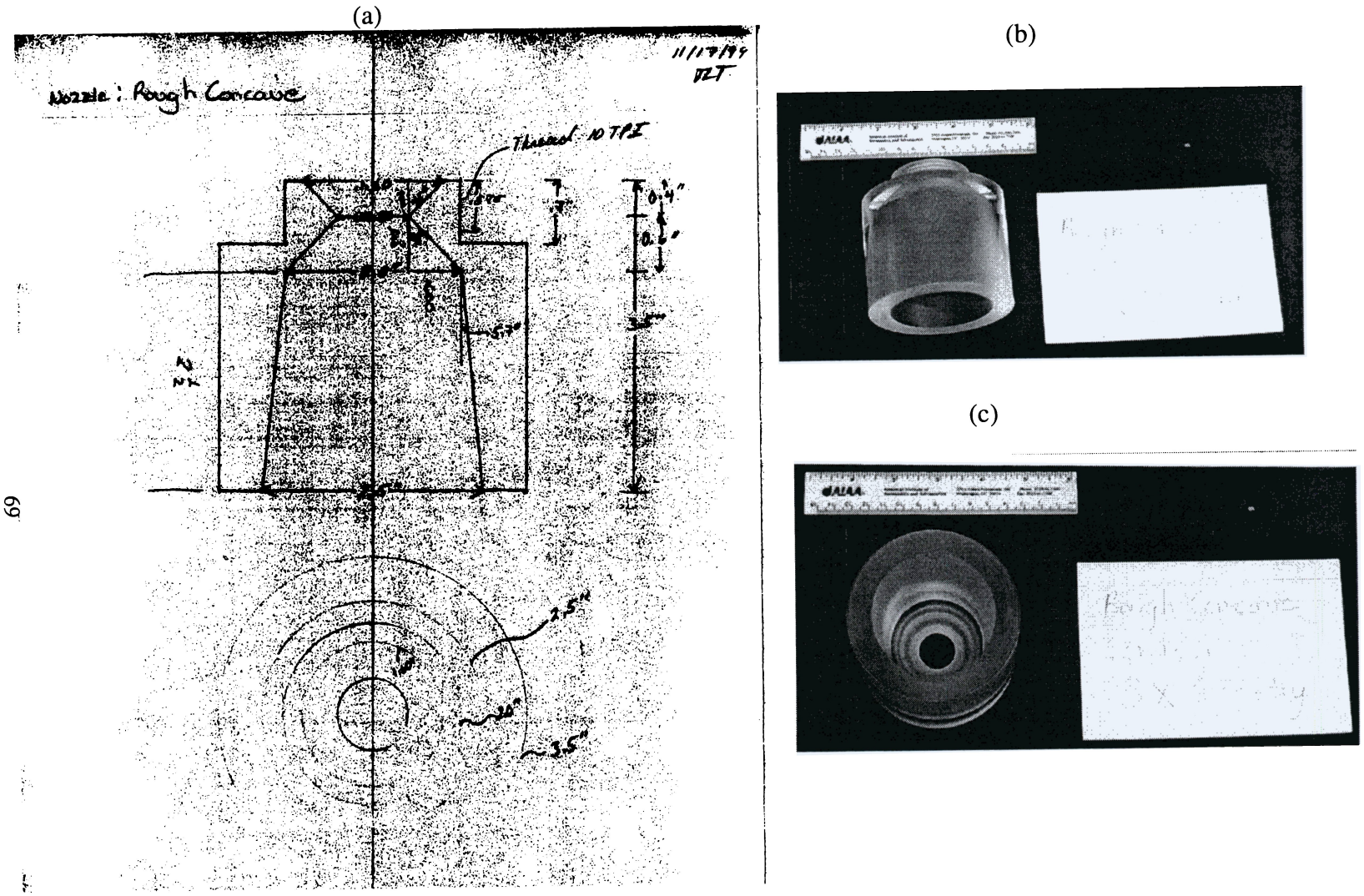

Figure 20: Rough concave nozzle geometry a) sketch, b) side view and c) bottom view.

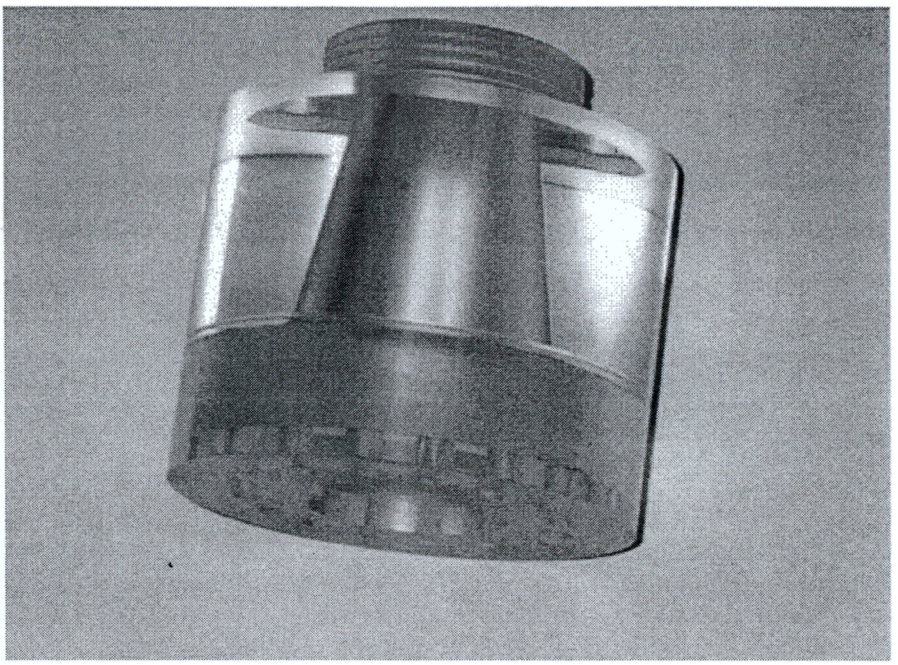

(a)

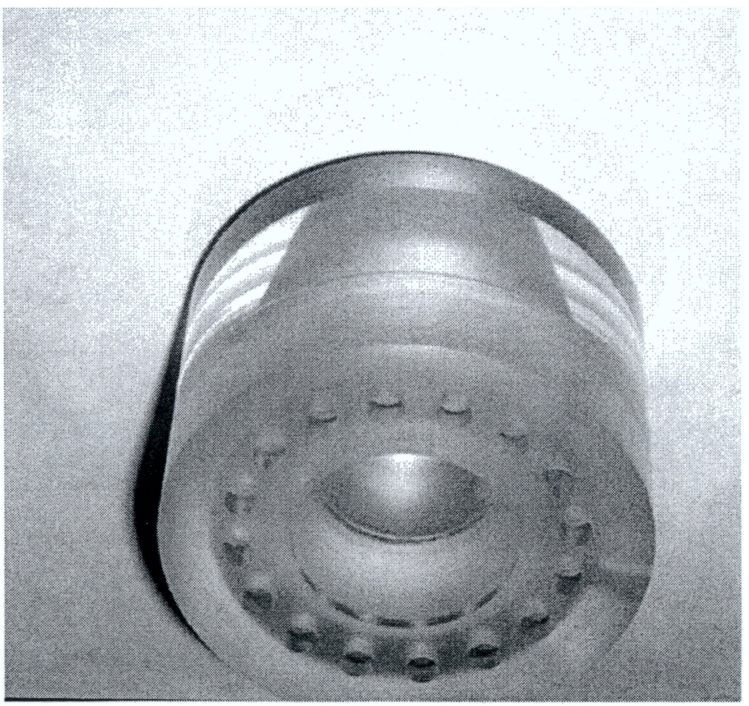

(b)

Figure 21: 7 ° simple divergent nozzle with holed shroud a) side view b) bottom view.

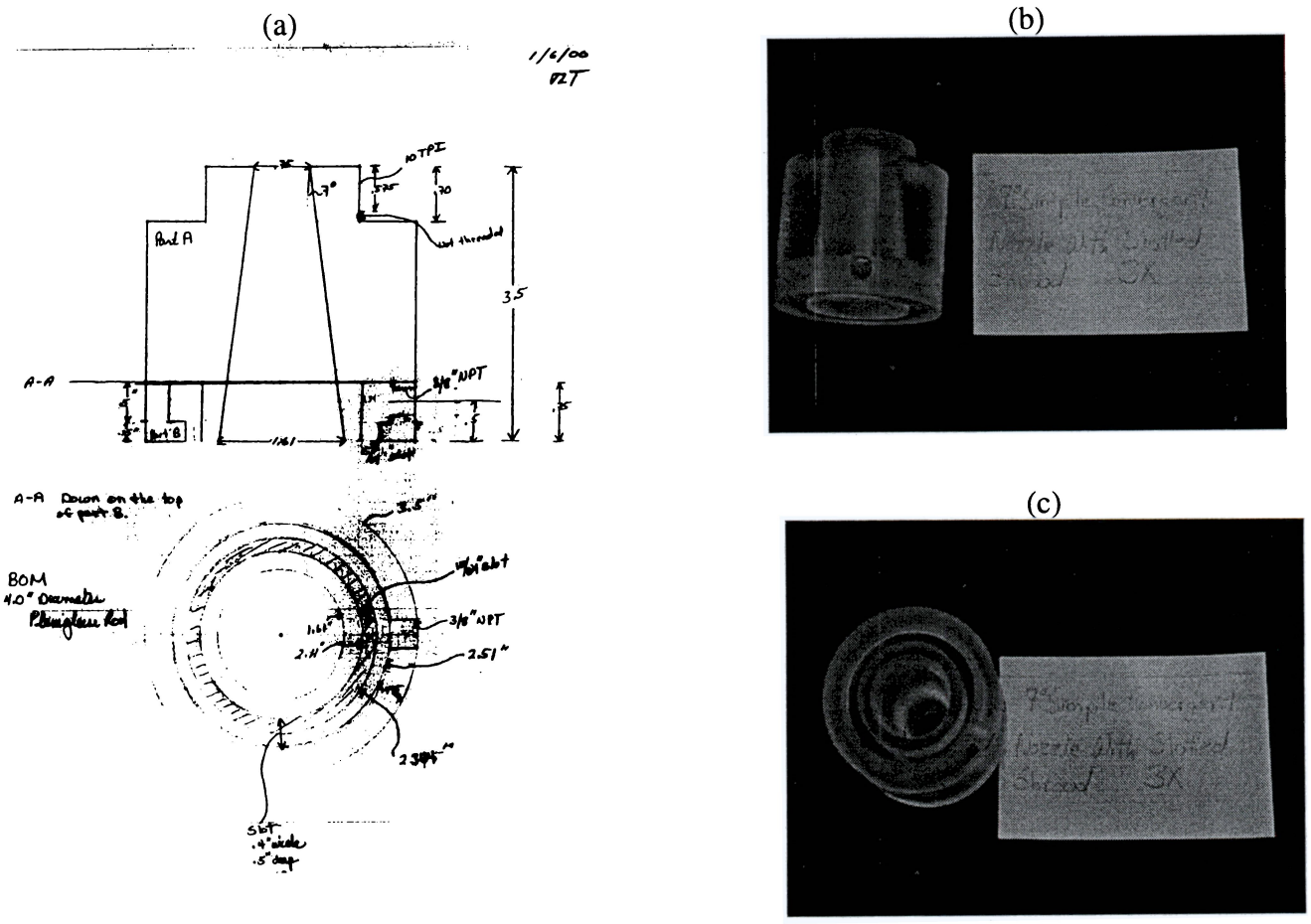

Figure 22: 7°simple divergent nozzle with slotted shroud a) sketch, b) side view and c) bottom view.

NOZZLE GEOMETRY WATER SIMULATION EVALUATION

Water tunnel simulations of aerodynamic flows are great for giving a quick visualization of the overall flowfield, and with a little effort they can also give insight into specific details. From the theory of jet impingement, we know what the general flowfield looks like: the potential jet, the impingement region and the wall flow, the water tunnel simulation quickly gave a general insight into what effects the 15 degree off-set (also known as a small oblique jet impingement) has on the previously known flowfield. Figure 23 shows the general features of the oblique jet impingement found by the water tunnel simulation. A skewed impingement region (1), front and rear recirculation zones (5) and (2), front and rear nozzle edge entrainment (4) and (3), radial wall flow (A), front and rear jet entrainment (E) and (B), and front and rear optics recirculation (D) and (C). In normal impingement the front and rear impingement flow field is the same. With the oblique impingement, the flow field is not the same in the front as it is in the rear. In most cases the rear recirculation or rear entrainment is more severe than the front. In all the geometric configurations tested, all the flow field phenomena shown in Figure 23 existed in some form. Another flowfield phenomena that was generally observed in the water tunnel simulation was the presence of a swirling motion in the plenum itself. The plenum was designed to be a replica of the existing laser surface alloying gas delivery package from the last lens to where the gas nozzle screws in. In the existing gas delivery package, the gas is fed into the entrance of the nozzle through the gas delivery package walls and injected perpendicular to and across the nozzle entrance. In the water simulation, water fills up the bottom of the plenum to a point where the pressures are

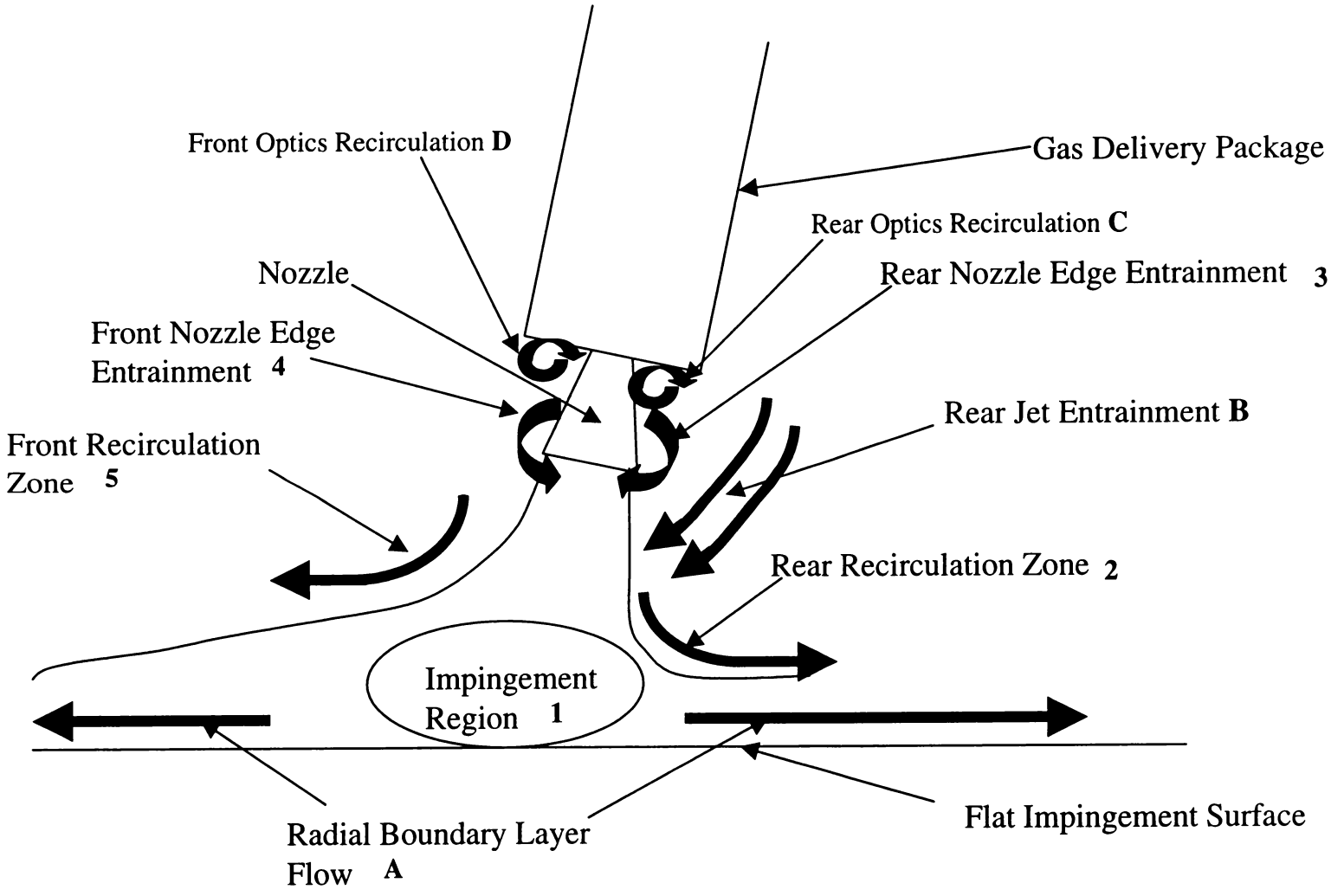

Figure 23: General features of oblique jet impingement.

balanced. The fluid injection across the nozzle entrance, in a volume of standing fluid, causes a strong, unsteady swirling motion to form. This swirling motion was always present in the water tunnel simulation; Figure 24 shows the swirling motion, which is outlined by the bubbles in the water supply.

The goal of this project was to evaluate nozzle geometries, not to develop a plenum; however, the flowfield in the plenum does effect the flowfield of the jet impingement. Occasionally the unsteady characteristic of the plenum swirling motion, feeds through to the nozzle edge entrainment, causing that to be cyclic following the swirling motion cycles. The unsteady swirling motion in the plenum affects the nozzle impingement performance, sometimes making the entrainment worse, and causing the impingement region's velocity components to be unsteady. As, ideally, the molten metal is under the impingement region; this may cause impressions in the final alloy layer.

Three different working distances were simulated in the water tunnel. 76 mm, 152 mm, and 229 mm (corresponding to 25 mm, 51 mm, and 76 mm in the prototype) were tested. In general, when the working distance was decreased, the impingement region and wall flow thickens, the jet entrainment decreases, and the footprint of the impingement regions increases (see Figure 25). The nozzle edge entrainment does not appear to be effected by the working distance. As the working distance is increased, the whole flowfield starts to lift up. The wall flow goes from having all radial velocity components, to having some vertical velocity components. The flow in the impingement region also starts to show vertical velocity components. The increase in working distance

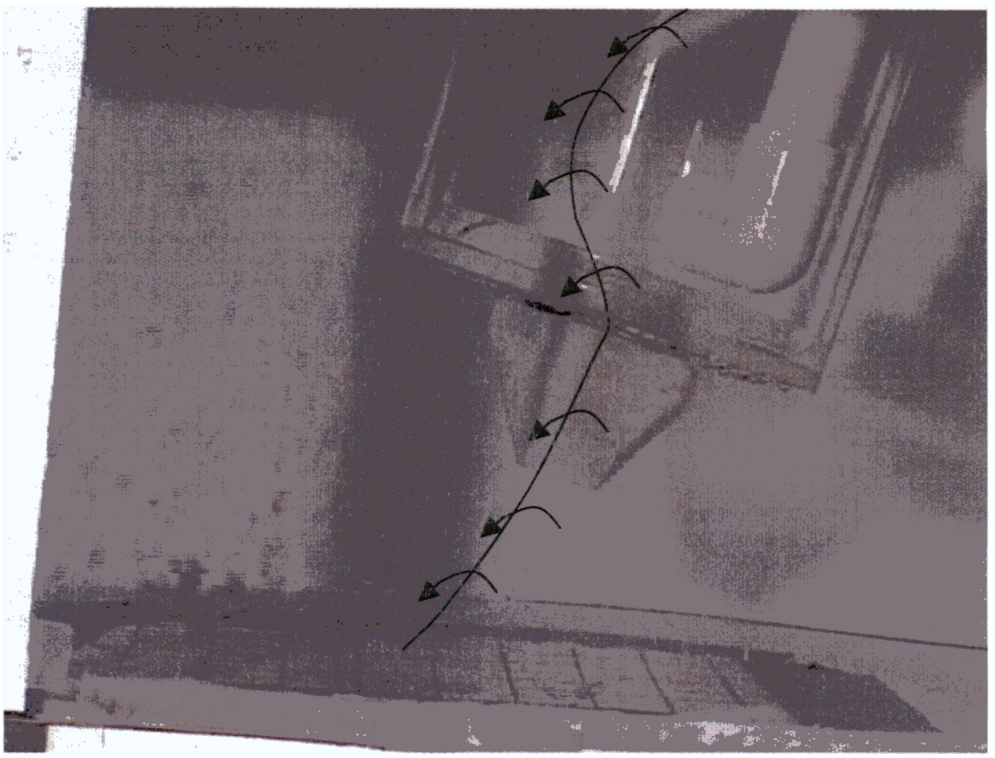

Figure 24: Swirling motion in plenum.

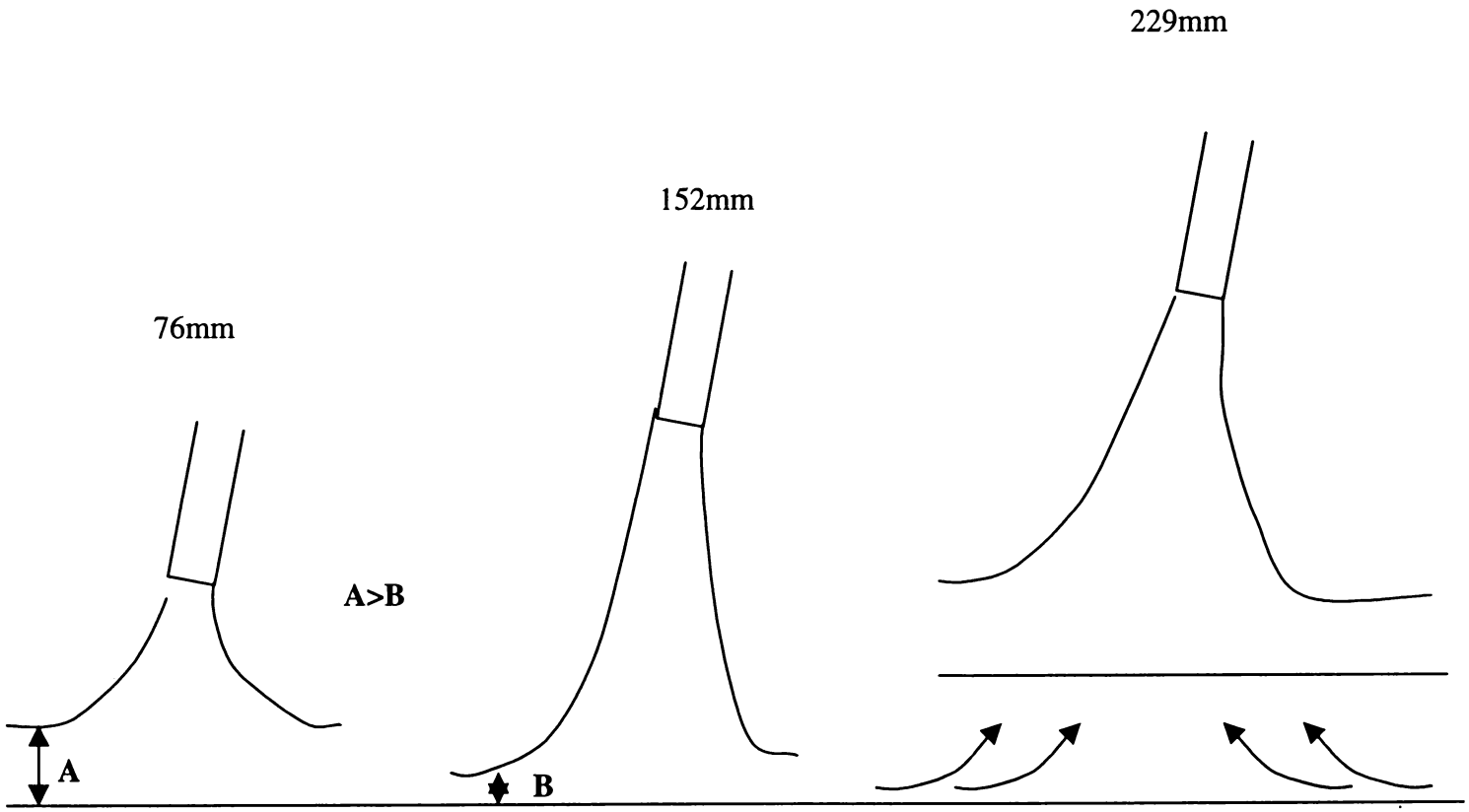

Figure 25: The general flow fields of the three working distances.

is also characterized by an elongated jet, which has more boundary area in which more fluid can be entrained.

The standard velocity of the optics package during the laser surface alloying process is between 1000 mm/min and 5000 mm/min. In this range, the crossflow is so small in comparison to the velocity of the jet, that it has a negligible impact on the flowfield and was not simulated in the water tunnel tests. However, a strong crossflow was applied in the water tunnel just to see what the effect would be. The resulting flowfield was similar to the flowfield produced by the long workings distance, except for the addition of a flow under the impingement region moving parallel to the wall. This is only mentioned as a warning that there will be a velocity limitation for the use of a gas protective nozzle, but that limit is somewhere beyond 5000mm/min.

EACH NOZZLE GEOMETRY'S WATER SIMULATION EVALUATION

Table 2 presents an attempt to objectively evaluate the nozzle geometries during a subjective simulation. For each nozzle geometry, the impingement footprint was estimated, the front and rear nozzle edge entrainment was rated, the front and rear jet entrainment was rated, the front and rear recirculation zones were rated and an attempt to measure the wall layer thickness was made. Many of the measurements were estimated by injecting the dye and making an estimate with the 2 cm grids that were placed in the water tunnel viewing field. Both the nozzle edge and the jet entrainments were rated by none, low, medium or high. It should be noted that the ratings are a subjective attempt to rate the velocity of the apparent entrainment.

TABLE 2. Summary of the water tunnel data.

Nozzle	Flow rate	Size	WD	Footprint	Front Nozzle	Rear Nozzle	Boundary	Front Jet	Rear Jet	Front	Rear	Shroud
	GPM		mm	mmXmm	Entrainment	Entrainment	Layer Thickness	Entrainment	Entrainment	Recirculati	Recirculation	Flowrate
Div1 (Checkout)	18	3X	152.4	N/A	Med	High	N/A	N/A		N/A	50.8mm	N/A
Div1	18	3X	152.4	152.4X101.6	Almost none	Med to High	?	?	?	?	63.5-76.2	None
Div1	18	3X	152.4	152.4X101.6	Almost none	None	?	None	?	?	63.5-76.2	2GPM/H
Div1	18	3X	152.4	152.4X101.6	Almost none	Slight	?	None	?	?	63.5-76.2	1GPM/H
60 deg Contraction	18	3X	152.4	101.6X38.1	Almost none	High	50.8mm	None	Med	2"	38.1	N/A
Conic	18	3X	152.4	101.6X50.8	None	None	?	High	Very High	?	None	N/A
Conic	18	3X	76.2	127.X76.2	None	None	50.8	High	Very High	?	None	N/A
Simple 7 deg	18	3X	152.4	127.X101.6	None	Low (Unst)	?	?	Low	Strong	Low	None
Simple 7 deg	18	3X	152.4	127.X101.6	None	Low (Unst)	?	None	Low	Strong	Low (1")	2GPM/H
Simple 7 deg	18	3X	228.6	76.2X76.2	None	Low (Unst)	?	None	Low	Strong	Low (1")	None
Simple 7 deg	18	3X	76.2	139.7X127.	None	Low (Unst)	Thick	None	Low	Strong	Low (1")	None
Rough Concave	18	3X	152.4	114.3X76.2	Low (Unst)	High	25.4	?	High	?	Into Nozzle	None
Rough Concave	18	3X	228.6	?	Low (Unst)	High		Higher	High	?	Into Nozzle	
Rough Concave	18	3X	76.2	?	Low (Unst)	High				?	Into Nozzle	
Convex	18	3X	152.4	120X160	None	Low (Unst)		None	Low		Low	None
Convex	18	3X	76.2	Scale Prob	None	Real Low						
Concave	18	3X	152.4		High	Low		?	High	Strong	Low	
Simple 7 deg	18	3X	152.4									2GPM/S
? Refers to conditions where the measurement												
was too difficult to obtain.												
One measurement of each configuration was made.												

An example of front, side, and rear nozzle edge entrainment is shown in Figure 26 a, b, and c. With the rough concave nozzle geometry the front nozzle edge entrainment starts to go into the inside of the nozzle, but was diverted at the nozzle edge and that particular streamline is redirected into the jet. The side and rear entrainment of the rough concave nozzle (shown in Figure 26b and c) starts on the outside of the nozzle and was entrained at the nozzle exit then sucked into the nozzle itself. The problem with the nozzle edge entrainment in a protective gas nozzle is that air will be pulled into the nozzle and the shielding gas would be contaminated with the air. One way to control the nozzle edge entrainment is with a nozzle edge shroud flow. This is a secondary flow that surrounds the core gas jet. The idea behind the shroud flow is to redirect the entrainment flow so that it converges with the jets outer shear layer. Figure 27a) shows the 7° Simple nozzle geometry with rear nozzle edge entrainment. Figure 27b) shows the 7° Simple nozzle geometry with shroud flow. The nozzle edge entrainment is redirected and it is not sucked into the nozzle flow. At first a "holed" shroud was tested, and while it did redirect some of the nozzle edge entrainment, it allowed some entrainment to get into the nozzle by going between the holes. To prevent the nozzle edge entrainment between the holes a continuous slotted shroud was built. Here the shroud flow is in a continuous ring around the jet and all nozzle edge entrainment is prevented.

Jet entrainment in a normal impingement occurs equally around the circumference. With the oblique impingement the entrainment appears to be worse in the rear of the flowfield (or in the direction of the angle). Figure 28(a) shows rear jet entrainment of the rough concave nozzle geometry. Far away from the nozzle edge the

a)

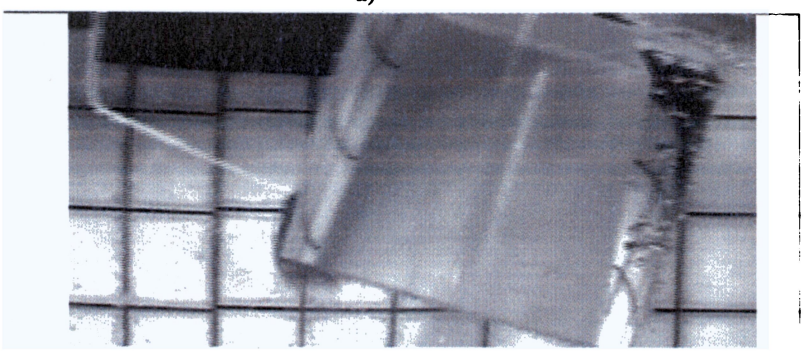

b)

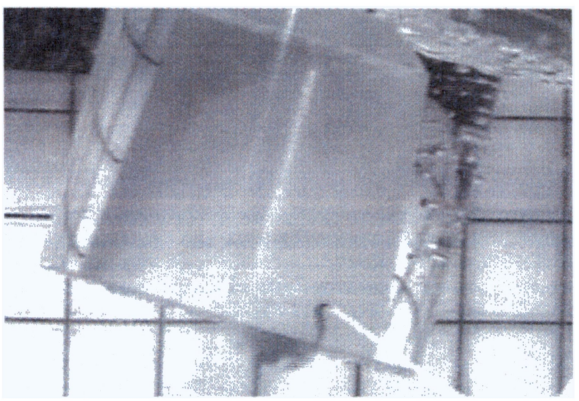

c)

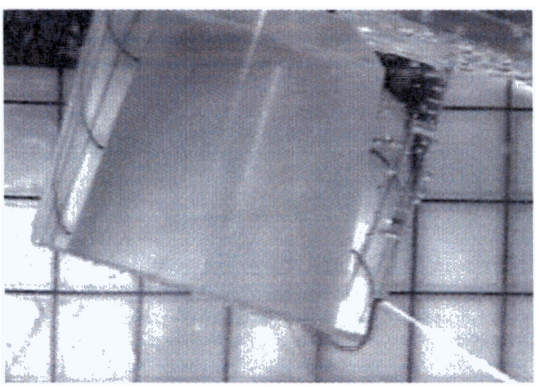

Figure 26: Nozzle Edge Entrainment a) Front nozzle edge entrainment, b) Side nozzle entrainment, c) Rear nozzle entrainment.

a)

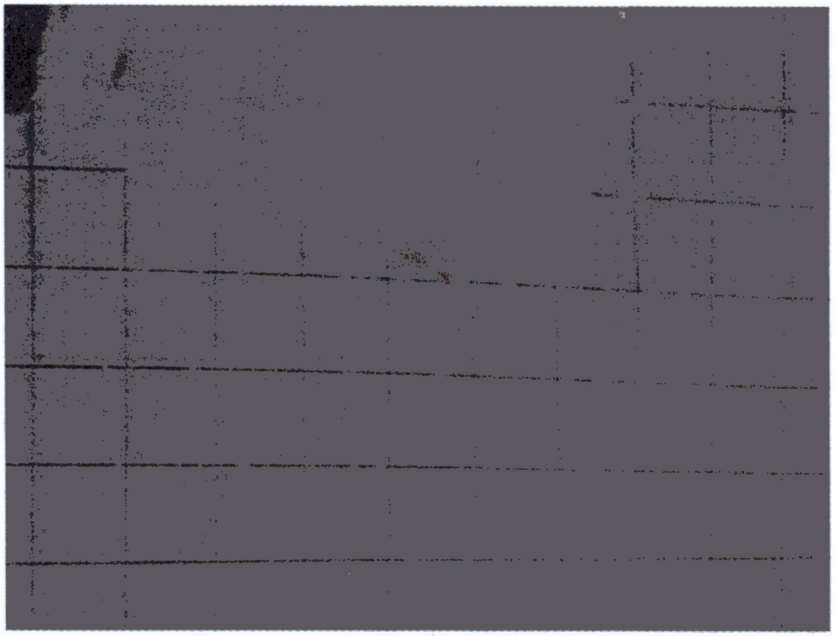

b)

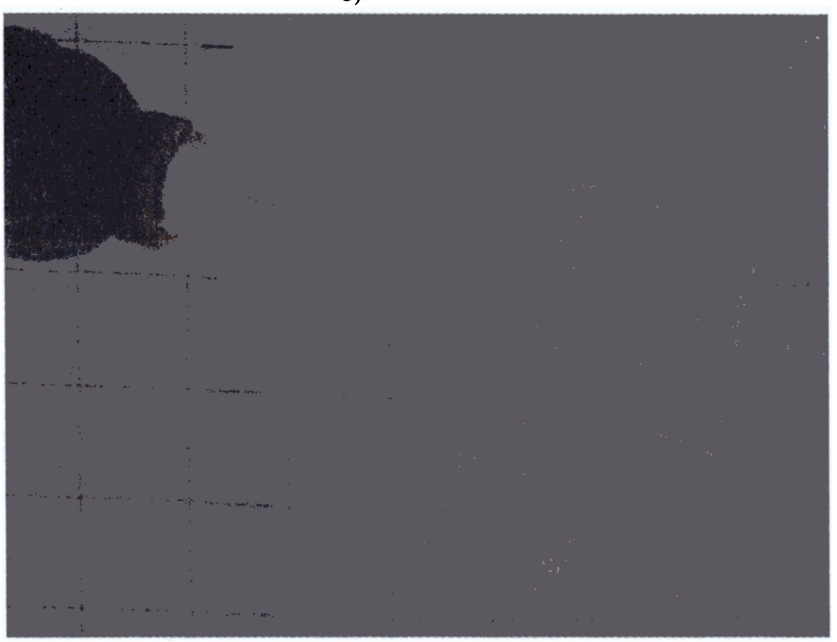

Figure 27: 7• Simple Divergent Nozzle Entrainment a) Rear nozzle edge entrainment, without shroud flow. b) Redirected rear nozzle edge entrainment, with 2 PGM shroud flow.

a)

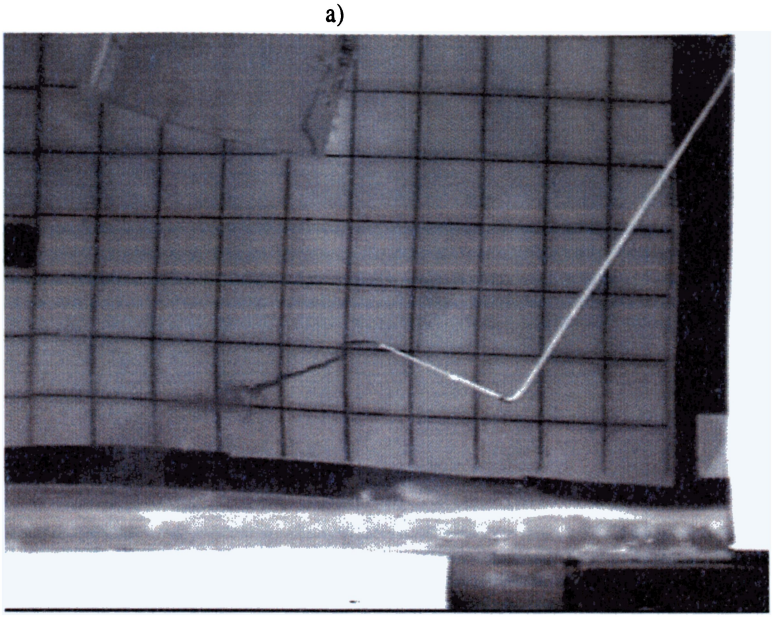

b)

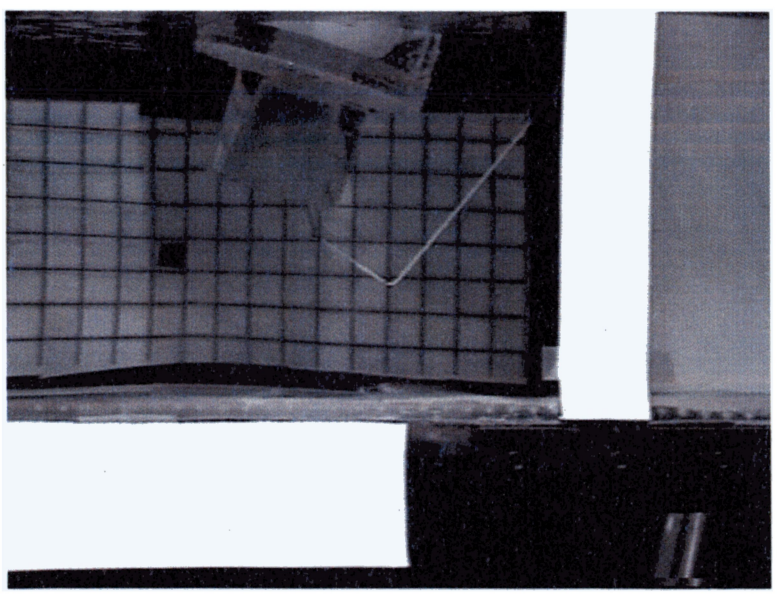

Figure 28: Rear Jet Entrainment a) into jet, b) being pulled into the nozzle.

jet entrainment is pulled into the jet itself. For the rough concave nozzle geometry the jet entrainment closer to the nozzle exit gets pulled into the nozzle itself, as shown in Figure 28(b). In front jet the jet entrainment is initially pulled toward the jet, then it appears to be redirected away from the impingement region by the front recirculation zone (Figure 29). While we know that nozzle edge entrainment that is pulled into the nozzle has a negative impact on gas contamination, the impact of jet entrainment is less obvious. It is not obvious from the water tunnel simulation how far into the jet core that the entrained fluid is carried. The whole point of using the protective gas is to protect the molten metal in the impingement region. How much of the jet entrainment is just pulled into the outer shear layer and how much of it gets to the impingement region is not known, and it cannot be known from the water tunnel simulation. It will take the O_2 gas sampling during the gas trials to quantify the effects of the jet entrainment. The use of the secondary shroud gas obviously reduced the nozzle edge entrainment, and ultimately jet core contamination. The effect of jet entrainment on the jet core contamination was not obvious from the water tunnel simulation, and will again have to be quantified with gas sampling during the gas trials.

A recirculation region is formed at the point where the impinging jet meets the wall flow and the impinging jet is turned. In that turning, a recirculation is formed. Again, with the oblique angle of impingement, the strength of this recirculation zone is uneven. Figure 30(a) shows the rear recirculation zone of the 7° Simple Nozzle with holed shroud nozzle geometry. Figure 30(b) shows the front circulation zone of the same nozzle geometry. As the recirculation zone is at the edge of the impingement region, it

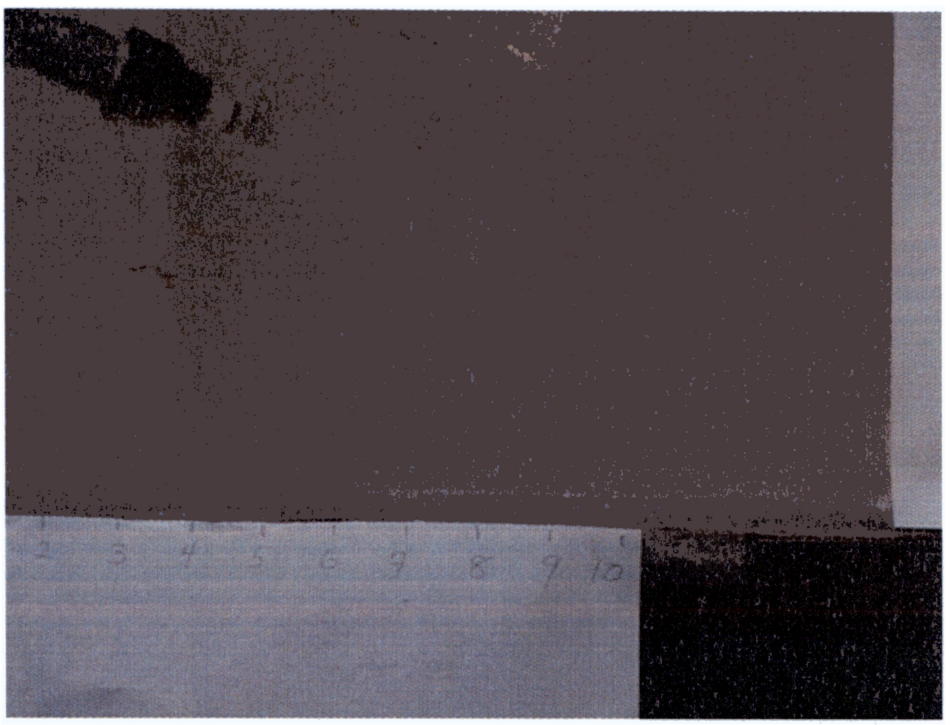

Figure 29: Front jet entrainment.

a)

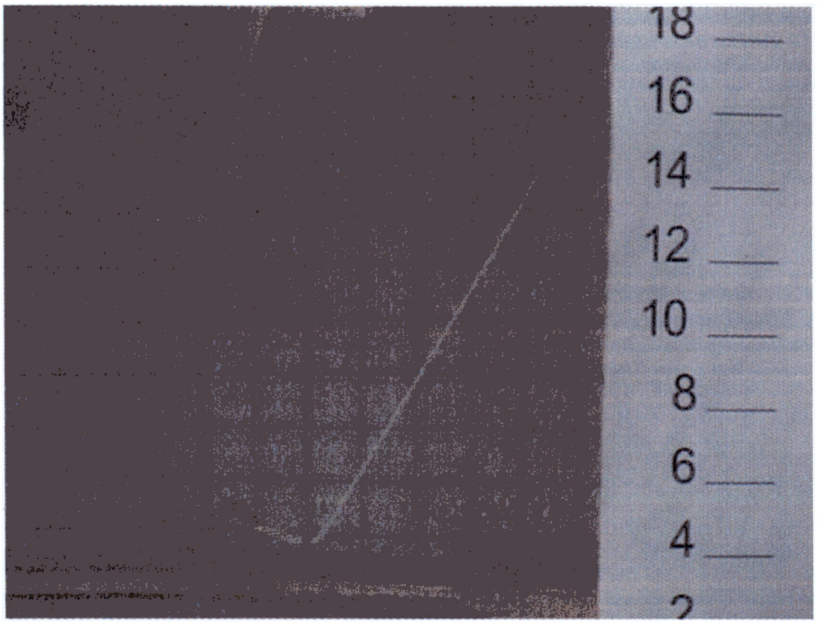

b)

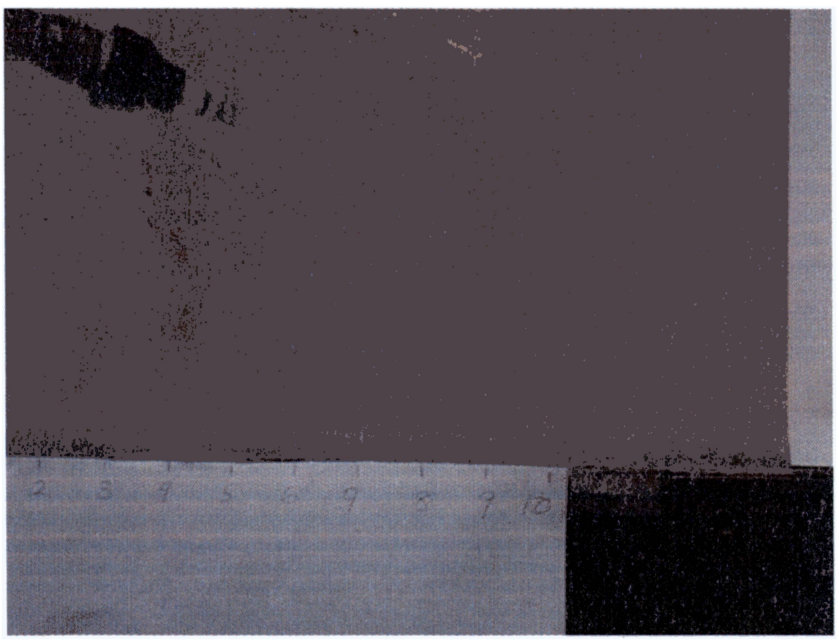

Figure 30: Recirculation zones a) Rear recirculation zone, b) front recirculation zone.

should not have much effect on the level of contamination of the core jet in the impingement region.

The impingement region is the region where the jet core slows down as it impinges on the flat surface. An attempt was made with each configuration to estimate the size of the impingement region by using the injected dye to find the edge of the impingement region on the bottom of the water tunnel (on the bottom was taped a letter size grid). Only one measurement of the impingement region was made for each configuration. The impingement region is where the jet core gas composition should be the purest, where the jet core gas has the least amount of contamination from the surrounding environment. In this impingement region, is where the molten metal should be most protected from the surrounding environment. One reason for trying to determine the size of the impingement region is to see if it is large enough to cover all of the area of the molten metal. The previous calculation showed that the area of steel to be protected was approximately 7.25 mm by 4.75 mm. Since the geometry of the water tunnel simulation is three times that of the prototype estimate, the minimum impingement area in the water tunnel would be approximately 21.75 mm by 14.25mm, or 2.175 cm by 1.425 cm. The smallest impingement area measured during the water tunnel simulation was 76.2 mm by 76.2 mm, and that occurred with the 7° simple nozzle geometry at a working distance of 228.6 mm (the largest tested). The impingement region of all tested configurations should be adequate to cover the molten metal from a line beam 4mm by 700 microns.

WATER TUNNEL CONCLUSIONS

From the table the overall two best nozzle geometries were the Conic (convergent) nozzle and the 7° Simple Divergent nozzle. The conic nozzle had no nozzle edge entrainment, while the 7° Simple Divergent nozzle has a low unsteady amount of edge entrainment at the rear of the nozzle. The unsteady nozzle entrainment feature observed was probably due to the swirling motion found in the plenum and should go away with a better plenum design, or it can be somewhat controlled with a shroud flow. The conic nozzle has a very high rear jet entrainment, while the 7° Simple Divergent nozzle has a low rear jet entrainment.

The conclusion of the water tunnel simulations, with these particular geometries tested, was that the 7° Simple Divergent nozzle with a slotted shroud appeared to be the best geometry for the laser surface alloying process. The gas tests proceeded with this geometry, plus the existing conic nozzle geometry. It should also be pointed out again that the water tunnel simulation provides flowfield visualization only in the looked at with the dye wand. The water tunnel simulation does not provide quantitative details or aerodynamic specifics, such as pressure or temperature distributions. The next step in this research project is to make a prototype of the 7° simple nozzle and evaluate it (along with the existing conic nozzle) with actual gases.

CHAPTER V

GAS TRIALS

The water tunnel simulation visualized the flowfield associated with the oblique jet impingement on a flat surface produced by several different nozzle configurations. From that flowfield visualization two nozzle geometries were chosen for further evaluation, the existing Conic nozzle and the 7° Simple Divergent nozzle with shroud flow. For quantitative evaluation of the jet impingement produced by these two different nozzles, gas trials of theses two nozzle geometries were performed. During these gas trials, the pressure profile and the oxygen content on a flat plate were measured with Argon (Ar), Nitrogen (N_2), and Helium (He) gas jets. In order to verify the flowfield seen in the water tunnel simulation, flow visualization was also performed during the gas trials.

HARDWARE AND Re DIFFERENCES

The water tunnel simulation work began in March of 1999 and the gas trials work began in February of 2000. During that time period the laser's gas delivery package (with its associated optics) was redesigned. As the laser beam leaves the end of the fiber optic cable, it diverges and goes into a collimating lens and then a series of focusing lenses. The threaded hole in the bottom of the gas delivery package I, where the conic nozzle screwed into the package, was too small and "clipped" the focused laser beam. The clipping of the laser beam resulted in less energy being delivered to the workpiece, and the gas delivery package absorbing a large amount energy from the laser

beam causing cracking in the optics lenses and heat damage to the end of the fiber optic cable. The redesign of the gas delivery package consisted of repositioning the lenses, enlarging the hole at the bottom, and removing the gas feed through the package. The redesigned gas delivery package will be referred to as gas delivery package II. See Figure 31 for a schematic of the two gas delivery packages.

The water tunnel model was based on the gas delivery package I. The volume of the package before the nozzle entrance is referred to as the plenum. The plenum model was based on the gas feed going through the package walls and being injected by one port across the entrance of the nozzle. The water flowrates and the geometry size used in the water tunnel simulation were based on the diameter of the gas delivery package I. The gas trials were planned using the gas delivery package I (with its existing gas path feed) and mounting different nozzle shapes into the gas delivery package. The decision had to be made whether to either continue on the current path, or redesign all the water tunnel and gas path hardware and repeat all the water tunnel simulation. It was decided to continue on with the gas trials as planned, and in parallel, to design a 7° Simple Nozzle with the larger diameter, and add on to the gas trials for an evaluation of the gas delivery package II. The reasoning for continuing with the current plan was that the water tunnel simulation was a qualitative evaluation. While it gave much needed insight into the flowfield produced by the oblique jet impingement, it did not provide quantitative results. The flowfield seen in the water tunnel should still be there during the gas trials, even with the larger diameter. Previous water tunnel work done by Dave Beale [56] evaluated the flowfield and vortex formation in a model of an engine test facility. In that work, it was

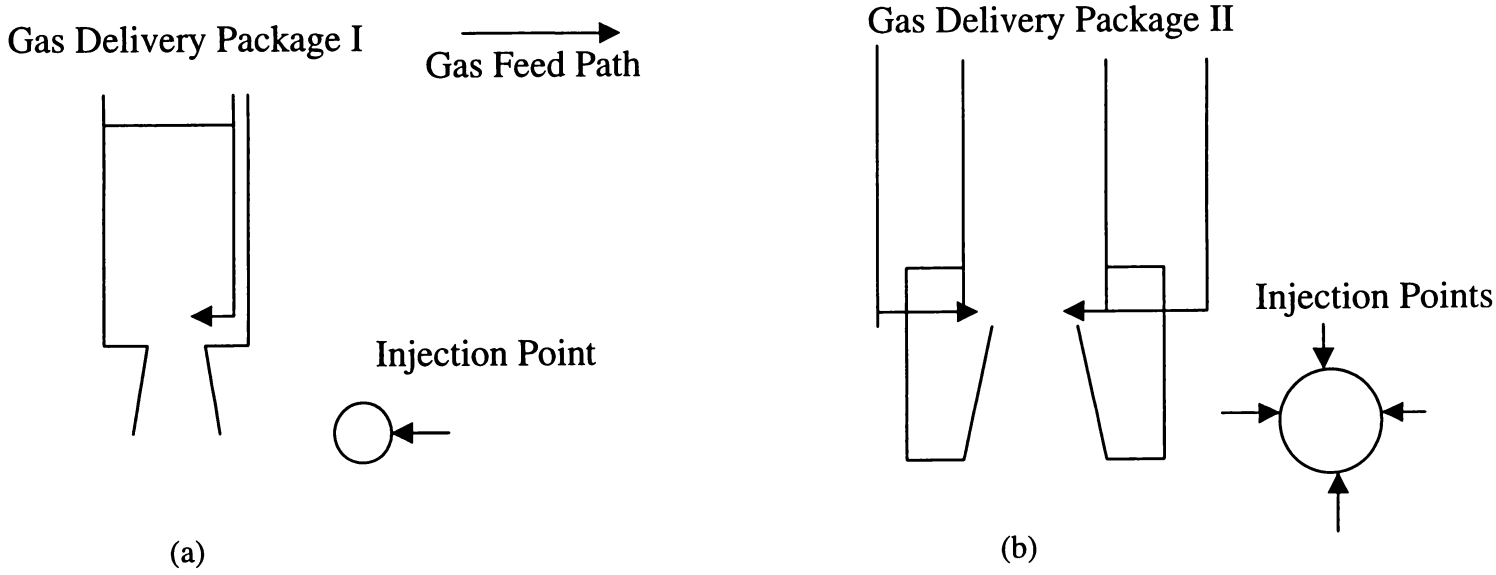

Figure 31. Differences between a) Gas Delivery Package I and b) Gas Delivery Package II.

found that the water tunnel visualization provided the correct general flowfield even though the Re was not matched between the water tunnel and the subscale gas tests. Even with the Re mismatch, the water tunnel simulation was useful in selecting a geometric fix for a vortex formation problem in a test cell. The plan for this current project was to continue the gas trials using the gas delivery package I and determine the pressure profiles and oxygen (O_2) content. At the end of the gas trials, the gas delivery package II would be evaluated for pressure profile and oxygen content and verify that it fell within the database produced by the gas delivery package I.

The nozzle design M=0.15 was determined by calculating the maximum pressure that the molten metal could take without being blown away. When that pressure ratio was set up during the initial gas trials it was discovered that the resulting jet did not even reach the plate (the sensitive pressure transducers did not register a change in pressure). It was decided at this time to increase the test matrix to include a larger range of total pressures (and flowrates) that could reach the plate and still is gentle enough (below 0.5 psi on the pressure transducers). The resulting nozzle exit M were still less than 0.3, so the flow is still incompressible and the water tunnel results are still valid. Here again, the original nozzle Re designed and tested in the water tunnel is not being met, but the resulting flow patterns and trends should be valid.

GAS TRIALS TEST PLAN

The general approach to the gas trials testing was to do a large detailed test matrix with Ar gas first, then after a review of the data, perform a smaller test matrix with He gas and N_2 gas. The larger Ar test matrix was performed with several parameter

levels: geometry (conic and 7° simple), shroud (with and without shroud flow, 7° simple only), flowrate (five levels corresponding to 60, 80, 100, 120, and 140 cubic feet of air per hour or cfhr), impingement angle (0° and 15° from the normal to the surface of the workpiece), and working distance (0mm, 3.15mm, 6.3mm, 9.45mm, and 12.6mm, or L/D of 0, 0.23, 0.47, 0.70, and 0.94). This basic test matrix was performed with the gas delivery package I and its smaller nozzles. The small test matrix (with He gas and N_2 gases) varied the following parameters: geometry (conic and 7° simple), shroud (with and without shroud flow, 7° simple only), flowrate (three levels corresponding to 80, 100, and 120 cubic feet of air per hour), impingement angle (0° and 15° from the normal to the surface of the workpiece), and working distance (6.3mm, 9.45mm, and 12.6mm).

The laser's nozzle had a bigger exit diameter (38.1mm compared to 13.46mm), more gas injection points into the nozzle entrance (four compared to one), more gas injection points into the shroud (two compared to one), one working distance (25mm or L/D of 0.66), and one flowrate. The laser's nozzle's flowrate was 180 cfhr of air with Ar and N_2, and 63 cfhr of air with He. The flowrate selected was based on the desire to keep the selection within the data base and the laser technician's instruction to keep the flowrate as low as possible. The focal length of the gas delivery package II's optics dictated the working distance since the processing occurs near focus. Since the laser's nozzle's exit area is three times that of the gas trial's nozzle, the corresponding flowrates were 180 cfhr of air to 420 cfhr of air. Mindful of the technician's concerns, the flowrate of 180 cfhr of air was selected. Because of the actual set conditions for laser processing were now set, the conditions tested with He and N_2 were now limited to those around the

laser's operating set points. The geometries and the impingement angles stayed the same, but the working distances became 6.3mm, 9.45mm, and 12.6mm and the flowrates 60, 80, 100, and 120 cfhr (except the large density difference of He required the flowrates to be 21, 28, 35, and 42 cfhr). The last part of the gas trials testing was taking the actual nozzle used on the laser for processing and performing gas flow tests on it with Ar, N_2, and He at the set conditions. The conditions used were 180 cfhr of air nozzle flow, 180 cfhr of air shroud flow and 25mm working distance.

EXPERIMENTAL SETUP

The gas trials experimental setup was designed around the gas delivery package I with its internal flow path feeding the nozzle. Figure 32 shows the gas delivery package I with the existing conic nozzle geometry screwed into the bottom of the package which consists of threaded aluminum and brass two inch diameter tubes. The gas path starts at the pressured gas bottles, goes through a regulator and a flowmeter to the top of the gas delivery package where the plastic tubing connects to the copper tube inlet to the gas path. Normally the pressure is regulated down to 40 psi or 2.76 X 10^5 Pa for the nozzle flow. The gas then proceeds through a drilled cylindrical path through the wall of the brass and aluminum tubes to the bottom of the gas delivery package where it is injected perpendicular through one hole across the entrance to the nozzle. The bottom brass piece is threaded with a one-inch hole for mounting protective gas nozzles. The gas delivery package was mounted on optics brackets over the simulated workpiece (an instrumented copper plate).

The gas delivery package I, with the conic nozzle, is mounted over an instrumented copper plate, which contains a copper tube for each static tap. The copper tubing can be connected to either the pressure transducers or the oxygen (O_2) analyzer. The gas delivery package (with mounting), the instrumentation electronics, and the analyzer are placed on a cart that can be moved to the laser when needed. The pressure transducers are hooked up to a DATAQ data acquisition box that is connected through a USB port to the computer. The computer is a Gateway P5-166, with a Pentium II chip running Windows 98 at 166 MHz.

A detailed picture of the instrumented copper plate is shown in Figure 33. The instrumented plate is a 20.32cm X 25.4cm (8"X10") rectangular piece of copper, 2.54cm (1") thick. Each of the four corners of the copper plate has 1.016cm (0.25") diameter by 10.16cm (4") long screws for supporting the heavy copper plate. Originally, the copper plate had eight static taps installed in a row, 0.635cm (1/4") apart. Each static tap consisted of a 0.15875cm (1/16") diameter hole in the surface of the plate (where the gas comes in contact with the plate), then the hole is counter sunk with a 0.3175cm (1/8") diameter hole for attaching the tubing. Copper tubing 0.3175cm (1/8"), outside diameter, is soldered to the 0.3175cm (1/8") hole and bent to the outside of the plate where the transducer tubing can be attached. The 0.635cm (1/4") spacing did not supply adequate resolution, so eight more static tap were added staggered in a row 0.47625 cm (or 0.1875") away. The additional static tap had to be staggered to minimize the damage to the original soldered tubing. The plastic tubing from the pressure transducers and the O2

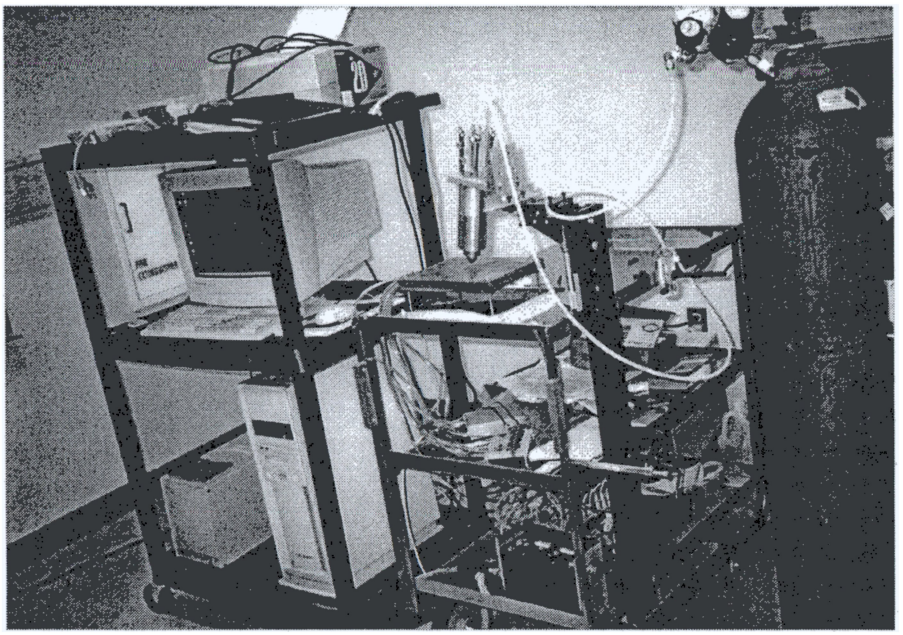

Figure 32: Picture of the gas trials experimental setup.

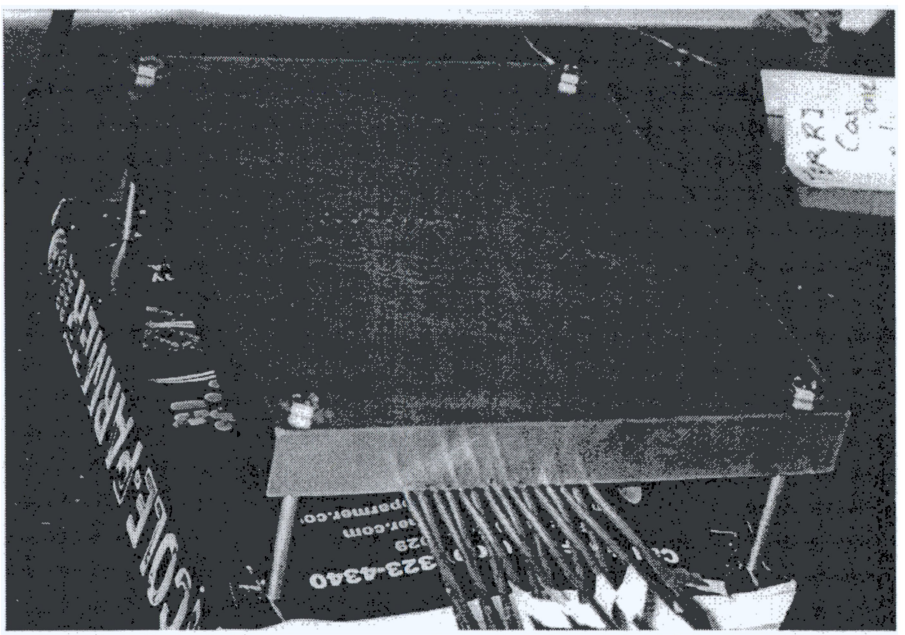

Figure 33: The instrumented copper plate used in the gas trials.

analyzer had clamps attached to the ends for easy disconnect from the copper tubing. The clamps had silicon rubber around it to prevent leakage.

The pressure transducers were the 24PC series from Micro Switch, a four-active-element piezoresistive bridge. When pressure is applied, resistance changes and the 24PC provides an output signal proportional to the input pressure. The transducer signal is passed through an operational amplifier with a gain of 10, and a voltage regulator. Both the transducers and the operational amplifiers are each powered by a 10VDC, 300 mA, regulated power supply. The transducer selected was a 0.5 psi differential with a sensitivity of 70 mV per psi, an overpressure of 10 psi and a calculated total error of 0.015187 psi.

The voltage output from the pressure transducer is acquired by DATAQ's DI-700 acquisition instrument. It permits data acquisition through the USB port on IBM personal computers and compatibles from Windows 98. The DI-700 allows for software-configurable settings for each channel, which allow for real-time conversion from volts to engineering units. The DI-700 can handle either 16 single ended inputs or 8 differential inputs. The maximum sampling rate is 975 samples per second with a 16-bit A/D converter. For this project the DI-700 was set up with a sampling rate of 29.59 samples per second. Each channel was set up with a gain of 100. The DI-700 comes with data recording software, a data viewing software, and a data-exporting feature. This data-exporting feature was used to convert the data into an Excel file where it could be manipulated and analyzed.

The static taps installed into the copper plate allow for pressure measurement or gas sampling, but not both at the same time. When the percent of O_2 was measured, all the pressure transducers were disconnected. The MSA Portable Indicator and Alarm (combustible gas and oxygen), model number 261, has a single probe that had to be individually put on each static tap's copper tube. Each reading took approximately three minutes to stabilize, mainly due to the static tap's tubing length. The accuracy of the oxygen measurement was +0.3% at constant temperature and pressure. The oxygen in the model 261 is sensed directly by a galvanic cell containing two dissimilar electrodes in a basic electrolyte. Oxygen diffusing through the cell face initiates redox reactions which generate a minute current proportional to the oxygen partial pressure. The signal is amplified through a battery-powered circuit. A temperature-compensated circuit converts the current to a proportional voltage which is displayed on the meter of the indicator as oxygen concentration in the range of 0-25% by volume. The oxygen concentration was then recorded by entering it into a notebook or a computerized spreadsheet.

Two types of data acquisition were obtained: quantitative and qualitative. The quantitative data was the pressure data and the percent O_2 data. The qualitative data was the flow visualization data. The quantitative data acquisition was described in detail in the previous paragraphs. The purpose of the qualitative flow visualization data was to record streaklines on videotape and compare them to the streaklines seen in the water tunnel simulation. Producing streaklines in gas flows tend to be more difficult than in water simulations. With some effort, dye can usually be injected into water and stay together long enough to form streaklines. With gas, it is difficult to inject gas in a

manner that the gas stays together long enough to form a streakline, especially in turbulent flow as we have here.

Flow visualization in the gas trials was obtained by using MSA's ventilation smoke tube with a ball aspirator. This technique was originally designed to determine air flow patterns in mines, but its ability to produce a small amount of concentrated white smoke in a controllable manner was ideal for this application. In order to record the white smoke on video tape an area around the gas trials hardware had to be draped in black (black poster board was used). The same camera was used that was used in the water tunnel simulation, see page 57 for a description.

Three nozzles were used in the gas trials testing. The conic nozzle was existing, while the 7° simple nozzle without, and the 7° simple nozzle with shroud had to be fabricated. The existing brass conic nozzle is shown in Figure 34. This was the actually nozzle used in previous LISI^{SM} processing on the Rofin Nd:YAG laser. The 7° simple nozzles were made out of plexiglass. The 7° simple nozzle without the shroud is shown in Figure 35, while the 7°simple nozzle with the shroud in shown in Figure 36.

EXPERIMENTAL PROCEDURE

Two types of data were obtained during the gas trials: quantitative and qualitative. The procedures varied somewhat between the two, but initially they are the same. The first step in the experimental procedure was to install the desired nozzle, and to set the impingement angle (15° from the normal to the surface required an angle bracket). The next step was to set the working distance height by sliding shims of know height between the nozzle bottom edge and the top of the copper plate. Here the procedure between

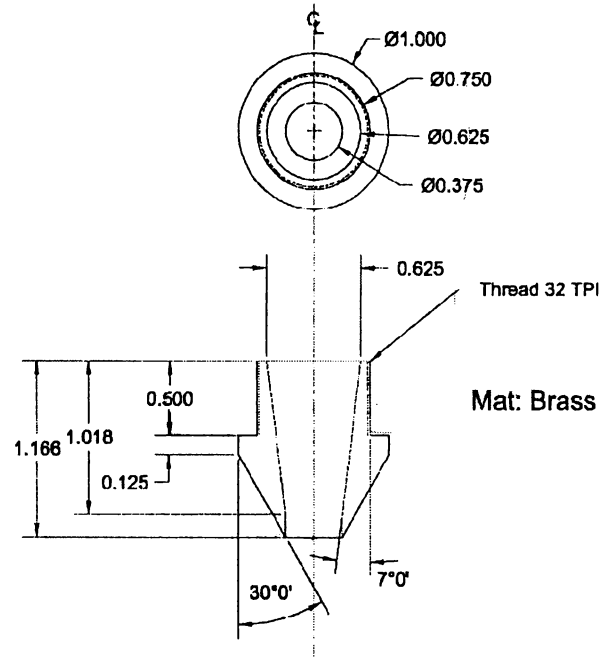

(a)

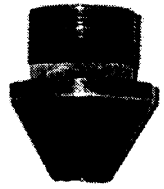

(b)



(c)

Figure 34: Gas trial's conic nozzle a) sketch, b) side view and c) bottom view.

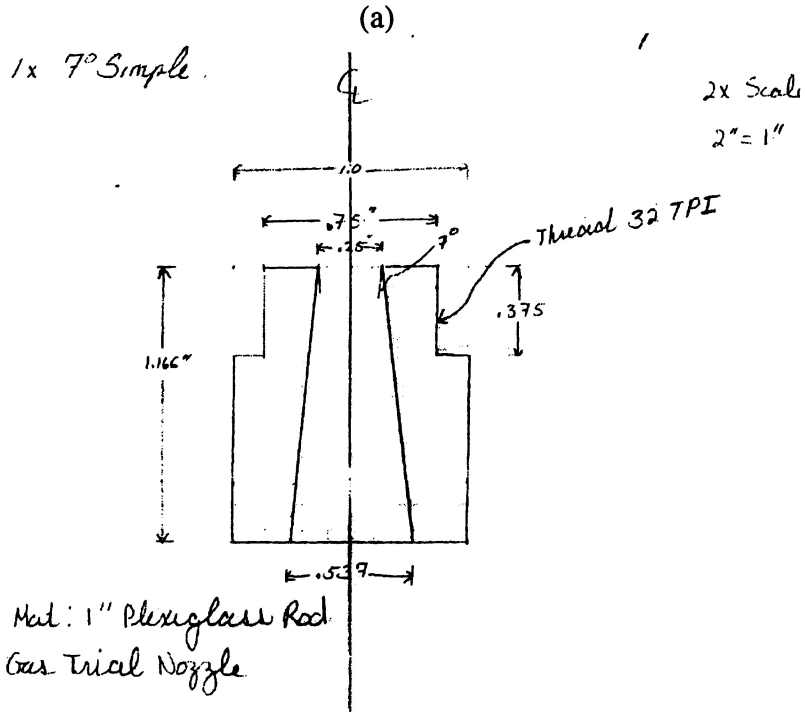

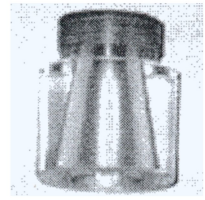

Figure 35: Gas trials' 7 degree simple nozzle a) sketch and b) side view.

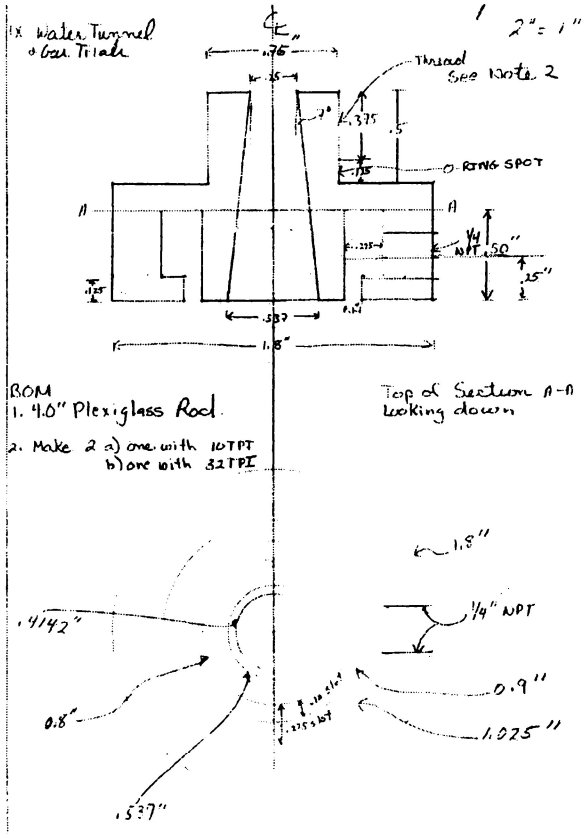

(a)

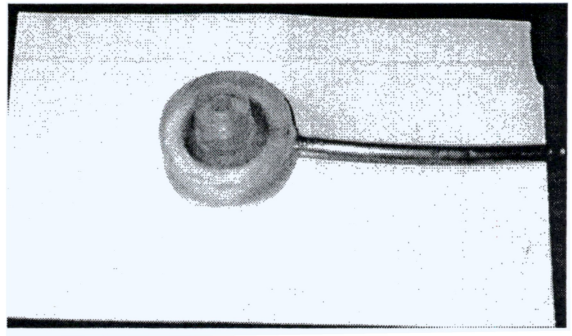

(b)

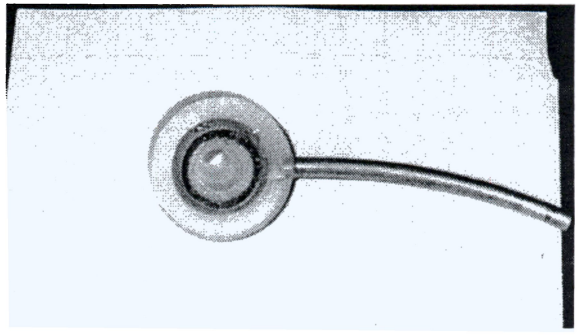

(c)

Figure 36: Gas trial's 7 degree simple nozzle with shroud a) sketch, b) top view and c) bottom view.

quantitative and qualitative data starts to vary. With the quantitative data, the nozzle/gas delivery package had to be aligned up over the desired static tap. This was done by placing a small cylindrical laser pointer into the hole for the fiber optic cable on top of the gas delivery package and moving the plate until the red spot was over the desired static tap. For all quantitative data the gas delivery package was lined up over the same static tap, number four. Figure 37 shows the staggered static tap arrangement and the number configuration used during the testing.

For pressure profile data, the tubing for each of the transducers was installed on to the static taps copper tubing. The DATAQ software for acquisition was launched on the computer and each channel was zeroed. Each static tap was checked for response by blowing through a tube directly over the tap, and the response was monitored on the computer. The DATAQ was then readied for data recording by naming a file and starting the recording process. After a no flow reading is recorded, the gas flow is set to the desired conditions. Normally the tests were run by gathering different levels of nozzle gas flow and pausing at each level and between levels. When shroud flow was used, it was set after the no flow reading and remained on for the entire range of nozzle flows, before being turned off right before the last no flow reading.

For the O_2 measurement, all the tubing from the pressure transducer were removed from the copper tubing. Here the gas flows (nozzle/shroud) were set and then the tube from the MSA O_2 analyzer was, in turn, attached to each desired tap's copper tubing. The response time for the O_2 analyzer was slow; it took approximately three

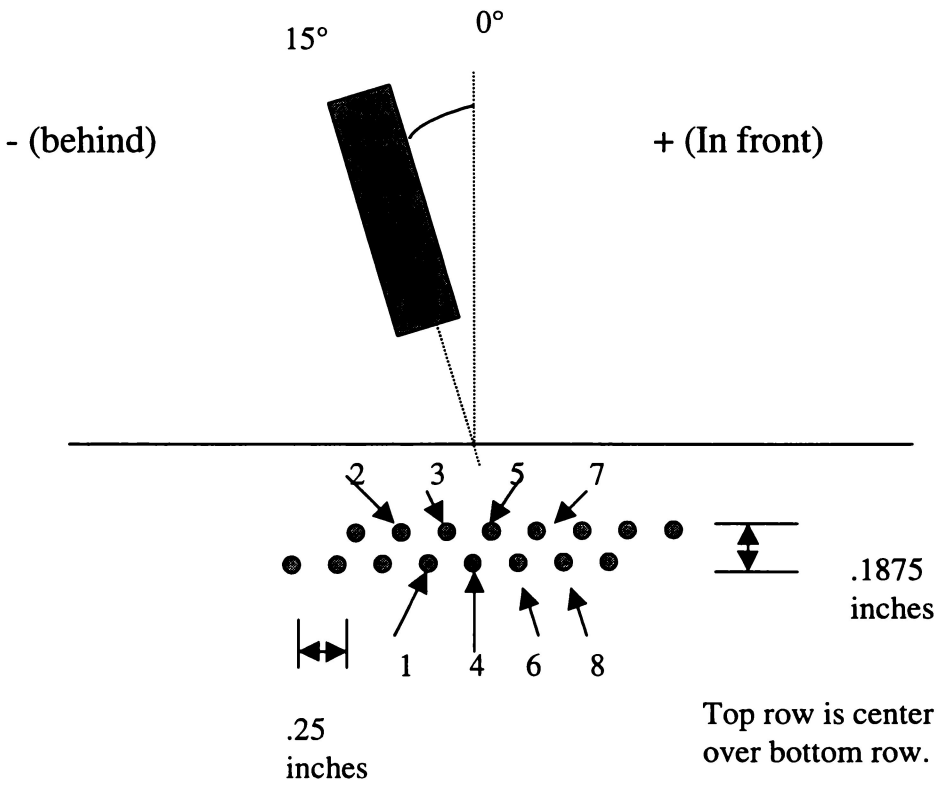

Linear Distance From Tap 4 (center)

Tap	mm	inches
1	-6.35	-.25
2	-10.65	-.4193
3	-5.72	-.225
4	0	0
5	5.72	.225
6	6.35	.25
7	10.65	.4193
8	12.7	.50

Figure 37: The copper plate's static tap arrangement.

minutes on each tap to obtain a steady reading. The readings were then recorded by hand in either a lab notebook or a computerized spreadsheet. Flow visualization required no instrumentation hookup or alignment of the nozzle/gas delivery package. Once the impingement angle and working distance were set, the black poster board was attached to the surround area to form an enclosure (far enough away as not to effect the flow patterns). Once the 16-bit video camera was set up and the lights in the room were lowered, the desired gas flow was set. The hand held smoke tube/aspirator directed a small amount of smoke in each area of interest and the video camera zoomed in to best capture the resulting flow pattern.

GENERAL GAS TRIALS RESULTS

The first question raised in the gas trials was whether or not the water tunnel simulation adequately predicted the flow pattern. Flow visualization was performed to determine this. Flow visualization in a gaseous environment like air is difficult to do. The white smoke used for visualization, while easy to see with the naked eye, was difficult to capture on video. Even when the white smoke was seen on the video, the process to capture a picture lost much resolution.

The flow phenomenon that was discovered through the water tunnel simulation were also present in the gas trials. This included the recirculation at the bottom of the optics package, the front and rear recirculation zones, the jet entrainment, and the nozzle edge entrainment. Figure 38 is an attempt to show the jet entrainment that was present during the gas trial with the conic nozzle. Figure 39 is an attempt to show the front nozzle edge entrainment that was present during the gas trials of the 7° simple

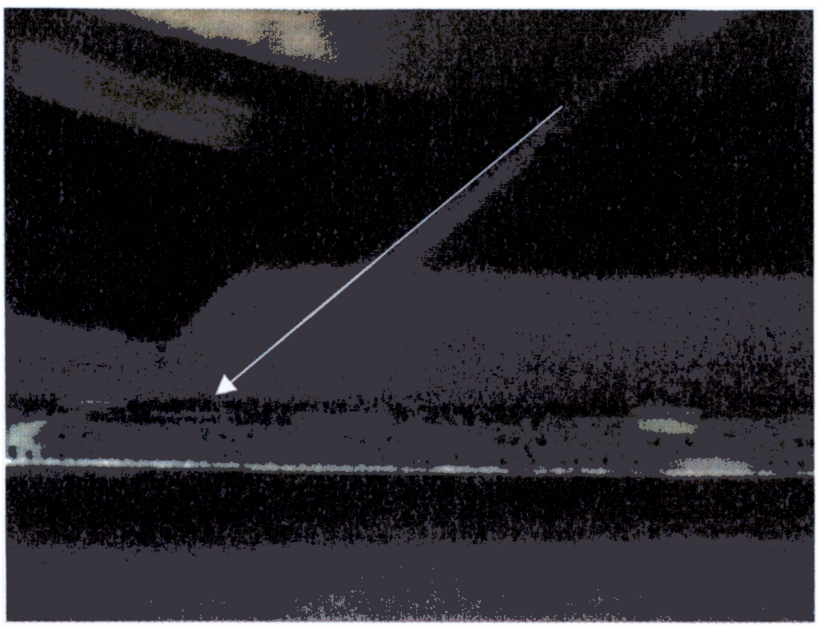

Figure 38: Jet entrainment in the gas trials with the conic nozzle.

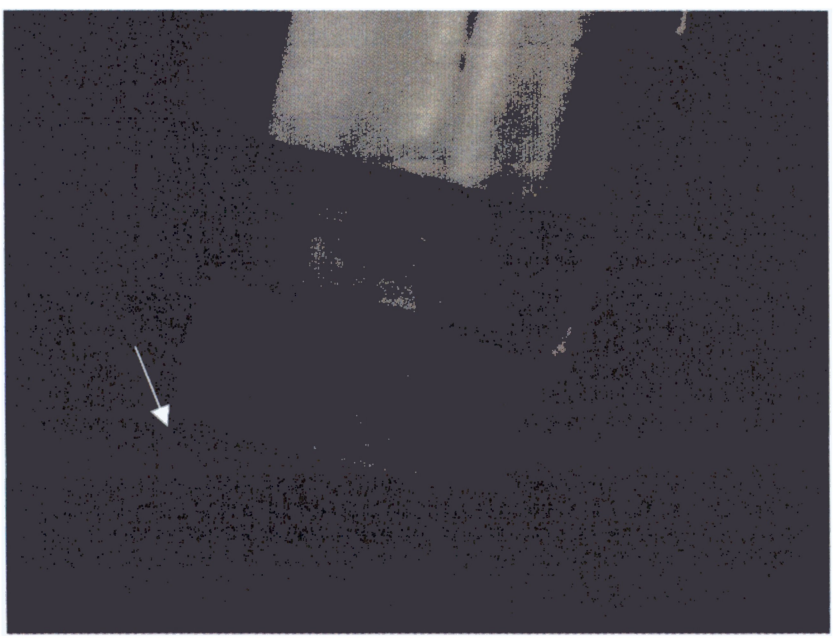

Figure 39: Nozzle edge entrainment during the gas trials with the 7 degree simple nozzle with shroud.

nozzle with shroud. For any future gas trials improvements need to be made in the recording and capturing of the flow visualization data. This author suggests the use of a high speed video camera with software that captures video frames at a high resolution. This research performed the gas trials flow visualization with white smoke and a dark background. Other color combinations could be tried to see if it is captured better on videotape.

Several flowrates of gas were run for each configuration tested. The flowmeter measured flow in cubic feet per hour (cfhr) of air. The flows tested were 60 cfhr, 80 cfhr, 100 cfhr, 120 cfhr, and 140 cfhr (but not all at each configuration) with the Ar and N_2 gases. In order to keep the same volumetric flowrate (Ar and N_2 densities were similar), the He flowrates (measured in cfhr of air) were 21 cfhr, 28 cfhr, 35 cfhr, and 42 cfhr (corresponding to the first four Ar and N_2 flowrates). Pressure data was obtained for the entire flowrate excursion at one time for analysis. Figure 40 shows the raw pressure data from all eight static taps at each of the flowrates, with Ar gas. There is a substantial level of unsteadiness or noise on each pressure channel; this required some mathematical effort to get a single number at each level. For each level (including each of the zero flow conditions) the average and standard deviation was calculated. The unsteadiness (or noise) of each measurement increased with increasing flow, suggesting that the noise is caused by the flow itself. The water tunnel simulation indicated an unsteady swirling motion in the plenum of the gas delivery package, which went through the nozzle and impinged along with the flow on the flat surface. In the water tunnel simulation, this unsteady swirling motion caused the impingement zone to oscillate. The same flow

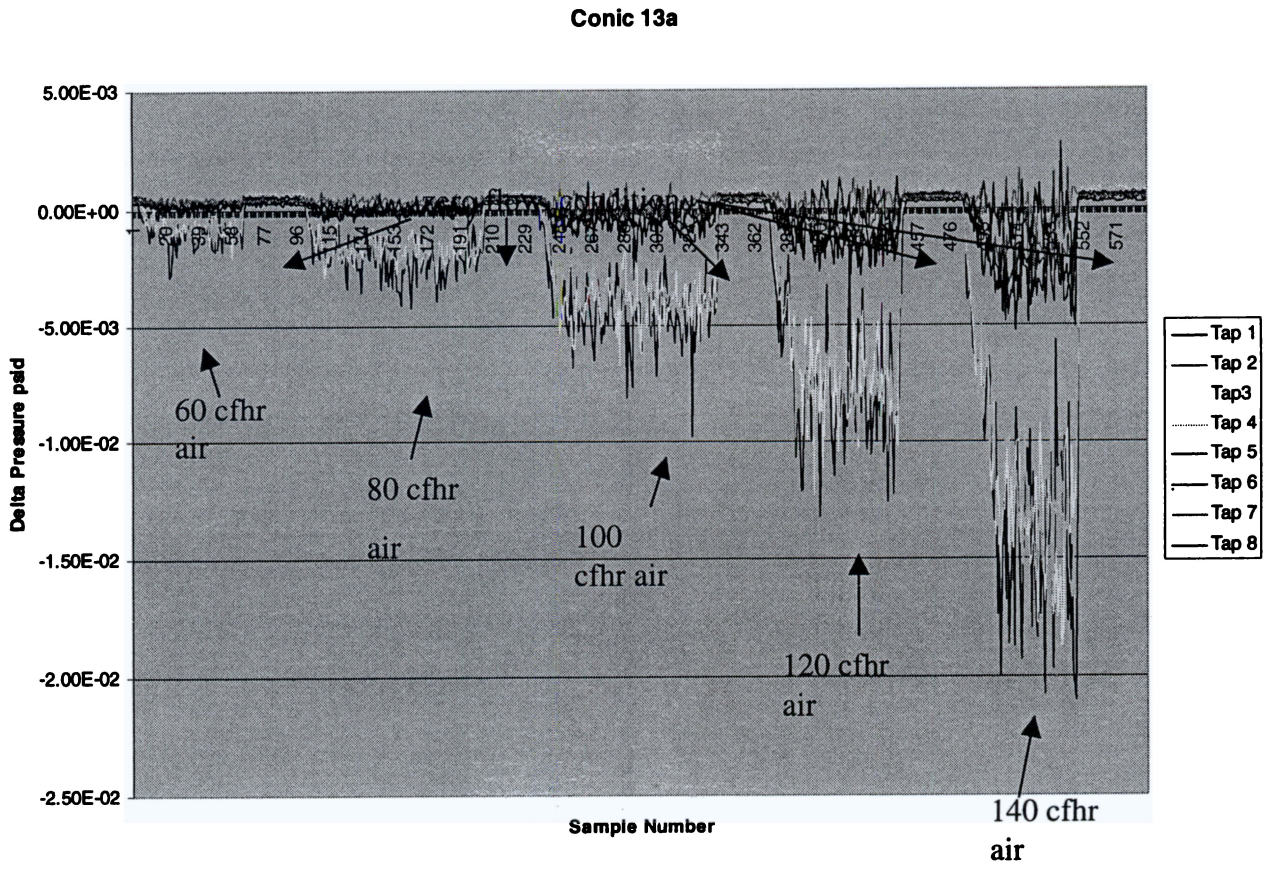

Figure 40: Raw pressure data from the conic nozzle, impingement angle of 15 °, working distance of 6.30mm, with Ar gas.

phenomena are most probably present also in the gas nozzle flow, perhaps causing the unsteadiness observed. Another possible cause of the measurement unsteadiness may be jet turbulence, which would increase with increasing flowrate (due to Re increase).

The first purpose of measuring the pressure of the impinging jet was to determine if the pressure would adversely effect the melt pool by blowing it out of the way. The calculation to determine the maximum impingement pressure was presented in Chapter 3, and the results were 0.1325 psi for aluminum and 0.2714 psi for steel. During the entire gas trials, the maximum impingement pressures occurred with Ar (7 ° simple nozzle, with shroud flow, at a working distance of zero) and was 0.0966 psi. This is below both the aluminum and the steel pressure limits.

The second purpose of measuring the pressure of the impinging jet was to help characterize the flow field. Some difficulties arose with measuring the low pressures for flow field characterization, especially with the He gas. While the Ar and N_2 gases usually resulted in nice readable pressure profiles (like in Figure 40), He produced almost unreadable profiles, at any flowrate. Figure 41 shows an example of the He pressure profile. The figure shows an excursion from zero flow to 21 cfhr of air, back to zero flow, to 28 cfhr of air, back to zero, to 35 cfhr of air, back to zero flow, to 42 cfhr of air, and then back to zero flow. The profile, at the first two flowrates, is not distinguishable from the noise at zero flow. The scale shown in Figure 41, is blown up considerably, when put on the same scale of the Ar and N_2 pressure profile, what little response seen at the two higher flowrates, disappears. Basically there was not enough pressure response

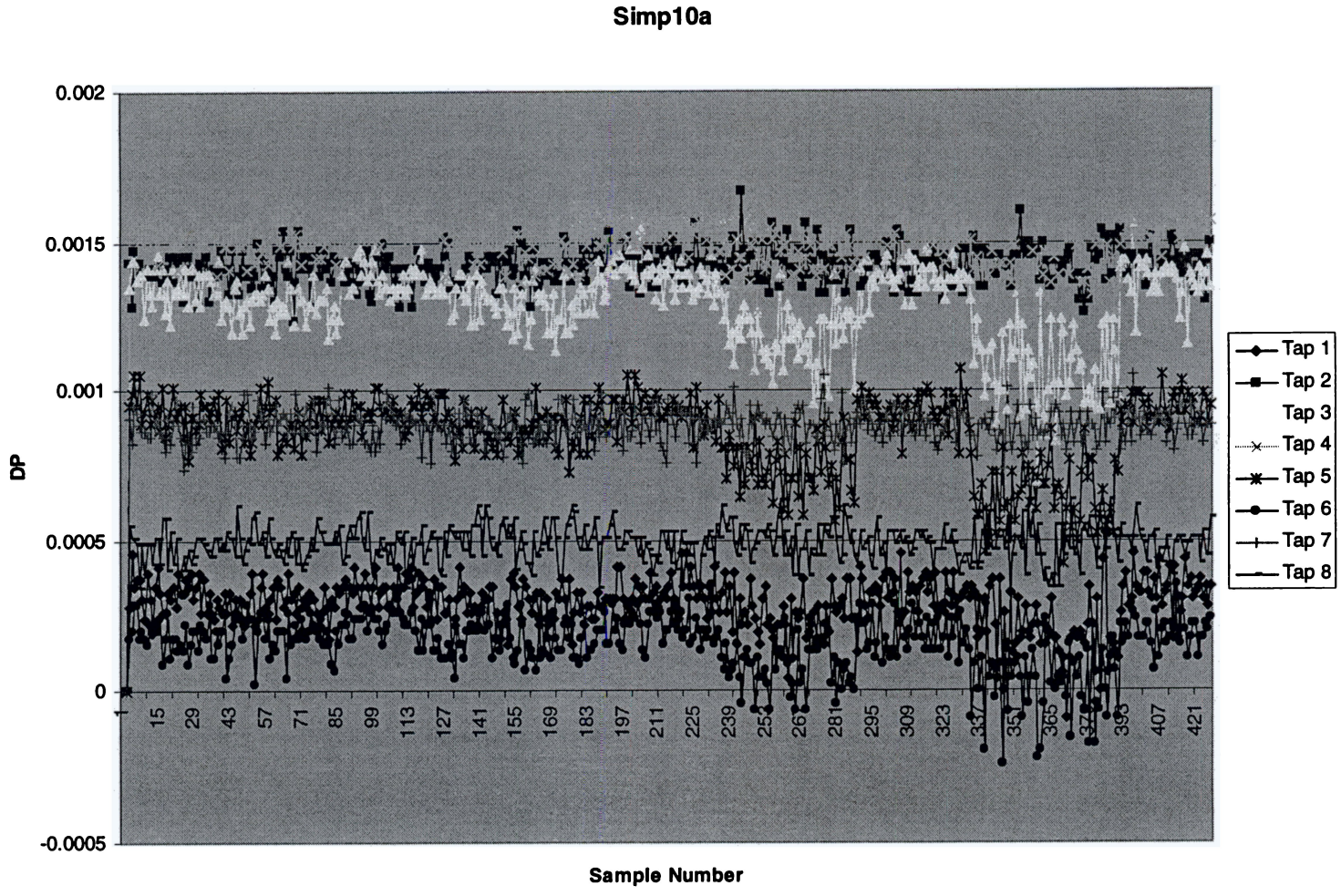

Figure 41: Typical He pressure profile, taken with the 7° simple nozzle without shroud.

with the He gas to perform any meaningful analysis. The remaining pressure analysis will be performed with the results from the Ar and N_2 gas trials.

With both the Ar and N2 gases, the impingement pressure increases with increasing flowrate, as expected. The results for Ar (at two different working distances) are shown in Figures 42 and 43. The lack of flow symmetry, which should be present at 0°, is noticed in both Figures 42 and 43. Some of the large asymmetry at the zero working distance can be contributed to the fact that the nozzle is sitting on the flat plate and the gas flow is having trouble finding its way out. The asymmetry can be explained by possible misalignment of the gas delivery package perfectly over tap 4 and slight unevenness of the flat plate (or the spacer used to raise the plate to the gas delivery package). It is possible that the asymmetry is due to a problem with the instrumentation, but since the asymmetry was not consistently caused by the same taps, it is unlikely. The impingement pressures also decrease with increasing working distance as shown in Figure 44. It is expected that the effect of the impingement would decrease with increasing working distance.

One of the most important questions to be answered is whether or not the jet impingement protects the area around the molten metal, or is the impingement region bigger than the work zone? The pressure profiles give an indication of impingement region size (to be verified by the percent O_2 measurements). In Figure 44, a bulge in the pressure profile is seen from about –6mm to approximately 5.5 mm, then the pressure profile starts to flatten out, even increasing at the extreme of the negative distance. This

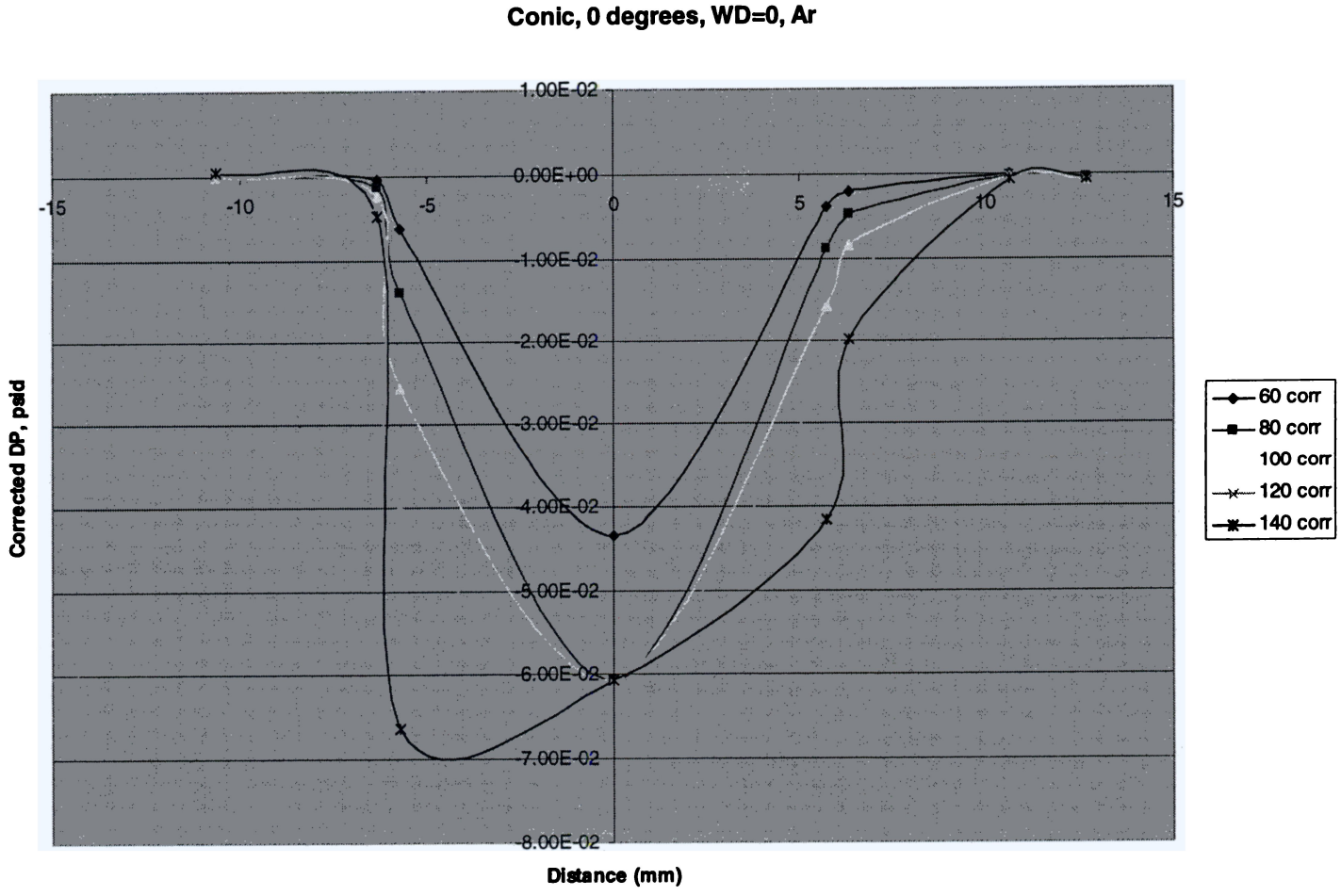

Figure 42: Increasing flowrate results in increasing impingement pressure.

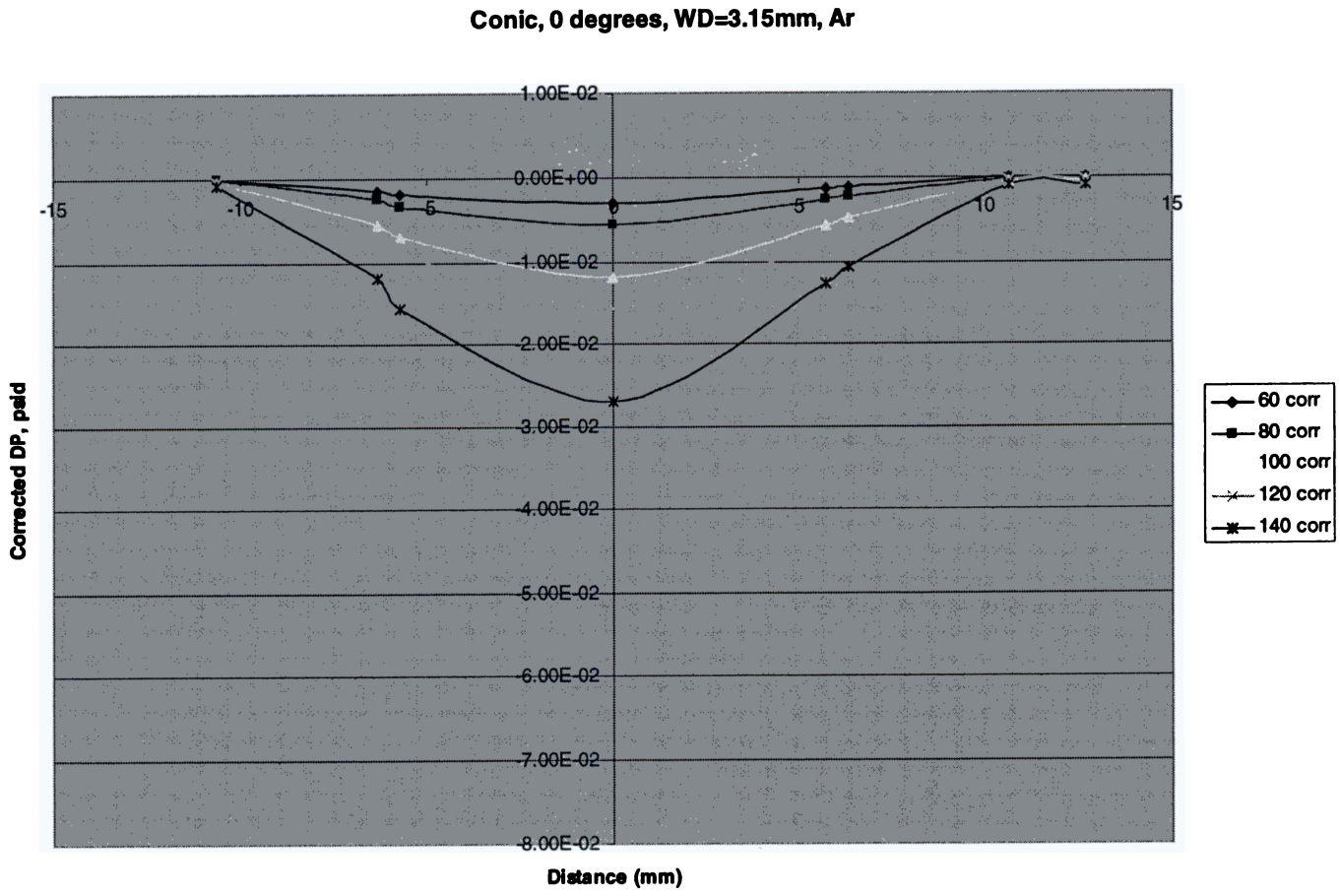

Figure 43: Increasing the working distance results in decreasing pressure.

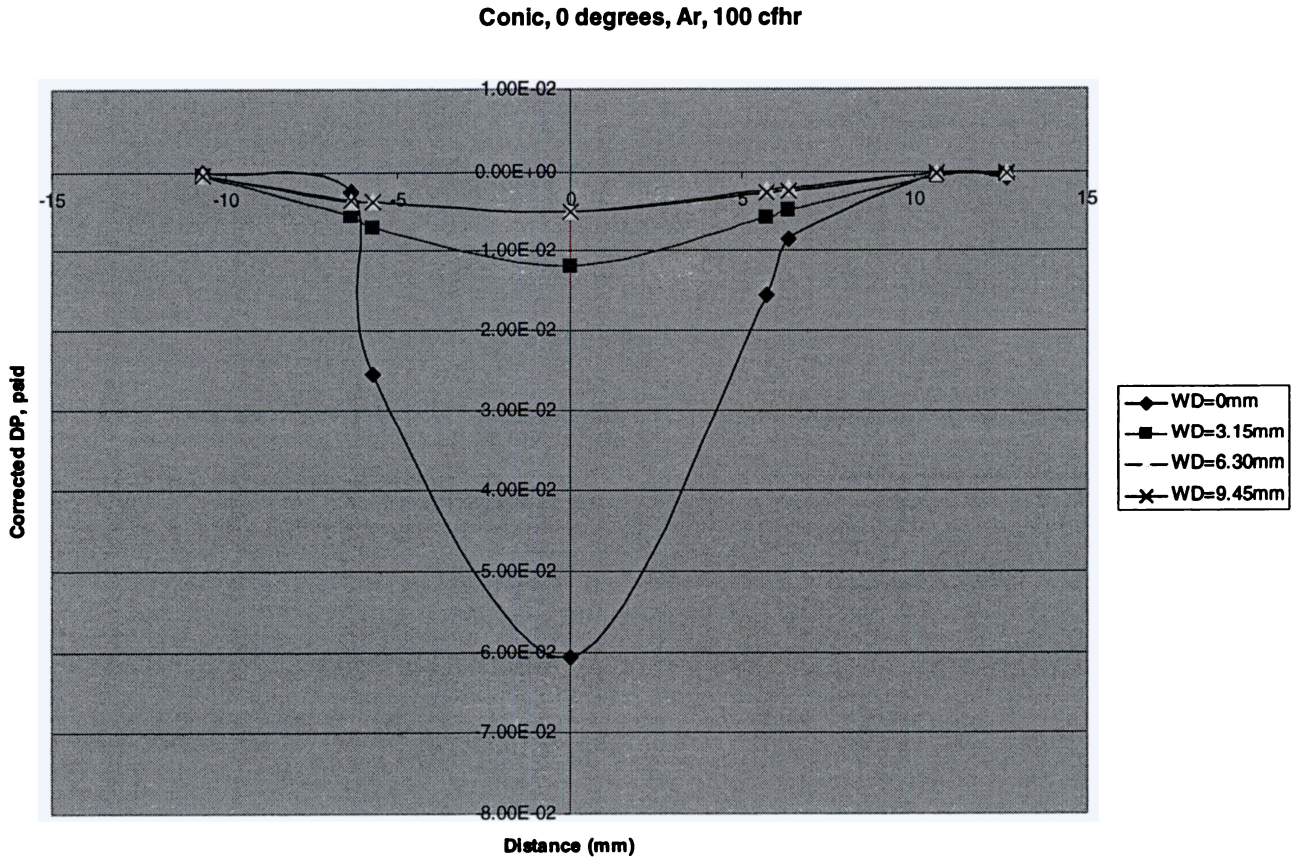

Figure 44: Pressure profile indicating impingement region.

bulge is an indication of the impingement region. At this size, roughly 11.5 mm diameter, it should be large enough to protect the work zone of 6.23mm by 4.61 mm.

The ideal jet impingement indicates that there will be an impingement region and a boundary layer flow region. From the gas sampling data, it seems that any major reduction of the percent of O2 occurs in the impingement region (with a slight improvement in the boundary layer region by the shroud flow). Again, this suggests that to minimize the exposure of the molten metal to entrained O2, then the molten metal must be moved into the impingement region. The boundary layer flow, while reducing the percent O2 somewhat, does not provide the best available protection.

The percent O_2 measurement is the most important measure taken during the gas trials. It gives the actual distribution of the composition of the jet impinging on the flat plate. Thinking simplistically, it would seem that the heavier gas, Ar, would provide better protection because it would lie on the flat plate better, than the light gas, He, which would float up. The data's results were completely opposite. Overall the He gas provided the largest percent O_2 reduction (average approximately 5% O_2), Ar the next best (average approximately 10% O_2), and N_2 the worst (approximately 15%). A review of free turbulent mixing was done to try to explain this seemly strange result.

When jets leave a nozzle exit, they are considered turbulent if their Re (based on exit diameter) is greater than around 10^3 to 10^4 (pipe flow is approximately Re=2300) [51]. Even if the Re indicates that the jet leaving the nozzle is laminar, the jet will quickly transition to turbulent. P.T. Harsha [57] reviewed experimental and theoretical turbulent jet mixing. Harsha evaluated the effects of light and heavy gases on

the mixing that starts to occur right after the jet leaves the nozzle. He found was that the lighter gas (in this case hydrogen) mixes quicker with air than the heavier gas (Ar) and reduces the length of the potential core. Here again, the flow going into the nozzle is assumed to be uniform. If the flat plate was placed far enough downstream from the nozzle exit to be out of the potential core, this quicker mixing would explain why there should be higher percent O_2 with He when compared to Ar. In our case the flat plate is only two to three nozzle exit diameters downstream of the nozzle exit; therefore, the flat plate should be entirely in the potential core, and turbulent mixing of jets does not explain the strange data. Also, when evaluating the potential core flow of any jet, the velocity (normally uniform) is high enough where buoyancy effects should not have a significant effect. Again to give a possible explanation to the reason why the He is providing better protection, the swirling motion in the plenum/nozzle must be looked to.

With the gas feed directly above the nozzle entrance and perpendicular to the flow direction, the gas may not have a chance to develop enough to completely fill the nozzle volume. The swirling motion is probably pulling outside air into the nozzle, as indicated by at least one of the water tunnel simulation nozzles. As mentioned earlier, He gas mixes faster with air than Ar, so it is possible that by the time the jet hits the flat plate the He is better distributed throughout the jet and provides better protection than Ar which mixes slower.

SPECIFIC GAS TRIALS RESULTS

Many combinations of working distance, nozzle geometry, gas composition, and impingement angle were tested with gas delivery package I. The following is a short summary of the observations seen during the gas trials.

Conic nozzle with all three gases: Figures 45, 46, and 47 shows the percent O_2 measurement for the conic nozzle as a function of working distance, for each of the three gases. Intuitively, one would expect that there would be more overall oxygen in the impingement region with the oblique impingement angle than with the normal impingement angle. It is expected that the oblique angle would pull more O_2 into the impingement region. With N_2 gas (Figure 46), this is the case. At the oblique impingement angle the average percent of O_2 is approximately 16 percent. At the normal impingement angle the average percent of O_2 is roughly 10-11 percent. With Ar and He gases, the results do not follow the same trends. With Ar (Figure 45) the lowest percent O_2 achieved is approximately 7 percent, but that is with the 15 degree oblique impingement angle, not the normal impingement angle, which produces a low measurement of approximately 14 percent. The oblique angle cuts the percent O_2 in half with Ar gas. He gas is similar to Ar in that with normal impingement the lowest percent O_2 was 5 percent while with the oblique impingement the lowest percent O_2 measured was about 3 percent. The gas that is most like air, entrains more air with an oblique impingement angle than with a normal impingement. The heavy gas and the light gas, entrain more air with the normal impingement than with the oblique impingement.

(a)

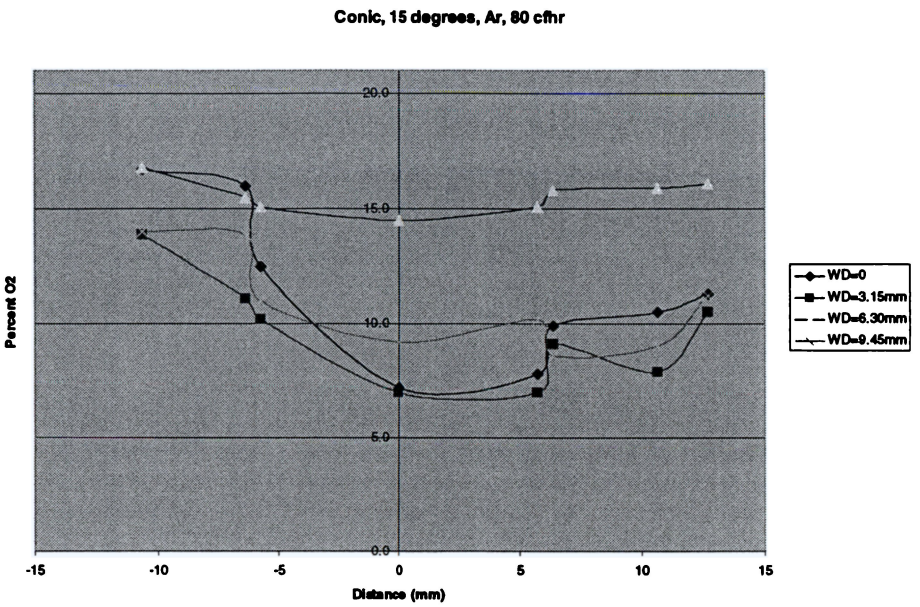

(b)

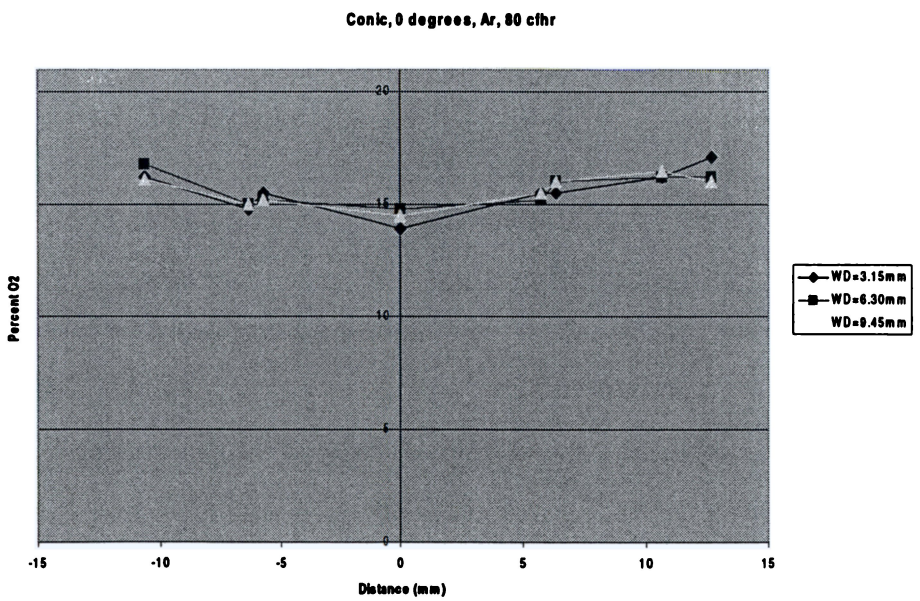

Figure 45: Conic nozzle, Ar, showing the percent O_2 at a) 15° impingement and at b) 0° impingement.

(a)

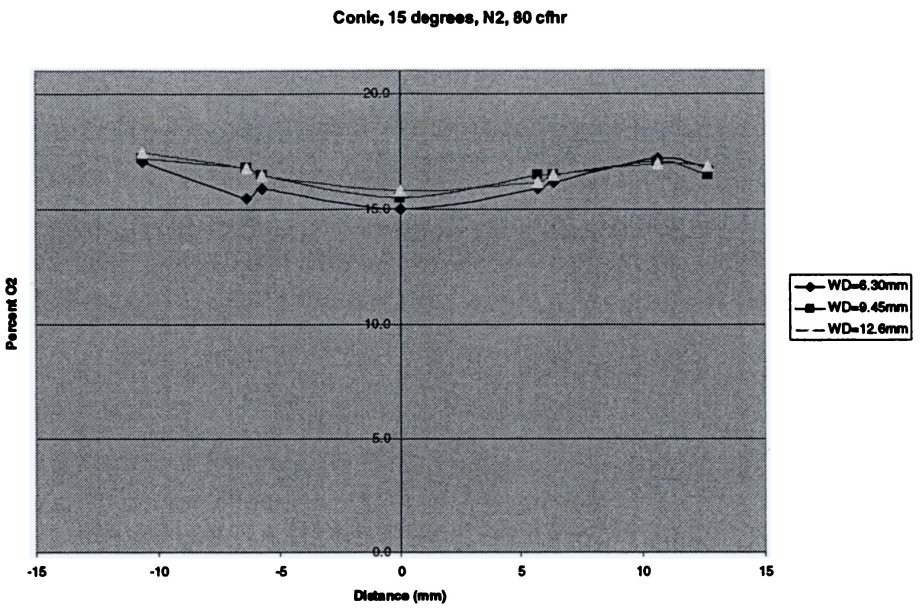

(b)

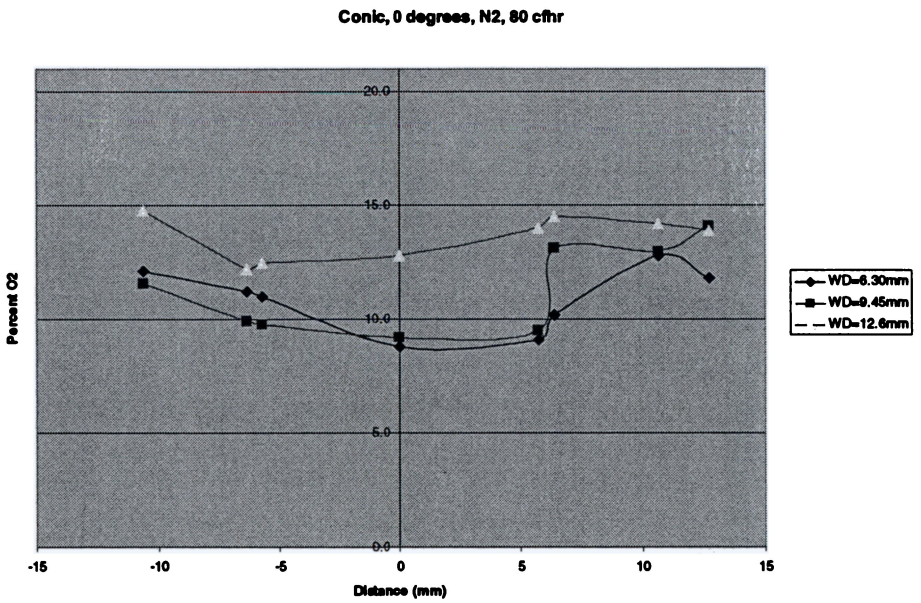

Figure 46: Conic nozzle, N_2, showing the percent O_2 at a)15° impingement and at b) 0 ° impingement.

(a)

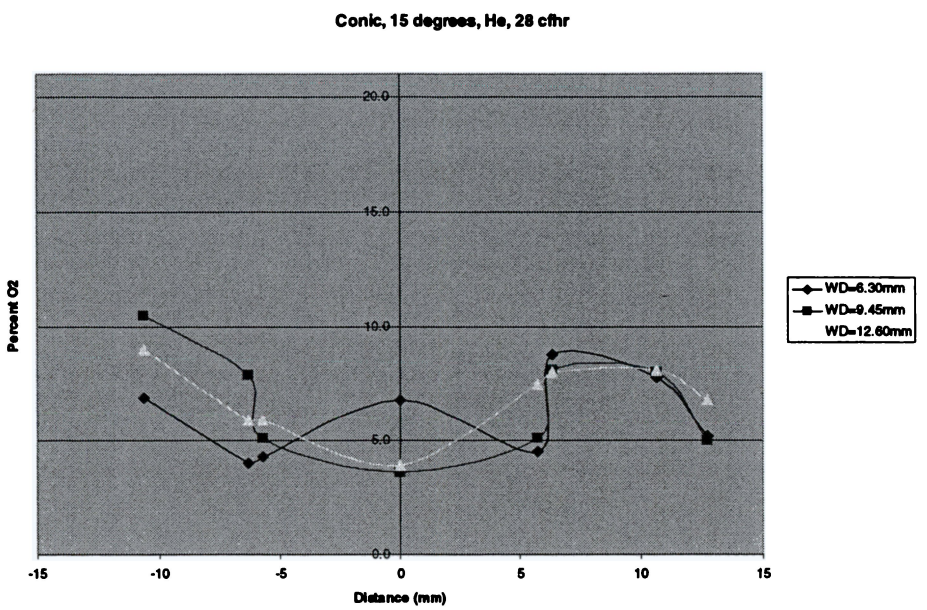

(b)

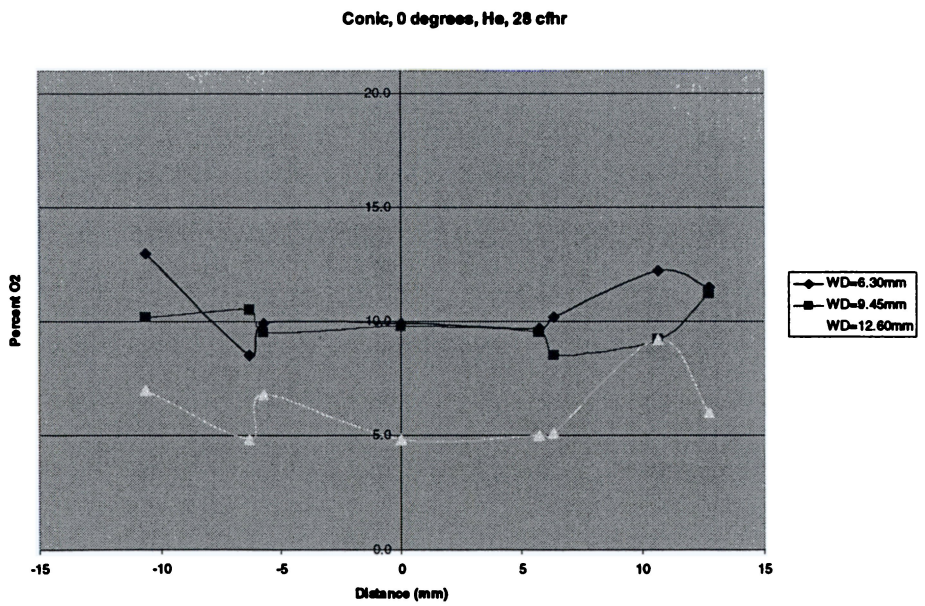

Figure 47: Conic nozzle, He, showing the percent O_2 at a)15° impingement and at b) 0 ° impingement.

Another aspect of the surface O_2 measurement is its distribution at the two different impingement angles. It is expected that the distribution would be evenly distributed with the normal impingement and skewed with the oblique impingement. This is the case with Ar gas (compare Figure 45a with Figure 45b). With N_2 gas the O_2 measurement is more evenly distributed around the impingement point at the oblique angle than at the normal angle. With He gas, the distribution of O_2 is evenly distribution for both impingement angle near the impingement point and starts to deviate more than 5 mm from the impingement point. One reason for this uneven distribution at the normal impingement may be a misalignment of the gas delivery package or slight differences in the machined static taps on the plate. The skewed distribution with the Ar gas at the oblique impingement angle results in a "bulge" of lower percent O_2. This protects bulge leads to the suggestion of changing the direction in which the laser is on during the processing. The current processing direction would put the molten metal (at least with Ar gas) opposite the impingement point (the 0 location on the figures) from the protective bulge. Changing the current processing direction would move the molten metal more under the protective bulge.

Another obvious point to mention from the previous three figures is that with the conic nozzle the He gas produces the lowest percent O_2 no matter what the working distance. With Ar and N_2, increasing the working distance usually results in a higher percent O_2, but with He the largest working distance resulted in the lowest percent O_2. This strange trend with the light gas was seen obtain during the gas trials testing.

The pressure distribution on the impingement plate was also measured for each configuration. The pressure distribution measured helps to determine whether or not the molten metal would be adversely effected by the impinging jet, and the distribution also gives another estimate of the impingement region's size (because the plate has only a limited number of static taps, the measurement is a rough estimate). Figure 48 shows the pressure distribution from the conic nozzle with Ar gas at the two impingement angles. This pressure distribution was pretty typical for the Ar and the N_2 gases. The large pressure drop on both figures shows the pressure at zero working distance. Once distance is put between the nozzle exit and the surface of the plate the pressure drops significantly. The pressures seen at all working distances is small for Ar and N_2. The pressure distribution is skewed at the oblique impingement angle and flat at the normal impingement angle. As noted before, it was not possible to obtain any pressure data with the He gas. This was because the pressures with He were so slight that the measurement itself was lost in the noise of the signal.

7° Simple nozzle with all three gases: Figures 49, 50 and 51 present the percent O_2 data with the 7° simple nozzle flowing all three gases. The effect of working distance on the percent O_2 is very slight with the Ar gas (Figure 49). The differences between the oblique impingement angle and the normal impingement angle on percent O_2 is slight with Ar gas, no matter what the working distance was. With N_2 gas (Figure 50), the effect of working distance is again slight at the oblique impingement angle, but is significant at the normal impingement angle. At the impingement point with the oblique angle, the percent O_2 varies only 1-2 percent between all three working distances. While

(a)

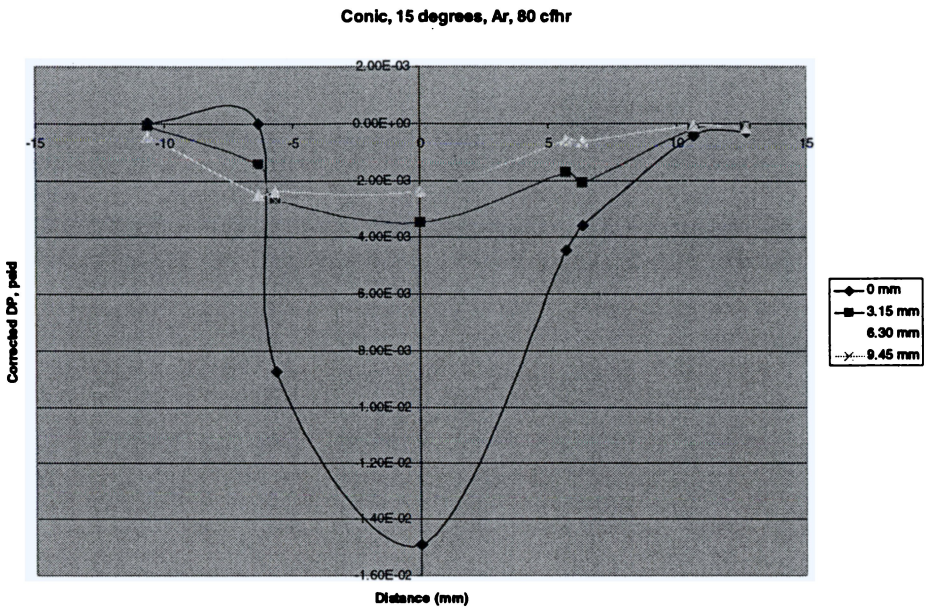

(b)

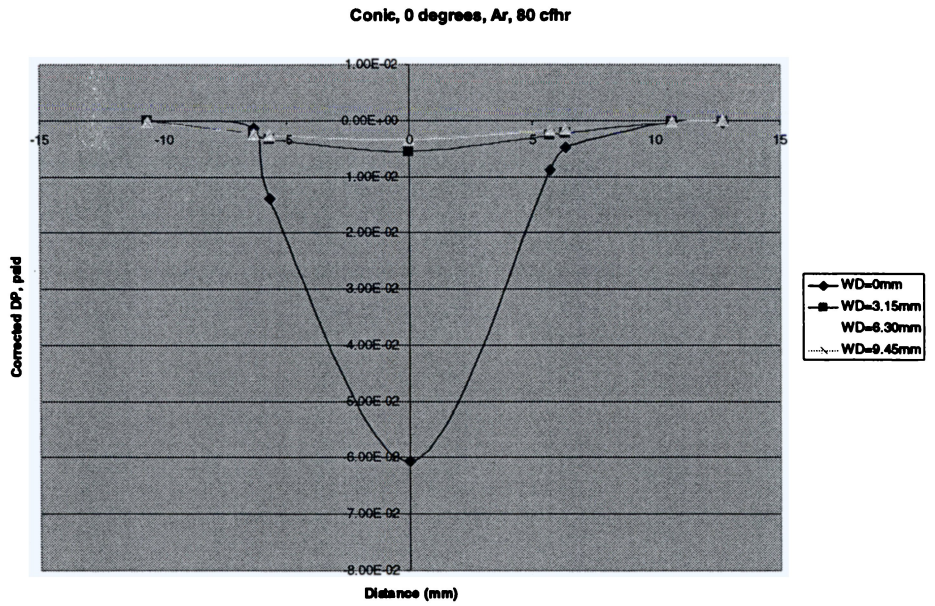

Figure 48: Conic nozzle, Ar, showing the pressure distribution at a) 15° impingement and at b) 0° impingement.

(a)

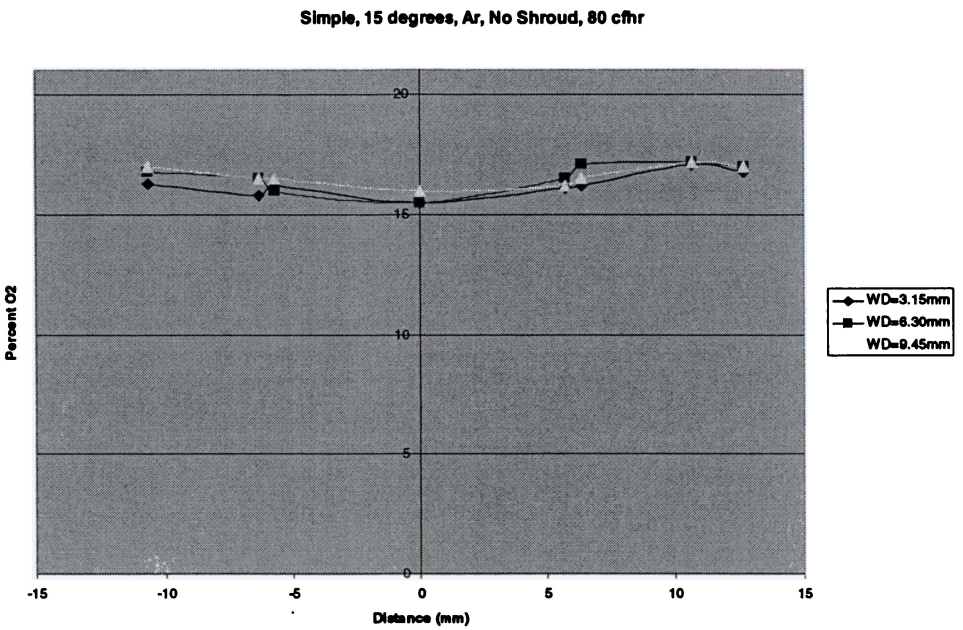

(b)

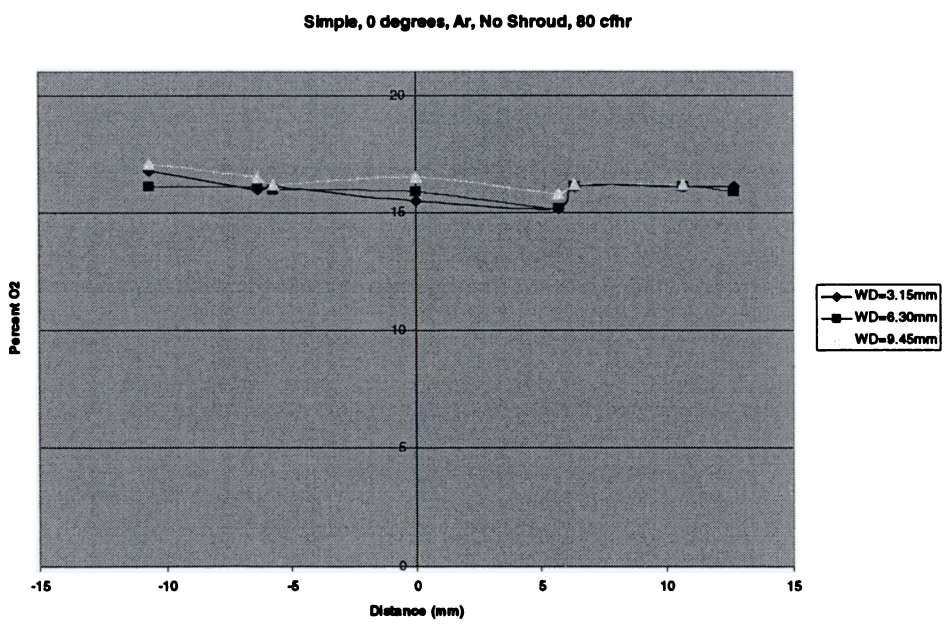

Figure 49: 7° Simple nozzle, Ar, showing the percent O_2 at a) 15 ° impingement and at b) 0 ° impingement.

(a)

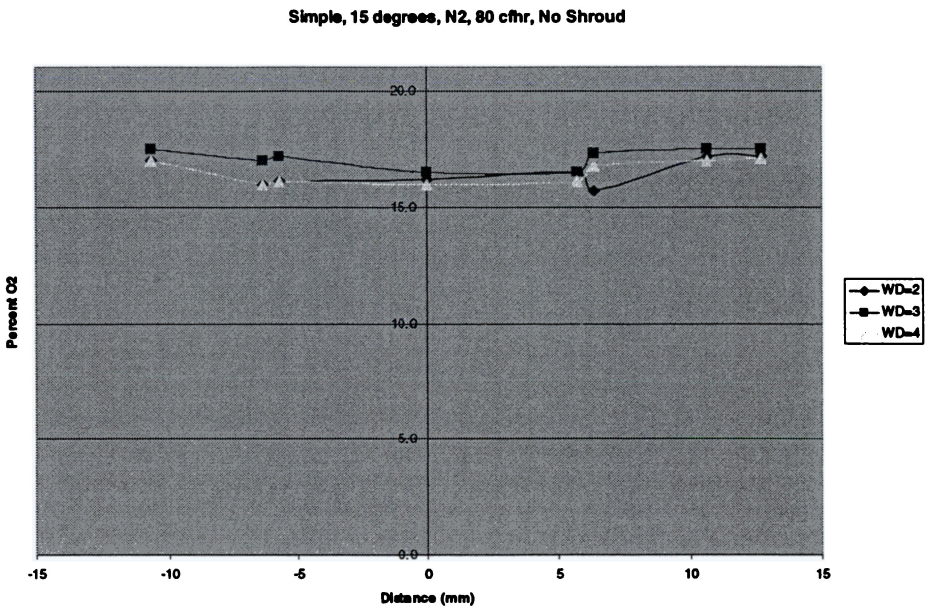

(b)

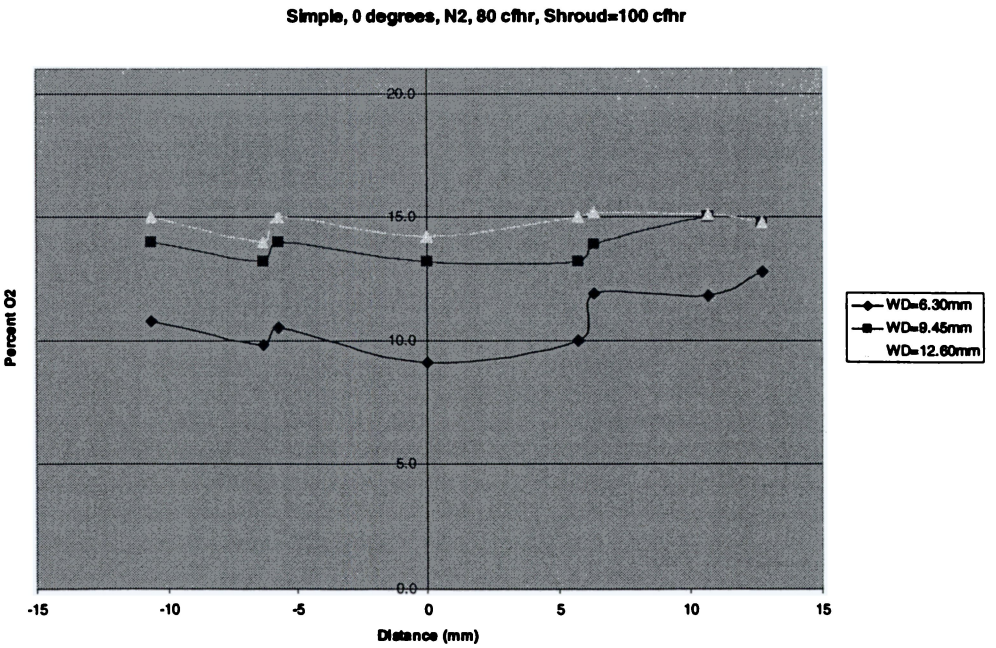

Figure 50: 7° Simple nozzle, N_2, showing the percent O_2 at a) 15 ° impingement and at b) 0 ° impingement.

(a)

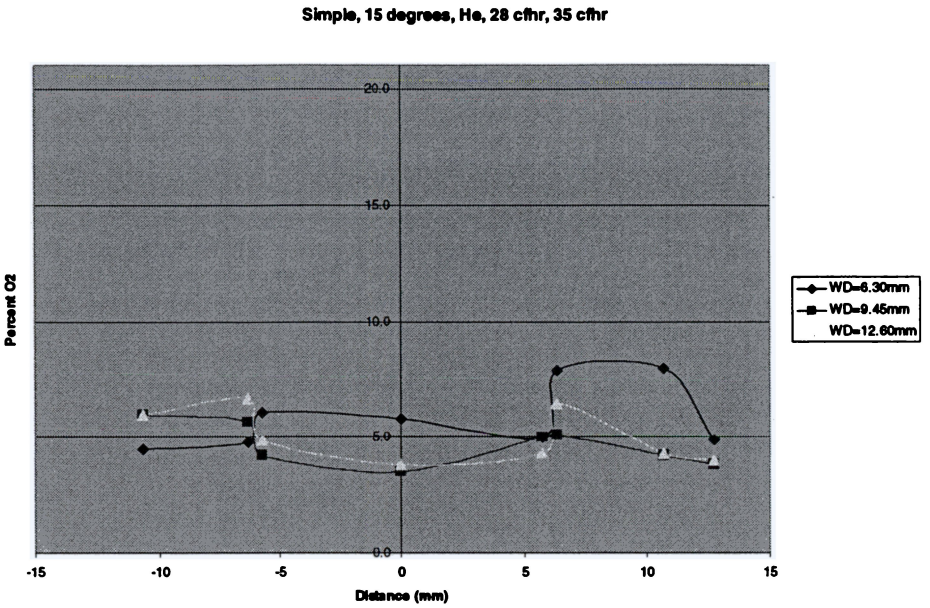

(b)

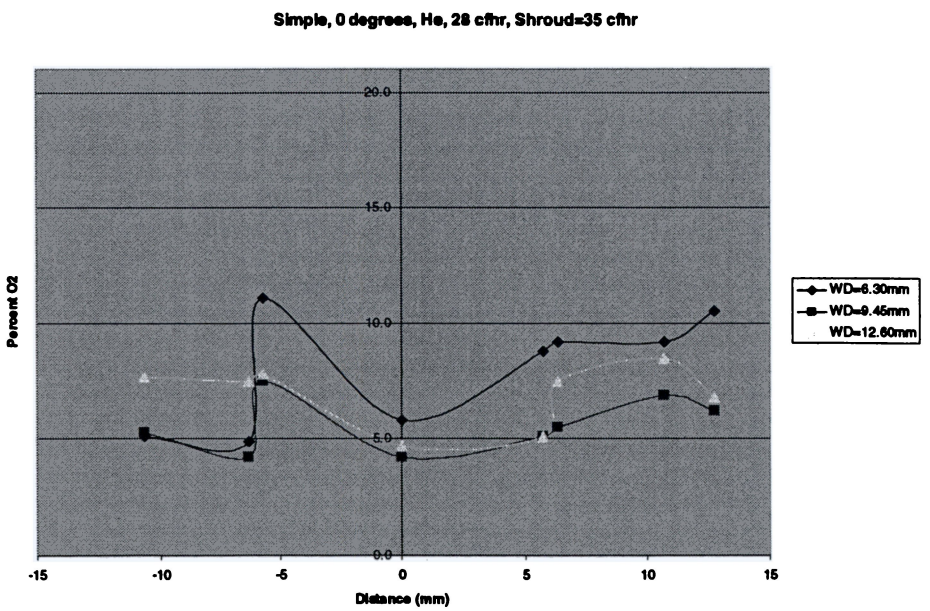

Figure 51: 7° Simple nozzle, He, showing the percent O_2 at a) 15 ° impingement and at b) 0 ° impingement.

at the impingement point with the normal angle, the percent O_2 varies from a low of about 9 percent to a high of about 14 percent. At should also be noted that with N_2 at the normal impingement angle, the percent O_2 increases with increasing working distance.

Like the conic nozzle, the 7° simple nozzle obtains the lowest percent O_2 with the He gas (Figure 51). Also like the conic nozzle, the percent O_2 again decreasing with increasing working distance for the He gas, and the lowest percent O_2 measurement occurs with the He gas.

Shroud flow Vs no shroud flow, all three gases: Figures 52, 53, 54, 55, 56, and 57 presents the shroud percent O_2 data for all three gases, at both the normal and oblique impingement angles. In general, the shroud flow decreases the percent O_2 at the end of the gas sampling region, where the flow is in the boundary layer regime. In addition to that general rule is 1) that with N_2 and He (Figures 54 and 56), at normal impingement, and working distance of 6.30mm the impingement region (the area around the impingement point) decreases with shroud flow. A slight decrease is also seen with He at the oblique angle (Figure 57).

It should be noted that all the shroud work was performed with the shroud flow set to 100 cfhr of air (or equivalent for He). Early experimentation showed that given a set nozzle flow, increasing the shroud flowrate decreased the percent O_2. It was decided to limit the test matrix to one shroud flowrate and 100 cfhr of air was selected because it was the largest shroud flowrate tested.

(a)

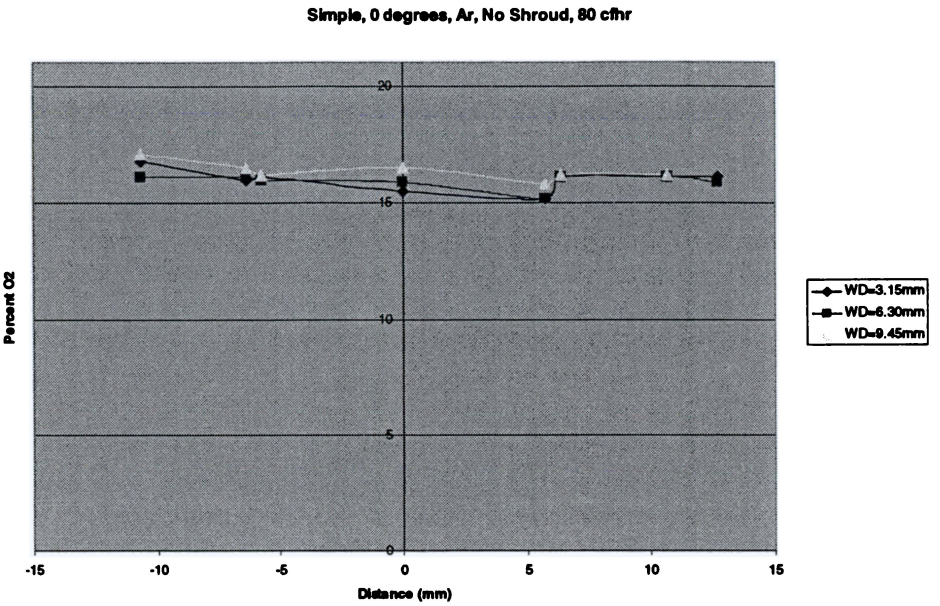

(b)

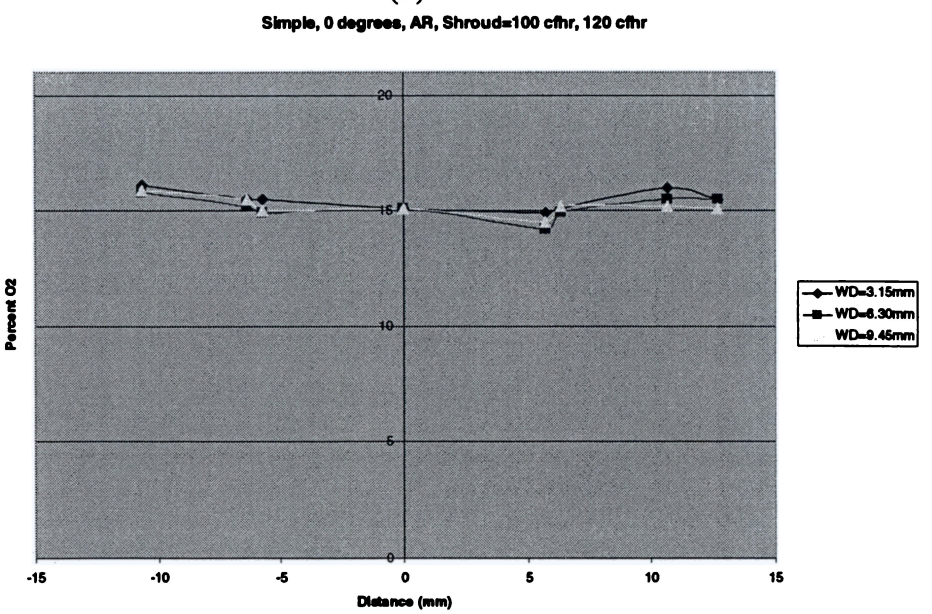

Figure 52: 7° simple nozzle, with Ar gas, comparison of a) without the shroud, and b) with the shroud flow at normal impingement angle.

(a)

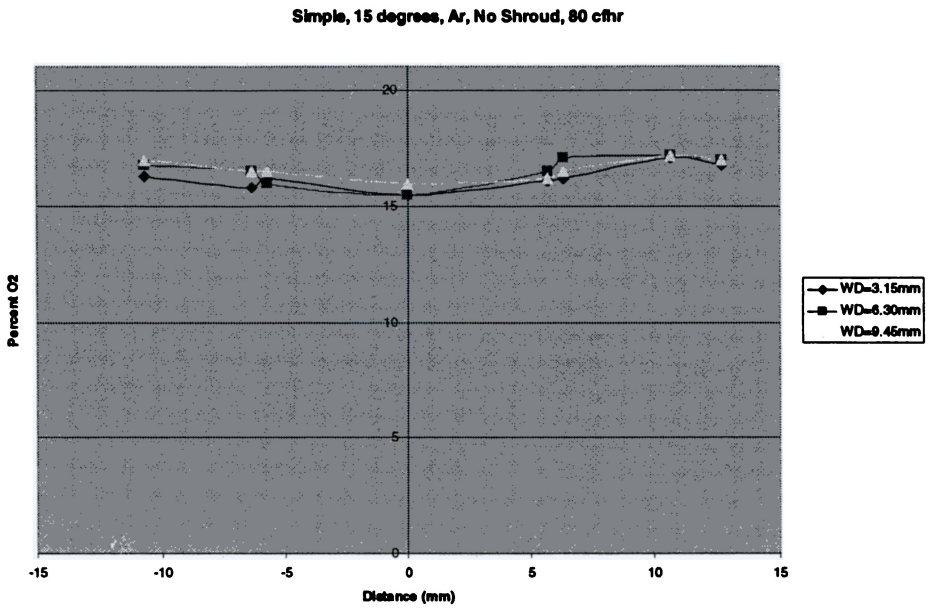

(b)

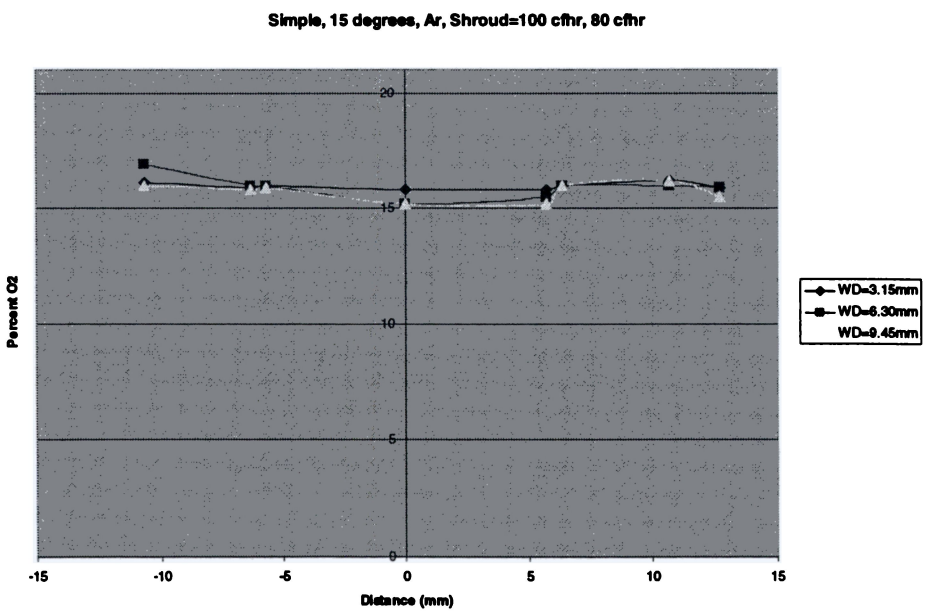

Figure 53: 7° simple nozzle, with Ar gas, comparison of a) without the shroud, and b) with the shroud flow at the oblique impingement angle.

(a)

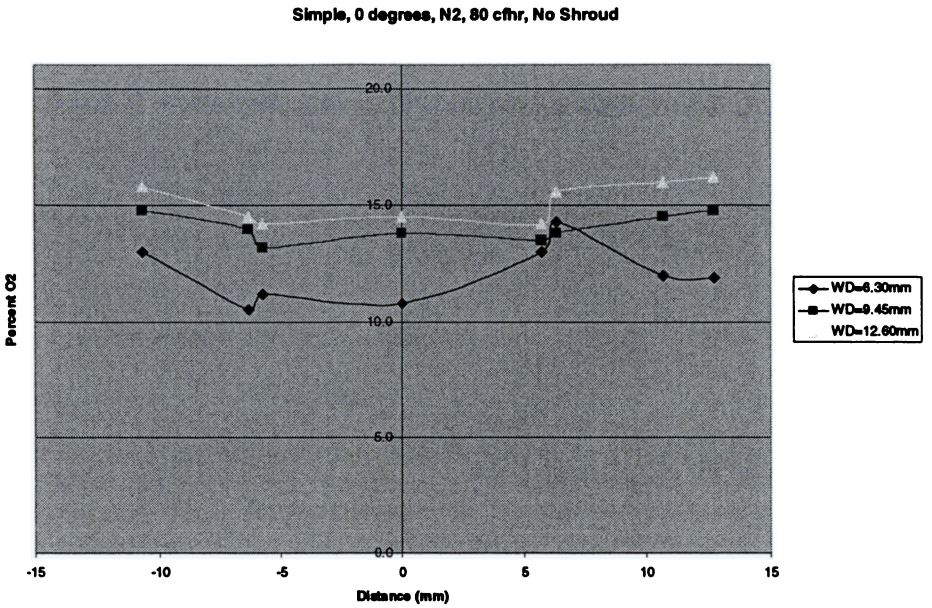

(b)

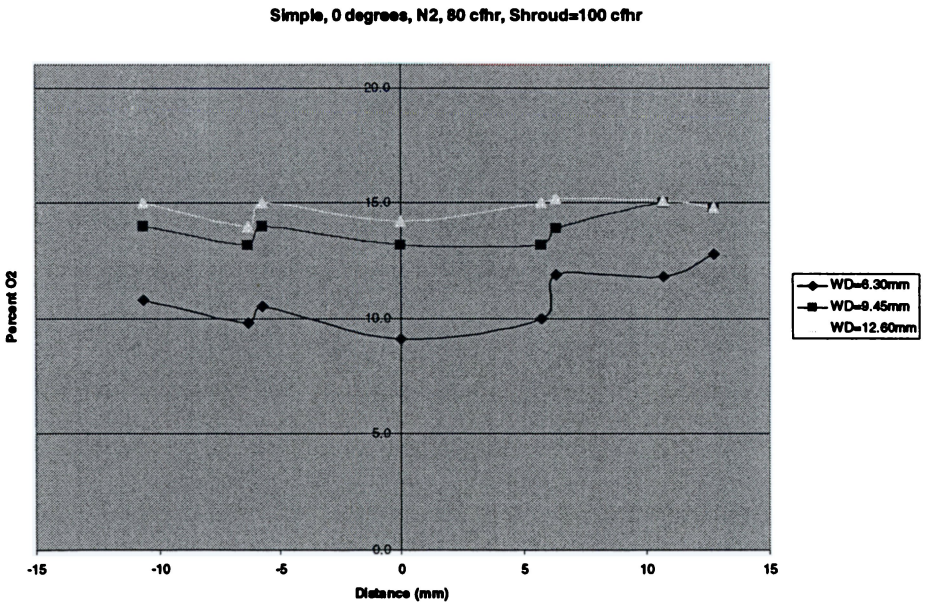

Figure 54: 7° simple nozzle, with N_2 gas, comparison of a) without the shroud, and b) with the shroud flow at normal impingement angle.

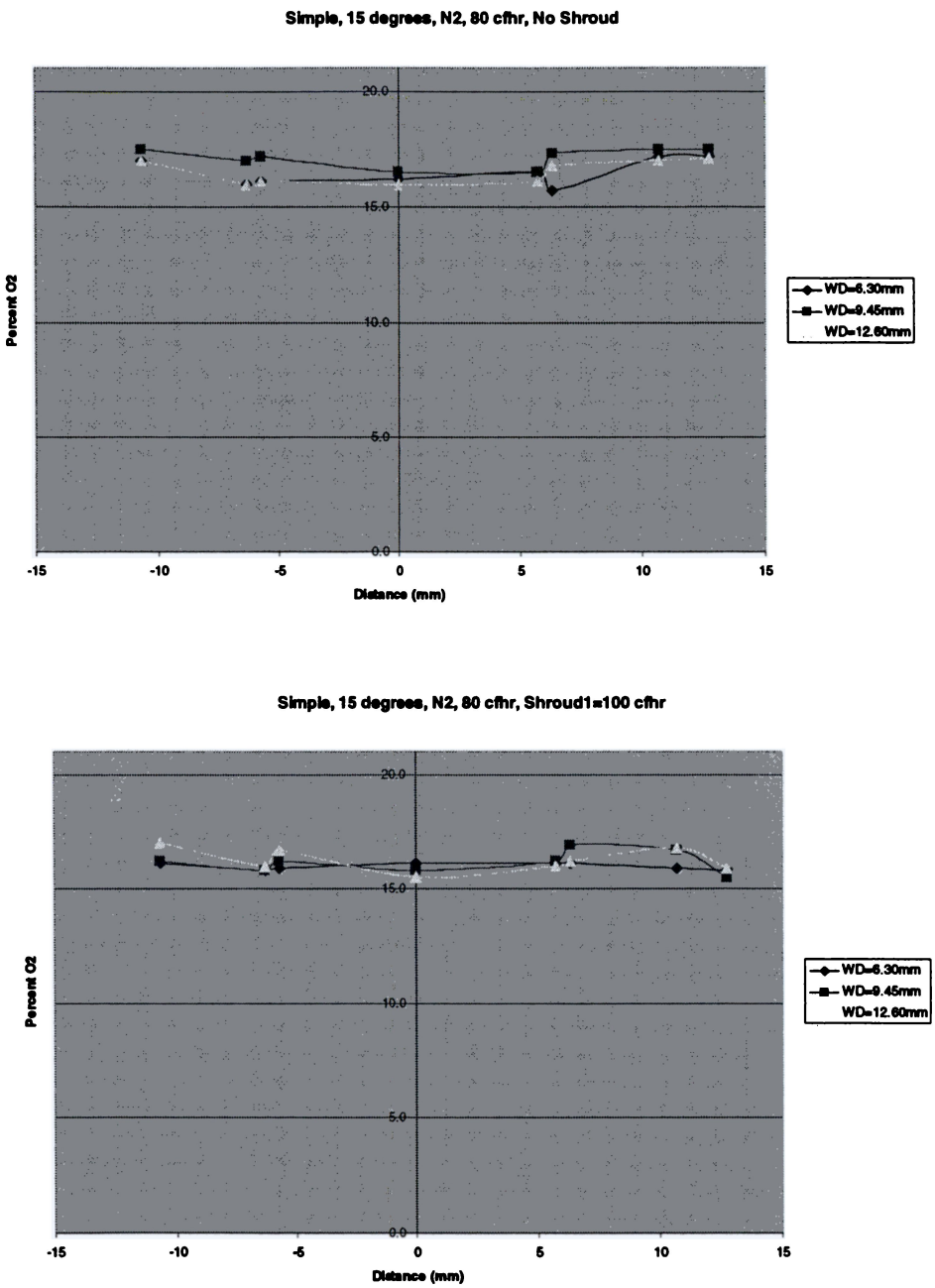

Figure 55: 7° simple nozzle, with N_2 gas, comparison of a) without the shroud, and b) with the shroud flow at the oblique impingement angle.

(a)

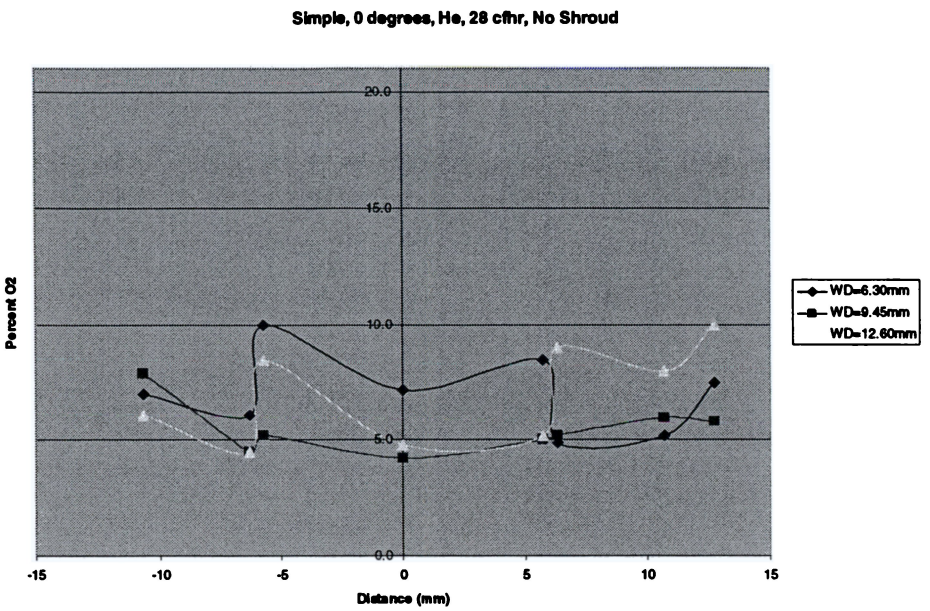

(b)

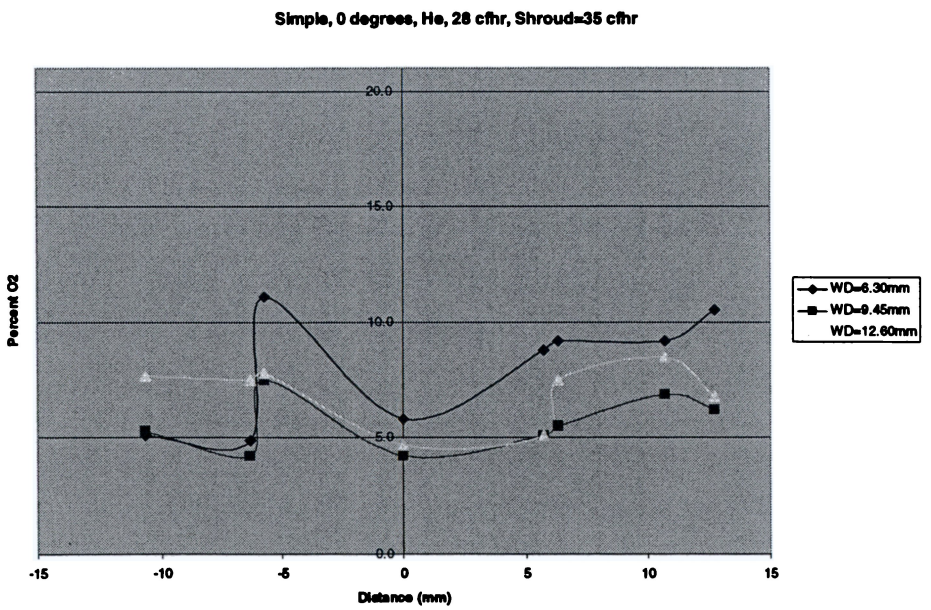

Figure 56. 7° simple nozzle, with He gas, comparison of a) without the shroud, and b) with the shroud flow at normal impingement angle.

(a)

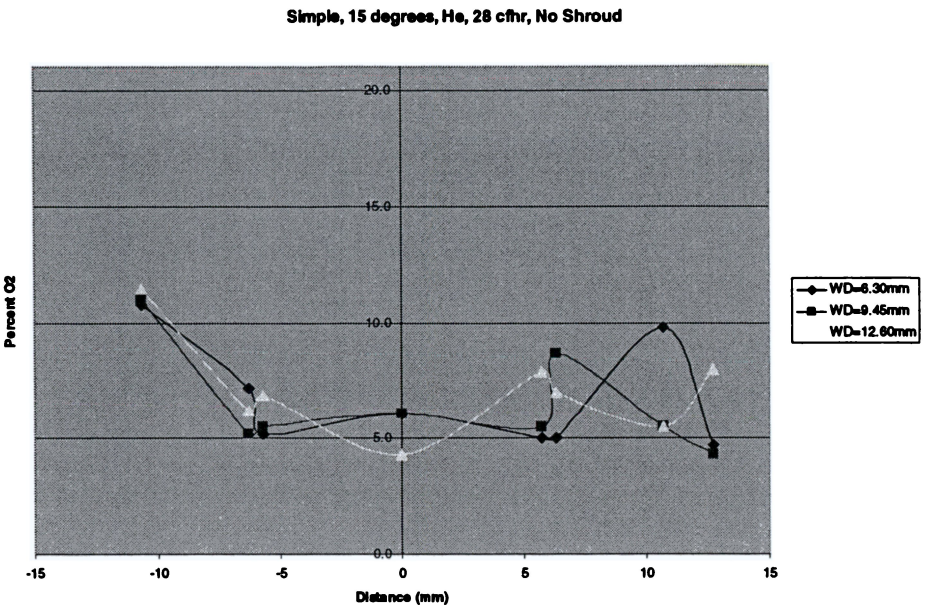

(b)

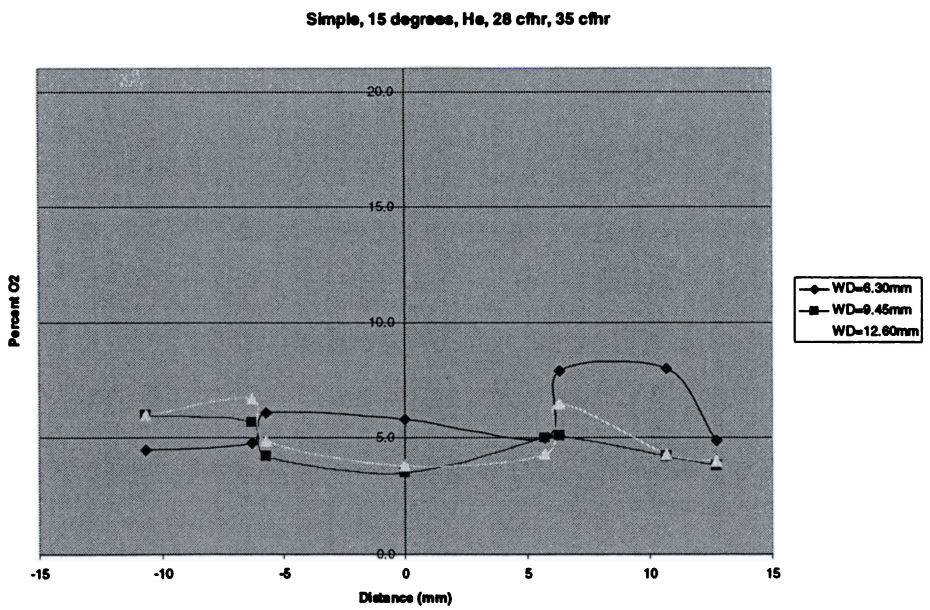

Figure 57: 7° simple nozzle, with He gas, comparison of a) without the shroud, and b) with the shroud flow at oblique impingement angle.

Conic nozzle geometry Vs 7° simple nozzle geometry, all gases: Figures 58, 59 and 60 compare the three nozzles (conic, 7° simple with shroud and 7° simple without shroud) ability to reduce the percent O_2 with each of the three gases. In the impingement region, Ar and N_2 gas produce roughly the same results (within 2-3 percent) no matter what nozzle is used. With He there appears to be some advantage in using the 7° simple nozzle with shroud to reduce the percent O_2 in the impingement region.

In summary, the selection of the protective gas nozzle geometry and the protective gas itself has a large effect on the percent O2 around the work zone. For the Ar and N_2 gases the existing conic nozzle or the 7° simple nozzle (with or without) all provide the lowest percent of O2 around the workzone. For the He gas, the 7° simple nozzle with shroud would provide the lowest percent of O2, but here the direction of processing will have to change for all working distances to improve (again at both impingement angles). For the N_2 gas, the impingement angle does matter when choosing a nozzle. For 0° impingement the 7° simple nozzle with shroud is the best, and at 15° impingement the conic nozzle is the best, but again with a change in processing direction.

It should also be noted that the results in this chapter were based on there NOT being a uniform flow entering the nozzle entrance. This flow has an unsteady swirling motion in its plenum that most probably entrains air throughout the jet, nozzle and plenum. Different results with probably occur with these two particular nozzles, if the flow field entering the nozzle is improved by making the velocity profile at the nozzle entrance more uniform. This can be done by increasing the number of gas injection

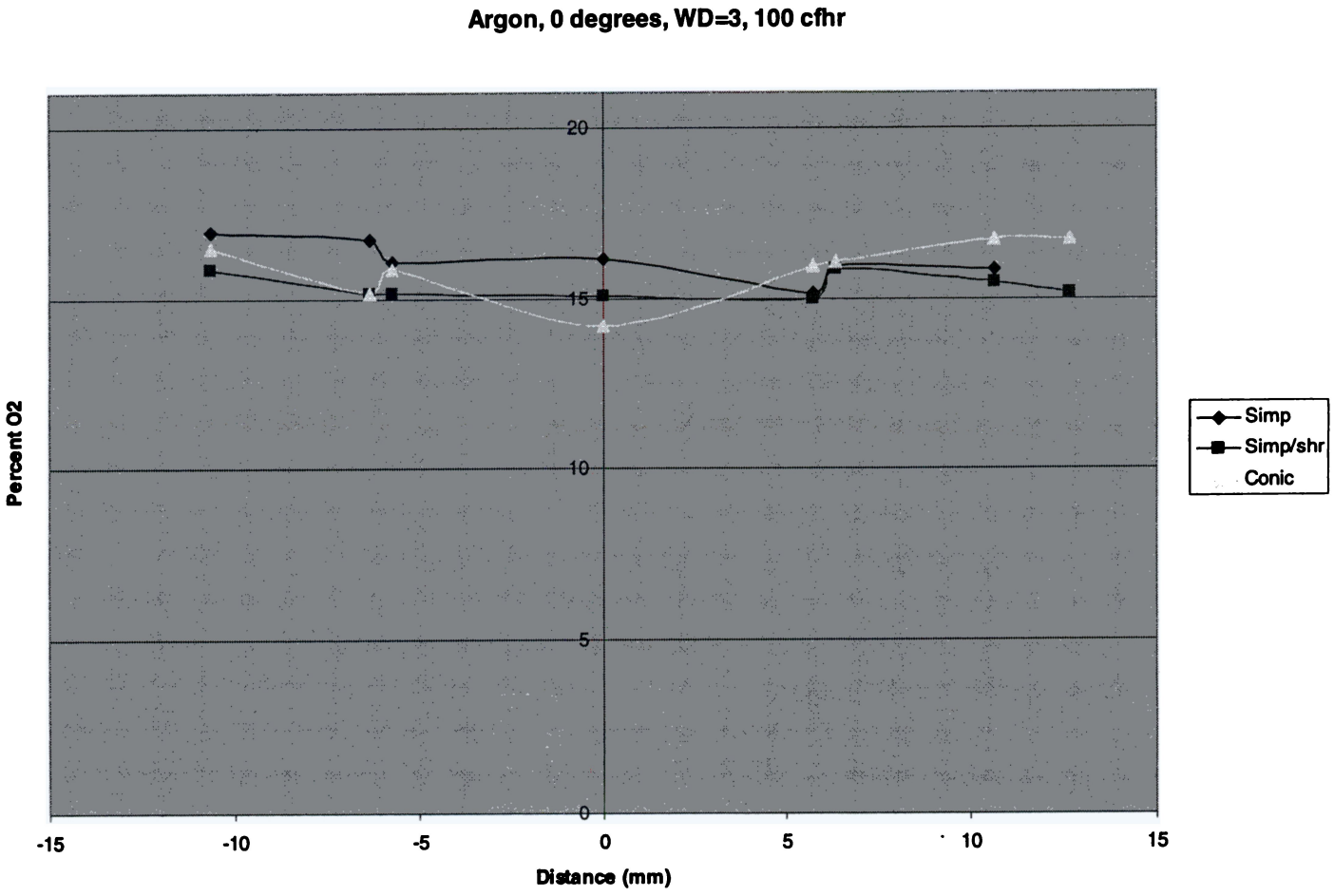

Figure 58: Argon gas nozzle comparison.

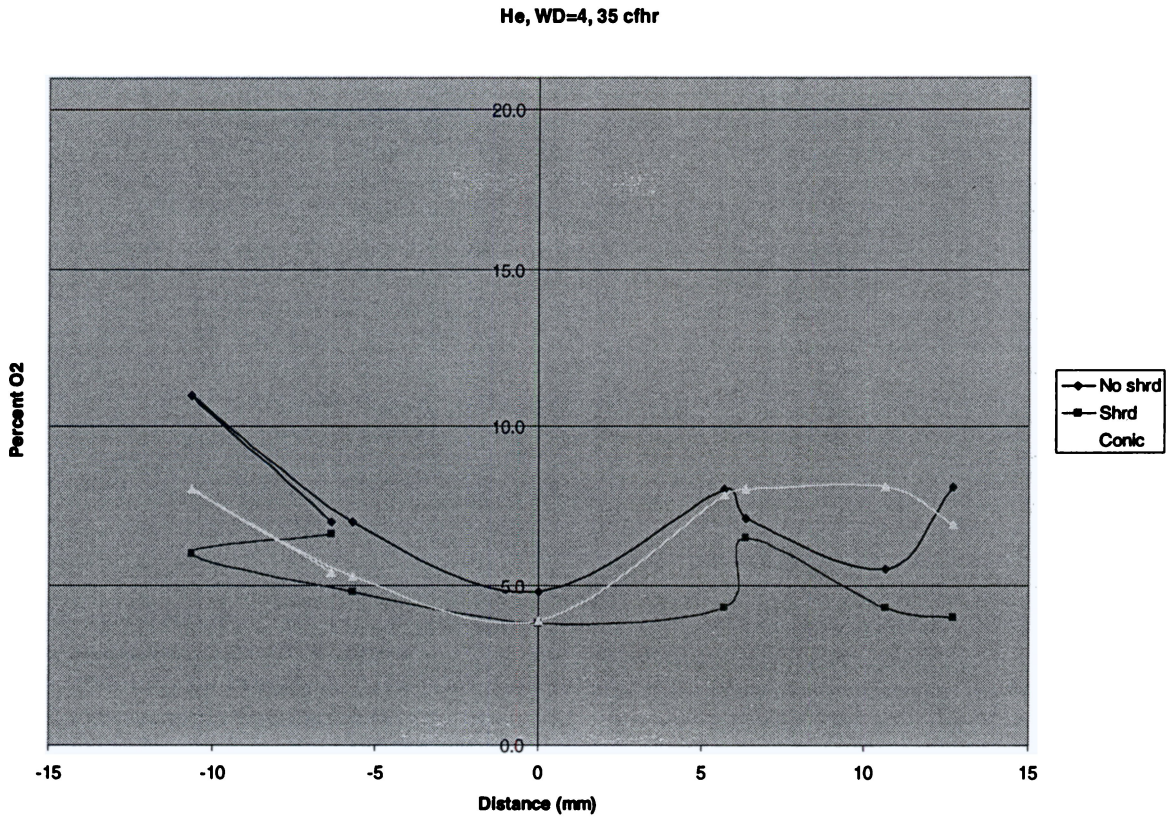

Figure 59: Nozzle comparison with He gas.

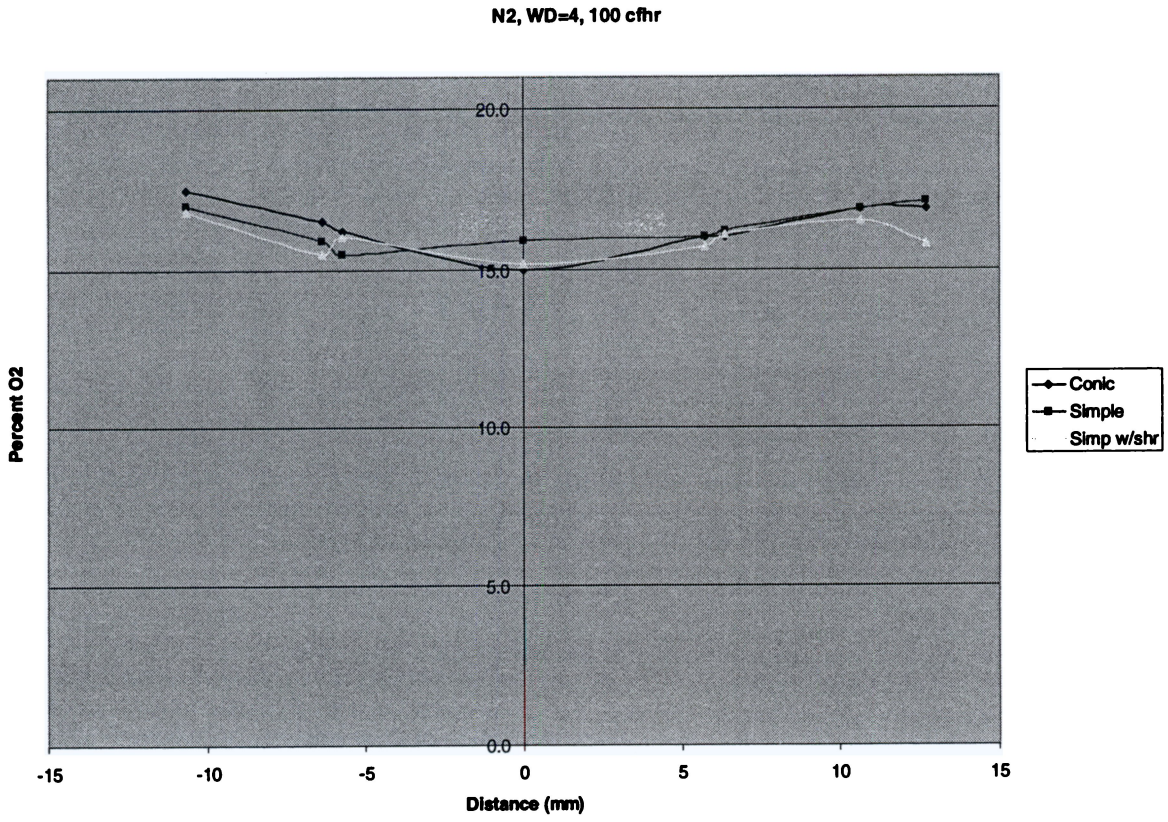

Figure 60: N2 gas comparison of the nozzles.

points feeding the nozzle entrance and moving that injection point farther upstream of the nozzle entrance.

CHAPTER VI

LASER TRIALS

The purpose of the laser trials was to actually create LISI[SM] surfaces with the new knowledge gained in the water tunnel simulation and the gas trials. The new 7° Simple nozzle with shroud was used to create the new LISI[SM] surfaces. These surfaces would then be metallurgically analyzed to determine if the new nozzle geometry and the proposed processing changes would reduce the O_2 content in the resulting alloy layer. Originally, one goal of the laser trials was to measure the O_2 content, like in the gas trials, but with the laser beam on. The idea was to determine how the temperature gradient caused by the laser beam effected entrainment (measured by the O_2 content). Unfortunately, the MSA O_2 analyzer was not designed for fast response and it could not keep up with the speed that the laser beam travels during the LISI[SM] creation process. Due to this limitation, the O_2 measurements were not made with the laser beam on.

LASER TRIAL'S HARDWARE

The laser used for this project was UTSI's Rofin-Sinar CW 020 Nd:YAG. The Rofin-Sinar was a computer controlled 2000 Watt laser with ramping, pulse generator, and superpulse capabilities. The 1.06 micron wavelength beam is delivered to the motion system by a fiber optics cable. Two motion systems are available, the Motomann K10 Manipulator (robot) and a X-Y-Z linear motion table. For this project the X-Y-Z linear motion table was used to create the LISI[SM] surfaces. Figure 61 shows the Rofin-Sinar lab setup for LISI[SM] processing.

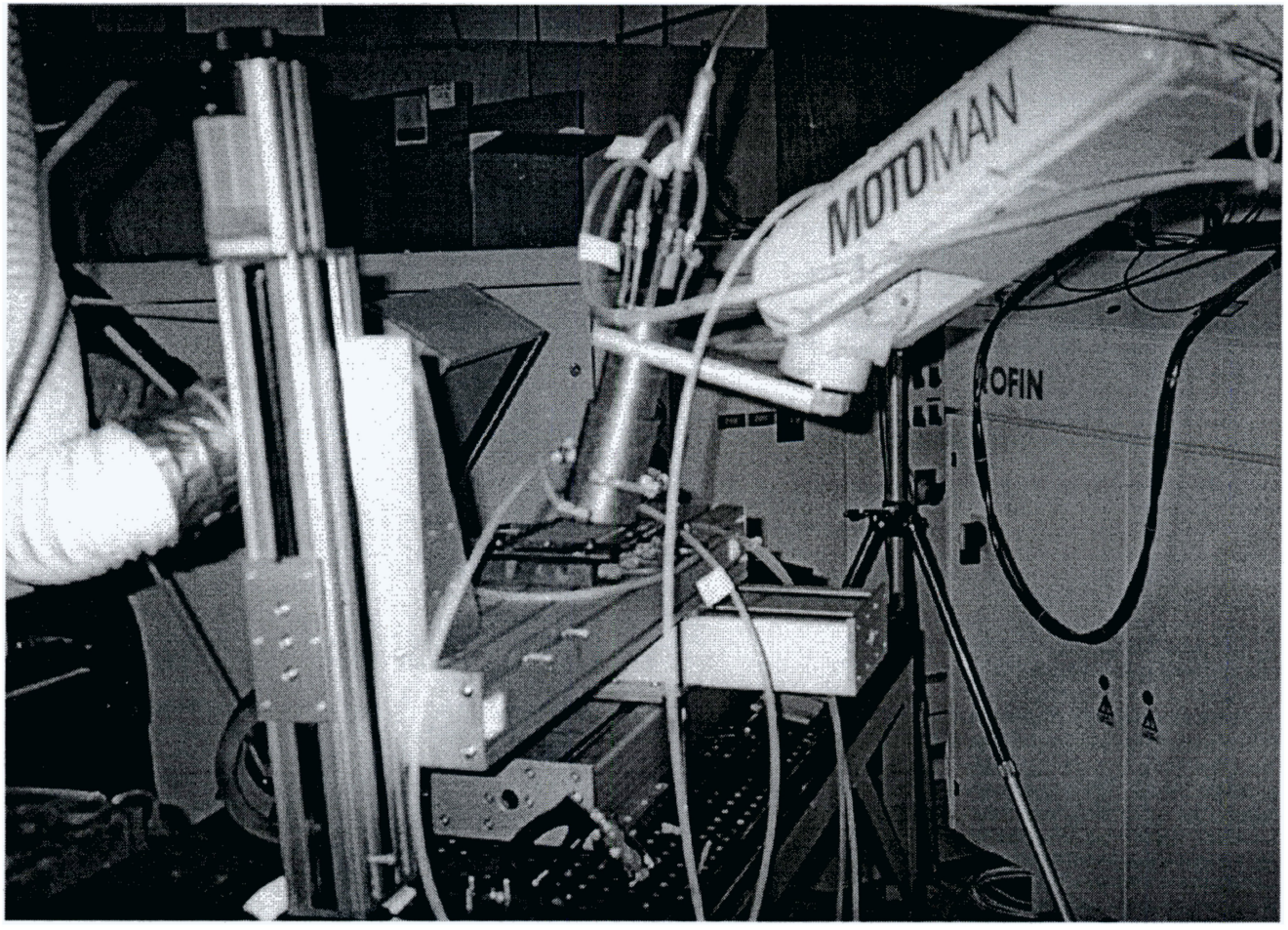

Figure 61. The Nd:YAG laser setup for processing LISI[SM] surfaces.

The protective gas nozzle for the laser was a 7° Simple Divergent nozzle with shroud, is shown in Figure 62. This nozzle was a larger version of the one used in the gas trials, with more gas injection point. This nozzle is made out of brass, it has an exit diameter of 3.81cm (1.5 inches), four gas feeds going into the nozzle inlet, and two gas feeds going into the shroud. The gas path from the gas bottle to the nozzle was the same of that used for the gas trials. The gas was delivered from pressurized tanks through a regulator and a flowmeter to the nozzle. Again the nozzle and the shroud are fed off separate sources.

LISI[SM] SURFACE PROCEDURE

The first step in creating a LISI[SM] surface begins with the substrate metal. For this project the substrate used was 1010 carbon steel. Sheets of 1010 steel, 0.635cm (1/4 inch) thick, are cut into 7.62cm (3 inch) by 15.24cm (6 inch) rectangular pieces. The surfaces of these pieces are then cleaned with a sandblaster to remove any contaminates. The edges are then rounded for safety. The next step is to spray the pre-cursor onto the cleaned surface of the 1010 steel. The pre-cursor for this project was a mixture of powdered chromium metal and liquid LISI[SM] binder (patent pending). The slurry mixture is then delivered onto the steel by a high pressure paint sprayer. The wet slurry mixture is allowed to dry under a heat lamp where the final pre-cursor thickness is approximately 100 microns.

The laser set conditions for processing these LISI[SM] surfaces were in the following manner. Three tracks were created for each condition with the power level set to 1400W,

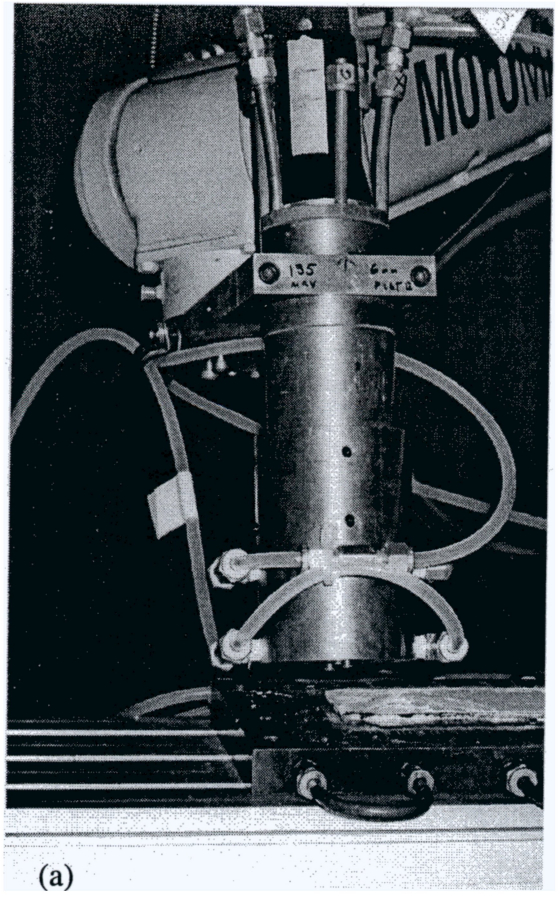

(a)

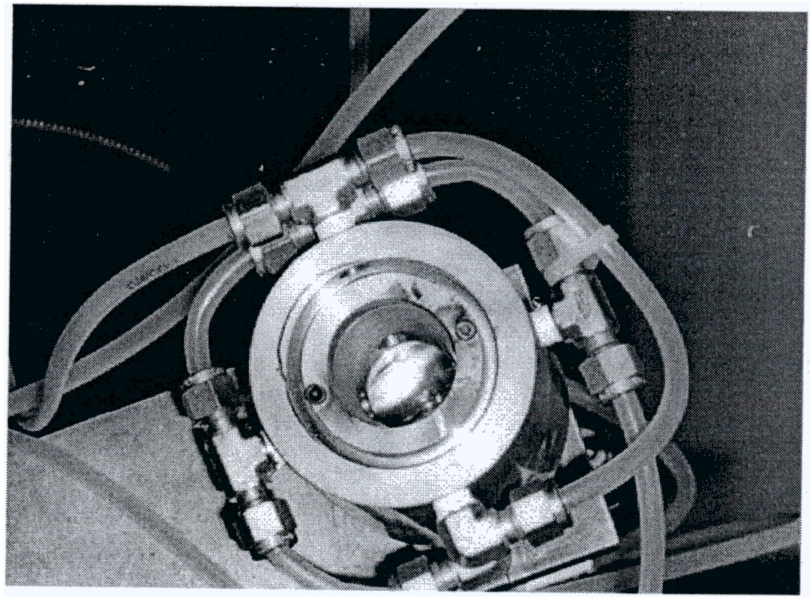

(b)

Figure 62. Full scale protective gas nozzle a) side view and b) bottom view.

the linear motion set to 1250mm/min, the distance between the bottom of the protective gas nozzle and the workpiece was 25mm, and the working distance (the distance between a position on the optics to the workpiece) was 132mm. The particular gas delivery/optics package used was number 4864 (UTSI model number).

The purpose here was to create LISI^{SM} surfaces with the knowledge gained in the water tunnel simulation and the gas trials. The water tunnel simulation first suggested that the direction of processing (when the laser beam is on) should change to move the molten metal pool under the protective gas jet. The point here was to process the LISI^{SM} surface in both directions. The current direction (as shown in Figure 1) is referred to as the backward direction (the melt pool trails behind the gas jet), and the opposite direction (the melt pool under the gas jet) is referred to as the forward direction. The water tunnel simulation showed that the oblique normal impingement angle caused much of the flow complexity (increased entrainment). To determine the effect of the oblique impingement angle on the LISI^{SM} surface, LISI^{SM} surfaces were created at both a zero normal impingement angle and the 15° normal impingement angle. To determine whether or not the shroud flow substantially reduces the resulting O_2 concentration in the alloy layer, the LISI^{SM} surface was created with and without the shroud on. The last parametric tested was that of the gases themselves. Samples were created at the two extremes, in open air without an assist gas jet (maximum entrainment) and bagged in Ar (no entrainment possible). This was done to get a baseline conditions for comparisons with the assist gas jets. Three gases were used with the new 7° Simple nozzle, Ar, He, and N_2. The test matrix used to create the LISI^{SM} surfaces is shown in Appendix C.

LISI[SM] SAMPLE ANALYSIS

Extensive analysis was performed on each of the samples listed in Appendix C. Some analysis was performed on the top of the LISI[SM] surface and some on the cross-section of the LISI[SM] surface. Surface data included profilometer data, x-ray analysis, SEM analysis, and Auger analysis. Profilometer data, measurement of the surface roughness, was performed across one LISI[SM] track and parallel to the center of that track. This measurement is similar to measuring the topography of the earth's surface. The data gives the maximum difference between the lowest point and the highest point measured on the surface. Profilometer (brand WYKO) data also gives the average roughness and a graphical representation of the data. The profilometer was being used in the VSI mode that with a single measurement has a vertical resolution of 3 nanometers. X-ray analysis was performed by a Phillips Electronic Instrument (Type 12215/0). X-ray analysis used the x-rays emitted by the surface when bombarded with X-ray tube with a copper emitter to produce a spectrum from which elements and compounds can be determined. X-ray analysis goes approximately 1 micron [58] into the sample, and has an uncertainty of less than 1 percent.

Elemental analysis was performed by SEM and Auger analysis. SEM analysis acquired by an energy-dispersive spectrometer (EDS) or a x-ray detector. The EDS allows the entire detectable spectral range to be recorded at the same time [58]. The emission of the x-rays is caused by the inelastic interaction (energy is lost) between the electron (from the electron gun) and the solid material. When an electron from the beam enters a material there is a high probability that it will hit an electron in orbit of the atom.

When the electron of the atom leaves, the atom is excited by the removal of an electron from an inner shell. After a very short time it returns to its ground state (before the electron beam hit the atom) when another electron from an outer shell fills the vacancy in the inner shell. The energy released in this transition is used to emit an x-ray or an Auger electron [59]. This x-ray is characteristic of the specimen and is used for identification by the EDS. For this analysis UTSI's International Scientific Instrument's (ISI) Super IIIA was used for the SEM work. Again a spectrum is produced, and the concentration of medium and heavy elements can be determined.

The Auger analysis was performed on a Physical Electronics (PHI) Model 680 Scanning Auger Nanoprobe System with a schottky field emission source and multichannel detector. The Scanning Auger is owned by the United State's Department of Energy's Oak Ridge National Laboratory's High Temperature Materials Laboratory (HTML). The Auger is a surface analysis technique, only going into the sample approximately 1 nanometer [58]. Like the SEM's x-ray analysis, the Auger analysis was performed by capturing electron that were created by an inelastic collision between an electron beam and the material. With Auger analysis, instead of x-rays, Auger electrons are emitted by the relaxation of atoms with vacancies in their inner electron shells. An electron gun (with Ar gas) first sputters the surface to remove contaminants, then it can perform periodic sputtering to accomplish depth profiling. Approximately 0.6 of a micron of material was removed for every six minutes of sputtering. The Auger analysis has an uncertainty of approximately 5% on an absolute basis and 2-3% on a sample to sample comparison. The PHI 680 set conditions were at 10kv and 10 nano amps during data

acquisition. Auger analysis differs from SEM analysis in that it is surface specific and its high sensitivity in analyzing light elements [58].

Cross-sectional data was obtained by cutting a small sample (approximately 10cm by 10cm) and metallurgically preparing (polished through a series of sand paper and abrasive polishes) the sample to show the alloy layer, the heat effected zone and the base metal. Analysis on these polished cross-sections was microscopy photography, SEM photography, SEM EDS elemental analysis, and Auger elemental analysis. The photography was taken on a Olympus BX60M microscope with digital acquisition. The SEM photography was taken by UTSI's ISI Super IIIA. The SEM and Auger analysis was the same as that described for the surface analysis.

RESULTS OF THE LASER TRIAL

Whether or not the new nozzle geometry and knowledge learned during the water tunnel and the gas trials actually resulted in less oxygen in the LISI^{SM} surface, was to be determined largely by the Auger analysis results. The Auger analysis was thought to be 3-5% accurately between samples and 10-20% off on an absolute basis. Originally this level of accuracy was thought to be good enough for this particular application. When the analysis began, it became obvious that determining the level of oxygen, O, in the surface would be much more difficult than originally thought. The problem arises with analyzing with iron, Fe, present. The primary peak for analyzing O occurs at 516 eV and a secondary peak for Fe occurs at 519 eV. These two Auger peaks of the two primary elements of interest being so close together caused the Auger analysis software package to produce a larger percent of O than is probably really there. In order to try to resolve

this issue, the base metal (assumed to be greater than 99.9% Fe on 1010 metal) was analyzed on two samples. Averaging the readings produced a O level of 7% and a Fe level of 93%. The conclusion drawn was that for this particular analysis, the Auger percent O results are +/- 7%. All the Auger results for this project are presented in Appendix C-2. The major results will be discussed in the following paragraphs.

Overall all most of the O data is within the 7% uncertainty band. While hard conclusions were difficult to draw, slight trends can be seen in the data. One of the first questions to be answered is whether or not changing the processing direction results in less O in the surface. The answer is dependent of the gas used. For He gas the resulting O in the forward processing direction (the new direction) was averaged 15% while the backward direction (the old direction) was averaged 6%. Looking at Figure 63 this trend might be explained. Figure 63 is the gas sampling results of the laser's nozzle with He gas at the oblique impingement angle. The negative direction is where the melt pool would be for the backward processing direction. As came be seen in Figure 63, the negative direction is where the largest area of reduce percent O_2. For N_2 gas the forward direction resulted in 8%, while the backward direction resulted in 2%. This may be again explained based on the gas sampling of the nozzle with N_2 gas (see Figure 64). The negative direction is again results (with shroud flow) in less measured O_2. For Ar gas, the forward direction resulted in 5%, while the backward direction was 9%. Again, this is explained with the gas sampling data (see Figure 65) the negative direction results in less percent O_2. All the data is within the +/- 7% uncertainty band so the Auger analysis does not provide a definitive answer to whether or not the change in processing direction will

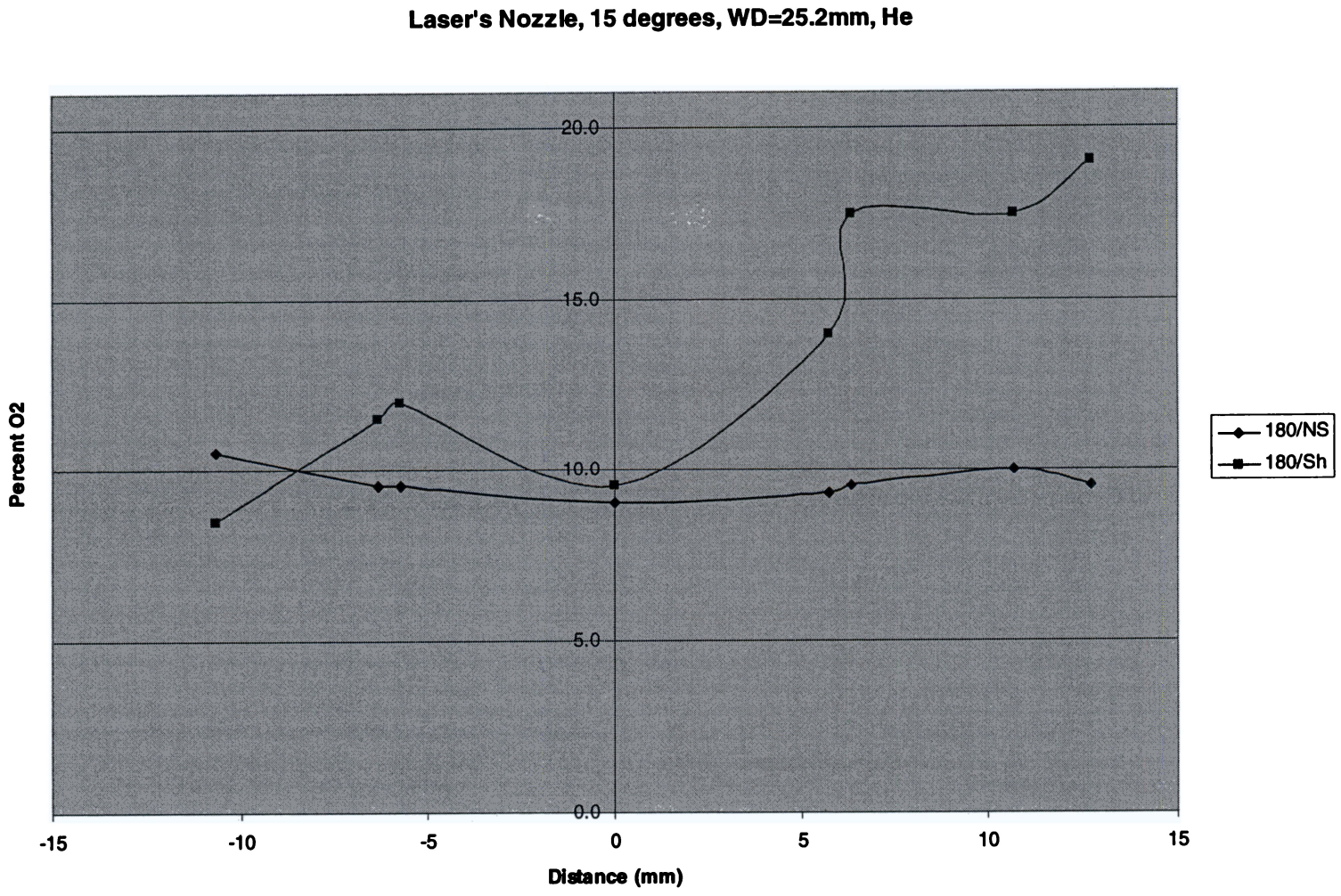

Figure 63: Percent oxygen measured with the processing nozzle using He gas, with oblique jet impingement.

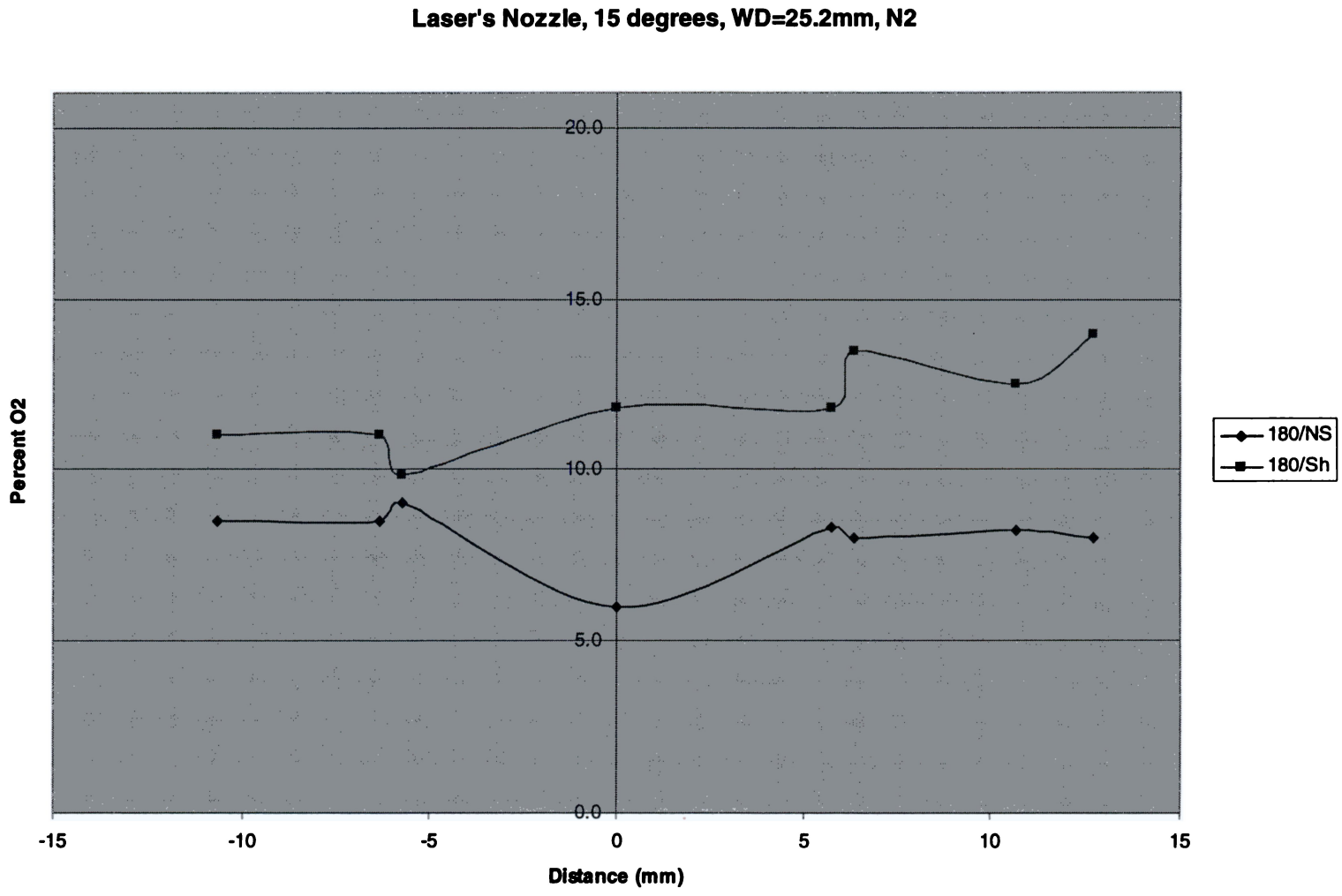

Figure 64: Percent oxygen measured with the processing nozzle using nitrogen gas, with oblique jet impingement.

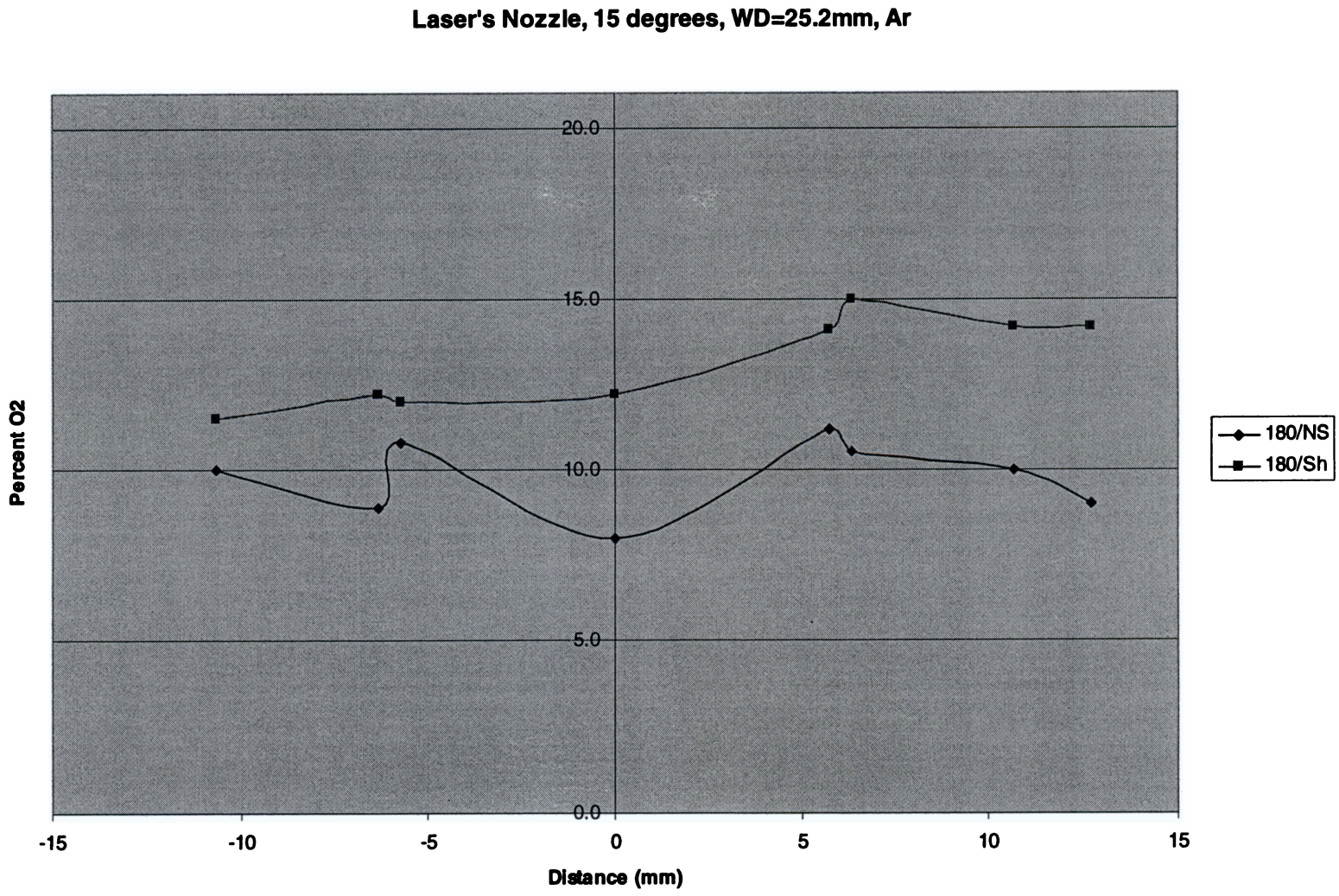

Figure 65: Percent oxygen measured with the processing nozzle using Ar gas, with oblique jet impingement.

reduce the level of O in the LISI[SM] surface. The gas sampling does indicate that perhaps the reduction in O_2 suggested by the water tunnel simulation may not be realized with the larger laser's nozzle.

Another question to be answered was whether or not the shroud flow results in reduced O content. With He gas at the normal jet impingement, the O content is about the same through the layer (8-12%), but near the surface the shroud appears to reduce the O content from 20% to 8%. With the oblique impingement and the backward processing direction, no shroud results in 0% O and with shroud flow results in 12% O. With the oblique impingement and the forward processing direction, there was basically no difference between shroud flow and no shroud flow (all measurements were between 15-17%). For He gas, it appears that to get no O in the layer, the processing direction should not change and there should be no shroud flow. With Ar gas, there were two shroud/nozzle flowrates at which samples were created, 50 cfhr of air and 180 cfhr of air. At normal impingement, the lower flowrate produced a O content of 3-4%, the higher flowrate produced a O content of 19-22%, and no shroud flow (but nozzle flow of 180 cfhr of air) the O content was 5-10%. While the data is limited, it does appear that at the normal impingement angle, with Ar gas, the lower the flowrate produces the least amount of O content in the resulting surface. At the oblique impingement angle in the backward processing direction, the low flowrate (with and without shroud flow) and the high flowrate without shroud flow produce similar O content (3-8%) while the high flowrate with the shroud flow results in a increase of O content to 14-16%. With Ar gas at processing in the forward direction data was only obtained at the higher flowrate and O

content was slightly better with the shroud (11-12%) than without the shroud (15%). Overall the data is limited in proving whether or not the shroud flow reduces the resulting O in the surface. It does appear that the flowrate does effect the results (at least in the backward direction) and that in the backward direction the shroud flow appears to increase the O content. It the forward direction the shroud appears to slightly reduce the O content in the layer.

Which is the overall best gas to use in the protective nozzle? The answer appears to depend on the angle of impingement. With the oblique impingement angle (15 degrees to the normal of the suface), He is the best gas to use. With no shroud flow and the backward processing direction, 0% O content was a result. At the normal impingement angle, N_2 appears to be the best gas. With shroud flow and the forward processing direction, 0% O content was a result. These to examples were the only times that 0% O content was achieved processing with a protective nozzle. 0% O content was always achieved when processing in a box void of all air, no matter what gas was used

While the Auger analysis was not as conclusive as originally hoped for, it was not the only measurement of O in the LISI^{SM} surface. X-ray analysis was performed on the same samples that Auger analysis was performed on. While the x-ray analysis provides compounds not elements, the presence of O with other elements can be detected but not measured. In general, if the Auger analysis picked up oxygen in layer of the LISI^{SM} surface then the x-ray analysis would pick up a iron oxide (FeO or $FeFe_2O_4$) or a chromium oxide (CrO or CrO_2). If the Auger analysis did not pick up oxygen neither did

the x-ray. The x-ray, while in this case did not provide quantitative analysis, it was a reliable indicator of the presence of oxygen.

It should be mentioned that for all the Auger analysis, except for one point on sample 2508-63, there was no indication of nitrogen in the alloy layer. At first this seemed puzzling, because air is approximately 21 percent oxygen and 79 percent nitrogen. It would seem that nitrogen is more available to be absorbed into the molten metal. One explanation for this lack of nitrogen can be found in the ternary alloy phase diagrams for the alloy Cr-Fe-N [62]. On average these alloy layers have roughly 15-20% of Cr in them. At that level of Cr, the amount of nitrogen that could be absorbed is less than one percent. This small amount of nitrogen is not measurable by the Auger analysis.

SEM analysis was also performed on the samples to see if any correlation could be derived between the SEM analysis, which could not detect oxygen, and the Auger analysis which did detect and quantified oxygen. After much statistical analysis, a correlation could not be found. The SEM was used to get detailed pictures of the cross-section of the LISI^{SM} surface. Figure 66 is a typical cross-section of the chromium on 1010 steel LISI^{SM} surface.

Profilometer data was gathered on each of the samples in hopes that a trend could be determined between the protective gas nozzle and the surface roughness of the sample. No trend could be determined based on flowrate, processing direction, the use of the shroud or not, and the different types of gas. The profilometer data appeared to be random.

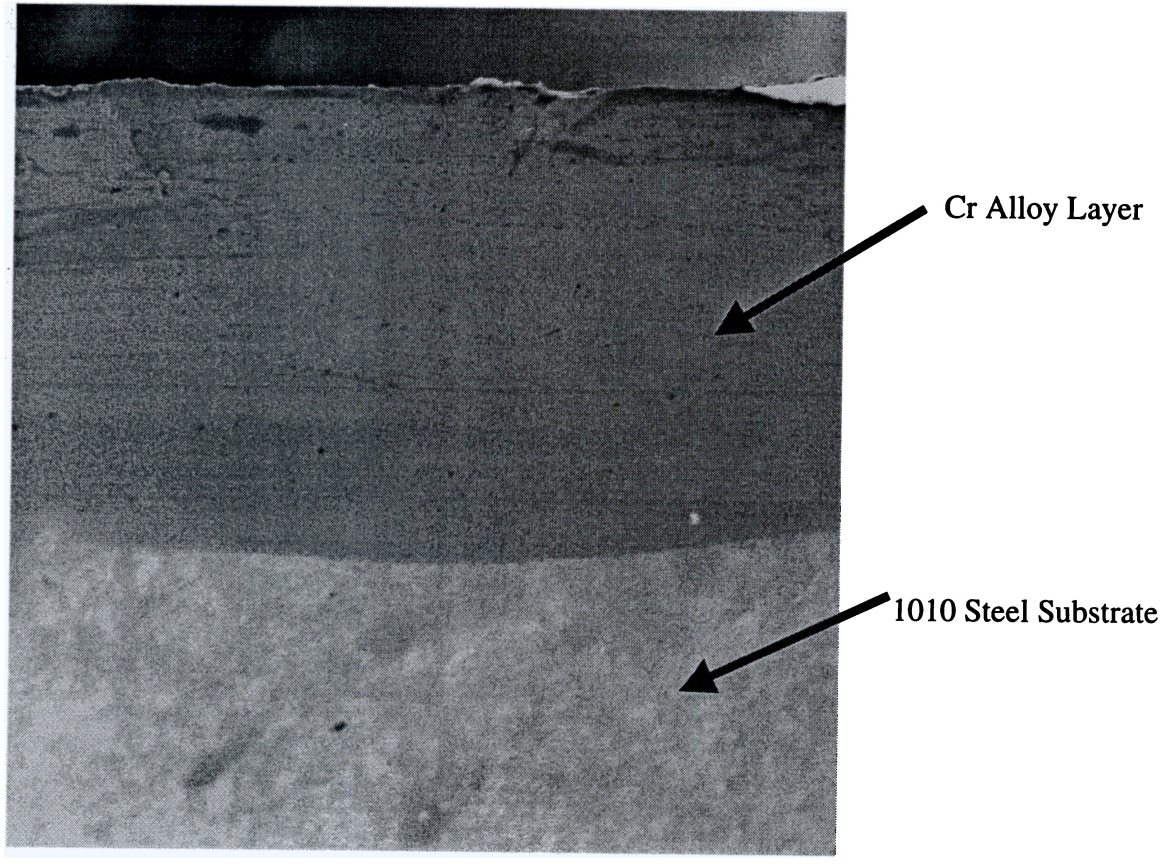

Figure 66: A SEM photograph of a typical cross-section of chromium on 1010 steel alloy layer (magnification 300X).

CHAPTER VII

CONCLUSIONS AND RECOMMENDATIONS

GENERAL CONCLUSIONS

The water tunnel simulation and the gas trials provided general knowledge about the oblique jet impingement flowfield associated with laser surface alloying. Laser surface alloying must take into account the surrounding aerodynamic flow patterns to produce a completely desired surface. The water tunnel simulation and the gas trials both showed that in an open environment, entrainment could not be eliminated. Through understanding the flowfield complexities, the effects of different gases, and the nozzle geometry selection the effects of air entrainment can be reduced. The gases and nozzle geometries evaluated here are not an exhaustive list. Only the three most popular protective gases were evaluated, and only a few known subsonic nozzle geometries were evaluated. The result of this limited research is that the only way to completely eliminate air entrainment was to enclosed the volume around the laser beam/material interaction and displace the air.

One requirement of this research was to characterize the flow field and evaluate nozzle geometries with the gas delivery package I. Gas delivery package I was designed with the optics in mind and not the flow quality entering the protective gas nozzle. One conclusion reached here is that the unsteady swirling motion in the gas delivery package (the nozzle's plenum) must be eliminated. The entire gas feed through the gas delivery package to the protective gas nozzle must be redesigned. One of the most fundamental

assumptions in nozzle flow is that the flow entering the nozzle entrance has developed into uniform flow. This uniform flow then goes through the nozzle contour to result in the potential core of the jet. The unsteady swirling motion that is present in the plenum of the nozzle, prohibits uniform flow from forming at the nozzle entrance. All nozzle theory is base on uniform flow at the nozzle's entrance, without uniform flow the behavior of the jet produced is unknown. While the general flowpatterns discovered during this research project should be still relevant, the selection of the 7° Simple Divergent nozzle geometry may not have been made with a better nozzle gas feed path.

SPECIFIC CONCLUSIONS

When using an oblique protective gas jet in laser processing, the processing direction should consider the location of the melt pool in relation to the impingement flow pattern. The water tunnel flow patterns and the gas trials gas sampling show that the most ideal processing direction is one that moves the melt pool into the impingement region of the oblique jet. The movement of the optics package causes the molten metal pool to trail behind the laser beam/material interaction point. The current processing direction, with a co-axial assist gas nozzle, puts the impingement region of the jet infront of the molten metal. The only protection the protective gas jet can provide is from the boundary layer flow, which has been shown not to be the minimum percent O_2. In fact the current processing direction can actually pull more entrained air over the molten metal, from the recirculation zone above it. Maximizing the protection of the assist gas jet can easily be accomplished by changing the direction on which the laser beam is

turned on during processing. This change will only modify a couple of lines of the computer code controlling the motion system and can be implemented immediately.

Like other researchers have found [42] the use of an outside annular gas shroud does reduce entrainment, but the reduction is slight in this application. The additional knowledge found in this project is that the shroud flow worked with a subsonic divergent nozzle (the other researchers used a supersonic conic nozzle). The reason previously cited, was that the shroud flow (with its non air composition) is a buffer that is entrained by the turbulence of centered jet instead of the surrounding air. That certainly attributes to the reduction of O_2 being entrained into the jet and ultimately finding its way into the final resolified alloy layer. However, the fact that an additional volume of protective gas is surrounding the molten metal in itself must contribute to the reduction of O_2 concentration on the surface. Again, the unsteady swirling motion in the plenum must be a large contributing factor for the lack of effect the shroud has. The unsteady swirling motion is large and reduces the buffer effect that the shroud has on the inner jet. From the water tunnel visualization and the gas trials visualization, the swirling motion is quite violent, whipping around quite forcefully. This forceful whipping is pulling more air into the jet itself. The shroud was designed to be a gentle buffer to the core jet. The shroud has the same velocity as the jet would have if it had uniform flow.

When comparing the results of the gas sampling of the laser's nozzles to the results of the Auger analysis on the resulting surfaces, similarities do occur. The gas sampling for the laser nozzle with He and Ar (Figures 63 and 65) show that the shroud flow actually increases the percent oxygen at the surface of the plate. This result was

verified by the Auger analysis where the O in the surface with He increased from 0% to 12% and with Ar the O in the surface increase from roughly 5% to 15% with shroud flow.

There are apparent differences between the smaller 7° Simple nozzle of the gas delivery package I and the larger 7° Simple nozzle of the gas delivery package II. The larger nozzle with the equally larger flowrate should have resulted in similar results, but it did not. The effect of using the shroud flow should have been the same. The pressure measurements should have been the same. The geometry of the two 7° Simple nozzles are the same except for one being three times larger. The big differences between the two are how they are mounted and how the gas is feed into them. As the larger nozzle does not supply the same impingement pressure as the smaller nozzle, there must be a larger pressure drop in the tubing system of the larger nozzle. This difference in the gas feed supply must account for the differences seen in the gas sampling and the pressure measurements.

Overall, the water tunnel did provide the correct flow patterns of the oblique impinging jet. It did show how the jet changes with increasing working distances. The larger impingement region at the smaller working distances was verified with the lower percent oxygen measured during the gas trials. Whether or not the water tunnel is successful at screening nozzle geometries is not clear. The unsteady swirling motion clouded some of the results and when it is gone perhaps the water tunnel could be used as a screening tool. Overall the gas sampling worked in providing the percent oxygen on the surface of the plate. Some of the results seen with the gas sampling was verified with the Auger analysis of the laser's nozzle. Unfortunately, the Auger analysis did not provide

many concrete conclusions in this research due to its large error when analyzing oxygen with iron.

RECOMMENDATIONS

Redesign the optics package gas feed to provide a more uniform flow to the assist gas nozzle entrance. The current situation of one injection point, perpendicular to the nozzle entrance, at the nozzle entrance, is causing the creation of the vortex and does not allow any time for a uniform flow to develop. A reasonable amount of distance/volume must be given between the point of gas injection and the assist gas nozzle entrance must be provided to allow for uniform flow to develop. In addition, more than one injection point is a must, in fact, if possible infinite injection points would be best. The point is to inject the gas feed in a manner that the individual streams have enough volume to mix and turbulence had a chance to damped enough to form uniform flow before entering the assist gas nozzle entrance. The next optics package design must include some concessions for flow quality going into the nozzle.

Preliminary data was gathered with a flow diverter installed. This flow diverter was a piece of foil installed around the nozzle entrance at the injection point of the gas delivery package I. With the diverter, the gas entering the nozzle entrance is fed continuously and diffusely around the circumference. The preliminary results with the flow diverter show a large decrease in percent oxygen measured at the plate when compared to the same test conditions without the diverter. The pressure measurements with the diverter show a remarkable decrease in the unsteadiness of the pressure measurements with the diverter. Initial smoke visualization indicate that the unsteady

swirling motion may be gone with the diverter. Further research is needed to determine if the diverter alone solves the problem of the unsteady swirling motion or if a change in the location of the gas injection points relative to the nozzle entrance is needed.

It is also recommended that before new nozzle geometries be evaluated that the gas path been thoroughly understand first. The first phase of any new research into protective gas nozzles should include a gas path screening. The water tunnel should be able to provide quick visualization of the flow pattern for each gas path and it should help in determining the best gas path. The best gas path would be the path that best provides the most uniform flow to the entrance of the nozzle without any obvious unsteady swirling motions.

Both the conic nozzle and the 7° simple nozzle geometries need to be re-evaluated with the improved gas feed path. At this stage it would be advantageous to evaluate other nozzle geometries with the gas sampling and the impingement pressure measurements. Simple shapes will be the easiest to make quickly to test. Simple convergent and divergent geometries would be best. The contraction angles could be varied to determine the optimal one for this application. The data from this research shows that the current conic nozzle should still be evaluated for this application. A conic nozzle with shroud flow show be evaluated during the next phase of research. The water tunnel simulation and the gas sampling of the smaller nozzle showed that the shroud is helpful. With the improved flow path the potential of the shroud may be realized.

The potential of increase protection of the molten metal might still be achieved with changing the processing direction. The results from this research were inconclusive

due to the presence of the unsteady swirling motion. The water tunnel simulation showed a region of increased protection. The gas trials indicated that there might be a benefit. This should, of course, be evaluated during the next phase of research.

LIST OF REFERENCES

REFERENCES

1. Belforte, D., "Machine Systems for Laser Processing-Cutting Emphasis," LIA: Guide to Laser Materials Processing, Edited by Sidney. S. Charschan, 1993, p210.

2. Hopkins, J.A., McCay, M.H., Dahotre, N., McCay, T.D., and Schwartz, F., "Performance of Laser Processed Aluminum Alloys for Engine Bore Applications," SAE Technical Paper Series, 980458, Reprinted from: Aluminum in Automotive Application (SP-1350), p. 56.

3. McCay, M.H., and Tramel, T.L., "The Performance of Laser Surfaced Processed Aluminum alloys for Commercial Applications," Presented at ICALEO, 1998, in Orlando, Florida, November 16-19.

4. American Welding Society, "Recommended Practices for Gas Tungsten Arc Welding of Titanium Pipe and Tubing," ANSI/AWS d10.6-91.

5. Woolcock, A. and Ruck, R.J., "Argon Shielding Techniques of TIG Welding Ti," Metal Construction, May 1980.

6. Lin, J., and Steen, W.M., "Design Characteristics and Development of a Nozzle for Co-axial Laser Cladding," Journal of Laser Applications, Vol. 10, No. 2, April, 1998.

7. Bower, W.W., Saripalli, K.R., and Agarwal, R.K., "Summary of Jet-Impingement Studies at McDonnell Douglas Research Laboratories," AIAA paper 81-2613.

8. Donaldson, C.D., and Snedeker, R., "A Study of Free Jet Impingement. Part 1. Mean Properties of Free and Impinging Jets," J. Fluid Mech., 1971, Vol. 45, 281-319.

9. Donaldson, C.D., Snedeker, R.S., and Margolis, D.P., "A Study of Free Jet Impingement. Part 2. Free Jet Turbulent Structure and Impingement Heat Transfer," J. Fluid Mech., 1971, Vol. 45, 477-512.

10. Kotansky, D.R., "Multiple Jet Impingement Flowfields," Recent Advances in Aerodynamics: Proceedings of an International Symposium, Held at Stanford University, August 22-26, 1983.

11. Saripalli, K.R., "Visualization of Multi-Jet Impingement Flow," AIAA paper 81-1364.

12. Saripalli, K.R., and Kroutil, J.C., "A Novel Experimental Facility for Conducting Jet Impingement Studies Related to VSTOL Aircraft," AIAA paper 85-0052.

13. La Rocca, A.V., Borsati, L., and Cantello, M., "Nozzle Design to Control Fluid Dynamic Effects in Laser Cutting," The Society of Photo-Optical Instrumentation Engineers, SPIE, Laser Materials Processing: Industrial and Microelectronics Applications, Proceedings EurOpto Series, Vol 2207, pp. 354-368.

14. Brandt, A.D., and Settles, G.S., "Effect of Nozzle Orientation on the Gas Dynamics of Inert-gas Laser Cutting of Mild Steel," Journal of Laser Applications, Vol.9, 269-277.

15. Leidinger, D., Peng, A., Schuocker, D., Geinzer, G, ect., "Nozzle Design and Simulation of Gas Flow for the Laser Cutting Process," ," The Society of Photo-Optical Instrumentation Engineers, SPIE, Laser Materials Processing: Industrial and Microelectronics Applications, Proceedings EurOpto Series, Vol 2207

16. Beyer, E., Cantello, M., La Rocca, A.V., ect., "Fundamental Mechanisms of Cutting Front Formation in Laser Cutting," ," The Society of Photo-Optical Instrumentation Engineers, SPIE, Laser Materials Processing: Industrial and Microelectronics Applications, Proceedings EurOpto Series, Vol 2207, 1994, p. 402.

17. Chryssolouris, G., and Choi, W.C., "Gas Jet Effects on Laser Cutting," SPIE, Vol 1042, CO_2 Lasers and Applications, 1989.

18. Edler, R., Berger, P., and Hugel, H., "Performance of Various Nozzle Designs in Laser Cutting," Proc. ECLAT, 1992, 111-116.

19. Gabzdyl, J.T., and Morgan, D.A., "Assist Gases for Laser Cutting of Steels," ICALEO, 1992, p 443.

20. Leidinger, D., and Schuocher, D., "Investigations of the Gas Flow of Conic-cylindrical and Supersonic Nozzles in a Laser Cut Kerf," 1995, SPIE, Vol. 2502, 577-582.

21. Powell, J., CO_2 Laser Cutting, Springer-Verlag, 1993.

22. Yoshiaki, A., "Challenges to Laser Advanced Materials Processing," LAMP 87, Osaka, May 1987.

23. Colt, J., "Longlife Oxygen Plasma Cutting," www.hypertherm.com, 1998.

24. Croyden Group, "Controlling Gases in Laser Cutting and Welding," Editor Waldbusser, Fabricator, December 1996.

25. Fieret, J., and Ward, B.A., "Circular and Non-circular Nozzle Exits For Supersonic Gas Jet Assist in CO_2 Laser Cutting," Proceedings of the 3rd International Conference on Lasers in Manufacturing, 3-5 June 1986, Paris, France.

26. Martin, H., "Heat and Mass Transfer Between Impinging Gas Jets and Solid Surfaces," H.P. Hartnet and T.F. Irvine Jr (Eds), Advances in Heat Transfer, Vol. 13, Academic Press, New York, 1977.

27. Striegl, S.A., and Diller, T.E., "The Effect of Entrainment Temperature on Jet Impingement Heat Transfer," J. of Heat Transfer, February 1984, Vol. 106.

28. Striegl, S.A., and Diller, T.E., "An Analysis of the Effect of Entrainment Temperature on Jet Impingement Heat Transfer," J. of Heat Transfer, November 1984, Vol. 106., 804-810.

29. Boldman, D.R., and Brinich. P.F., "Mean Velocity, Turbulence Intensity and Scale in a Subsonic, Turbulent Jet Impinging Normal to a Flat Plate," NASA Technical Paper 1037, September 1977.

30. Theobald, C., "The Effect of Nozzle Design on the Stability and Performance of Turbulent Water Jets," Fire Safety Journal, Vol. 4, No. 1, August 1981, pp. 1-13.

31. Jankovic, M. and Mostaghimi, J., "A New Nozzle Design for dc Plasma Spray Guns," Plasma Chemistry and Plasma Processing, Vol. 15, No. 4, 1995.

32. Smith, C.E., Fuller, E.J., and Crocker, D.S., "Dual-Spray Airblast Fuel Nozzle for Advanced Small Gas Turbine Combustion," Journal of Propulsion and Power, Vol. 11, No. 2, March/April, 1995.

33. Abramovich, G.N., The Theory of Turbulent Jets, MIT Press, 1963.

34. Popiel, C.O. and Trass, O., "Visualization of a Free and Impinging Round Jet," Experimental Thermal and Fluid Science, 1991; 4: 253-264.

35. Bower, W.W., Kotansky, D.R., and Hoffman, G.H., "Computations and Measurements of a Two-Dimensional Turbulent Jet Impingement Flowfield," Symposium on Turbulent Shear Flows, April 19-20, 1977, University Park, Pennsylvania, Vol. 1, p. 3.1-3.8.

36. Hryck, P., Lee, D.T., Gauntner, J.W., and Livingood, J.N.B., "Experimental Flow Characteristics of a Single Turbulent Jet Impinging on a Flat Plate," NASA TN D-5690, 1970.

37. Fondse, H., Leijdens, H., and Ooms, G., "On the Influence of the Exit Conitions on the Entrainment Rate in the Development Region of a Free, Round, Turbulent Jet," Applied Scientific Research, Vol. 40, 1983, pp 355-375.

38. Rae, W.H. and Pope, A., Low-Speed Wind Tunnel Testing, John Wiley and Sons, 2nd Edition, 1984.

39. Man, H.C., Duan, J., Yue, T.M., and Dong, P., "Design of Supersonic Nozzle for Laser Cutting with High Pressure Gas," Laser Institute of America, ICALEO 97 Proceedings, Laser Materials Processing, Vol. 83, Part 1, Section B, pp. 118-127.

40. O'Neill, W., Gabzdyl, J.T., and Steen, W.M., "A Study of Gas Entrainment Effects Operating During the Laser Cutting Process," Laser Institute of America, Proceeding from ICALEO 93, Vol. 77, Laser Materials Processing, pp. 21-29.

41. Mazumder, J., "Laser Assisted Surface Coating, " Metallurgical, Ceramic Protective Coatings, Editorial By Kurt H. Stern.

42. Chande, T. and Mazumder, J.: Applied Phys. Lett., 41, (1982), 42.

43. Belforte, D.A., "Laser Surface Treatment," Presented at Colloguium on Laser and Electro-Optical Equipment, Tokyo, Japan, 1978.

44. Ready, J.F., "Absorption of Laser Engergy," LIA: Guide to Laser Materials Processing, Edited by Sidney. S. Charschan, 1993, p73-95.

45. Rosenthal, D., "Mathematical Theory of Heat Distribution During Cutting and Welding ," The Welding Journal, 20, Research Suppl. 220-s to 234-s, 1941.

46. Dahotre, N., Notes from Laser Materials Processing Class, University of Tennessee Space Institute, Fall of 1997.

47. Adams, C.M. Jr., "Cooling Rates and Peak Temperatures in Fusion Welding," The Welding Journal, Welding Research Supplement, 210-s to 215-s, May 1958.

48. Ames Research Staff, "Equations, Tables, and Charts for Compressible Flow," NACA Report 1135, 1953.

49. Semak, V., Meeting at University of Tennessee's Space Institute on February 25, 1999.

50. Iida, T., and Guthrie, R.I.L., The Physical Properties of Liquid Metals, Oxford Science Publications, 1993.

51. White, F.M., Fluid Mechanics, Second Edition, McGraw-Hill Company, 1986.

52. Sheikholeslami, A.H. "Design of a Hot-Flim Probe Calibrator, Calibration of UTSI Water Tunnel, and Flow Visualization Study of Secondary Flow in a Laminar Corner," Master's Thesis, The University of Tennessee, Knoxville, December 1981, pp 22-24.

53. Merkle, C., Conversation with author, February 16, 1999, UTSI

54. Taylor. D., "Ejector Design for a Variety of Applications", Prepared for Von Karman Short Course on Ejectors, March 17-22 1969, research sponsored by Arnold Engineering Development Center.

55. O'Neill, W.O., Gabzdyl, J.T., and Steen, W.M., "The Dynamical Behaviour of Gas Jets in Laser Cutting," Laser Institute of America, Proceedings from ICALEO 1992, Vol. 75, Laser Materials Processing, pp. 449-458.

56. Beale, D.K., "Suppression of Secondary Vortical Flow in Nozzles for Free-jet Ground Testing Facilities", 38th Aerospace Sciences Meeting and Exhibt, 10-13 January 2000, Reno, NV, AIAA paper 2000-0152.

57. P.T. Harsha, "Free Turbulent Mixing: A Critical Evaluation of Theory and Experiment, "AEDC-TR-71-36, February 1871.

58. Fuchs, E, Oppolzer, H., and Rehme, H., Particle Beam Microanalysis, Fundamentals, Methods, and Applications, published by VCH Verlagsgesellschaft mbH, Weinheim (Federal republic of Germany), 1990.

59. Chapman, S.K., Working with a Scanning Electron Microscope, Lodgemark Press, England, 1986.

60. Liepmann, H.W., and Roshko, A., Elements of Gasdynamics, John Wiley and Sons, 1957, pp 125-130.

61. Hughes, W.F., and Brighton, J.A., Theory and Problems of Fluid Dynamics, Schaum's Outline Series in Engineering, McGraw-Hill Book Company, 1967, 77, 139-140.

62. ASM International, Metals Handbook, Vol. 3: Alloy Phase Diagrams, 1992, p. 3.43.

APPENDICES

APPENDIX A: CALCULATIONS

APPENDIX A-1: WORKZONE CALCULATIONS

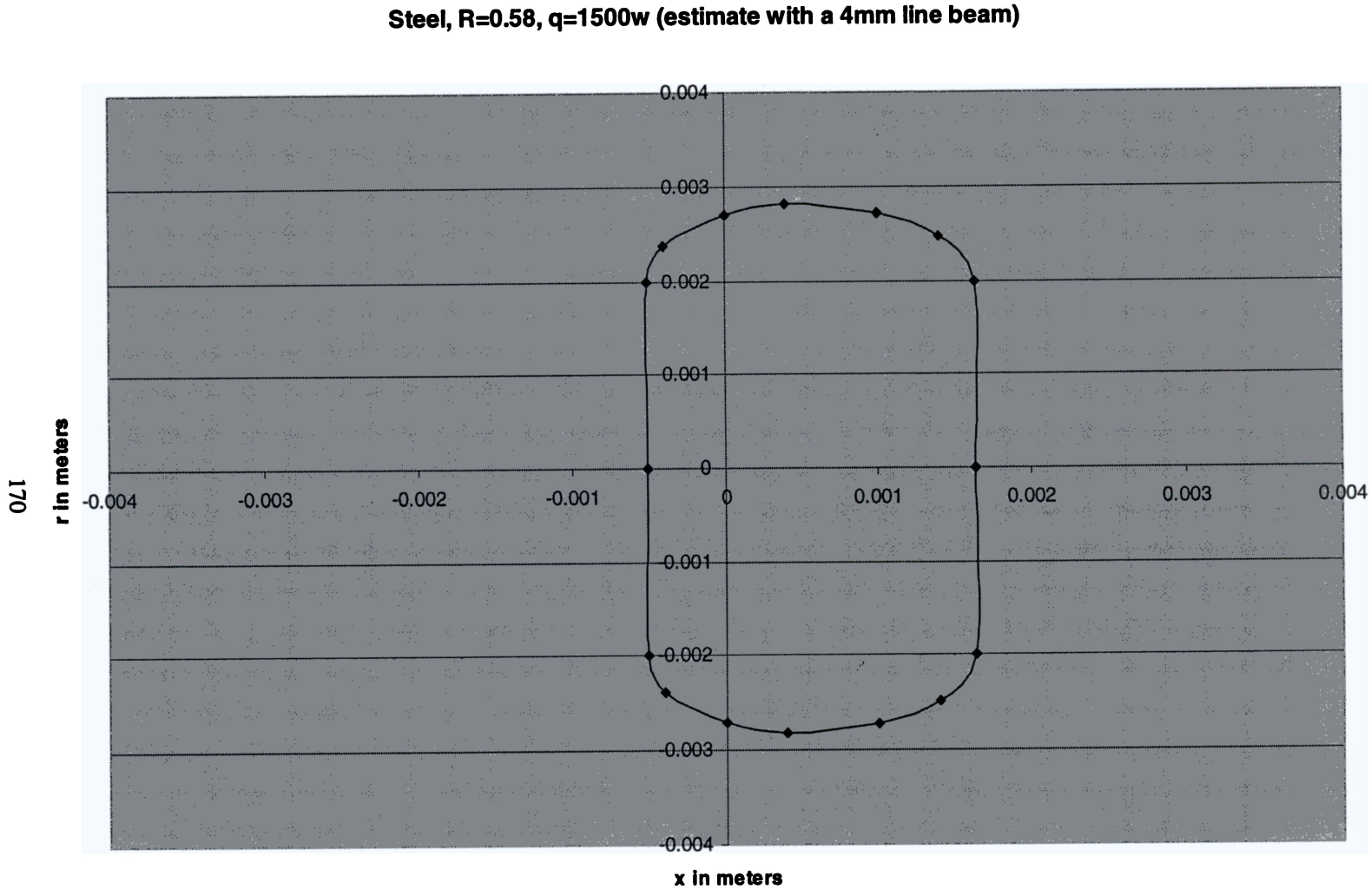

Figure A-1. Work Zone Calculation of Steel at R=0.58, 4mm line beam

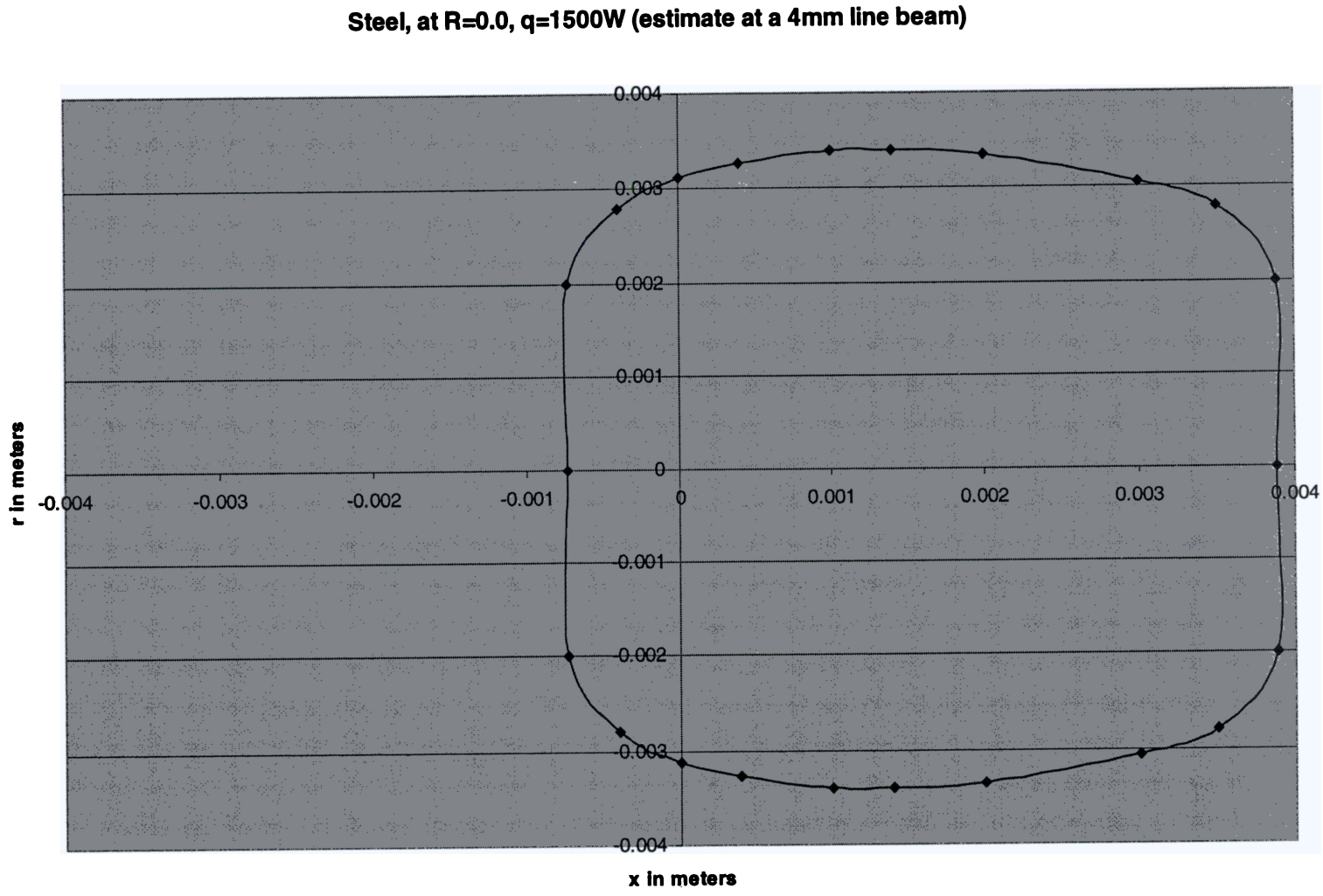

Figure A-2. Work Zone Calculation of Steel at R=0.0, 4mm line beam.

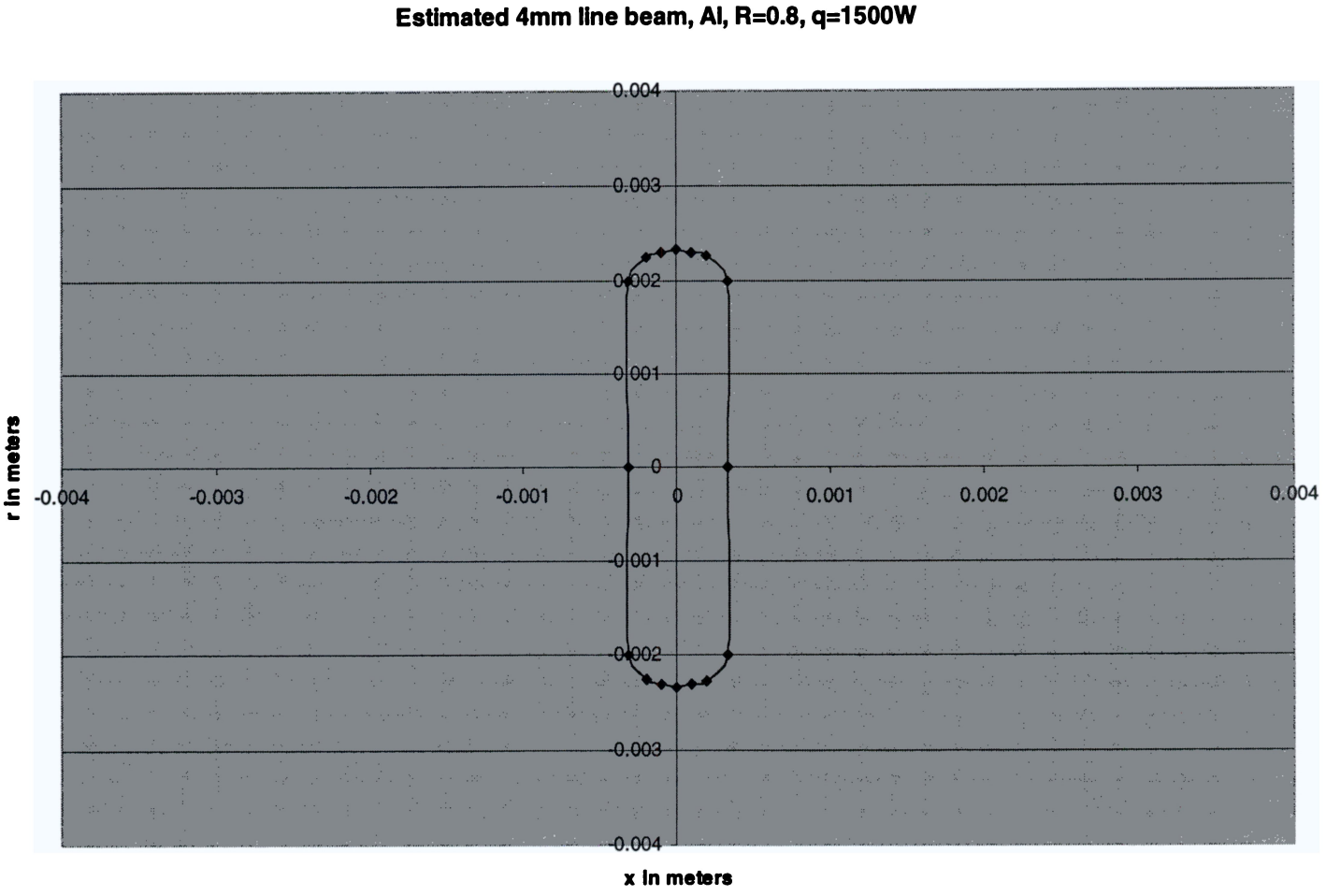

Figure A-3: Melt zone of aluminum at R=0.8.

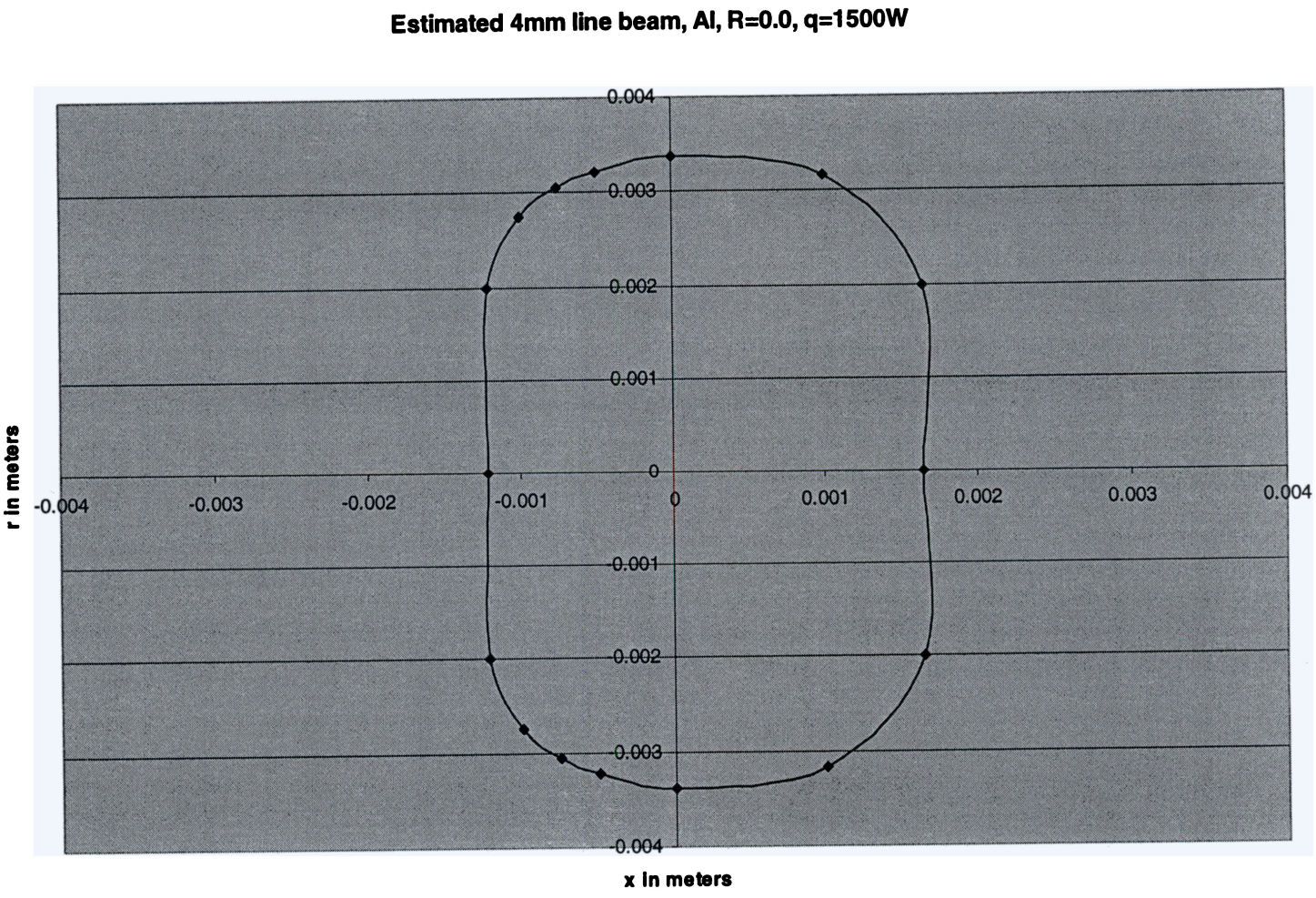

Figure A-4: Melt zone of aluminum at R=0.0.

APPENDIX A-2: Re CALCULATIONS

Re Calculations

Prototype

$$\mathrm{Re}_{pro} = \frac{\rho_{pro} V_{pro} D_{pro}}{\mu_{pro}}$$

$$V_{pro} = M_{pro} a_{pro}$$

$$a_{pro} = \sqrt{gRT_s\gamma}$$

$$\frac{T_0}{T_s} = \left(1 + \frac{\gamma - 1}{2}\right) M^2$$

where

He: μ=4.75X10^{-7} lb$_f$-sec/ft^2, ρ=0.01039lb$_m$/ft^3, γ=1.66

Ar: μ=4.67X10^{-7} lb$_f$-sec/ft^2, ρ=0.1037lb$_m$/ft^3, γ=1.67

N_2: μ=4.X10^{-7} lb$_f$-sec/ft^2, ρ=0.0727lb$_m$/ft^3, γ=1.41

The first step is to calculate the static temperature at M=0.15 and ambient conditions:

$$T_{sHe} = \frac{530}{\left(1 + \frac{1.66 - 1}{2}(0.15)^2\right)} = 526 \deg F$$

$$T_{sAr} = \frac{530}{\left(1 + \frac{1.67 - 1}{2}(0.15)^2\right)} = 526 \deg F$$

$$T_{sN2} = \frac{530}{\left(1 + \frac{1.4 - 1}{2}(0.15)^2\right)} = 528 \deg F$$

The next step is to calculate the speed of sound.

$$a_{He} = \sqrt{(32.2)(1543.5/4)(526)(1.66)} = 3294\,ft/s$$

$$a_{Ar} = \sqrt{(32.2)(1543.5/39.9)(526)(1.67)} = 1046\,ft/s$$

$$a_{N2} = \sqrt{(32.2)(1543.5/28)(528)(1.4)} = 1145\,ft/s$$

and the velocity at M=0.15

$$V_{He} = 0.15(3294) = 494\,ft/s$$
$$V_{Ar} = 0.15(1046) = 157\,ft/s$$
$$V_{N2} = 0.15(1145) = 171.75\,ft/s$$

The Re of each of the gaes for the prototype:

$$\mathrm{Re}_{He} = \frac{(0.01039)(494)(0.0679)}{(4.75X10^{-7})(32.2)} = \frac{\left(\frac{lb_m}{ft^3}\right)\left(\frac{ft}{s}\right)(ft)}{\left(\frac{lb_f - \sec}{ft^2}\right)\left(\frac{lb_m - ft}{lb_f - \sec^2}\right)} = 22757.97$$

$$\mathrm{Re}_{He} \cong 23{,}000$$

$$\mathrm{Re}_{Ar} = \frac{(0.1037)(157)(0.0679)}{(4.67X10^{-7})(32.2)} = \frac{\left(\frac{lb_m}{ft^3}\right)\left(\frac{ft}{s}\right)(ft)}{\left(\frac{lb_f - \sec}{ft^2}\right)\left(\frac{lb_m - ft}{lb_f - \sec^2}\right)} = 73514.9$$

$$\mathrm{Re}_{Ar} \cong 74{,}000$$

$$\mathrm{Re}_{N2} = \frac{(0.0727)(172)(0.0679)}{(4.X10^{-7})(32.2)} = \frac{\left(\frac{lb_m}{ft^3}\right)\left(\frac{ft}{s}\right)(ft)}{\left(\frac{lb_f - \sec}{ft^2}\right)\left(\frac{lb_m - ft}{lb_f - \sec^2}\right)} = 65919.93$$

$$\mathrm{Re}_{N2} \cong 66{,}000.$$

Now the next step is to equate the prototype Re with the Re of the water tunnel simulation. The properties of water for the Re calculation are:

μ=2X10^{-5} lbf-sec/ft^2, ρ=62.4lbm/ft^3

$$\mathrm{Re}_{He} = \mathrm{Re}_{w(He)} = 23{,}000$$

$$V = \frac{(\mathrm{Re})(\mu)(g)}{(\rho)(D)} = \frac{(23000)(2X10^{-5})(32.174)}{(62.4)(.2038)} = 1.16 ft/s$$

for the He simulation, the D is 3 times that of the prototype. At a velocity of 1.16ft/s, the flowrate is :

$$VA = volumetric_{flow} = 1.16X\pi(.2038/2)^2 = 0.0378 ft^3/s$$
$$= 2.27 ft^3/\min = 16.98 GPM$$

For the Ar simulation:

$$\mathrm{Re}_{Ar} = \mathrm{Re}_{w(Ar)} = 74{,}000$$

$$V = \frac{(\mathrm{Re})(\mu)(g)}{(\rho)(D)} = \frac{(74000)(2X10^{-5})(32.174)}{(62.4)(.2038)} = 3.74 ft/s$$

Which at a size of three times the prototype the flowrate of water would be:

$$VA = volumetric_{flow} = 3.74X\pi(.2038/2)^2 = 0.1275 ft^3/s$$
$$= 7.65 ft^3/\min = 57.2 GPM$$

As there is only 18GPM available at the UTSI water tunnel, a different size will have to be used for the Ar simulation. The calculation for 1 times the prototype follows:

$$\mathrm{Re}_{Ar} = \mathrm{Re}_{w(Ar)} = 74{,}000$$

$$V = \frac{(\mathrm{Re})(\mu)(g)}{(\rho)(D)} = \frac{(74000)(2X10^{-5})(32.174)}{(62.4)(.0679)} = 11.10 ft/s$$

That corresponds to a flowrate of

$$VA = volumetric_{flow} = 11.10X\pi(.0679/2)^2 = 0.0402 ft^3/$$
$$= 2.412 ft^3/\min = 18.04 GPM$$

The N2 simulation, at 1 times the prototype size:

$$\mathrm{Re}_{N2} = \mathrm{Re}_{w(N2)} = 66{,}000$$

$$V = \frac{(\mathrm{Re})(\mu)(g)}{(\rho)(D)} = \frac{(66000)(2X10^{-5})(32.174)}{(62.4)(.0679)} = 10.02 ft/s$$

The corresponds to a flowrate of

$$VA = volumetric_{flow} = 10.02 X \pi (.0679/2)^2 = 0.03628 ft^3 / s$$
$$= 2.18 ft^3 / \min = 16.28 GPM$$

APPENDIX B: SUPPLEMENTAL BACKGROUND

THEORECTICAL NOZZLE FLOW

In order to have a complete review of jet flow; nozzle flow must be looked at first. A nozzle is defined as a short tube with a constriction in it designed to speed up or direct a flow. This flow is referred to as a jet. Nozzles are used to produce jets in applications from aircraft engines to garden hoses and are usually described by the speed range of the flow. Subsonic nozzles produce at their exit a jet speed less than the speed of sound; sonic nozzles produce at their exit a jet at the speed of sound; and supersonic nozzles produce at their exit a jet at a speed greater than the speed of sound. Whether or not a nozzle produces supersonic or subsonic flow is a function of both the nozzle geometry and the pressure conditions at the nozzle entrance and nozzle exit, specifically the total pressure, P_0, at the entrance of the nozzle geometry and the static pressure at the nozzle geometry exit, P_e. This relationship is presented for isentropic flow in the Area-Mach number relationship [60].

$$\left(\frac{A^*}{A}\right)^2 = \frac{1}{M^2}\left[\frac{2}{\gamma+1}\left(1+\frac{\gamma-1}{2}M^2\right)\right]^{\frac{\gamma+1}{\gamma-1}}$$

Where A* is the area at the throat where the Mach number, M, equals 1, and A is the area at the axial position at which M is to be calculated (in this case the nozzle exit), and γ is the ratio of specific heats (specific heat at constant pressure to the specific heat at constant volume). Applying the isentropic relationship between the pressure ratio P_e /P_0 and M, the ratio of A*/A becomes:

$$\frac{A^*}{A} = \frac{\left[1-\left(\frac{p_e}{p_0}\right)^{\frac{\gamma-1}{\gamma}}\right]^{1/2}\left(\frac{p_e}{p_0}\right)^{\frac{1}{\gamma}}}{\left(\frac{\gamma-1}{2}\right)^{\frac{1}{2}}\left(\frac{2}{\gamma+1}\right)^{\left(\frac{1}{2}\right)\left(\frac{\gamma+1}{\gamma-1}\right)}}$$

The area-Mach number relationship is an equation that is double valued, for each A*/A ratio two Mach number (or pressure ratio) satisfy the equation. This equation is plotted in Figure B-1 . The top leg of the curve is the subsonic leg and the bottom leg is the supersonic leg. Notice that the same nozzle geometry, or A*/A, can produce either subsonic flow or supersonic flow. It is a combination of A*/A and pressure ratio, $P_e / P_{0,\text{that}}$ determines whether a nozzle produces subsonic or supersonic flow.

Converging nozzle flow is illustrated in Figure B-2. This geometrically is a circular cross-section reducing down to a smaller circular cross-section, normally called a conic nozzle. To analyze the flow in this nozzle, one must begin with the conservation equations of mass and energy.

Energy equation:

$$\frac{V^2}{2} + c_p T = 0$$

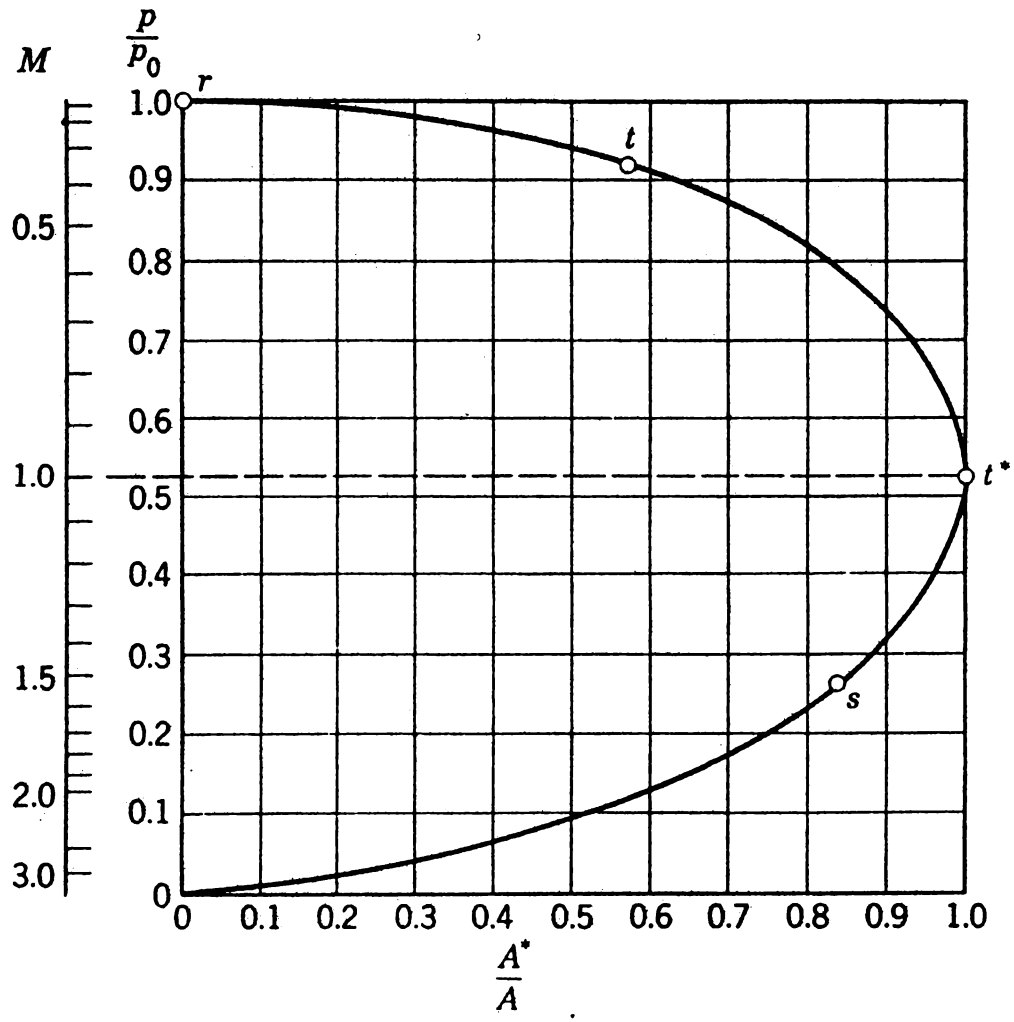

Figure B-1. The Area-Mach Number Relationship Plotted, Showing The Two Values of Mach Number for Each Area Ratio [60]

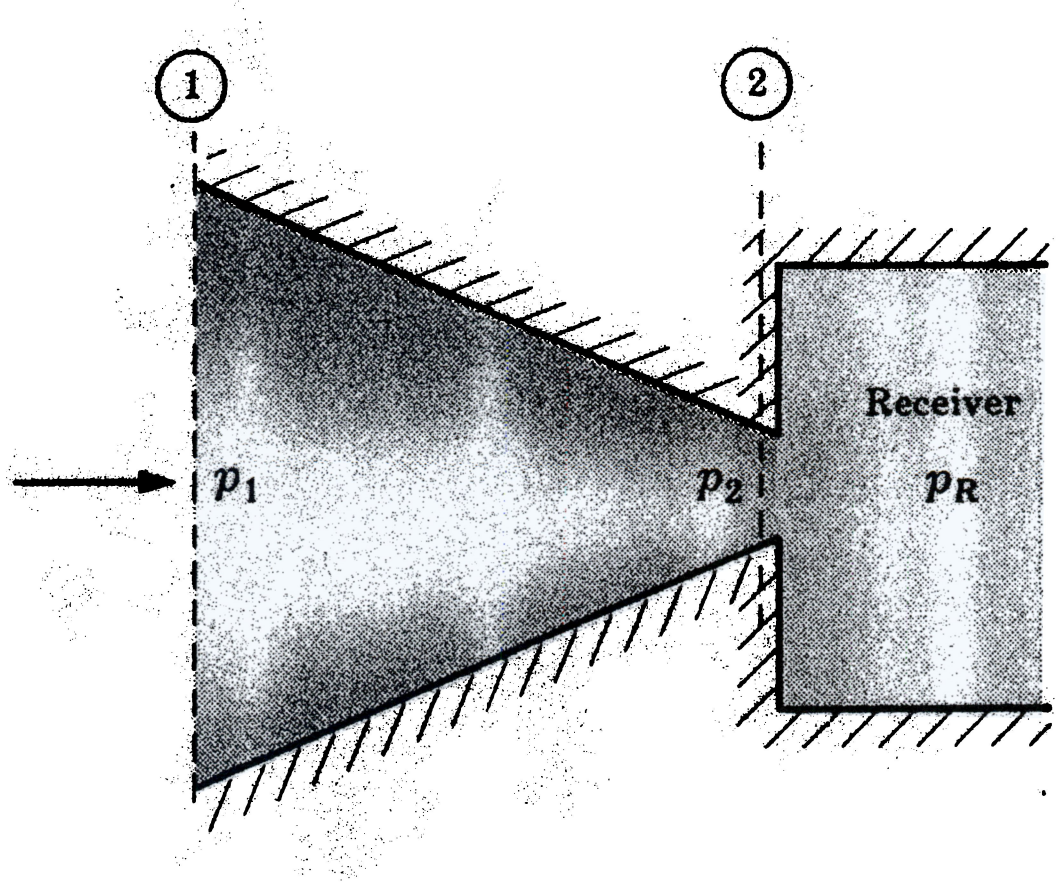

Figure B-2. The Geometry for Converging Nozzle Flow into a Receiver [61]. The large arrow is the airflow direction, 1 indicates the position of station 1, and 2 indicates the position of station 2.

Mass (or continuity) equation for a control volume:

$$\rho AV = (\rho + \delta\rho)(V + \delta V)A$$

Where V is the velocity in the axial direction of the nozzle, c_p is the specific heat at constant pressure of the gas, ρ is the density of the gas, A is the cross-sectional area of the nozzle, T is the static temperature of the gas and δ is the difference of each parameter between the first location and the second location. Combining and manipulating these two equations results in a simpler area-Mach number relationship [61]:

$$\frac{dA}{A} = \frac{dV}{V}\left(M^2 - 1\right)$$

This equation has a couple of surprising results. For M less than one (subsonic flow), an increase in area results in a decrease in velocity. The opposite is true for M greater than one (supersonic flow), an increase in area produces an increase in velocity. How the flow responds to changes in geometric area is dependent on the initial conditions of the flow and those changes are predictable by applying the conservation laws. For the converging nozzle, with subsonic flow at the entrance to the nozzle, the velocity of the flow at the exit (or minimum area or throat) is greater because of the decreasing area. If the nozzle geometry was a divergent one, one where the circular cross-section increases as the flow travels through the nozzle, the same conservation laws apply.

Nozzles that have a geometric minimum have the unique feature that they can choke. This phenomena, called choking, can be illustrated by the following equation, developed by Hughes and Brighton in reference 61:

$$\frac{\overset{0}{m}}{A_2} = \left\{ \frac{2\gamma}{\gamma - 1} \frac{p_1}{v_1} \left[\left(\frac{p_2}{p_1} \right)^{\frac{2}{\gamma}} - \left(\frac{p_2}{p_1} \right)^{\left(\frac{\gamma+1}{\gamma} \right)} \right] \right\}^{\frac{1}{2}}$$

This equation results in the curve presented in Figure B3a. The only problem is that the curve is roughly half incorrect. When the pressure at station 1 is kept constant and the pressure at the exit of the nozzle is reduced, the pressure gradient between the two stations cause the mass to flow. The more the pressure at station two is reduced the more the mass flow increases through the nozzle, but only to a point. Once the point is reached, the mass flow remains constant, no matter how much further the reservoir pressure is reduced. This is the choke point. In actuality, the right hand portion of the curve in Figure B3a is correct to a point, where the reservoir pressure is now called the critical pressure, p_c. To find that point, the proceeding equation is differentiated with respect to the pressure ratio, then the equation is set to zero to obtain the critical pressure ratio. The curve presented in Figure B3a, is now modified to include the constant mass flowrate beginning at the critical pressure ratio. This modified curve is presented in Figure B3b. One remaining fact is that the Mach number reached at the critical pressure ratio is one, and remains at one upon further pressure ratio reduction. One is the maximum Mach number that can occur in converging nozzle geometry and that occurs always at the minimum area, or the nozzle throat.

Another important feature of converging and diverging circular geometries, is that of the boundary layer development. Immediately near the surface of any wall with flow is a region of shear flow where viscosity and/or turbulence are important. This region has a

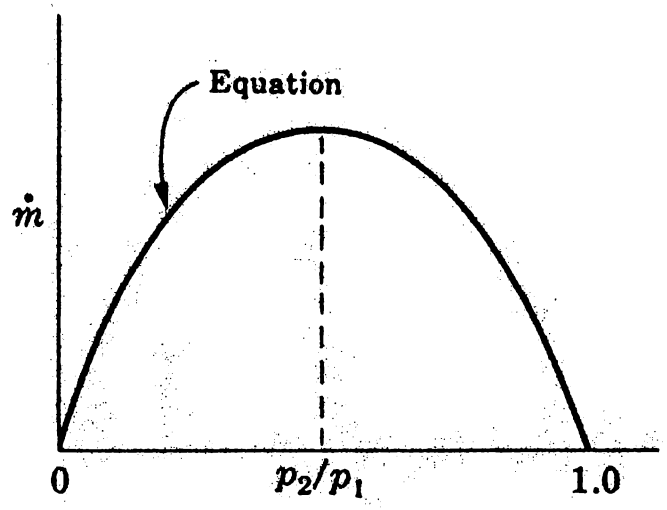

B-3a. Ideal Mass Flow

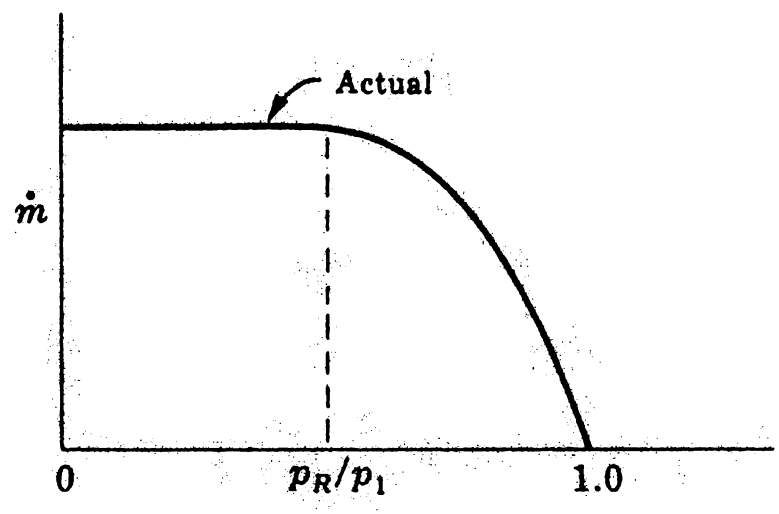

B-3b. Actual Mass Flow

Figure B-3. Mass Flow in a Converging Nozzle [61].

zero velocity right at the wall itself and an increasing velocity profile throughout the thickness of the region. The limit of the region is determined when the local velocity matches that of the free-stream. The pressure gradient along the wall downstream is vital to boundary layer development. If the pressure along the wall is increasing downstream, it is called an adverse pressure gradient. It is called adverse because the increasing pressure gradient will cause the boundary layer to increase rapidly. If the pressure gradient is too large, the boundary layer will grow so quickly that it will literally separate from the wall. If the pressure gradient is decreasing downstream, the boundary layer increases slowly, prolonging when the boundary layer separation occurs.

Figure B4 shows the effect of the boundary layer on diverging and converging subsonic nozzles (the diverging subsonic nozzle is sometimes called a diffuser). The diverging nozzle has a positive pressure gradient. As mentioned before, this will eventually lead to boundary layer separation given enough length. A large divergent angle can also cause the boundary layer to separate sooner than it would have without the angle. If this separation occurs, the cross-sectional area available for mass flow decreases. area available decreases because the separated boundary layer becomes a detached shear layer forming an outer ring around the mass flow. This reduction in available area results in a reduction of mass flow and performance of the nozzle. The design of divergent subsonic nozzle (diffusers) is an art based on empirical data, that gives combinations of divergent angles and nozzle lengths that produce controllable boundary layers and thus acceptable nozzle performance. Convergent nozzle geometries produce decreasing pressure

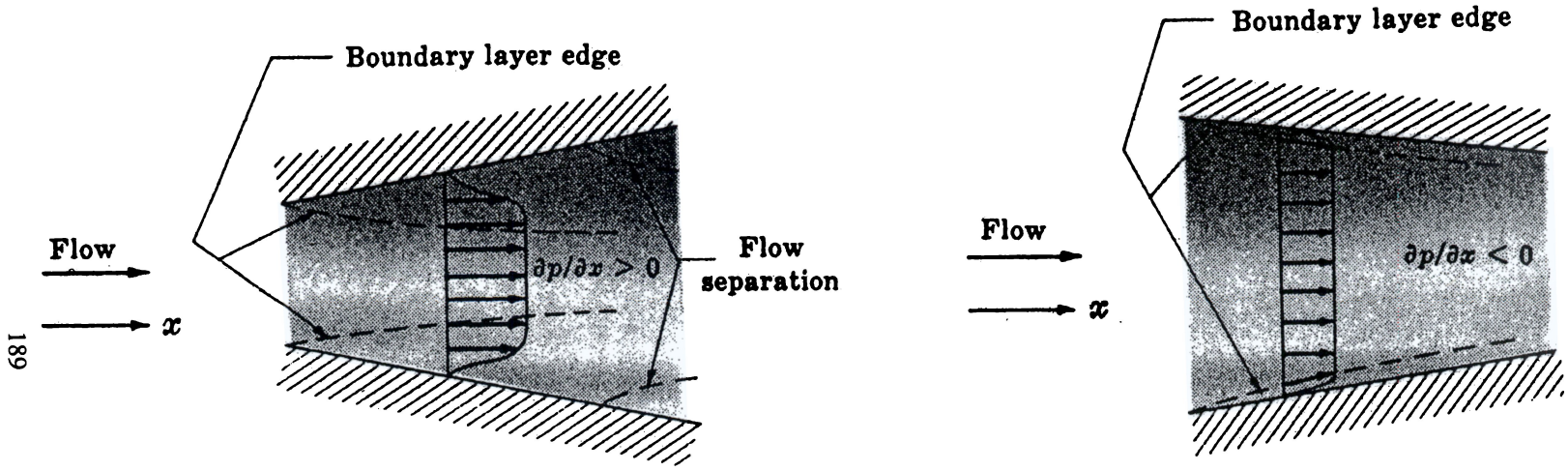

(a) Subsonic diffuser
(Diverging
Nozzle)

(b) Subsonic nozzle
(Converging
Nozzle)

Figure B-4. The Effect of the Boundary Layer on Subsonic Flow [61].

gradients thus boundary separation is normally not a problem and the design is much simpler.

As mentioned earlier, in order for supersonic flow to increase above Mach one, the area must increase from a condition of Mach one. The geometry needed to produce this is a combination of the two previously described geometries, the convergent-divergent nozzle as shown in Figure B5a. This geometry can produce either a subsonic flow at its exit or a supersonic flow at its exit depending on the pressure conditions at the nozzle entrance and nozzle exit. To explain the behavior of this nozzle, let's supply a constant pressure to the entire system, then reduce the pressure at the exit of the nozzle by a small amount as shown in Figure B5b by the a pressure contour a. The flow begins to flow with the velocity increasing in the convergent section to a maximum at the throat (or area minimum), then the velocity decreases in the divergent section producing a subsonic flow at the nozzle exit. The flow here is compressed isentropically and expanded isentropically, which means that the entire process is adiabatic and reversible. Since there are no thermodyamic losses or frictional losses, the total and static pressure at the nozzle entrance and the nozzle exit are the same. For curve b, the pressure at the nozzle exit is reduced further. The pressure ratio at the throat increases and the flowrate also increases, but the flow remains isentropic so again the total and static pressure at the nozzle entrance and exit is the same. Curve c represents the pressure profile when the nozzle exit pressure is reduced low enough to increase the Mach number in the throat to one. Here the flowrate reaches the maximum that this geometry can flow with this particular

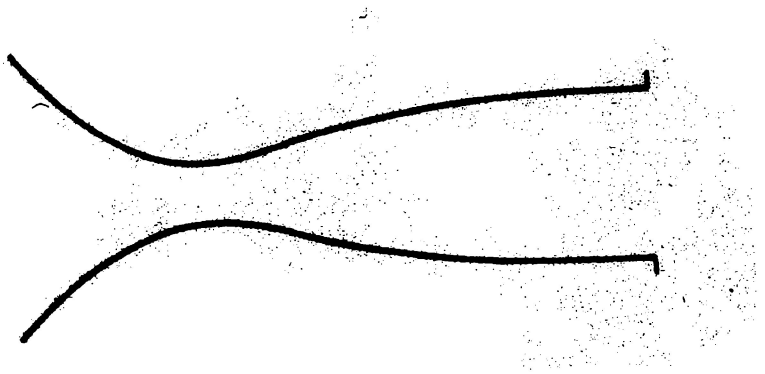

B-5a. Generic Converging/Diverging Geometry [60].

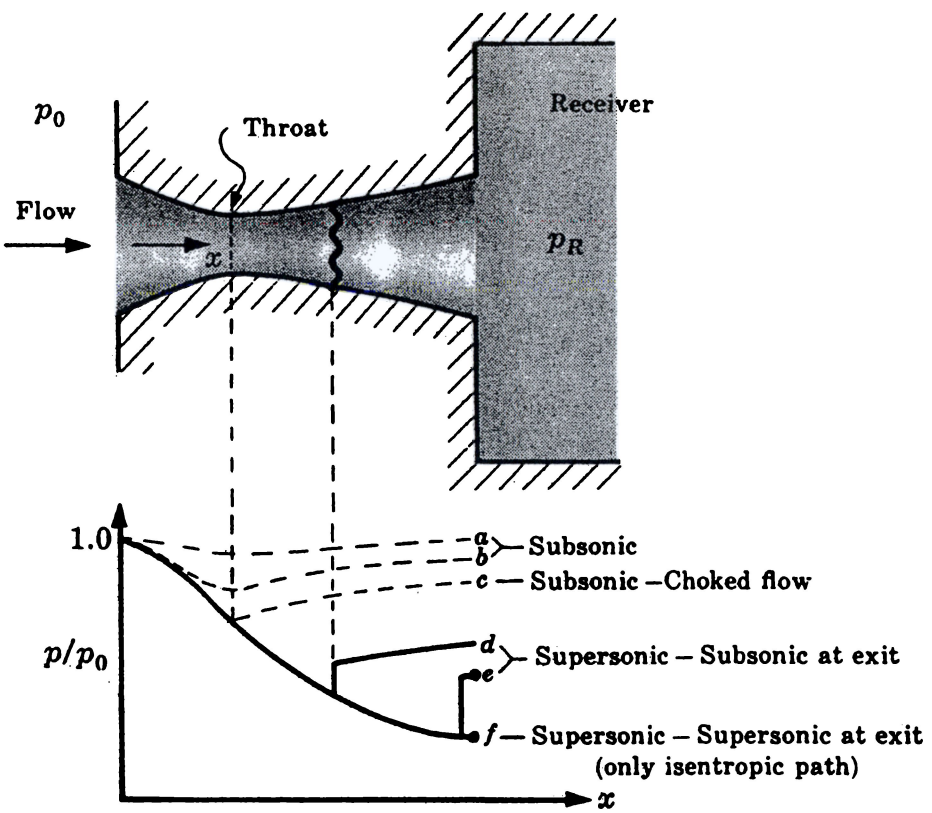

B-5b. Flow Regimes of a Converging/Diverging Nozzle [61].

Figure B-5. The Converging/Diverging Flow

set of inlet conditions. Again the flow isentropically expands subsonicly back to the entrance conditions in the divergent section. Lower the nozzle exit pressure slightly further (curve d) and a normal shock is formed in the nozzle throat and moves downstream and sits somewhat between the throat and the nozzle exit. A normal shock is an extremely thin region, situated perpendicular to the nozzle walls, across which the flow properties can change drastically. With the formation of the normal shock, the isentropic process that was throughout the entire nozzle is now only present from the nozzle entrance to the shock. Flow across a shock is not isentropic, there is a discontinuity in pressure across the shock. The total pressure decreases and the static pressure increases across the shock, and the flow is always subsonic after a normal shockwave. Lower the pressure enough, and the normal shock moves to the nozzle exit (curve e). Any further reduction in nozzle exit pressure moves the shock out of the nozzle and supersonic flow is established to the nozzle exit. Once the appropriate nozzle pressure ratio is established the Mach number produced at the exit of the nozzle is a function of the ratio of throat area to nozzle exit area, as determined by the area-Mach number relationship previously mentioned. Curve f is where the nozzle is perfectly expanded and no shock wave is found an ideal situation that does not normally exist in nature.

APPENDIX C: LASER TRIALS SUPPLIMENTAL DATA

GAS TRIAL'S TEST MATRIX

RDY Number 2508	Test Matrix Gas	Precursor	Direction	Impingement Angle	Nozzle Flow	Shroud Flow
-1	None (In Air)	None	Forward	0 degrees	None	None
-2	None (In Air)	None	Forward	0 degrees	None	None
-3	None (In Air)	None	Forward	15 degrees	None	None
-4	None (In Air)	None	Forward	15 degrees	None	None
-5	None (In Air)	None	Backward	0 degrees	None	None
-6	None (In Air)	None	Backward	0 degrees	None	None
-7	None (In Air)	None	Backward	15 degrees	None	None
-8	None (In Air)	None	Backward	15 degrees	None	None
-9	None (In Air)	Cr	Forward	0 degrees	None	None
-10	None (In Air)	Cr	Forward	0 degrees	None	None
-11	None (In Air)	Cr	Forward	15 degrees	None	None
-12	None (In Air)	Cr	Forward	15 degrees	None	None
-13	None (In Air)	Cr	Backward	0 degrees	None	None
-14	None (In Air)	Cr	Backward	0 degrees	None	None
-15	None (In Air)	Cr	Backward	15 degrees	None	None
-16	None (In Air)	Cr	Backward	15 degrees	None	None
-17	N2	None	Forward	0 degrees	50 cfhr	None
-18	N2	None	Forward	0 degrees	50 cfhr	50 cfhr
-19	N2	None	Forward	15 degrees	50 cfhr	None
-20	N2	None	Forward	15 degrees	50 cfhr	50 cfhr
-21	N2	None	Backward	0 degrees	50 cfhr	None
-22	N2	None	Backward	0 degrees	50 cfhr	50 cfhr
-23	N2	None	Backward	15 degrees	50 cfhr	None
-24	N2	None	Backward	15 degrees	50 cfhr	50 cfhr
-25	N2	Cr	Forward	0 degrees	50 cfhr	None
-26	N2	Cr	Forward	0 degrees	50 cfhr	50 cfhr
-27	N2	Cr	Forward	15 degrees	50 cfhr	None
-28	N2	Cr	Forward	15 degrees	50 cfhr	50 cfhr
-29	N2	Cr	Backward	0 degrees	50 cfhr	None
-30	N2	Cr	Backward	0 degrees	50 cfhr	50 cfhr

-31	N2	Cr	Backward	15 degrees	50 cfhr	None
-32	N2	Cr	Backward	15 degrees	50 cfhr	50 cfhr
Table 3	Continued.					
-33	He	None	Forward	0 degrees	50 cfhr	None
-34	He	None	Forward	0 degrees	50 cfhr	50 cfhr
-35	He	None	Forward	15 degrees	50 cfhr	None
-36	He	None	Forward	15 degrees	50 cfhr	50 cfhr
-37	He	None	Backward	0 degrees	50 cfhr	None
-38	He	None	Backward	0 degrees	50 cfhr	50 cfhr
-39	He	None	Backward	15 degrees	50 cfhr	None
-40	He	None	Backward	15 degrees	50 cfhr	50 cfhr
-41	He	Cr	Forward	0 degrees	50 cfhr	None
-42	He	Cr	Forward	0 degrees	50 cfhr	50 cfhr
-43	He	Cr	Forward	15 degrees	50 cfhr	None
-44	He	Cr	Forward	15 degrees	50 cfhr	50 cfhr
-45	He	Cr	Backward	0 degrees	50 cfhr	None
-46	He	Cr	Backward	0 degrees	50 cfhr	50 cfhr
-47	He	Cr	Backward	15 degrees	50 cfhr	None
-48	He	Cr	Backward	15 degrees	50 cfhr	50 cfhr
-49	Ar	None	Forward	0 degrees	50 cfhr	None
-50	Ar	None	Forward	0 degrees	50 cfhr	50 cfhr
-51	Ar	None	Forward	15 degrees	50 cfhr	None
-52	Ar	None	Forward	15 degrees	50 cfhr	50 cfhr
-53	Ar	None	Backward	0 degrees	50 cfhr	None
-54	Ar	None	Backward	0 degrees	50 cfhr	50 cfhr
-55	Ar	None	Backward	15 degrees	50 cfhr	None
-56	Ar	None	Backward	15 degrees	50 cfhr	50 cfhr
-57	Ar	Cr	Forward	0 degrees	50 cfhr	None
-58	Ar	Cr	Forward	0 degrees	50 cfhr	50 cfhr
-59	Ar	Cr	Forward	15 degrees	50 cfhr	None
-60	Ar	Cr	Forward	15 degrees	50 cfhr	50 cfhr
-61	Ar	Cr	Backward	0 degrees	50 cfhr	None
-62	Ar	Cr	Backward	0 degrees	50 cfhr	50 cfhr
-63	Ar	Cr	Backward	15 degrees	50 cfhr	None
-64	Ar	Cr	Backward	15 degrees	50 cfhr	50 cfhr
2508A						
-1	None (In Air)	Cr	Backward		15 None	None
-2	None (In Air)	Cr	Forward		15 None	None
-3	None (In Air)	Cr	Backward		0 None	None
-4	None (In Air)	Cr	Forward		0 None	None
-5	Bagged in Ar	Cr	Backward		15 None	None
-6	Bagged in Ar	Cr	Forward		15 None	None
-7	Bagged in Ar	Cr	Backward		0 None	None
-8	Bagged in Ar	Cr	Forward		0 None	None
2508B						
-17	N2	None	Forward	0 degrees	180 cfhr	None
-18	N2	None	Forward	0 degrees	180 cfhr	180 cfhr

-19	N2	None	Forward	15 degrees	180 cfhr	None
-20	N2	None	Forward	15 degrees	180 cfhr	180 cfhr
Table 3	Continued					
-23	N2	None	Backward	15 degrees	180 cfhr	None
-24	N2	None	Backward	15 degrees	180 cfhr	180 cfhr
-25	N2	Cr	Forward	0 degrees	180 cfhr	None
-26	N2	Cr	Forward	0 degrees	180 cfhr	180 cfhr
-27	N2	Cr	Forward	15 degrees	180 cfhr	None
-28	N2	Cr	Forward	15 degrees	180 cfhr	180 cfhr
-31	N2	Cr	Backward	15 degrees	180 cfhr	None
-32	N2	Cr	Backward	15 degrees	180 cfhr	180 cfhr
-33	He	None	Forward	0 degrees	63 cfhr	None
-34	He	None	Forward	0 degrees	63 cfhr	63 cfhr
-35	He	None	Forward	15 degrees	63 cfhr	None
-36	He	None	Forward	15 degrees	63 cfhr	63 cfhr
-39	He	None	Backward	15 degrees	63 cfhr	None
-40	He	None	Backward	15 degrees	63 cfhr	63 cfhr
-41	He	Cr	Forward	0 degrees	63 cfhr	None
-42	He	Cr	Forward	0 degrees	63 cfhr	63 cfhr
-43	He	Cr	Forward	15 degrees	63 cfhr	None
-44	He	Cr	Forward	15 degrees	63 cfhr	63 cfhr
-47	He	Cr	Backward	15 degrees	63 cfhr	None
-48	He	Cr	Backward	15 degrees	63 cfhr	63 cfhr
-49	Ar	None	Forward	0 degrees	180 cfhr	None
-50	Ar	None	Forward	0 degrees	180 cfhr	180 cfhr
-51	Ar	None	Forward	15 degrees	180 cfhr	None
-52	Ar	None	Forward	15 degrees	180 cfhr	180 cfhr
-55	Ar	None	Backward	15 degrees	180 cfhr	None
-56	Ar	None	Backward	15 degrees	180 cfhr	180 cfhr
-57	Ar	Cr	Forward	0 degrees	180 cfhr	None
-58	Ar	Cr	Forward	0 degrees	180 cfhr	180 cfhr
-59	Ar	Cr	Forward	15 degrees	180 cfhr	None
-60	Ar	Cr	Forward	15 degrees	180 cfhr	180 cfhr
-63	Ar	Cr	Backward	15 degrees	180 cfhr	None
-64	Ar	Cr	Backward	15 degrees	180 cfhr	180 cfhr

Forward Direction- Opposite of current processing direction (Jet is over melt pool)
Backward Direction- Current processing direction (Jet is in front of the melt pool)

TABLE C-1. Auger Test Results.

RDY	Test Matrix						composition										
Number	Gas	Precursor	Direction	Impingment	Nozzle	Shroud	Area O2	Area Fe	Area Cr	Area Oth	Pt 1 O2	Pt 1 Fe	Pt 1 Cr	Pt1Other	Pt 2 O2	Pt 2 Fe	Pt 2 Cr
2508				Angle	Flow	Flow											
-1	None (in Air)	None	Forward	0 degrees	None												
-2	None (in Air)	None	Forward	0 degrees	None												
-3	None (in Air)	None	Forward	15 degrees	None												
-4	None (in Air)	None	Forward	15 degrees	None												
-5	None (in Air)	None	Backward	0 degrees	None												
-6	None (in Air)	None	Backward	0 degrees	None												
-7	None (in Air)	None	Backward	15 degrees	None												
-8	None (in Air)	None	Backward	15 degrees	None		0	100	0	0							
-9	None (in Air)	Cr	Forward	0 degrees	None												
-10	None (in Air)	Cr	Forward	0 degrees	None												
-11	None (in Air)	Cr	Forward	15 degrees	None												
-12	None (in Air)	Cr	Forward	15 degrees	None												
-13	None (in Air)	Cr	Backward	0 degrees	None												
-14	None (in Air)	Cr	Backward	0 degrees	None												
-15	None (in Air)	Cr	Backward	15 degrees	None												
-16	None (in Air)	Cr	Backward	15 degrees	None						8	82	10	0	8	81	11
-17	N2	None	Forward	0 degrees	50 cfhr	None											
-18	N2	None	Forward	0 degrees	50 cfhr	50 cfhr											
-19	N2	None	Forward	15 degrees	50 cfhr	None											
-20	N2	None	Forward	15 degrees	50 cfhr	50 cfhr											
-21	N2	None	Backward	0 degrees	50 cfhr	None											
-22	N2	None	Backward	0 degrees	50 cfhr	50 cfhr											
-23	N2	None	Backward	15 degrees	50 cfhr	None											
-24	N2	None	Backward	15 degrees	50 cfhr	50 cfhr	50	50	0	0	0	100	0	0			
-25	N2	Cr	Forward	0 degrees	50 cfhr	None											
-26	N2	Cr	Forward	0 degrees	50 cfhr	50 cfhr											
-27	N2	Cr	Forward	15 degrees	50 cfhr	None											
-28	N2	Cr	Forward	15 degrees	50 cfhr	50 cfhr	69	4	18	c 9	3	89	9	0	0	77	23
-29	N2	Cr	Backward	0 degrees	50 cfhr	None											
-30	N2	Cr	Backward	0 degrees	50 cfhr	50 cfhr											
-31	N2	Cr	Backward	15 degrees	50 cfhr	None											
-32	N2	Cr	Backward	15 degrees	50 cfhr	50 cfhr					5	77	18	0	6	76	18
-33	He	None	Forward	0 degrees	50 cfhr	None											
-34	He	None	Forward	0 degrees	50 cfhr	50 cfhr											
-35	He	None	Forward	15 degrees	50 cfhr	None											
-36	He	None	Forward	15 degrees	50 cfhr	50 cfhr											
-37	He	None	Backward	0 degrees	50 cfhr	None											
-38	He	None	Backward	0 degrees	50 cfhr	50 cfhr											
-39	He	None	Backward	15 degrees	50 cfhr	None											
-40	He	None	Backward	15 degrees	50 cfhr	50 cfhr	33	67	0	0							
-41	He	Cr	Forward	0 degrees	50 cfhr	None											
-42	He	Cr	Forward	0 degrees	50 cfhr	50 cfhr											
-43	He	Cr	Forward	15 degrees	50 cfhr	None											
-44	He	Cr	Forward	15 degrees	50 cfhr	50 cfhr	75	3	22	0	6	84	10	0	9	75	16
-45	He	Cr	Backward	0 degrees	50 cfhr	None											
-46	He	Cr	Backward	0 degrees	50 cfhr	50 cfhr											
-47	He	Cr	Backward	15 degrees	50 cfhr	None											
-48	He	Cr	Backward	15 degrees	50 cfhr	50 cfhr	50	6	18	C22,Si3	9	71	20	0	7	64	29
-49	Ar	None	Forward	0 degrees	50 cfhr	None											
-50	Ar	None	Forward	0 degrees	50 cfhr	50 cfhr											
-51	Ar	None	Forward	15 degrees	50 cfhr	None											
-52	Ar	None	Forward	15 degrees	50 cfhr	50 cfhr											
-53	Ar	None	Backward	0 degrees	50 cfhr	None											
-54	Ar	None	Backward	0 degrees	50 cfhr	50 cfhr											
-55	Ar	None	Backward	15 degrees	50 cfhr	None											
-56	Ar	None	Backward	15 degrees	50 cfhr	50 cfhr											
-57	Ar	Cr	Forward	0 degrees	50 cfhr	None											

TABLE C-1 (Continued). Auger Test Results.

-58	Ar	Cr	Forward	0 degrees	50 cfhr	50 cfhr	75	4	21	0	3	70	26	0	4	71	25
-59	Ar	Cr	Forward	15 degrees	50 cfhr	None											
-60	Ar	Cr	Forward	15 degrees	50 cfhr	50 cfhr											
-61	Ar	Cr	Backward	0 degrees	50 cfhr	None											
-62	Ar	Cr	Backward	0 degrees	50 cfhr	50 cfhr											
-63	Ar	Cr	Backward	15 degrees	50 cfhr	None	67	4	18	C11	8	72	20	0	8	56	18
-64	Ar	Cr	Backward	15 degrees	50 cfhr	50 cfhr	57	13	19	C10	6	72	21	0	5	75	20
2508A																	
-1	None (In Air)	Cr	Backward	15	None	None	70	9	22	0	9	73	18	0	0	79	21
-2	None (In Air)	Cr	Forward	15	None	None	77	6	18	0	3	75	22	0	4	75	21
-3	None (In Air)	Cr	Backward	0	None	None	76	7	17	0	6	74	20	0	10	72	19
-4	None (In Air)	Cr	Forward	0	None	None	68	7	17	C9	7	78	15	0	4	72	15
-5	Bagged in Ar	Cr	Backward	15	None	None	62	5	21	C12	0	74	26	0	0	76	24
-6	Bagged in Ar	Cr	Forward	15	None	None	76	4	20	0	0	74	26	0	0	67	33
-7	Bagged in Ar	Cr	Backward	0	None	None	58	4	20	C18	0	77	23	0	0	64	36
-8	Bagged in Ar	Cr	Forward	0	None	None	79	2	19	0	0	67	23	C10	0	73	27
2508B																	
RDY	Test Matrix						composition										
Number	Gas	Precursor	Direction	Impingment	Nozzle	Shroud	Area O2	Area Fe	Area Cr	Area Oth	Pt 1 O2	Pt 1 Fe	Pt 1 Cr	Pt1Other	Pt 2 O2	Pt 2 Fe	Pt 2 Cr
-17	N2	None	Forward	0 degrees	180 cfhr	None											
-18	N2	None	Forward	0 degrees	180 cfhr	180 cfhr											
-19	N2	None	Forward	15 degrees	180 cfhr	None											
-20	N2	None	Forward	15 degrees	180 cfhr	180 cfhr											
-23	N2	None	Backward	15 degrees	180 cfhr	None											
-24	N2	None	Backward	15 degrees	180 cfhr	180 cfhr											
-25	N2	Cr	Forward	0 degrees	180 cfhr	None											
-26	N2	Cr	Forward	0 degrees	180 cfhr	180 cfhr	78	4	17	0	0	64	19	C 17	0	74	26
-27	N2	Cr	Forward	15 degrees	180 cfhr	None											
-28	N2	Cr	Forward	15 degrees	180 cfhr	180 cfhr	74	7	19	0	18	61	21	0	14	64	22
-31	N2	Cr	Backward	15 degrees	180 cfhr	None											
-32	N2	Cr	Backward	15 degrees	180 cfhr	180 cfhr	59	8	15	C 18	11	68	21	0	8	64	28
-33	He	None	Forward	0 degrees	63 cfhr	None											
-34	He	None	Forward	0 degrees	63 cfhr	63 cfhr											
-35	He	None	Forward	15 degrees	63 cfhr	None											
-36	He	None	Forward	15 degrees	63 cfhr	63 cfhr											
-39	He	None	Backward	15 degrees	63 cfhr	None											
-40	He	None	Backward	15 degrees	63 cfhr	63 cfhr											
-41	He	Cr	Forward	0 degrees	63 cfhr	None	75	5	20	0	8	48	11	C 34	12	50	12
-42	He	Cr	Forward	0 degrees	63 cfhr	63 cfhr	70	6	24	0	11	78	11	0	9	66	25
-43	He	Cr	Forward	15 degrees	63 cfhr	None	77	3	20	0	15	63	22	0	17	57	26
-44	He	Cr	Forward	15 degrees	63 cfhr	63 cfhr	74	4	22	0	17	60	23	0	17	65	18
-47	He	Cr	Backward	15 degrees	63 cfhr	None	67	5	19	C 9	0	68	32	0	0	71	29
-48	He	Cr	Backward	15 degrees	63 cfhr	63 cfhr	77	3	20	0	12	69	19	0	12	65	23
-49	Ar	None	Forward	0 degrees	180 cfhr	None											
-50	Ar	None	Forward	0 degrees	180 cfhr	180 cfhr											
-51	Ar	None	Forward	15 degrees	180 cfhr	None											
-52	Ar	None	Forward	15 degrees	180 cfhr	180 cfhr	64	36	0	0	13	87	0	0	11	89	0
-55	Ar	None	Backward	15 degrees	180 cfhr	None											
-56	Ar	None	Backward	15 degrees	180 cfhr	180 cfhr	66	34	0	0	10	90	0	0	11	89	0
-57	Ar	Cr	Forward	0 degrees	180 cfhr	None	75	5	21	0	10	68	22	0	9	72	19
-58	Ar	Cr	Forward	0 degrees	180 cfhr	180 cfhr	78	2	20	0	19	70	12	0	20	57	11
-59	Ar	Cr	Forward	15 degrees	180 cfhr	None	77	3	20	0	15	68	17	0	15	62	22
-60	Ar	Cr	Forward	15 degrees	180 cfhr	180 cfhr	79	0	21	0	11	71	18	0	12	64	23
-63	Ar	Cr	Backward	15 degrees	180 cfhr	None	78	2	20	0	5	74	21	0	3	79	18
-64	Ar	Cr	Backward	15 degrees	180 cfhr	180 cfhr	80	2	18	0	16	70	14	0	15	71	13

Forward Direction- Opposite of current processing direction (Jet is over melt pool)

Backward Direction- Current processing direction (Jet is in front of the melt pool)

VITA

Terri Lynn Brock Tramel was born at Beale AFB, California on October 28, 1964. She attended public schools in Japan, Australia, California, West Virginia, Virginia, Illinois, Oklahoma, Colorado, and Tennessee. She graduated high school from Hedgesville High School in West Virginia in 1981. She entered college at Shepherds College in Sheperdstown West Virginia and transferred to West Virginia University where she received a Bachelor's of Science in Aerospace Engineering. After a short time in the United States Air Force, she began working at Aerojet Strategic Propulsion Company in 1986. She continued her education at Sacramento State University and the University of California at Davis, where she received at Master's of Science in Mechanical Engineering/Aeronautical Sciences in 1989. In 1990 she began working with Sverdrup Technology Inc. at Arnold Engineering and Development Center, AEDC, and continued her education at the University of Tennessee's Space Institute, UTSI. In 1997 she left AEDC to pursue her Ph.D. full-time at UTSI. The doctoral degree was received May 2001.

She is presently working with NASA at Marshall Space Flight Center in their Experimental Facilities Group. She is a member of the American Institute of Aeronautics and Astronautics, AIAA, and the Laser Institute of America, LIA.